

Functional coatings für steel melt filtration/ Funktionale Beschichtungen für die Stahlschmelzefiltration

Von der Fakultät für Maschinenbau, Verfahrens- und Energietechnik
der Technischen Universität Bergakademie Freiberg
genehmigte

DISSERTATION

zur Erlangung des akademischen Grades

Doktor-Ingenieur

Dr.-Ing.

vorgelegt

von Dipl.-Ing. Anne Schmidt

geboren am 25.01.1991 in Freiberg, Sachsen

Gutachter: Prof. Dr.-Ing. habil. Christos G. Aneziris, Freiberg
Prof. Dr.-Ing. Olena Volkova, Freiberg

Tag der Verleihung: 02.02.2022

Versicherung

Hiermit versichere ich, dass ich die vorliegende Arbeit ohne unzulässige Hilfe Dritter und ohne Benutzung anderer als der angegebenen Hilfsmittel angefertigt habe; die aus fremden Quellen direkt oder indirekt übernommenen Gedanken sind als solche kenntlich gemacht.

Die Hilfe eines Promotionsberaters habe ich nicht in Anspruch genommen. Weitere Personen haben von mir keine geldwerten Leistungen für Arbeiten erhalten, die nicht als solche kenntlich gemacht worden sind.

Die Arbeit wurde bisher weder im Inland noch im Ausland in gleicher oder ähnlicher Form einer anderen Prüfungsbehörde vorgelegt.

Acknowledgement

This PhD thesis was accomplished within the frame of the Collaborative Research Center 920 "Multifunctional filters for metal melt filtration – a contribution to zero defect materials." at the Institute of Ceramics, Refractories and Composite Materials of the Technische Universität Bergakademie Freiberg. Thankfully, it has been financially supported by the German Research Foundation (DFG).

Many people have assisted me over the course of this PhD. First of all, I would like to thank my primary supervisor, Prof. Christos G. Aneziris, for his advise, trust and guidance throughout the entirety of this PhD.

Secondly, my sincere thanks go to Prof. Olena Volkova for being my second supervisor.

Furthermore I thank my fellow co-workers for their patience with my endless questions and discussions, especially Dr.-Ing. Jens Fruhstorfer, Dr.-Ing. Steffen Dudczig, Tony Wetzig, Dr.-Ing. Nora Brachhold, Dr.-Ing. Tilo Zienert and Dr.-Ing. Anton Salomon. I acknowledge Dr.-Ing. Jana Hubalkova for CT characterization, Dr.-Ing. Bruno Luchini for CT data analysis, Dr.-Ing. Gert Schmidt for scanning electron microscopy (SEM) and Aspex, Dr.-Ing. Harry Berek for electron backscatter diffraction (EBSD), Carolin Ludewig for sample preparation for SEM and EBSD, David Thiele and Ricardo Fricke for support during experiments, Ursula Querner and Madlen Müller for particle size distribution and mercury pressure porosimetry, Jaquelin Höhne for cold crushing strength. My thanks go to my student assistant Bastian Matzke for his support with lab tasks during my pregnancy.

I thank Dr.-Ing. Jens Fruhstorfer and Katja Fröhlich for proof reading this thesis.

My deepest thanks go to my friends and family for their unwavering support. Kati, Ute, and my loving husband, Peter, who have been incredibly supportive and encouraging me in every possible way on this journey.

Abstract

In order to considerably improve the quality of steel products, efforts are being made to increase the cleanness of steel. It is known that the size, type and distribution of non-metallic inclusions (NMIs) in metals significantly influence their mechanical properties. Within the frame of the Collaborativ Research Centre 920 "Multifunctional filters for metal melt filtration – a contribution to zero defect materials.", carbon-bonded alumina filters for steel melt filtration has been investigated. In the present thesis, the interactions between coated carbon-bonded alumina filters and a steel melt were investigated in more detail, with the porous coatings being based on alumina. The time-depended behaviour was evaluated by immersing coated filters for different dwell times. After the immersion tests, the microstructure of the filter surface and the NMIs remaining in the solidified steel were examined to comprehend the interactions.

The here presented results imply that carbon of the carbon-bonded alumina substrate took part in the filter–steel interactions. The presence of dissolved carbon at the filter–steel melt interface is essential to promote alumina dissolution and precipitation processes. Thereby, the melt was locally supersaturated with aluminium, which reacted with dissolved oxygen to form secondary corundum. During these interactions, a liquid oxide film was formed directly at the ceramic surface and provided nuclei for heterogeneous nucleation of secondary corundum. After immersion during cooling, a characteristic layer built-up formed at the filters surface. All alumina-based coated filters contributed to the filtration of especially alumina-based NMIs, and outperformed the uncoated carbon-bonded alumina filter.

During the first experimental trials, it became obvious that the thermal shock resistance of the alumina coating has to be enhanced. For this purpose, a material combination was investigated which so far has not been used as a coating material to the author's knowledge: alumina-zirconia-titania in the ration 95:2.5:2.5. This material is known for its excellent thermal shock resistance. Thereby, the influence of zirconia or titania doping of the coating were considered. The addition of titania enhanced wetting of this filter by the steel melt. As a result, alumina inclusions of the steel melt were modified: they were more in number, but distinctly smaller compared to trials without filter or the immersion of the other filter types. Especially, the

decreased average area of the alumina inclusions is interesting because the particle size of NMIs strongly influences the fatigue life of a steel product. The deformability of a steel product, however, is determined by the amount of NMIs. Thus, the modification of alumina inclusions by adding titania to the filter coating might present a way to tailor these inclusions depending on the product's application.

Zusammenfassung

Damit die Qualität von Stahlerzeugnissen entscheidend verbessert werden kann, werden Maßnahmen zur Erhöhung der Reinheit von Stahl erforscht. Es ist bekannt, dass Größe, Art und Verteilung von nichtmetallischen Einschlüssen (NME) in Metallen deren mechanische Eigenschaften maßgeblich beeinflussen. Im Rahmen des Sonderforschungsbereichs "Multifunktionale Filter für die Metallschmelzefiltration - Ein Beitrag zu Zero Defect Materials" werden unter anderem kohlenstoffgebundene Aluminiumoxidfilter für die Stahlschmelzefiltration entwickelt. In der vorliegenden Arbeit wurden die Wechselwirkungen zwischen beschichteten kohlenstoffgebundenen Aluminiumoxidfiltern und Stahlschmelzen näher untersucht, wobei die porösen Beschichtungen auf Aluminiumoxid basieren. Das zeitabhängige Verhalten dieser Wechselwirkungen wurde anhand des Eintauchens von beschichteten Filtern für unterschiedliche Verweilzeiten erforscht. Im abgekühlten Zustand wurden die Mikrostruktur der Filteroberfläche und die im erstarrten Stahl verbliebenen NME analysiert, um die Wechselwirkungen nachzuvollziehen.

Die hier vorgestellten Ergebnisse legen nahe, dass sich der Kohlenstoff des kohlenstoffgebundenen Aluminiumoxid-Substrats an den Filter-Stahl-Wechselwirkungen beteiligte. Die Präsenz von gelöstem Kohlenstoff an der Grenzfläche zwischen Filter und Stahlschmelze ist für die dortigen Lösungs- und Ausscheidungsprozesse von Aluminiumoxid unerlässlich. Dabei übersättigte die Schmelze lokal mit Aluminium, welches wiederum mit gelöstem Sauerstoff Sekundärkorund bildete. Derartige Wechselwirkungen führten zur Ausbildung eines flüssigen Oxidfilmes direkt an der Keramikoberfläche, der Keime für die heterogene Sekundärkorundbildung bereitstellte. Während des Abkühlens nach dem Eintauchen bildete sich ein charakteristischer Schichtaufbau auf der Oberfläche der untersuchten Filter. Alle Filter mit Aluminiumoxid-basierter Beschichtung trugen zur Filtration von NME auf Aluminiumoxidbasis bei und übertrafen dabei den unbeschichteten kohlenstoffgebundenen Filter.

Nach der ersten Versuchsreihe wurde deutlich, dass die Temperaturwechselbeständigkeit der Aluminiumoxidbeschichtung verbessert werden muss. Aufgrund dessen wurde eine bisher noch nicht untersuchte Materialkombination zur Beschichtung getestet: Aluminiumoxid-Zirkoniumdioxid-Titandioxid im Verhältnis 95 : 2,5 : 2,5 ist

für seine hervorragende Temperaturwechselbeständigkeit bekannt. Dabei wurde auch der Einfluss der Dotierung des Beschichtungsmaterials mit Zirkondioxid oder Titandioxid untersucht. Die Zugabe von Titandioxid verbesserte die Benetzung des Filters durch die Stahlschmelze. Dies beeinflusste die Aluminiumoxideinschlüsse im Stahl: Sie waren zahlreicher, aber deutlich kleiner im Vergleich zu Tauchversuchen ohne Filter oder mit den anderen Filtertypen. Insbesondere die verringerte durchschnittliche Fläche der Aluminiumoxideinschlüsse ist interessant, da die Partikelgröße der NME die Ermüdungslebensdauer eines Stahlprodukts stark beeinflusst. Dessen Verformbarkeit wird jedoch durch die Menge der NME bestimmt. Die Modifizierung von Aluminiumoxideinschlüssen durch Zugabe von Titandioxid zur Filterbeschichtung könnte daher eine Möglichkeit darstellen, diese Einschlüsse je nach Anwendung des Produkts anzupassen.

Contents

List of Figures	xi
List of Tables	xiv
List of Abbreviations and Symbols	xvi
1. Introduction	1
2. Literature Review	4
2.1. Material system under investigation	4
2.1.1. Ceramic filters for steel melt filtration	4
2.1.2. Coating materials: alumina, titania, and zirconia	6
2.1.3. Investigated steel grade: 42CrMo4	9
2.2. Brief excursus into the physical chemistry of metallurgical processes .	11
2.2.1. How behave selected elements in molten steel	11
2.2.2. The role of gases	14
2.2.3. Redox-reactions in molten steel	16
2.2.4. Wetting phenomena	23
2.3. Non-metallic inclusions in steelmaking	27
2.3.1. What are NMIs and why are they detrimental?	28
2.3.2. Inclusion agglomeration	31
2.3.3. Detection of non-metallic inclusions	37
2.3.4. Removal of non-metallic inclusions	38
2.4. Interactions of ceramic filter and molten steel	41
2.4.1. Insights from searching appropriate refractory materials for steel melt processes	41
2.4.2. Steel melt filtration	42
2.4.3. Prior studies of the CRC 920	44
2.5. Summary and implications for the present thesis	51
3. Methodology	54
3.1. Filter manufacturing I: carbon-bonded alumina filter substrate	54
3.2. Filter manufacturing II: alumina based coatings	58

Contents

3.3. Immersion tests	59
3.4. Characterisation methods	60
4. Results and Discussion	66
4.1. Properties of the as-manufactured filters	66
4.1.1. Carbon-bonded alumina substrate	66
4.1.2. Coated filter	67
4.2. Layer build-up on immersed filters	74
4.2.1. In-situ formed, vitreous layer	76
4.2.2. Secondary alumina particles	77
4.2.3. Deposited cluster	79
4.2.4. Iron-based beads and the decarburised zone	80
4.3. Impact of immersion time: Alumina coated filters	81
4.3.1. Filters after immersion	81
4.3.2. Steel characterization	84
4.4. Influence of Carbon: Carbonaceous alumina coating	90
4.4.1. Microstructure after immersion	90
4.4.2. Steel characterization	93
4.5. Discussion: Impact of time on and role of carbon in the filter-steel melt interactions	97
4.5.1. Formation of the observed layer build-up	97
4.5.2. What happens with increasing immersion time?	100
4.5.3. Effect of carbon added to the alumina coating on the filter- steel interactions	103
4.5.4. Summary of the time dependent filter-steel interactions	104
4.6. Impact of Carbonaceous Alumina-Zirconia-Titania coatings	107
4.6.1. Microstructure after immersion tests	107
4.6.2. Steel characterisation	113
4.6.3. Discussion	116
4.6.4. Summary: Influence of the titania and/or zirconia doping of the coating.	121
5. Conclusion and Outlook	123
Bibliography	127
A. Preliminary tests: Slurry development	I
A.1. Coatings A and AC	I
A.2. AC coatings with ZrO ₂ and/or TiO ₂	V

B. Filters with coating A or AC	VI
B.1. Chemical and Phase analysis of the coating material	VI
B.2. Parameters of the immersion trials	X
B.3. Microstructure characterisation	XI
B.4. Steel composition	XIV
C. Supplement information for the filters with ZrO_2 and/or TiO_2 in the coating	XVII

List of Figures

2.1. $\text{Al}_2\text{O}_3\text{-TiO}_2\text{-ZrO}_2$ phase diagram.	10
2.2. Fe-C phase diagram.	13
2.3. Bubble formation and interface reactions.	15
2.4. Ellingham diagram.	19
2.5. Cr/Mn-aluminate-spinel solid solutions.	20
2.6. $\text{MnO-SiO}_2\text{-Al}_2\text{O}_3$ phase diagram.	22
2.7. Scheme of wetting iron on $\text{Al}_2\text{O}_3\text{(-C)}$	24
2.8. Scheme interactions during wetting.	27
2.9. Morphologies of alumina inclusions in solidified steel	30
2.10. Capillary attraction forces between NMIs	32
2.11. NMI movement investigated by CLSM.	33
2.12. Clogging mechanism at an SEN wall.	36
2.13. Scheme of filtration mechanism.	40
2.14. Layer build-up on the filter surface and possible interactions.	45
2.15. $\text{Al}_2\text{O}_3\text{-C-steel}$ interface by SPS.	48
2.16. $\text{Al}_2\text{O}_3\text{-C-steel}$ interface and penetration depth.	48
2.17. Simulation of immersion trials using the SCS set-up.	50
3.1. Temperature regimes for filter production.	57
4.1. Microstructure of an uncoated filter.	67
4.2. Microstructure of A or AC coated filters by light microscopy.	68
4.3. Microstructure of an "A" coated filters after coking by SEM.	69
4.4. Microstructure of an "AC" coated filters after coking by SEM.	71
4.5. Microstructure of coated filter with titania and/or zirconia doping by light microscopy.	72
4.6. Cross-section of the titania doped coating by SEM.	73
4.7. Microstructure of coated filter with zirconia doping by SEM.	74
4.8. Summarised layer build-up on the filter surface after immersion trials.	75
4.9. Cross-section showing the vitreous layer of a filter with coating A immersed for 120 s.	77
4.10. Grain orientation of alumina at the filter surface after immersion.	78

List of Figures

4.11. Layer build-up: cluster.	79
4.12. Layer build-up: Iron-based beads on carbon particles.	80
4.13. Filters with coating A after immersion - photographs.	82
4.14. Filter with coating A after 1 s immersion - Microstructure by light microscopy.	82
4.15. Filters with coating A after immersion - Microstructure by light mi- croscopy.	83
4.16. Filters with coating A after immersion - Microstructure by SEM. . . .	84
4.17. Immersion trials of AC coated filters - Microstructure by light mi- croscopy.	90
4.18. Microstructure of an AC coated filter after 30 s immersion by electron microscopy.	91
4.19. Microstructure of an AC coated filter after 120 s immersion by elec- tron microscopy.	92
4.20. Cross-section of an AC coated filter after 30 s immersion by electron microscopy.	93
4.21. Scheme of filter-steel interactions.	105
4.22. Microstructure of coated filter with titania and/or zirconia doping after immersion by light microscopy.	109
4.23. Microstructure of uncoated filter after immersion by SEM.	110
4.24. Microstructure of a filter with coating A after immersion by SEM. . .	110
4.25. Microstructure of a filter with coating AC after immersion by SEM. .	111
4.26. Microstructure of a filter with coating AC-T after immersion by SEM.	111
4.27. Microstructure of a filter with coating AC-Z after immersion by SEM.	112
4.28. Microstructure of a filter with coating AC-ZT after immersion by SEM.	113
A.1. Slurry development AC - Slurry stability, photos	II
A.2. Slurry development AC - Slurry stability, graphs.	III
A.3. Slurry development AC - Rheology.	IV
A.4. Slurry development zirconia and/or titania doped coatings - Rheology.	V
B.1. XRD of Coating A.	VII
B.2. XRD of Coating A.	VII
B.3. SNMS of an alumina coated filter.	VIII
B.4. SNMS of an AC coated filter.	IX
B.5. Shrinkage of coated samples.	IX
B.6. Microstructure of an AC coated filters by light microscopy.	XI
B.7. Crystallinity, phase and element distribution for an 120 s immersed filter.	XII

List of Figures

B.8. Microstructure of immersed filters by light microscopy.	XIII
C.1. Supplement information: Microstructure after immersion by light microscopy, filters AC-Z and AC-ZT.	XVIII

List of Tables

2.1. Composition of the 42CrMo4 according to the standard DIN EN ISO 683-2:2018-09. [DINb]	10
2.2. Effect of selected elements of the system under investigation on the surface tension of liquid iron.	12
2.3. Diffusivity values (D_i) of various ions typical for slags in steelmaking at 1600 °C. [Tur96, p. 176]	21
3.1. Ceramic slurry compositions.	55
3.2. Particle size distribution of the raw materials.	56
3.3. Composition of the used 42CrMo4 steel	60
3.4. Rule-filed used for NMIs characterisation.	64
3.5. Adjusted rule-filed used for NMIs characterisation.	65
4.1. Strut thickness of coated filters.	69
4.2. Immersion test parameters of time-depending trials with alumina coated filters.	85
4.3. Chemical composition (extract) of the steel from the test series with filter type A.	87
4.4. Number of inclusions remaining in the solidified steel from the test series with filter type A, classified by their chemistry.	88
4.5. Inclusion size distribution of NMIs of the class " Al_2O_3 " of the immersion trials with filter type A.	89
4.6. Immersion test parameters of time-depending trials with filter samples AC.	94
4.7. Chemical composition (extract) of the steel before and after the immersion tests with the AC coated filters.	95
4.8. Number of inclusions remaining in solidified steel after immersion trials with filter type AC, classified by their chemistry.	95
4.9. Alumina inclusions remaining in solidified steel after immersion trials with the filter type AC, classified by size.	96
4.10. Immersion test parameters of time-depending trials with titania and/or zirconia doping.	114

List of Tables

4.11. Chemical composition of the steel before and after the immersion tests - AZT series.	115
4.12. Number of inclusions remaining in solidified steel after immersion tests of the AZT-test series, classified by their chemistry.	117
4.13. Alumina inclusions remaining in solidified steel after the immersion tests of the AZT-test series, classified by size.	118
 B.1. Parameter of the immersion trials with varying immersion duration of filters A and AC	 X
B.2. Chemical composition (complete) of the steel from the test series with filter type A.	XV
B.3. Chemical composition (complete) of the steel from the test series with filter type AC.	XVI
 C.1. Chemical composition of the steel before and after the immersion tests.	 XIX

List of Abbreviations and Symbols

A	coating containing alumina
AC	coating containing alumina and carbon
AC-T	coating containing alumina, titania and carbon
AC-Z	coating containing alumina, zirconia and carbon
AC-ZT	coating containing alumina, zirconia, titania and carbon
AZT	alumina-zirconia-titania
BSE	backscattered electrons
CCS	cold crushing strength
CFF	ceramic foam filter
CLSM	confocal laser scanning microscope
CRC 920	Collaborativ Research Centre 920
CT	computer tomography
EBSD	electron backscatter diffraction
EDS	energy dispersive X-ray spectrometry
FIB	focused ion beam
MWCNT	multi-walled carbon nanotube
NMI	non-metallic inclusion
OES	optical emission spectrometer
SCS	steel casting simulator
SE	secondary electrons
SEM	scanning electron microscopy

List of Abbreviations and Symbols

SEN	submerged entry nozzle
SNMS	secondary neutral mass spectroscopy
SPS	spark plasma sintering
TEM	transmission electron microscopy
ULC	ultra low carbon
WDS	wavelength dispersive X-ray spectrometry
XRD	X-ray diffraction

The denotation of the phase state of elements and their oxides orientates on the usual one in metallurgy:

{M} gaseous phase

[M] dissolved in the metal melt

(MO) dissolved in an oxide melt

1. Introduction

Permanently, the steel industry is highly interested in improving their steel products. China is a large market producing tons of mass steel products. Thus, European manufacturers compete with high-performance steel grades for special applications. To constantly improve their quality, methods to increase the purity of steel are examined because non-metallic inclusions (NMIs) and other impurities downgrade the properties of cast products. Size, type and distribution of NMIs in metals are well known to distinctly impair their mechanical properties. Especially fracture toughness, tensile strength, ductility and fatigue of the products are affected, which may result in excessive casting repairs or rejected products.[Kre+15; Mor03; ZT03b; Asl+19] Thus, not only the product properties can be improved by the removal of NMIs, it also contributes to make the whole production process more economical through reduction of scrap.

NMIs get usually trapped by slags during steelmaking. Nevertheless, small inclusions are too light though to move towards the slag by buoyancy force. During cooling, they can form larger clusters with a critical defect size. That is why numerous investigations have tackled the possibility of metal melt filtration. For decades, ceramic foam filters have successfully been applied in iron and aluminium melt filtration.[OM05] In the case of steel melt filtration, filters based on partially stabilized zirconia or carbon-bonded alumina have been used [OM05] and are still in the product portfolio of well-known foundry suppliers [Dra21; ves21; ASK21]. Especially, carbon-bonded alumina filters show very promising properties, which partially exceed the zirconia ones.[Mor03; Lip+14; Kar+14; Asl+19]

This material has been further investigated by the Collaborativ Research Centre 920 (CRC 920) "Multifunctional filters for metal melt filtration – a contribution to zero defect materials.", which started in 2011. The CRC 920 is examining the process of metal melt filtration on the basis of basic research in difference to the aforementioned reports. Different fields of science are working together to illuminate the different aspects of metal melt filtration. Thus, this work is created in an environment in which the properties of the ceramic filters as well as the separation processes of NMIs from the melt are scientifically described and investigated in order to enable their simulation. All these investigations shall lead to a fundamental

1. Introduction

understanding of the processes occurring during metal melt filtration. In the end, conclusions should be drawn from the simulations how the filters should be designed (especially with regard to the geometry and surface properties) in order to remove NMIs from molten metals most efficiently.

The Professorship of Ceramics, Refractories and metal-ceramic Composites at the TU Bergakademie Freiberg is contributing to this project with the development and manufacturing of the ceramic filters and—in the case of steel melt filtration—with immersion tests. The present thesis is based on two previous doctoral theses: the ones of Marcus Emmel [Emm14] and Enrico Storti [Sto18]. Within the first mentioned, carbon-bonded alumina filters were successfully developed and tested by industrial trials. During such trials, it was observed that the surface chemistry distinctly influences the amount of deposited inclusions at the filter surface.[Emm+13] Thereby, alumina coated $\text{Al}_2\text{O}_3\text{--C}$ filters performed best regarding inclusions smaller than $50\text{ }\mu\text{m}$ compared to uncoated, mullite coated, and carbon-bonded magnesia coated filters. These findings are supported by studies using a confocal laser scanning microscope (CLSM) [Yin+97b; Ane+13d; Ane+13a], which showed that alumina particles within a steel melt are strongly attracted by alumina. Based on these findings, investigations of the influence of different coatings on the removal of NMIs from a steel melt began. In the case of Enrico Storti [Sto18], coatings based on multi-walled carbon nanotubes (MWCNTs), calcium aluminates, and electro-spun nano-wires were investigated.

The present thesis, however, will continue to investigate the interactions of coated carbon-bonded alumina filters and molten steel in more detail. Alumina, alumina-C, and alumina-C doped with titania and/or zirconia has been investigated as coating materials. Respecting the results of Marcus Emmel as well as Enrico Storti, the time-dependend behaviour of the interactions is investigated by immersing filters for different dwell times in molten steel of the grade 42CrMo4: from 10 s, which is the shortest immersion time that can be sensibly performed with the experimental set-up, to 30 s, 60 s and 120 s.[Sch+17a] Comparing alumina coatings with and without carbon (4 mass%), the role of carbon on the time-dependend interactions will be examined more closely. In the last section of the thesis, the alumina based coating is modified by a doping of ZrO_2 and/or TiO_2 . Whereas ZrO_2 acts as strong deoxidiser, TiO_2 lowers the surface tension of liquid iron, and thereby might influence the filter interactions with the NMIs. Further, the combination of both dopants is known to posses excellent thermal shock properties, which are essential for the filter coating to avoid spalling. To the authors knowledge, these material combinations have not been investigated yet as filter coatings.

The findings will contribute to the present understanding of the processes taking

1. Introduction

place during steel melt filtration. A hypothesis regarding the interactions of a coated carbon-bonded alumina filter and a steel melt will be elaborated and shall give some inspiration for ongoing research of that topic as well as input to optimise steel melt filtration in industrial application.

2. Literature Review

For steel melt filtration, ceramic foam filters (CFFs) are usually used. [VH14] The application of CFFs and their properties had been reviewed by Emmel [Emm14] and Storti [Sto18]. A general overview about the manufacturing, characterization and application of ceramic foam filters is given in the book "Cellular Ceramics" by Schefler and Colombo [SC05]. Thus, properties of CFFs will only briefly be mentioned in the following if there is an impact on the reactions taking place between filter and steel melt. The focus of this thesis lays on the interactions of the filter material with molten steel to derive strategies for efficient steel melt filtration by selecting appropriate coating materials for carbon-bonded alumina filters. As the possible interactions in molten steel are manifold, this chapter begins with a brief introduction of the materials under investigation, which are considered in the following excursus into the physical chemistry of metallurgical processes. The interactions between elements in molten steel leads inevitably to the discussion of non-metallic inclusions: How they were formed, how they can be detected, and how they can be removed from the melt. The subsequent section reviews theories regarding steel melt filtration by ceramic foam filters, and the findings gained in the CRC 920. Finally, they will be summarised in order to outline remaining open questions and to formulate the quest of this thesis.

2.1. Material system under investigation

2.1.1. Ceramic filters for steel melt filtration

The filter application for molten steel has high requirements for the materials used: The filter has not only to withstand high temperatures ($>1560^{\circ}\text{C}$), usually they are also not preheated and thus experience a strong thermal shock. Furthermore, they have to resist the thermo-mechanical stress during casting when the hot melt initially hits the filter and subsequently flows through it. Additionally, their heat capacity should be low to reduce the quantity of heat which is absorbed from the molten steel before the filter reaches the same temperature as the metal. To compensate a high heat capacity of a filter, the melt has to be overheated to prevent it from strongly

2. Literature Review

cooling down and solidifying inside the filter in the initial phase of filter-melt contact. During casting, the filter requires a high creep resistance to keep its geometry during casting to ensure a constant flow rate. The corrosion resistance against the molten steel and the mechanical strength of the filter are essential to prevent contamination of the melt by or a failure of the filter. In addition, the strength should be sufficiently high to ensure a damage-free transport and installation of the filter. [Mor03; OM05]

These demands limit the materials which can be used. In 1990, Kondrat'ev et al. [Kon+90] tested different available ceramic materials (Al_2O_3 , ZrO_2 , MgO , CaO , alumina-graphite, and mullite). They concluded that compositions based on Al_2O_3 , ZrO_2 and their mixtures are most promising. In the following years, ceramic filters made of alumina or Mg partially stabilized ZrO_2 were developed and tested for steel melt filtration. [OM05; VH14] As the latter one meets the aforementioned demands, zirconia has been used as a filter material for steel melt filtration [RW07, p. 350-351], [OM05] and is still commercialised. [Dra21; ves21; ASK21] Nevertheless, zirconia filters exhibit some drawbacks like a high heat capacity and insufficient creep resistance in the processing environment. That led to the development of carbon-bonded alumina filters which stand out with their low heat capacity and high thermal shock resistance. [Mor03; Asł+19]

Usually, adding carbon to refractories increases the thermal shock resistance and the high temperature strength of the materials. Further, wetting by metallic melts is decreased. [RRA04] The well known drawback of carbon-bonded refractories is that carbon oxidises already from 400°C in the presence of oxygen. [Ell+91] Thereby, metals forming stable oxides at elevated temperatures, such as Al, Zr, Mg, and Si, can be added to the carbon-bonded refractory as metals, carbides or other non-oxides to diminish oxidation of carbon-bonded refractories. [YZY96].

Within the first period of the CRC 920, Emmel [Emm14] developed carbon-bonded alumina filters and successfully tested them in industrial trials. The carbon binder of these filters based on a modified coal tar pitch, which had a reduced Benzo[a]pyren content and was thus less carcinogenic. Without further modification, these filters were used as substrates in the present study. Nevertheless, there remains still a high potential for further optimisation regarding the filters. For example, Asłanowicz et al. [Asł+19] added caking coal to their slurry system and demonstrated also successful industrial casting trials. In a parallel work within the CRC 920 [Him+18], an environmentally friendly binder that based on lactose and tannin was developed, too. Another aspect is to improve the mechanical properties of such filters [Luc+18; Sal+19] or to tailor the macro-porosity of the filter by additive manufacturing. [Her+19a; Her+19b]. But these approaches are out of the scope of this thesis.

2.1.2. Coating materials: alumina, titania, and zirconia

Materials that are known to enhance clogging of submerged entry nozzles (SENs), modify non-metallic inclusions (NMIs), or benefit the coatings properties are of interest as coating materials. Aneziris et al. [Ane+13a] observed increased clogging of carbon-bonded alumina nozzles if they were coated with an alumina coating compared to non-coated nozzles. Based upon these findings, the idea that the removal of NMIs might be influenced by filter coating was born. This is the approach in the CRC 920. In the following, industrial filtration trials were conducted with coatings made of mullite, MgO–C and alumina.[Emm+13] According to the results of Emmel et al. [Emm+13]¹, alumina based NMIs preferably deposited on the alumina coated filter, the uncoated Al₂O₃–C filter, the mullite coated filter, and the MgO–C coated one in descending order. In a parallel work, Dudczig et al. [Dud+13] coated aforementioned nozzles with mullite, too. Due to its decomposition under the process conditions, it was concluded that mullite is inappropriate as coating material for steel melt filtration. Carbon-bonded alumina filters coated with carbon-bonded magnesia [Ane+13c] resulted in an in-situ spinel-formation during application.[Emm+14] According to Bock et al. [Boc+19] and confocal laser scanning microscope (CLSM) studies [Ane+13b; Ane+13c; Sch+17b] with alumina, spinel, and magnesia (described in more detail in Section 2.3.2 on page 31), carbon-bonded magnesia and spinel resulted in low rates of NMIs removal. In parallel works, Storti [Sto+15; Sto+16b; Sto+17b; Sto18] investigated the effect of fast dissolving carbon at the filter surface by coating the filters with multi-walled carbon nanotubes (MWCNTs), and also in combination with Al₂O₃ nano-sheets. Furthermore, he applied calcium aluminates [Sto+17a] as coating which resulted in interestingly high rates of NMIs removal.

Here, the track of the positive effect of the alumina coating on NMIs deposition is to be pursued further. Thus, alumina was chosen as base material for the coatings. Carbon was added in a low amount to investigate its influence on the interactions and to improve the thermal shock resistance of the coating. Further, the coating was doped with zirconia and/or titania to reflect their influence on the NMIs removal because alumina-zirconia-titania (AZT) materials were reported to have superior thermo-shock properties which is essential in the harsh environment of steel melt filtration. To the authors knowledge, these combinations were not tested yet as coating materials for this approach. Hereinafter, the applied coating materials are regarded in more detail.

¹They assessed the filtration effect by comparing the amount of inclusions being attached on the filter surface after the casting trials. Cross-sections of the filter embedded in solidified steel were evaluated by SEM image interpretation combined with EDS.

2. Literature Review

Alumina The melting point of alumina is 2050 °C. [SST07, p. 236] Furthermore, it has a high electrical resistance, hardness, resistance to wear, and chemical inertness. [Mor87, pp. 2, 39][Dan02, p. 136-139] These properties make alumina a widely used oxide ceramic material, e.g. as abrasive media, insulator or refractory material. The α -modification of alumina is the only one which is thermodynamically stable at high temperatures. Apart from the α -phase, there are also metastable modifications of Al_2O_3 , like $\gamma\text{-Al}_2\text{O}_3$ which transforms to $\alpha\text{-Al}_2\text{O}_3$ at about 1200 °C. All phase transformations to the α -phase are irreversible. [Dan02, pp. 136-139] Thus, if not mentioned otherwise, $\alpha\text{-Al}_2\text{O}_3$ is considered if spoken of alumina in this thesis.

During the application at high temperatures, the sintering characteristics of alumina are of interest. Except for utmost pure alumina, a discontinuous and anisotropic grain growth during sintering is typical. If alumina is doped with zirconia, an increased grain size is observed, and if doped with titania, anisotropic grain growth is reported. In presence of silica or lime, low melting phases are formed which induce liquid phase sintering. [SST07, pp. 793-799] It is expected that sintering under reducing atmosphere, which is the case during filter manufacturing, will result in less densification of alumina compared to sintering under oxidising conditions. [BGB88; Mir+90; Pap+97]

Titania and mixed phases with alumina Anatase, rutile and brookite are the main crystal phases of titanium dioxide, whereby rutile has the lowest free energy compared to the other two modifications and is considered as the thermodynamically stable phase. The transformation of anatase to rutile proceeds over the temperature range of 300 °C to 500 °C, depending on several factors including the annealing atmosphere, impurities or doping, grain size and strains in the microstructure. Titania is known as an environmentally friendly, non-toxic, economically accessible and corrosion resistant oxide material with interesting photo-electrochemical properties. [NPS10; HS11; RBS11; Reg+13a; Reg+13b] It is used e.g. as white pigment in print, sunscreen or food paint (E 171). The melting point of titania under oxidizing atmosphere is about 1855 °C. [21] The here used titania raw material consists of rutile.

In combination with alumina, titania is known as a sintering agent causing accelerated grain growth of alumina during sintering under oxidizing atmosphere. McKee and Aleshin [MA63] investigated the solid solubility of titania in alumina under air as well as under hydrogen at temperatures of 1400 °C, 1600 °C and 1700 °C. Under air, no solid solubility but the formation of Al_2TiO_5 was observed for all temperatures. Under hydrogen, a solubility of Ti_2O_3 of 1.0 mol%, 1.8 mol% and 2.5 mol% with increasing temperature was observed. A second phase was observed but could

2. Literature Review

not be explained, only excluded that it is Al_2TiO_5 . They observed following colour changes:

- faint pink or tan with Ti_2O_3 contents less than 1 mol%
- brown if Ti_2O_3 content is larger and darker shades with increasing Ti_2O_3 contents
- typical color of Ti_2O_3 : violet (not observed in their study)
- blue: slightly reduced TiO_2

In the end, sintering under hydrogen resulted in less densification as under air if the same sintering temperature and time were applied. According to the authors, a small amount of Ti^{4+} might diffuse in the alumina cell and cause oxygen vacancies, which promote intragrain diffusion.

As mentioned above, alumina and titania form reversibly Al_2TiO_5 , a material of which favourable thermal shock properties are reported due to the formation of a microcrack network at the grain boundaries. The formation of Al_2TiO_5 from alumina and rutile is accompanied with a volume expansion (about 11 vol%). The theoretical density of Al_2TiO_5 is 3.7 g cm^{-3} , whereas the aluminas is 3.99 g cm^{-3} and the one of rutile is 4.25 g cm^{-3} . [KG12] Much research has been undertaken to investigate the microcrack network and the resulting properties. [MA63; CB78; FM87; ONH87; KG08; NRG09; Kim10; KG12; Kim+14] Nevertheless, aluminium titanate decomposes in the temperature range of 750°C to 1300°C , by which the favourable thermal shock properties are diminished. [KG12] By adding dopants, like MgO , Fe_2O_3 , SiO_2 or mullite, the thermal stability can be improved. [Til91; KG12] Further, Naghizadeh et al. [NRG09] investigated the influence of composition and sintering atmosphere on the Al_2TiO_5 formation. They concluded that under a reducing atmosphere, Al_2TiO_5 formation is either decreased or it intensively decomposes during cooling as the phase was not detected in graphite-containing annealed sample.

Zirconia and mixed phases with alumina There are three modifications of zirconia whose transformations are reversible: [RW07, p. 137][SST07, p. 817]



The transformation of monoclinic to tetragonal is accompanied with a volume change of 5 % to 8 %. Thus, the high temperature phases are stabilized using lime, magnesia, yttrium oxide or rare earth oxides. [RW07, p. 137] The melting temperature is in the range of 2680°C to 2710°C . [SST07, p. 817-824] In special cases, the volume expansion accompanying the tetragonal to monoclinic transformation is exploited

2. Literature Review

in order to produce microcracks in a targeted manner. For example, in the case of alumina composites, the fracture energy and/or strength, and therewith the resistance to thermal (tensile) stresses can be improved by adding up to 15 vol% ZrO_2 to alumina. [Bec81] Usually, zirconia is highly resistant towards corrosion and is almost inert against other oxides, except of silica. If it is attacked by corrosion, secondary phases are involved or the stabilizers are withdrawn. [RW07, p.137] In the present work, unstabilised zirconia is used as a raw material due to its high purity.

Experiments by Svensson et al. [Sve+18] implicate that pure zirconia might be inappropriate as coating material for filtration purposes as they observed reduced nozzle clogging of Ce-treated steels if the nozzle was coated with yttrium stabilized ZrO_2 .

Alumina-zirconia-titania phases Combining alumina, titania and zirconia, a phase composition of $\alpha\text{-Al}_2\text{O}_3$, Al_2TiO_5 , ZrTiO_4 , TiO_2 , and ZrO_2 is obtained in thermodynamical equilibrium, cf. Figure 2.1. [Par90; Bon+94; VP94; ISF17] Thereby, Bonhomme-Courty et al. [Bon+94] obtained their first crystalline phases within the $\text{Al}_2\text{O}_3\text{-TiO}_2\text{-ZrO}_2$ -system at 870°C (ZrTiO_4), followed by α -alumina at about 1045°C . The desired $\text{Al}_2\text{TiO}_5\text{-ZrO}_2$ powders formed after heat treatments up to 1500°C . The resulting composite material exhibit very low thermal expansion which is attributed to the combination of microcracking and contractive phase transformation. [Par90] That microcrack network can be exploited for refractories to improve the thermal shock resistance significantly. [Ane+07; Ane+08; Ane+10; Dud+12] Thereby, Fruhstorfer et al. [Fru+15] are recommending sintering temperatures above 1300°C and particle sizes below $63\mu\text{m}$ (depending on the composition of the raw materials) to utilise the full potential regarding the thermal shock resistance. Aneziris et al. [ASU07] reported excellent thermal shock resistance for fine grained AZT materials if the ratio alumina:zirconia:titania equals 95:2.5:2.5.

2.1.3. Investigated steel grade: 42CrMo4

The here used steel grade 42CrMo4 (1.7225) is a heat-treatable steel. Such a steel is hard to form but suitable for applications with high strength requirements. [BM18, p.142] It is applied in automotive engineering and vehicle construction. For special applications like mining machinery components, a variant to cast is available (G42CrMo4, 1.7231). [Arn+15] The standard DIN EN ISO 683-2:2018-09 [DINb] defines the composition and properties of 42CrMo4, cf. Table 2.1.

Chromium as an alloy element increases the tensile strength, while the elongation is only slightly degraded. By reducing the critical cooling rate, the hardenability is significantly increased. An increase in hardness is also caused by the carbide-forming

2. Literature Review

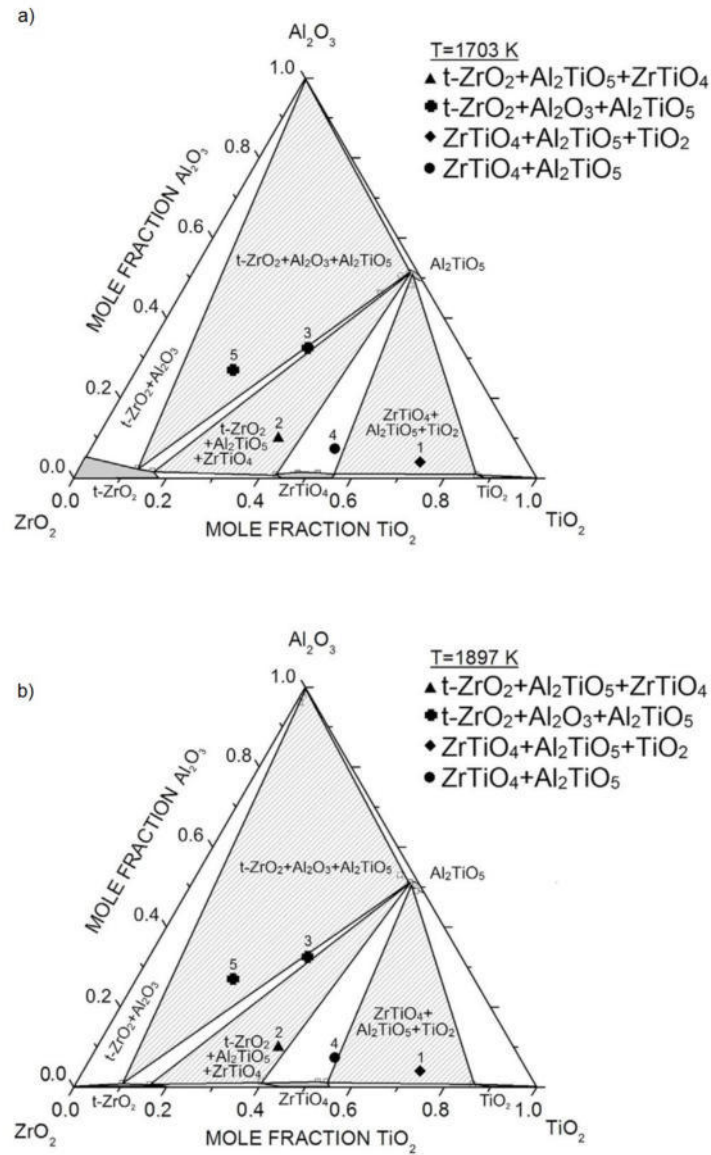


Figure 2.1.: $\text{Al}_2\text{O}_3\text{-TiO}_2\text{-ZrO}_2$ phase diagram at (a) 1703 K (1430 °C) and (b) 1897 K (1624 °C) calculated by Ilatovskaia et al. [ISF17, p. 3464].

Table 2.1.: Composition of the 42CrMo4 according to the standard DIN EN ISO 683-2:2018-09. [DINb]

Element	C	Si	Mn	P	S
(mass%)	0.38 - 0.45	0.1 - 0.4	0.6 - 0.9	0.025	0.035
Element	Cr	Mo	Ni	Cu	
(mass%)	0.9 - 1.2	0.15 - 0.3	-	0.4	

effect of the chromium. [BM18, p. 65] Manganese not only acts as deoxidation agent, but increases the hardening depth by lowering the critical cooling rate in the case of heat-treatable steels. [BM18, p. 64]

42CrMo4 has a relatively high sulphur content and was used for the laboratory immersion tests in the first funding period of the CRC 920, i.e. in the experiments of Emmel [Emm14], Dudczig et al. [Dud+14] and partly Storti [Sto18]. For the second funding period, the same steel grade but with a reduced sulphur content was molten. That one is used in the present study as well as in the later experiments of Storti [Sto18]. According to Zienert et al. [ZF15] that steel grade melts in the range of 1443 °C to 1499 °C.²

2.2. Brief excursus into the physical chemistry of metallurgical processes

To understand where NMIs come from and how refractory materials interact with molten steel, a little excursus into the physical chemistry of metallurgical processes has to be undertaken. In order to not exceed the scope of this thesis, it focuses on the main elements and their oxides of the aforementioned system under investigation: Fe, O, C, Cr, Mn, Si, Mo, Al, Zr, and Ti. Properties which are related to the interactions of refractory material and steel melt are discussed—including activity, solubility of elements in the melt, viscosity and surface tension of the melt, wetting behaviour of melt and refractory/oxide inclusions, and redox-reactions. Thereby, the role of gases on the interactions between refractory material and steel melt as well as their influence on inclusion removal from the melt are described. The chapter closes with an review of interactions observed between refractories and molten steel which are of interest regarding the system under investigation.

2.2.1. How behave selected elements in molten steel

Pure iron has a melting point of 1537 °C. [Tur96, p. 100] At 1600 °C and with a carbon content lower than 1 %, the density of liquid iron is about 7 g/cm³. [Tur96, p. 126] Reviewing the available data of the 1950s to 1970s, Keene [Kee88] summarised in a comprehensive review a mean value of the surface tension of pure iron of (1865 ± 50) mN/m at 1550 °C. Due to the fact that iron is usually accompanied by oxygen and carbon, it is almost impossible to investigate the surface tension of pure iron or the binary systems. Already low contaminations of surface active elements, like sulphur or oxygen, might alter the obtained results. Especially investigations

²Results obtained by differential thermal analysis.

2. Literature Review

Table 2.2.: Effect of selected elements of the system under investigation on the surface tension of liquid iron (γ_{Fe}): strongly decreasing (- - -), slightly decreasing (- -), barely decreasing (-), no influence (o), barely increasing (+). Based on the data reviewed by Keene [Kee88].

Solute element	Effect on γ_{Fe}	Solute element	Effect on γ_{Fe}
O	- - -	Mo	+
C	- -	Al*	o
Cr	-	Zr*	-
Mn*	- -	Ti	- -
Si*	- -		

* reacting strongly with dissolved oxygen, thus used as deoxidation agent, cf. Section 2.2.3 on page 20.

by sessile drop methods, which were conducted in that time to evaluate the surface tension of molten metals, suffer from these contaminations. In the meantime, the levitating method has been developed to achieve more accurate results. [Kee+86; Kee88] That is why this approach is followed nowadays. [EB09; Egr+10] Table 2.2 summarises the effect of selected elements on the surface tension of pure iron. The reviewed data covered a wide temperature range, including 1500 °C to 1650 °C.

Liquid iron reacts with diluted as well as gaseous oxygen but oxygen is only soluble to a limited extend. In the case that more oxygen is available, a liquid oxide phase is formed. At the eutectic temperature (1527 °C), the maximum amount of dissolved oxygen is 0.16 mass% and the forming liquid oxide phase contains 22.6 mass% oxygen. With increasing temperature, the solubility of oxygen in liquid iron increases³ whereby the solubility in liquid iron oxide keeps almost constant with a slight tendency to decrease. [Tur96, pp. 110–113], [Sha16, p. 253] According to Turkdogan [Tur96, p. 135], dissolved oxygen has a lower diffusivity in liquid iron than carbon. Oxygen decreases the surface tension of molten iron strongly, because it is highly surface active, cf. Table 2.2. Rzehak [Rze13, pp. 66–68] reported an increased wetting of molten steel on iron oxide under air atmosphere compared to argon atmosphere during wetting experiments. According to him, the increased oxygen partial pressure lowered the surface tension of the melt and therewith enhanced wetting of the iron oxide.

Carbon is highly soluble in liquid iron and can form iron carbides during solidification, whereby cementite (Fe_3C) is the most common modification. [BM18,

³The maximum solubility of oxygen in liquid iron at 1600 °C is 0.23 mass%.

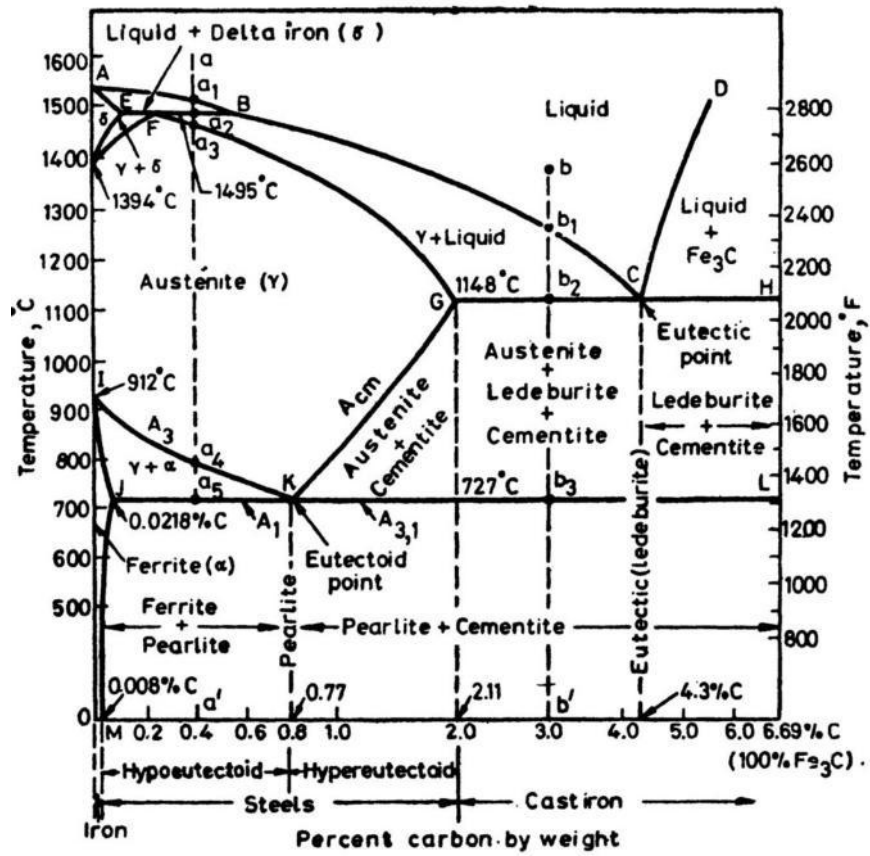


Figure 2.2.: Fe-C phase diagram by Hawkins and Hultgren (1973), adapted from Chanda [Cha81, p. 66].

pp.62–63] In the region of steel, i.e. $<2\text{ mass\% C}$, the liquidus temperature decreases with increasing carbon content, cf. Figure 2.2. The solubility of carbon in molten iron, however, is affected by the presence of other elements. For example, chromium or manganese increase the solubility of carbon in iron, whereas aluminium or silicon decrease the carbon solubility. [Sha16, p. 253] [TGD63, p. 103] The viscosity of liquid iron decreases slightly with increasing carbon content. [Tur96, p. 130] Keene [Kee88] summarised that carbon decreases the surface tension of molten iron slightly. Graphite is wetted by molten iron, whereby Zhao and Sahajwalla [ZS03] observed a decreasing contact angle with increasing carbon dissolved in the melt until saturation. In their case, the contact angle decreased from 64° to 38° .

Dissolved silicon can easily react with oxygen to form silica inclusions which results in a lower content of dissolved oxygen. For that reason, silicon is used as deoxidation agent. By lowering the content of dissolved oxygen, silicon decreases the surface tension of molten iron slightly. Chromium decreases the surface tension of molten iron barely. Molybdenum, however, tends to increase the surface tension. Manganese decreases the surface tension of molten iron, especially for low amounts [Kee88], cf. Table 2.2. Based on the reviewed data, aluminium barely influences the surface tension of molten iron. [Kee88] Nevertheless, aluminium is a strong deoxidation agent and, therefore, its addition to the melt will influence the soluble oxygen content. Titanium decreases the surface tension of molten iron, according to Kishimoto et al. [KMK84] (i.e. under hydrogen atmosphere). Other authors reported no significant effect of Ti on the surface tension of molten iron. [Kee88] Zirconium is a strong deoxidiser. [Fru74] It decreases the surface tension of molten iron slightly. [Kee88] Whereby, again, desoxidation effects have to be considered.

2.2.2. The role of gases

In general, the amount of gases is objected to be as low as possible to reduce the formation of porosity in the solidified product. This porosity results from the decreasing solubility of gases during cooling and solidification of the steel. Nevertheless, bubbles play an essential role in steelmaking and fulfil following tasks: [Sha16, p. 290]

- they allow reactions with gas formation to take place by acting as nucleation side for the gaseous phase,
- to consume smaller bubbles and rise up faster, i.e. to enhance degassing of the melt, and
- to drag NMIs with them to the slag-metal interface.

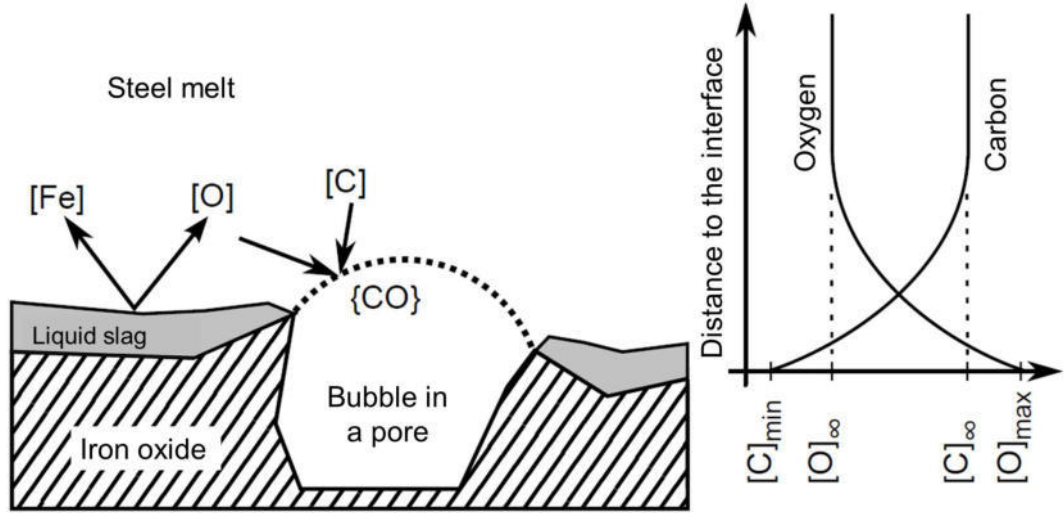


Figure 2.3.: Bubble formation and interface reaction in the system iron oxide - molten steel - and CO-bubble. [Rze13, p. 151], translated from German to English.

Thereby, argon and nitrogen do not react with elements of the steel melt and are used for stirring and purging to homogenize and to degas the melt. Hydrogen has a potential to reduce metal oxides in a steel melt more efficiently than CO due to its high diffusivity. According to Shamsuddin [Sha16, p. 161], however, this advantage is only valid up to a temperature of 800 °C because above this temperature the reaction kinetics of CO are more favourable. Oxygen is strongly avoided and objected to be removed to prevent reoxidation and therewith NMI formation. CO as a product of redox-reactions with carbon is highly interesting for the interactions of carbon-bonded refractories and the liquid steel. Thus, it will be in the focus of the following detailed discussion of the role of gases in molten steel.

As mentioned above, bubbles play an essential role to allow redox-reactions within the melt to take place. These redox-reactions will be discussed in the next section, cf. Section 2.2.3. Thereby, the reduction by carbon accompanied by the formation of CO-gas makes a significant contribution to them. However, gas is formed if either an nucleus for bubble formation or a gas/metal interface exists. Homogeneous nucleation is practically impossible in liquid metals. From a practical point of view, bubbles introduced into the melt by stirring, purging with gas (e.g. argon) or pores of the refractory provide the required gas/metal interface. [Sha16, pp. 205–206]

The importance of the gas bubbles as reaction zones shall be illustrated by the following examples. In 1988, Shinme et al. [SMM88] investigated how blowing of powdered oxides accelerates nitrogen removal under reduced pressure. They observed that the enhanced decarburisation of the melt, compared to oxygen blowing, supported nitrogen removal. They declared that the oxide particles enhanced decar-

2. Literature Review

burisation because they are, on the one hand, a source of oxygen for $\text{CO}_{(g)}$ formation and, on the other hand, they penetrated the melt deeply and were well dispersed acting as nuclei for bubble formation. Thereby, they observed a decreasing bubble size if oxide particles were blown in the melt resulting in an increased interfacial area of bubbles and melt. Rzehak [Rze13], too, stated an enhanced decarburisation of steel melts if iron oxide particles are blown into the melt. In his thesis, he investigated how different steel grades⁴ decarburized if treated by an oxide particle aided vacuum oxygen decarburisation process. In all his different trials he found that the addition of iron oxide based particles enhanced decarburisation. According to him, iron oxide particles acted as CO bubble nuclei and enhanced decarburisation by bubble formation. Figure 2.3 illustrates the interface reactions between melt, oxide particle and bubble. Rzehak states that the iron oxide particles melt at the process temperatures of 1600 °C on the particles edge. Due to that the iron melt near the surface is diluted by dissolved iron and oxygen. If fresh melt (containing more carbon) is mixed with that diluted melt, CO forms from the solute carbon, whereby open pores or roughness have the potential to act as nuclei for bubbles. He calculated that such small bubble nuclei are stable under his experimental conditions.

Further, Zhang and Taniguchi [ZT00] reviewed how bubbles can aid inclusion removal from a steel melt. They described the overall process of inclusion flotation by gas bubbles in six main steps: (i) the bubble approaches an inclusion, (ii) in the first stage of contact, a thin liquid film forms between inclusion and bubble, (iii) the inclusion oscillates and/or slides on the bubble surface until (iv) the liquid film drains or breaks, and makes the formation of a dynamic three-phase contact possible. Subsequently, (v) the bubble-inclusion aggregate stabilises with respect to external stresses and (vi) floats upwards. According to their mathematical model, an optimal bubble size to remove SiO_2 -NMIs during continuous casting of steel is in the range of 1 mm to 5 mm.

2.2.3. Redox-reactions in molten steel

Due to the high affinity of elements to oxygen, redox-reactions are an omnipresent phenomena in steelmaking. As Birat [Bir16, p.6] put it aptly for reoxidation in steelmaking:

An important point regarding reoxidation phenomena is that the phenomenon does not take place at the thermodynamic equilibrium, but rather generates oxides of whichever element happens to meet the incoming oxygen, most often generating iron oxides. Out of equilibrium in

⁴Containing high or low amounts of chromium and nickel.

2. Literature Review

deoxidized liquid steel, they will later reverse back to equilibrium NMI, if time allows.

In 1944, Ellingham summarised the oxide formation in metallurgical processes by plotting the Gibbs free energy of different components being oxidised versus the temperature. [Ell44] Thereby, it has to be noted that such Ellingham diagrams represent the thermodynamic equilibrium of oxide formation with an oxygen partial pressure of 1 atm and unit activities of the reactants and products. These assumptions, however, do not apply to the real process, which is beyond equilibrium, and neglects e.g. the reaction kinetics. [Sha16, p.151] Nevertheless, it is still used for rough estimations which oxide formation is favoured under given conditions and meets the experience in steelmaking regarding the recovery of added elements during refining.⁵ In the real dynamic system, oxygen reacts with the element it meets first, as mentioned above, and thermodynamic stable oxides form subsequently—if possible. Thereby, carbon is an important reduction agent for the redox-reactions at high temperatures (above 800 °C). Whereas the oxidation reactions are usually exothermic, reduction of metal oxides by carbon is endothermic. [Sha16, p.157] The oxidation according to Reaction {1} can only take place at a gas-metal melt interface due to the required nucleation of gas bubbles. [Sha16, p.206]



The Massachusetts Institute of Technology (USA) provides an Ellingham diagram including the elements and oxides of interest of this thesis (cf. Figure 2.4). [Ell] The immersion test experiments described in the present thesis were conducted at 1580 °C and 1650 °C, respectively. Thus, the following discussion will focus on this temperature range. The colourful highlighted oxidation reactions in the diagram mark relevant reactions for the system under investigation. The reaction lines of the circled oxides on the ordinate superpose the reaction lines of corresponding colour. According to it, alumina and zirconia (blue highlights) are the most stable oxides in the system, as they are situated in the lower part of the diagram and do not cross the red line representing carbon monoxide formation. Therefore, zirconium

⁵Elements, which are easily recovered, i.e. reduced in the incidence of oxidation, can be found in the upper part of the Ellingham diagram, like Cu, Ni, Co, Mo, and W. They can be added easily/without problems as alloy element at any state of the melt. Alloying elements like Zn, Cd, and Pb suffer from their high vapour pressure at steelmaking temperatures and are, thus, difficult to add to the melt. Elements of the middle section of the Ellingham diagram, like P, Mn, and Cr, are added with care to the partial deoxidised melt, as their oxides are more stable than the aforementioned ones. Highly oxidising elements like Si, Ti, Al and Zr (found in the lower part of the diagram) can only be added as alloy element after adequate deoxidation. [Sha16, pp.299–300]

2. Literature Review

and aluminium will strongly favour to oxidise as soon as oxygen is available, either as dissolved oxygen in the melt or by reducing other oxides, which lay above them in the diagram. The Gibbs free energy lines of the oxidation of silicon and titanium both cross the line of carbon monoxide formation (yellow lines and red line in Figure 2.4, respectively). From this, it is expected that dissolved silicon and titanium as well as their oxides will be present, i.e. they are partially reduced by carbon. The other main elements of the steel (manganese, chromium, molybdenum and iron) are supposed to be completely reduced by carbon or the other aforementioned elements at these temperatures. Thereby, manganese and chromium might have the potential to reduce iron oxide as well as molybdenum oxide.

Nevertheless, the reaction path will be more complex in the real system, as side reactions and solid solution formations will occur. For example, Kim and McLean observed that already small amounts (<0.5 mass%) of chromium [KM79a] or manganese [KM79b] in iron melts distinctly influence the residual oxygen concentration during deoxidation by aluminium, cf. Figure 2.5. By forming solid solutions with iron and aluminium, these spinel phases are changing from $\text{FeO} \cdot \text{Al}_2\text{O}_3$ to $\text{FeO} \cdot \text{Cr}_2\text{O}_3$ and $\text{MnO} \cdot \text{Al}_2\text{O}_3$, respectively. These reversible reactions are able to act as oxygen buffers.

In the following paragraphs important redox-reactions regarding this thesis are described in detail.

Carbo-thermal reduction of alumina With the object to find an alternative production route of aluminium to the energy-intensive Hall–Héroult process, the carbo-thermal reduction of alumina to aluminium was intensively investigated. Usually, it is described that reactions with alumina and carbon to form aluminium and carbon monoxide take place at temperatures higher than 2100°C . In praxis, usually alumina carbides and alumina sub-oxides are formed under such conditions, which hinder the complete reduction of alumina. [Bal+11] At temperature above 1900°C , aluminium oxycarbides easily form, are thermodynamically stable and influence further reactions with carbon. [FLH56] In the following years, many researches verified by theoretical considerations and calculations [HFS07; HES12; HC06; Zie+15] as well as by experiments [LTT93; Li+11] that the reduction of alumina by carbon is accompanied with the formation of mainly alumina (oxo)carbides, but also minor amounts of alumina sub-oxides and gaseous aluminium. Rhamdhani et al. [Rha+13] summarized that direct carbo-thermal reduction of alumina requires still extreme conditions and results in low metallic aluminium yields. The complexity of the reduction process of alumina resulted in suggestions of multi-stage processes which include chloride, sulphur or nitride. Nevertheless, none of these processes have been

2. Literature Review

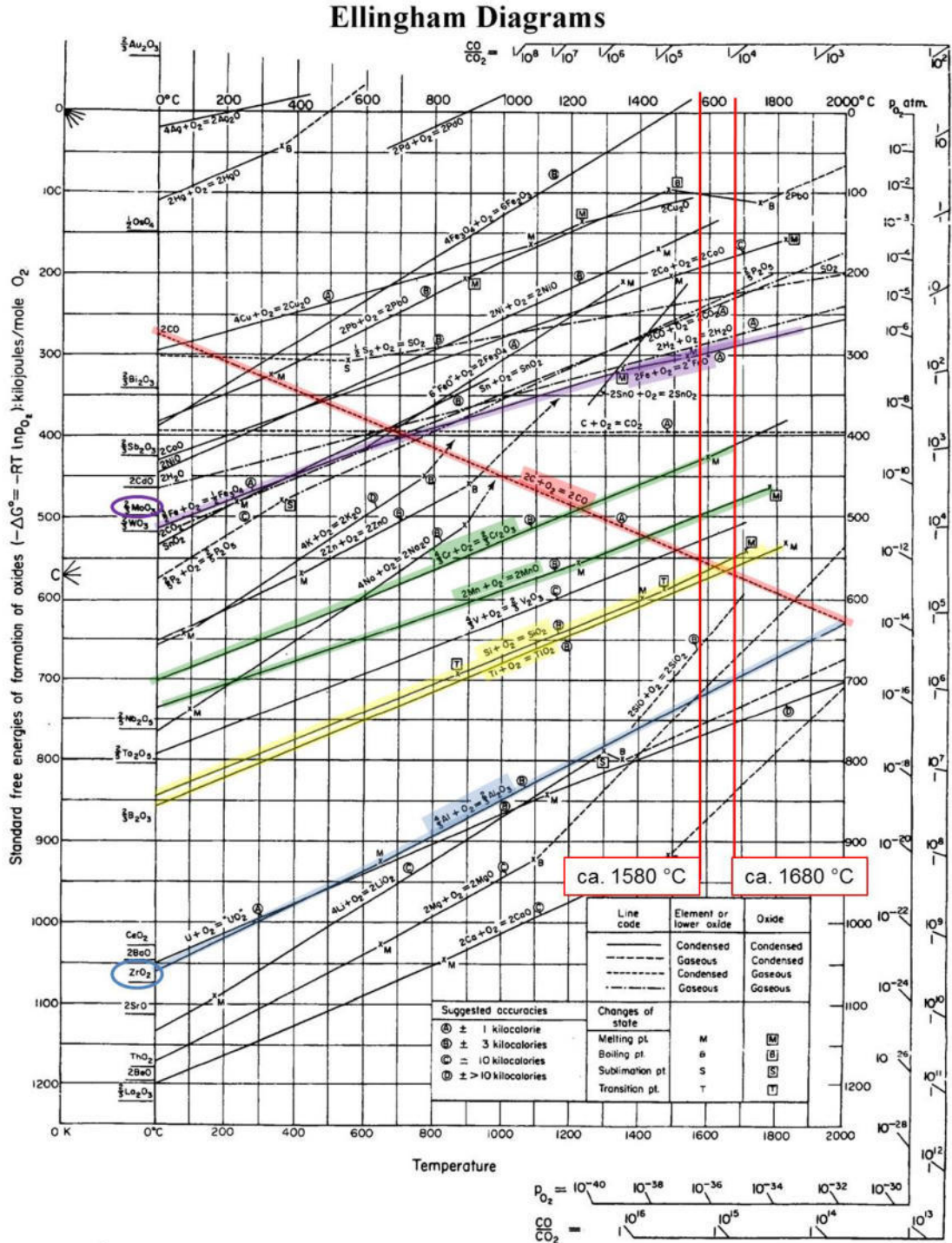


Figure 2.4.: Ellingham diagram. Vertical red lines mark the operation temperatures of this thesis' experiments. Colourful lines and circles highlight oxide formation of relevant elements of the here investigated system.[Ell]

2. Literature Review

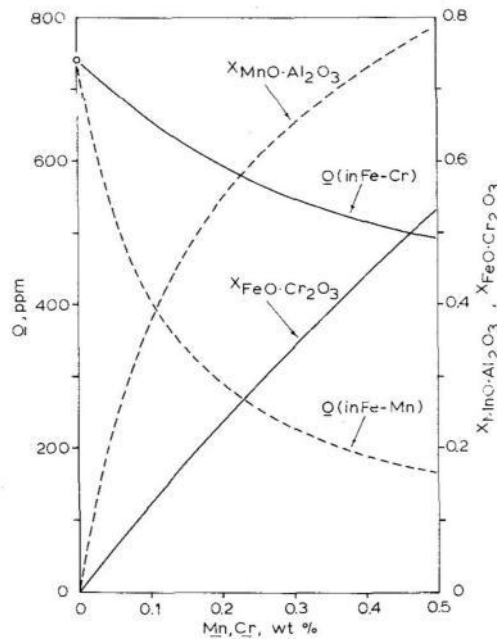


Figure 2.5.: Effect of small amounts of Mn or Cr on the residual oxygen concentrations in iron melts, and on the mole fractions of galaxite or chromite in the spinel solid solutions, at 1600 °C. Underlined symbols denote elements dissolved in liquid iron.[KM79a, p. 593]

successfully commercialized according to the authors.

To avoid any confusion, the term "carbothermal reduction of alumina" is only used in this thesis to describe the reaction $\text{Al}_2\text{O}_3 + 3\text{C} \rightarrow 2\text{Al} + 3\text{CO}_{(g)}$. Otherwise the term "carbothermal reaction of alumina" is used to describe any other reactions involving carbon and alumina.

Deoxidation Redox-reactions are exploited to reduce the content of dissolved oxygen in the melt by adding deoxidising elements. That process step is known as deoxidation and is essential to add afterwards alloy elements to the steel melt which would otherwise easily oxidise. The choice of the deoxidiser depend on the steel grade and desired application. Due to their relatively low price by good deoxidation behaviour⁶ aluminium and silicon are the most common deoxidisers. In most cases, a mixture of deoxidising agents is more powerful than the use of single ones. In addition, the formation of solid NMIs can be avoided by combining aluminium or silicon with manganese and/or calcium to obtain liquid inclusions. [Sha16, pp. 293–298], [Tur96, pp. 262–269] For special alloys, the costlier zirconium or titanium are used for deoxidation, whereby zirconium is the most powerful deoxidiser. For comparison, the extent of deoxidation achieved by 8 wt% Si can be obtained by 0.7 wt%

⁶in means of low dissolved oxygen after desoxidation

2. Literature Review

Table 2.3.: Diffusivity values (D_i) of various ions typical for slags in steelmaking at 1600 °C. [Tur96, p. 176]

Ion	D_i (cm ² /s)
Si ⁴⁺ , O ²⁻	$4 \cdot 10^{-7}$ - $1 \cdot 10^{-6}$
Al ³⁺	$\approx 1 \cdot 10^{-7}$
Ca ²⁺ , Mg ²⁺ , Fe ²⁺	$6 \cdot 10^{-6}$ - $1 \cdot 10^{-5}$

B or 0.1 % Ti or 0.002 % Al or 0.000 03 % Zr. [Tupkary cited by Sha16, pp. 293–294]

Liquid oxide phases in steelmaking/slag reactions A slag is a tailored oxide melt to protect the metal melt from the atmosphere⁷, for thermal isolation and to entrap NMIs. [PJL06; Lee+01; VSS06] Within the frame of this thesis, there is no tailored slag investigated. Nevertheless, the formation of a liquid oxide film on the filter surface–steel melt interface is expected. For that reason some aspects of slag reactions will be discussed here. The composition of the liquid oxide film, however, should differ from commercially used slags, which are usually from the CaO – Al₂O₃ – SiO₂ system. In the case of the liquid film, higher contents of iron oxide and alumina are expected.

The mass diffusion in slags occurs by ions. Thereby, the diffusion of a cation is always accompanied by diffusion of an oxygen ion due to the electro neutrality. The mobility of oxygen is usually smaller than of the bivalent cations, cf. Table 2.3. Thus, the dissolution of solid oxides in the slag is usually controlled by the diffusivity of oxygen ions. Oxygen, as a surface active component, lowers strongly the surface tension of a CaO – Al₂O₃ – SiO₂ slag. The surface tension of iron oxide is decreased by adding TiO₂, SiO₂, CaO (up to 16 mol%), or MnO, but enhanced by adding Al₂O₃. [Tur96, pp. 166–167] There are complex interactions between the liquid oxide phase and the molten metal, whose viscosities and surface tensions are always influenced by the dynamic composition resulting from the ongoing redox-reactions at the metal melt-oxide melt interface. For example, the Al-transfer from liquid iron to an aluminosilicate melt containing iron oxide caused a significant decrease of interfacial tension which recovered after 20 min in a study described by Turkdogan. [Tur96, pp. 168–170]

The absorption of inclusions by slags is reviewed by Reis et al. [RBV14], whereby they focused on slags of the CaO – Al₂O₃ – SiO₂ system. According to them, an essential step of inclusion absorption by a slag is the inclusion arrival at the metal-slag interface and subsequent separation from the metal melt. This step is mainly

⁷especially against reoxidation

2. Literature Review

determined by the wetting angle between melt and inclusion, and especially in the case of solid NMIs, high wetting angles benefit the separation. Once separated, the inclusions shall dissolve in the slag to count as being removed from the metal melt. For that, the slag composition and therewith properties linked with it like the viscosity is a determining factor. Solid alumina NMIs, for example, form liquid calcium aluminate phases with lime from the slag. Holappa et al. [Hol+13] exemplified the potential of slag engineering to optimise the inclusion entrapment and dissolution in slags, as they found that the basicity has a high impact on the dissolution kinetics of NMIs in the slag.

Jung et al. [Jun+04] described liquid phases in the $\text{MnO}-\text{SiO}_2-\text{Al}_2\text{O}_3$ -system at steelmaking temperatures (cf. Figure 2.6), which might be exploited for slag and inclusion engineering. Their findings are based on thermodynamic calculation and comparison with experimental data.

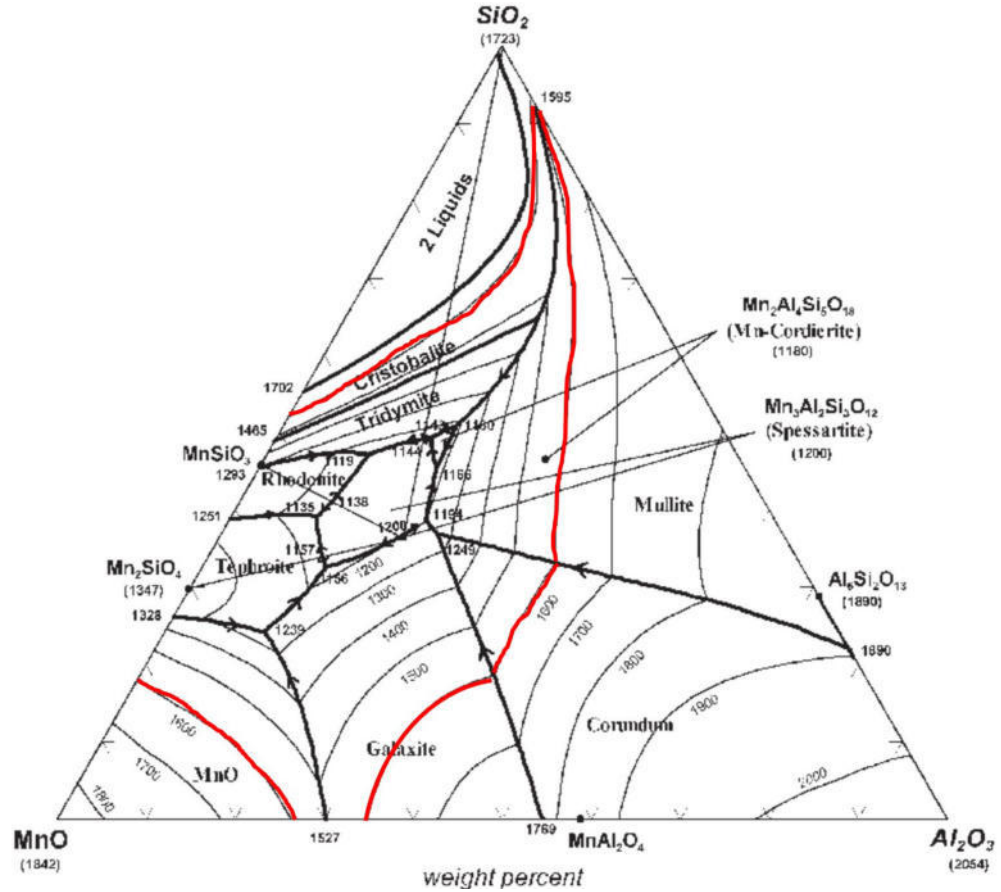


Figure 2.6.: $\text{MnO}-\text{SiO}_2-\text{Al}_2\text{O}_3$ phase diagram presenting liquid phases under steel-making conditions. Temperatures in °C. [Jun+04, p. 263] The red line highlights the temperature line of 1600 °C.

2.2.4. Wetting phenomena

Manifold experiments were conducted to investigate the wetting behaviour of liquid iron on alumina, graphite or alumina-carbon-mixed substrates. Figure 2.7 illustrates the refining of alumina-steel interactions from early observations made by Nizhenko and Floka [NF72] in 1972 to recent results reported by Khanna et al. [Kha+11; Kha+12] using the sessile drop method. Nizhenko and Floka reported increased wetting of an alumina substrate with an increasing amount of carbon dissolved in liquid iron. Thereby, they observed gas formation as a result of reactions taking place at the interface of the substrate and the liquid iron drop. These results were verified and extended by Zhao and Sahajwalla [ZS03]. They investigated the wetting behaviour of molten iron on alumina, graphite or mixed substrates. Thereby, graphite was wetted by molten iron and the contact angle decreased from 64° to 38° with increasing carbon content dissolved in the melt until saturation. They found, too, that alumina is not wetted by liquid iron; the wetting angle was constant 125° over their experimental time. In the case of mixed substrates, they observed an increasing wetting angle with increasing alumina content of the substrate and a decreased amount of carbon dissolved in the iron. Between an alumina content of 16.7 mass% to 23.1 mass%, they reported the change from wetting to non-wetting behaviour. [ZS03]

Kapilashrami et al. [Kap03; KS05; Wan+16] investigated the influence of the oxygen partial pressure as well as temperature⁸ on the contact angle of iron on alumina, silica or mullite. In the case of alumina, they reported a decrease of the wetting angle of iron on alumina if the oxygen partial pressure is increased. They discussed in detail that the contact angle of iron decreased in an initial state because oxygen was adsorbed on the drop surface resulting in a decreased surface tension. That sharp drop was followed by a plateau due to the diffusion of oxygen into the bulk material, whereby at the same time new oxygen on the surface was provided by the atmosphere. As soon as oxygen saturation of iron was reached, hercynite (FeAl_2O_4) formed at the alumina substrate-iron interface, whereby the substrate was still non-wetted by the melt.

Khanna et al. [Kha+11; Kha+12; Kha+16] investigated the interactions of iron and carbon-bonded alumina at 1550°C under argon-atmosphere by sessile drop experiments. The iron sample contained 0.03 mass% carbon, 3 ppm to 5 ppm oxygen were determined in the argon gas used to flush the furnace, and about 2 ppm oxygen observed in the exhaust gas of the furnace. The carbon-bonded alumina substrate contained 12.9 mass% carbon. They observed that with time carbon is dissolved in

⁸The atmosphere consisted of either argon or a mixture of argon, CO and CO_2 , and the temperature varied from 1550°C to 1600°C

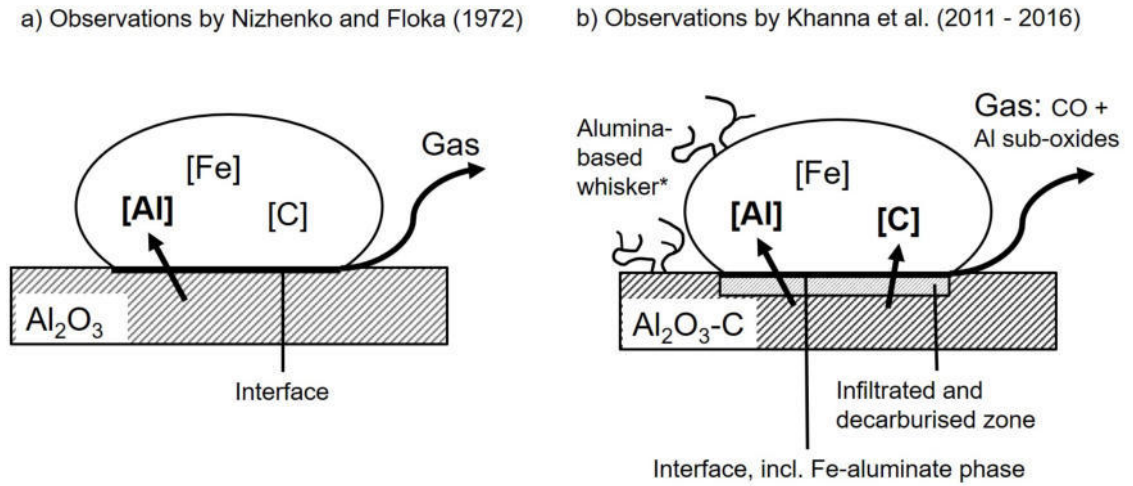


Figure 2.7.: Summary of interactions observed during sessile drop experiments: a) by Nizhenko and Floka in 1972 [NF72]. Reactions of iron with the Al_2O_3 substrate under gas formation and dissolved Al in the metallic iron, if the carbon content of the iron drop increases. b) Results by Khanna et al. [Kha+11; Kha+12] obtained by studies of iron on $\text{Al}_2\text{O}_3\text{-C}$. The interactions of metal and substrate resulted in a decarburised reaction zone at the interface, where an iron-aluminate phase formed, and gas formation, containing CO and Al-sub-oxides. Under special conditions, the Al sub-oxides formed whiskers on the iron-drop surface and on the substrate surface (*). This scheme is not true to scale.

2. Literature Review

the iron drop and after a few minutes a strong formation of $\text{CO}_{(g)}$ took place. Between 75 min to 180 min, they observed the formation of whiskers covering the iron drop and the substrate surface, cf. Figure 2.7b). Thereby, the iron drop became more flat and the wetting angle increased. Energy dispersive X-ray spectrometry (EDS) of such whiskers indicated that they consist of aluminium and oxygen. The authors deduced from the aluminium-oxygen ratio that the whiskers were made of alumina sub-oxide. According to Newbury and Ritchie [NR15], however, high deviations of EDS-Signals on rough surfaces, as has been performed in that study by Khanna et al. [Kha+11], have to be expected. In contrast to a pure alumina substrate, iron infiltrated the carbon-bonded substrate up to a depth of 1.5 mm. They concluded that alumina sub-oxides and aluminium gas, which resulted from interfacial reactions between substrate and iron, reacted with available oxygen to alumina and formed the observed whiskers. Khanna et al. [Kha+12] continued their series of experiments with tests in which the carbon content of the $\text{Al}_2\text{O}_3\text{-C}$ substrate (22.8 mass%) as well as the iron melt (0.06 mass%) was enhanced. Pure iron⁹ was further investigated, too. If the carbon content of the steel and/or in the substrate was increased, no whisker formed. If both carbon levels were enhanced, however, the substrate became distinctly thinner with the contact time. Thereby, the metal drop flattened indicating increasing wetting, which is in accordance with the above mentioned studies. Beneath $\text{CO}_{(g)}$ formations, they observed a carbon-pick up of iron. Further, unreacted alumina and carbon as well as a new phase consisting of aluminium and iron was observed at the interface. In subsequent studies [Ikr+14; Kha+16], they confirmed the formation of an iron-aluminium alloy by advanced X-ray diffraction (XRD) methods and showed that an Fe_3AlC alloy continued to form Fe_3Al with ongoing time. It has to be noted that the authors stated a carbo-thermal reduction of alumina under these conditions. As discussed in Section 2.1.1, the author of this thesis is not convinced that a low-temperature direct reduction of alumina takes place. More reasonable appears the alternative explanation of dissolution and precipitation reactions triggered by carbon presented by Zienert et al. [Zie+15], which will be described in more detail in Section 2.4.3.

In parallel work within the CRC 920, Janovský et al. [Jan+18a; Jan+18b] investigated the influence of a graphene oxide–MWCNTs coating on the interactions between carbon-bonded alumina and molten steel (42CrMo4) by wetting experiments. They observed the formation of secondary alumina at the steel–refractory interface. Compared to the bulk material, Al-rich iron was found near the secondary alumina particles. As they expected, the graphene oxide–MWCNTs coating was consumed during the tests due to the high solubility of carbon in iron. The combination of

⁹C content is 0.03 mass%

2. Literature Review

graphene oxide and MWCNTs in the coating resulted in the thickest secondary layer compared to coatings containing only graphene oxide or MWCNTs. [Jan+18b] Due to the reactions between coated $\text{Al}_2\text{O}_3\text{-C}$ and molten steel, the wetting angle slightly decreased with time and in accordance with the results described by Zhao and Sahajwalla [ZS03]. However, Janovský et al. [Jan+18a; Jan+18b] observed an increased contact angle at slightly higher temperatures, which is unusual on the first glance, but can be attributed to the intensified formation of secondary alumina and was explained by the increasing roughness by the authors. Furthermore, a new phase close to Fe_3Al was detected after wetting tests at 1500°C , similar to Khanna et al. [Kha+16]. Samples treated at 1520°C and 1540°C , respectively, did not contain that phase. According to Janovský et al. [Jan+18a; Jan+18b], it might have been decomposed at higher temperatures or destroyed during preparation. They summarised their results in Figure 2.8 and assumed that the MWCNTs reacted firstly due to their high reactivity, i.e. they dissolved in the steel melt. Thereby, pores underneath the steel drop are created, which could be filled by CO-gas emanating from reactions of carbon and oxygen dissolved in the liquid steel (cf. Figure 2.8 B). Figure 2.8 C describes the subsequent stage wherein graphene reacted, too. Thereby, the refractory surface became rougher, and the resulting surface could be described by a hydrophobic rough surface. Usually a movement of the steel drop during wetting tests was recognised, which was explained by that rougher surface.

The aforementioned studies exemplified the complex interactions taking place between $\text{Al}_2\text{O}_3\text{-C}$ and molten steel during sessile-drop methods and how they affect the wetting behaviour. Further, liquid phases forming at the refractory-steel melt interface influence the wetting behaviour, as shown by Park et al. [Par+18]. They reported how liquid phases ($\text{FeO-Al}_2\text{O}_3\text{-SiO}_2$ or FeO-MgO-SiO_2) at the interface of refractory and melt enhanced wetting in the case of liquid iron being in contact with oxide refractories of the system $\text{MgO-Al}_2\text{O}_3\text{-SiO}_2$. For zirconia substrates, Dubbenstein et al. [Dub+11] demonstrated by a sessile drop method a decreased contact angle with a Cr-Mn-Ni-steel alloy if the zirconia substrate was coated by a TiO_2 layer.

Nevertheless, the Slag Atlas [All08, pp. 522–523, 532] summarises wetting angles of liquid iron or steel on alumina, TiO_2 or ZrO_2 substrates. According to these data, which were almost all determined under Ar or H_2 atmosphere, alumina and zirconia are not wetted by liquid iron or steel, whereby titania is wetted with following wetting angles:

- iron on alumina amounts between 130° to 140° in the temperature range of 1530°C to 1600°C , depending on the purity of alumina.

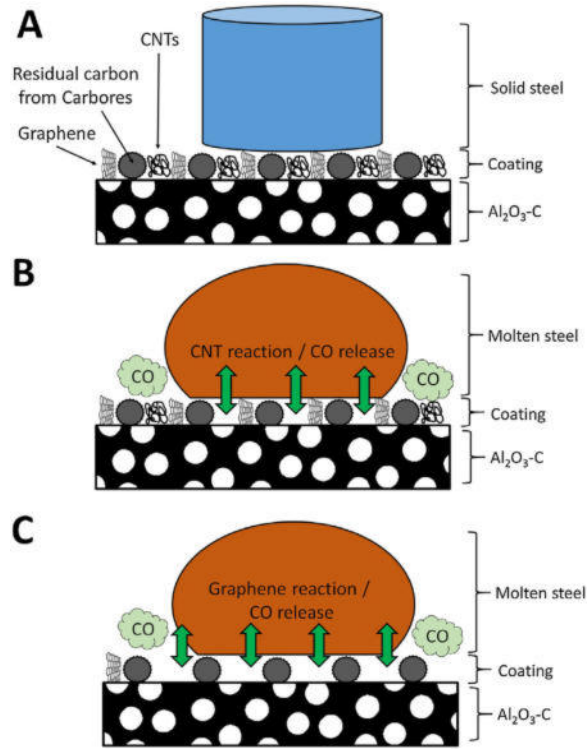


Figure 2.8.: Interactions during wetting experiments of graphene oxide plus MWCNTs coated carbon-bonded alumina with steel by [Jan+18a, p. 30].

- steel on alumina amounts between 105° to 120° at a temperature about 1550°C , depending on the purity and porosity of alumina as well as the steel melt composition.
- iron or steel on TiO_2 amounts around 80° at temperatures of 1550°C and 1600°C .
- iron on ZrO_2 (stabilized with 4% CaO) amounts between 100° to 120° in the temperature range of 1530°C to 1600°C .

2.3. Non-metallic inclusions in steelmaking

In many cases a previously formed oxide inclusion acts as nucleation site for further non-metallic phases to form complex multi-phase inclusions during solidification. This chapter focuses on oxide NMIs as they are reported usually as most detrimental. Thus, a brief overview is given why these inclusions are detrimental and where they come from and how they behave within the melt. Afterwards detection methods of these inclusions are described. Here, a method combining automatically scanning electron microscopy (SEM)/EDS is discussed in particular, as it was also

used for characterisation in the present work. This section closes with some aspects of inclusion removal including steel melt filtration.

2.3.1. What are NMIs and why are they detrimental?

Steel is defined as material consisting mainly of iron and other elements, whereby the maximum carbon content is usually 2 mass%. [DINa] A wide variety of elements are dissolved in molten steel which originate from the initial raw materials (esp. iron ore and coke) or added materials involved in the iron and steelmaking process. Some of them have benefits for the product's properties and are added as alloy elements. Undesired phases are referred to as impurities. Therefore, the distinction between alloying element and impurity depends on the steel being considered and its application. [Bir16]

NMIs form due to (re-)oxidation, slag emulsification, and erosion of and/or reactions with the refractory material.[Sch92, p.211],[ZT03a] The temperature and phase depend solubility limit of elements dissolved in steel cause the formation of carbides, nitrides, sulphides and oxides during cooling and solidification. Usually, the density of oxide inclusions is smaller than that of the steel melt, thus they float up. Large inclusions are nowadays removed by an optimized melt flow and by an adjusted slag, which absorbs NMIs. But the rising velocity of tiny inclusions is too low to reach the slag during the process and, thus, they remain in the melt. [RBV14] For example, Novokhatskii and Yaroshenko [NY99] calculated that from a physical point of view solid oxide inclusions smaller than 30 μm do not float up because their buoyancy is negative. If they would remain finely dispersed, they could have a positive effect on the steel microstructure because they can act as nucleation sites during solidification. [Bir16; Cos18],[Sha16, p.298] But usually they agglomerate and form larger cluster. Thereby, a high contact angle to the melt, like between alumina and molten iron (about 125° to 140°), favours agglomeration to decrease the surface in contact with the liquid steel. [ZT03b] Additionally, small inclusions resulting from deoxidation can act as nuclei for the solidification of non-metallic phases with a lower melting point. For example, often alumina inclusions are surrounded by an MnS-based shell. [Gle+18],[Sch92, p.163] Thereby, the inclusion size in the end product may be increased.

Remaining NMIs are detrimental because they have usually a different thermal expansion coefficient than the surrounding iron and thus induce mechanical stresses during solidification. That way, they can alter mechanical properties. [ZT03b] For example, large inclusions enhance fatigue failure. [Kre+15; Sel+20] According to Turkdogan[Tur96, p.291], the most detrimental inclusions to fatigue life are calcium

2. Literature Review

aluminates, alumina, spinels, silicates and nitrides in this descending order whereas MnS inclusions are the most innocuous. Thereby, alumina inclusions are less detrimental when they are enclosed in an MnS shell. Further, highly abrasive NMIs like alumina may shorten tool life. [Sha16, pp. 308–309],[Tur96, p. 290]

The morphology of NMIs depends on the melt properties, supersaturation, and dwell time. Yang et al. [Yan+13] as well as Dekkers et al. [DBW03; Dek+13] investigated under which conditions different shapes of alumina inclusions form in laboratory and industrial trials, respectively. In both cases, these inclusions were the deoxidation product and were extracted from the solidified steel to investigate them in more detail. The NMIs were extracted by dissolving the iron matrix in a solution of hydrochloric acid. This method is not appropriate to investigate sulphide, silicate, and calcium aluminate inclusions. [DBW03; Dek+13] Yang et al. [Yan+13] as well as Dekkers et al. [DBW03; Dek+13] defined their categories slightly differently, however, their observed shapes were quite similar and are exemplified in Figure 2.9. The most frequent type were spherical inclusions. As the process time increases, the probability that clusters and agglomerates form increases, too. Due to sintering effects and Oswald ripening, such clusters become smoother and form coral-like structures. In combination with small amounts of magnesium or other impurities, faceted and platelike alumina inclusions were formed. In addition, Yang et al. [Yan+13] accompanied their observations with thermodynamic considerations regarding the nucleation of alumina inclusions. They summarised that an increased surface tension of the melt results in a higher supersaturation required for the (homogeneous) nucleation of alumina inclusions. Of course, in the real melt process, heterogeneous nucleation of inclusions is more likely, as it requires less energy and there exist plenty nucleation sites, like refractory interfaces or already existing NMIs. [Sha16, p. 203]

Mizoguchi et al. [Miz+13] investigated the formation of alumina clusters in molten steel. They summarised that the coagulation behaviour of the inclusions depend on Brownian motion, van-der-Waals force and other fluid dynamic forces. From their analysis of samples from industrial trials, they deduced that the coagulation behaviour depends on liquid capillary forces, which are induced by tiny amounts of liquid iron oxide bridging solid alumina particles in the melt and thus acting as "binder" due to the good wettability. Thereby, nano-sized iron oxide particles within the alumina aggregates were only detected in samples taken during the melting process, but not in inclusions of the solidified product. The authors assumed that during the residual casting process, iron oxide is either reduced or diffuses outside the crystal structure due to grain boundary diffusion. They calculated that the presence of iron oxide increases the attraction forces of alumina particles, which is in accordance with Zhang et al. [Zha+06] and Shamsuddin [Sha16] who mentioned

2. Literature Review

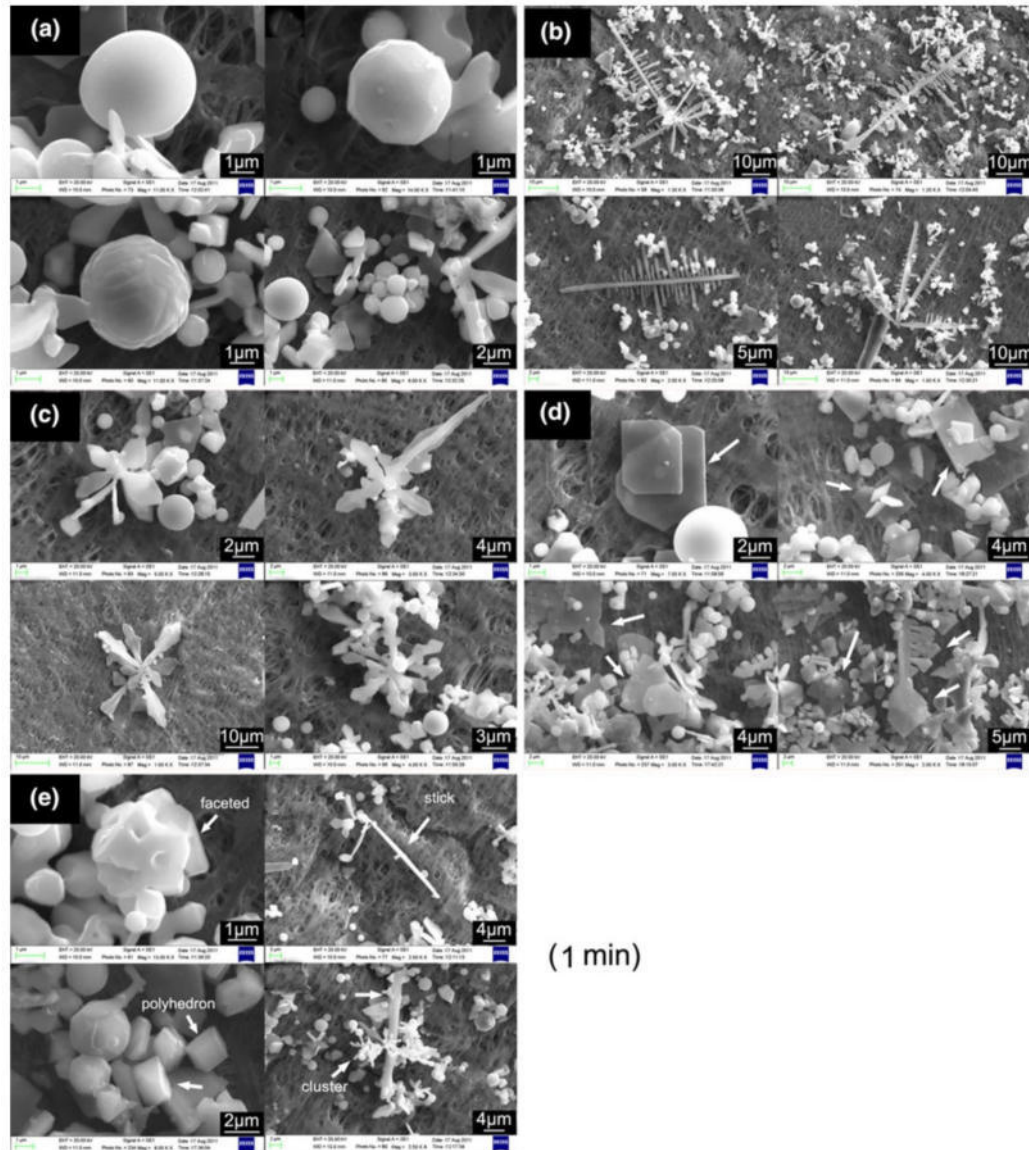


Figure 2.9.: Morphologies of extracted alumina inclusions 1 min after deoxidation (laboratory trials): (a) spherical, (b) dendritic, (c) flower, (d) plate-like (marked by white arrows), and (e) irregular (faceted, stick-like, polyhedral, and cluster). [Yan+13, p. 1176]

that a liquid phase can accelerate coagulation of NMIs.

If titanium is added to the melt, local formation of inclusions from the Al-Ti-O-system is observed, which were reduced by dissolved aluminium during the processing time. Thereby, the particles size distribution of the inclusions became more narrow. [Yan+15] Zhang et al. [Zha+18] showed that there were liquid phases in the Ti-Al-Ca-O system, which reveal the possibility of inclusion modification by calcium in Ti-bearing, Al-killed steel. Thereby, they observed that the liquid phases with alumina were either formed with high titanium and low calcium or low titanium and high calcium contents. Thermodynamic calculations supported their experimental results. In an earlier study, Zhang et al. [ZLJ16] investigated how magnesium influences the size and morphology of Al-Ti-O inclusions. They found that a liquid phase with these inclusions was formed if small amounts of Mg were added, whereas excessive Mg-addition rose the solidus temperature resulting in the formation of solid inclusions.

2.3.2. Inclusion agglomeration

To exploit the influence of the filter surface chemistry on the filtration efficiency of NMIs from molten steel, it is essential to analyse their agglomeration behaviour. For the investigation of agglomeration behaviour, the confocal laser scanning microscope (CLSM) has proven to be extremely useful as an in-situ method. Therefore, the following section summarises the findings of such investigations. The subsequent section describes studies of the so-called clogging phenomena. Knowledge gained from this undesirable blockage of nozzles in steel production can, conversely, be utilised as useful for the effective separation of inclusions from the melt on the filter.

Observation of NMI collision behaviour by CLSM. In 1997, Yin et al. [Yin+97a; Yin+97b] performed CLSM experiments to investigate the collision behaviour of inclusions in various steel melts. In the case of solid alumina inclusions, they observed long-range attractive forces which they attributed to capillary attraction. Within less than 120 s, small clusters (up to 50 μm) were quickly formed. There was no case in which they observed disintegration of the formed clusters. Inclusions containing silica, which formed low melting point phases with alumina and thus enhanced sintering of formed inclusion clusters, densified faster than pure alumina inclusions, but lower attraction forces with a lower range were observed. They further concluded that fine alumina inclusions agglomerated quickly on gas bubbles within the melt due to capillary attraction. According to them, the capillary attraction depends on the contact angle between inclusion and melt, inclusion size and density, and the surface tension of the melt. Thereby, the capillary attraction decreases with de-

2. Literature Review

creasing surface tension as it becomes more difficult for the inclusions to overcome the liquid phase between them.

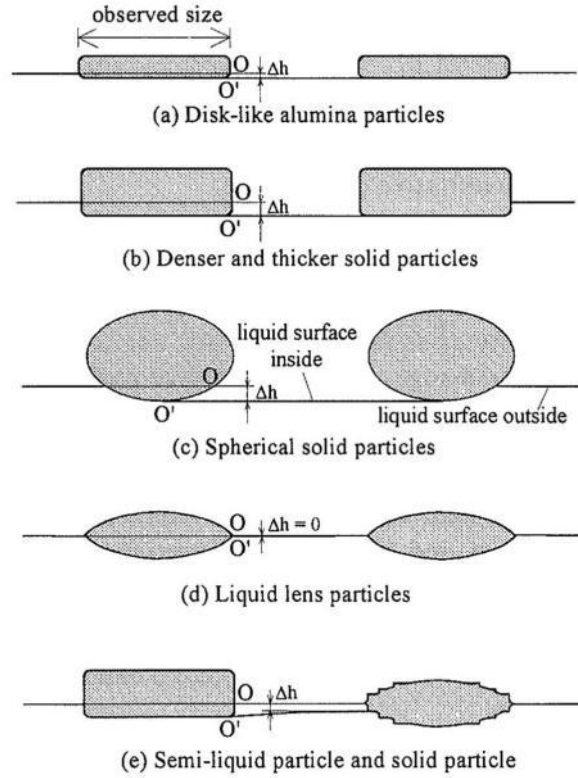


Figure 2.10.: Scheme showing the influence of the particle shape on capillary attraction forces. Increasing deformation of the melt surface (represented by Δh) caused by a pair of particles results in an increasing capillary attraction force. [Yin+97b, p. 953]

Yin et al. [Yin+97b] could verify the alumina cluster shapes¹⁰ observed by CLSM with alumina inclusions detected in quenched samples of an industrial casting trial. Liquid inclusions, i.e. less alumina in combination with lime and silica, showed very low capillary attraction forces. They discussed the influence of the inclusion shape on capillary forces with the three-phase interface (gas–inclusion–melt). According to them, the capillary attraction force increases with increasing deformation of the melt surface between a pair of particles compared to the surrounding melt, cf. Figure 2.10. [Yin+97a]

In a series of studies, our research group of the CRC 920 investigated the interactions of different particles¹¹ with inclusions of a steel melt: alumina [Ane+13b], spinel [Ane+13c], and magnesia [Sch+17b]. To do so, the particle of interest was

¹⁰Clusters composed of agglomerates sizing 5 μm to 10 μm .

¹¹Called exogenous inclusions in these studies and exemplifying a refractory material in contact with the liquid steel.

2. Literature Review

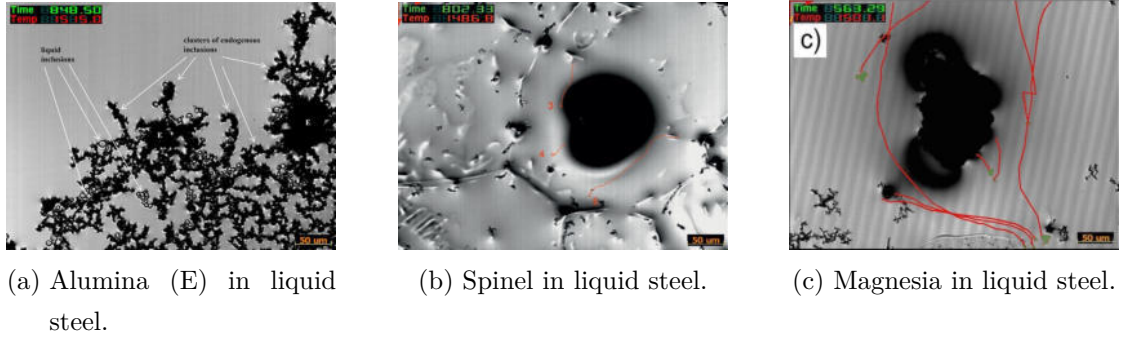


Figure 2.11.: Behaviour of NMIs in liquid steel investigated by CLSM: a) Exogenous (E) Al_2O_3 inclusions, endogenous solid clusters and liquid inclusions. [Ane+13b, p. 960], b) Spinel surrounded by an meniscus. [Ane+13c, p. 1173] and (c) MgO surrounded by a liquid reaction phase, which partially dissolved with time. [Sch+17b, p. 4]. Thereby, tracks of endogenous particles are presented by the red lines in b) and c).

mounted on a steel disk made of X15CrNiSi25.20¹² and heated under argon atmosphere within the furnace device of the CLSM until the steel began to melt. At this temperature, the interactions were observed over a certain period of time. Different behaviour of these exogenous particles within the liquid steel were observed: In the case of alumina, endogenous inclusions of the melt strongly agglomerated and finally deposited on the exogenous alumina particle, as presented in 2.11a. In addition, liquid inclusions containing alumina and titania were detected, which were afterwards characterized as $\alpha\text{-Al}_2\text{O}_3$ and Ti_2O_3 by electron backscatter diffraction (EBSD) analysis at room temperature. These liquid inclusions were observed to be attached on solid inclusions as well as forming their own clusters. Further, it was found that the rougher surface of the exogenous particle resulted in a stronger deformation of the surrounding liquid surface which shall attribute to the observed higher attraction force between exogenous (alumina) inclusion and endogenous inclusions in comparison to the attraction forces determined between endogenous inclusions pairs. In the case of spinel, however, the formation of a meniscus around the particle was observed. Thereby, the exogenous particle immersed at least partially in the liquid steel. Although many endogenous inclusions seemed to be attracted by the exogenous particle, only a few actually deposited on it, and the others either bypassed or detached after a while, cf. Figure 2.11b. In post-mortem characterisations by SEM and EDS, an enrichment with manganese of the spinel particle was determined,

¹²Used instead of the usual 42CrMo4 due to a melting range which is more suitable for CLSM investigations.

2. Literature Review

leading to a partial decomposition of the spinel phase. Further, the inclusions that attached to the spinel particle were alumina inclusions containing traces of Ti. In the case of magnesia, strong reactions with elements of the molten steel (especially Al, Ti, Si and Cr) were observed resulting in a liquid phase surrounding the magnesia particle. According to a characterization at room temperature, the MgO particle was surrounded by two shells: an inner shell made of an Al- and/or Ti-rich phase, and an outer shell enriched with Mg, Si, and Cr. Thereby, the attraction force towards endogenous inclusions of the melt seemed to be lowered, cf. Figure 2.11c, which is in accordance with Yin et al. [Yin+97a; Yin+97b] who reported highest capillary attractions forces between solid-solid inclusion pairs, lower ones between solid-liquid pairs, and lowest ones for liquid-liquid inclusion pairs, as discussed above.

Clogging phenomena In steelmaking practice, cluster formation is experienced during clogging of nozzles, especially in continuous casting. Thereby, inclusions deposit on the refractory's wall and constrict the cross-sectional area of the nozzle resulting in a diminished melt flow. Already in 1974, Singh [Sin74] described the formation of a clogging layer on nozzles made of zirconia in contact with steel in laboratory scale experiments. He observed that the layer consisted of alumina particles with sizes of about 2 μm to 3 μm . Between nozzle wall and solidified steel, a thin layer containing spinel crystals formed. He supposed that iron oxide formed at the refractory pores which subsequently reacted with deposited alumina inclusions. As soon as the iron oxide was consumed, no further reaction between refractory material and deposited alumina inclusions would occur. He summarised that there are three steps required for the observed layer build up on the nozzle wall: (i) the inclusions approach to the refractory surface and come in contact, (ii) the inclusions adhere to the refractory surface, and (iii) the inclusions adhere to each other to form a network, e.g. by sintering.

Tsujino et al. [Tsu+94] compared clogging phenomena of $\text{Al}_2\text{O}_3\text{--C}$ nozzles with $\text{Zr}_2\text{O--CaO--C}$ ones¹³. Thereby, they tested these nozzles with steel alloys of different aluminium levels: low (0.015 mass% to 0.026 mass%), medium (0.04 mass% to 0.085 mass%), and high (0.21 mass% to 0.28 mass%). In the case of the low-Al-steel alloy, more NMIs deposited on the $\text{Al}_2\text{O}_3\text{--C}$ nozzles. For higher contents of dissolved aluminium in the melt, a thicker clogging layer on the $\text{Zr}_2\text{O--CaO--C}$ nozzle was observed. In the first case, a thin alumina layer formed at the $\text{Al}_2\text{O}_3\text{--C}$ nozzle-steel interface, which is assumed to benefit inclusion deposition from the melt. In the other two cases, an calcium-aluminate containing layer formed at the $\text{Zr}_2\text{O--CaO--C}$ nozzle-steel interface that seemed to be more attractive to the inclu-

¹³Both nozzle types contained also up to 20 mass% SiO_2 .

2. Literature Review

sions. Thereby, Tsujino et al. discussed the positive effect of $\text{CaO} \cdot 6 \text{Al}_2\text{O}_3$ on NMIs deposition, which is in accordance with results of a study performed by Storti et al. [Sto+17a]: they performed immersion trials with $\text{CaO} \cdot 6 \text{Al}_2\text{O}_3$ or $\text{CaO} \cdot 2 \text{Al}_2\text{O}_3$ coated Al_2O_3 –C-filters and obtained superior filtration results for the $\text{CaO} \cdot 6 \text{Al}_2\text{O}_3$ coated filters. Despite providing a theory about the ongoing reactions, Tsujino et al. [Tsu+94] were not able to clarify how ZrO_2 participated in the interactions. They discussed the formation of a ZrO–gas resulting from ZrO_2 –graphite reactions, which might be subsequently reduced by dissolved aluminium of the steel melt.

In the same year in Europe, Poirer and Thillou [PT94] published their results regarding interactions between carbon-bonded alumina and molten steel causing clogging of submerged entry nozzles (SENs). They observed that the amount of deposited alumina particles on alumina–graphite samples increased with

- increasing carbon content of the refractory
- increasing amount of impurities of the refractory (esp. the carbon source), and
- decreasing carbon content of the steel.

According to them, $\text{CO}_{(\text{g})}$ of the refractory decomposed in the liquid steel as a result of the lower CO partial pressure of the melt, which is usually the case for (ultra) low carbon steel grades in contact with carbon-bonded refractories. Thereby, the decarburization of the refractory triggered the dissolution of alumina, because the increased amount of dissolved carbon near the refractory–steel interface increased the aluminium activity in steel. Poirer and Thillou observed the formation of a vitreous phase containing Al_2O_3 , SiO_2 , and alkalis, which was assumed to originate from impurities of the refractory. Subsequently, various redox-reactions involving $\text{CO}_{(\text{g})}$ provided oxygen for reoxidation of aluminium. These alumina particles deposited on the vitreous layer in form of plate-like crystals. [PT94; Poi15]

In recent years, numerical studies investigated the clogging phenomena. For example, Mohammadi-Ghaleni et al. [Moh+16] studied how the thickness of the clogging layer depends on the melt flow condition through the nozzle by comparing an SEN after use and a simulation of the corresponding process. The clogging thickness of the investigated nozzles was not homogeneous over the nozzle length. They showed that the clogging thickness correlated positively with the melt flow velocity and turbulences. Thus, thick clogging layers were observed in areas of slow and laminar flow, whereas thin clogging layers were found in areas of fast and turbulent flow. They concluded that the latter case benefited detachment of inclusions from the nozzle wall. Further, such flow conditions should hamper the probability of inclusions to attach on the nozzle wall. Salgado et al. [Sal+18] calculated forces required

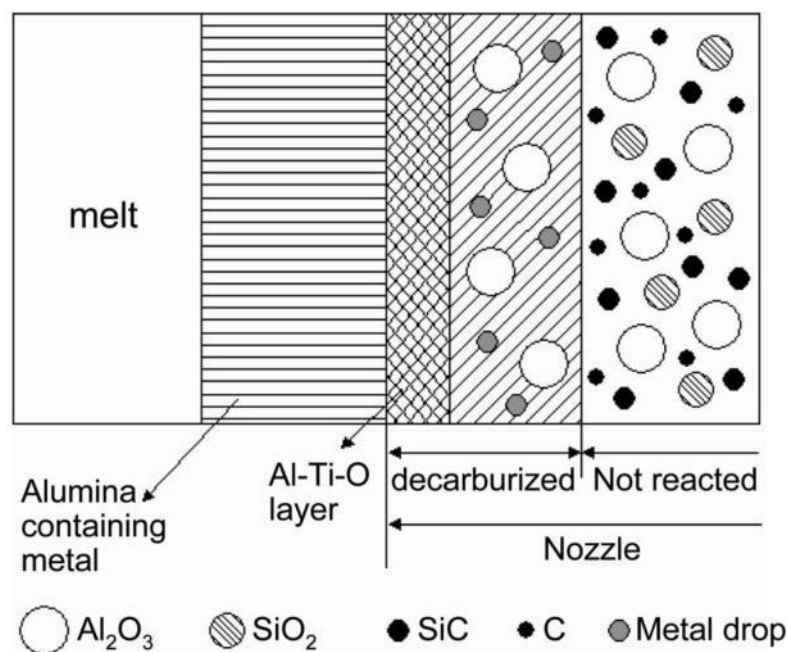
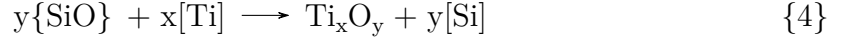
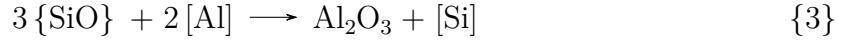


Figure 2.12.: Clogging mechanism.[JKC09, p. 477]

to detach an NMI from a refractory's wall in the case of SEN clogging. They applied their model on three cases: (1) alumina inclusions - alumina nozzle wall, (2) alumina inclusions - zirconia nozzle wall, and (3) like case one but with liquid FeO in between. The adhesion force is reduced from case (1) to case (3), which resulted in a lower melt flow velocity required to detach the inclusions. They conclude, that the effect of wetting angle (comparison of case (1) and (2)) had a minor effect on inclusion detachment, but the liquid phase benefited detachment, which is in accordance with the observations made by Yin et al. [Yin+97a; Yin+97b]. Thereby, Salgado et al. did not involve the influence of nano-bubbles on inclusion adhesion in their model. Svensson et al. [Sve+16] observed less clogging of zirconia SENs if they were plasma coated. The coating was a mixture of yttria stabilised zirconia and CaTiO_3 . The coating was consumed during steel contact. According to the authors, alumina inclusions from the melt and CaTiO_3 from the nozzle's coating formed a liquid calcium-aluminate phase at the process temperatures of 1550 °C to 1600 °C. Such a liquid calcium-aluminate phase was also detected by Tuttle et al. [TSP05], if SENs were coated with CaTiO_3 to reduce clogging of Al-killed steel.

For steel alloys containing up to 0.055 mass% Ti, Jung et al. [JKC09] observed the formation of an Al-Ti-O layer at the steel-refractory interface, cf. Figure 2.12. The SEN consisted of alumina, silica, SiC, and carbon. According to them, in the decarburised zone of the nozzles wall the following redox-reactions took place and

resulted in the deposition of alumina inclusions:



Their results are in agreement with the extreme clogging of SENs in contact with Ti containing steel reported by Basu et al. [BCG04]. They compared the clogging behaviour of SENs in contact with Ti-bearing ultra low carbon (ULC) steel alloys (about 0.05 mass%) or Ti-free ones. They, too, detected titania-alumina mixed inclusions in the clogging layer, and residual steel dispersed between alumina and spinel inclusions.

2.3.3. Detection of non-metallic inclusions

There are direct and indirect methods to characterize the steel purity. Direct methods include extraction and 2-D methods, and indirect ones include tracking of oxygen, sometimes also N₂ or Al, whereby they suffer from a lower accuracy than the direct methods. [ZT03a; ZT03b], [Sch92, p. 213]

The extraction methods are based on the principle that the steel matrix is etched and the residual inclusions analysed. On the one hand, an advantage of these methods is that the three dimensional structure of the inclusions can be characterized. On the other hand, these methods are very time-consuming as the etching has to be done carefully to avoid an alteration of the inclusions under investigation. Of course, only inclusions which withstand the etching compared to iron can be analysed by these methods. [DBW03; Gle+18] More detailed information about etching methods can be found in References [Bir16; ZT03a; ZT03b].

For decades, it has been common to collect representative samples, polish them and characterise observed inclusions by light microscopy (2-D methods). This method requires experienced operators to analyse the inclusions correctly and categorise them to their chemical composition. [Bir16] Further, it is time-consuming as each inclusion is evaluated individually. The detectable inclusion size is limited by the detection limit of the light microscope. The standard DIN EN 10247:2017-09 [DINc] describes this metallographic detection method of NMIs. In recent time, an automated combination of SEM and EDS is utilised to shorten operation times and identify also small inclusions which cannot be detected by light microscopy. Further, this method offers the possibility to gain statistic information about the inclusion size distribution combined with information of the chemical composition of the inclusions. The inclusion identification of this system is based on different gray

values in backscattered electrons (BSE) mode of the SEM. This method is utilised in this thesis. Both mentioned 2-D methods have disadvantages arising from the analysis of three dimensional structures on a two dimensional surface: information about the inclusion size are misinterpreted because the three dimensional structure is cut in an arbitrary area, which is analysed. Further, the surface pretreatment during sample preparation (polishing etc.) may lead to misinterpreted inclusions or let inclusions fall out of the matrix resulting in a hole which only contains traces of the previous inclusion. In the case of the automatic software interpreting the X-ray signals for EDS analysis, the accuracy of quantitatively analysis of the chemical composition suffers tremendously from surface roughness of the sample.[NR15] Such roughness is inevitably formed if inclusions break out or lay in scratches.

2.3.4. Removal of non-metallic inclusions

Having the interactions between steel melt and oxides in mind, many strategies to remove NMIs or avoid their formation are obvious. In the following, strategies concerning process parameters are briefly summarised, the principle of inclusion modification is presented, and the removal by steel melt filtration is illustrated.

... by process parameters, melt flow control, and slag reactions

As mentioned in Section 2.3.1, NMIs origin from (re)oxidation, slag emulsification, erosion of and/or reactions with the refractory material, and precipitation from the steel due to the temperature and phase depend solubility of elements dissolved in steel. As soon as oxygen is accessible, oxides will form. As a consequence, inhibiting reoxidation is only possible by most carefully avoiding oxygen contamination, e.g. by covering the melt by a slag, protecting the pouring jet by nozzles or an inert gas atmosphere [Sch92, p. 226],[Cos18; ZT03b], and by selecting suitable refractory materials [Poi15]. Further, oxygen can be removed from the melt by appropriate degassing with vacuum. An elaborated melt flow control can reduce slag emulsification resulting from high flow velocities and turbulences. In the beginning of pouring, a smooth pouring jet decreases the probability of reoxidation by avoiding splashes and therewith minimizing the surface area in contact with the atmosphere. [Sch92, pp. 211–212]

The selection of an appropriate slag is further highly important to absorb NMIs floating up from the melt, as discussed in Section 2.2.3 on page 21. Due to the density difference of NMIs and the steel melt, NMIs tend to float up. That way, large inclusions (radius >0.01 cm) are usually entrapped by the slag if time allows it.[Sch92, p. 211],[Sha16, p. 301] In the case of small inclusions, however, the surface

2. Literature Review

tension and therewith the wetting behaviour of the melt has a larger impact on the inclusions removal than the inclusions density. [Ros60; Sin74] For example, alumina is not wetted by molten steel resulting in a lower dragging force of the melt on the alumina particle compared to silicates. That way Rosegger et al. [Ros60] explained why smaller alumina inclusions rose faster than the larger silica inclusions.

Further, stirring is used to promote clustering of NMIs and/or to move them towards the slag or the walls to remove them from the melt. There is an optimum stirring power as too powerful stirring can increase the inclusions number by slag entrapment and reoxidation. [Cos18; ZT03b] A recent review of numeric modelling of stirring and its effects is given by Liu et al. [Liu+19]. Exogenous inclusions as result of refractory erosion can be diminished by selecting appropriate refractory materials and melt flow control. [ZT03a; Poi15]

... by inclusion modification

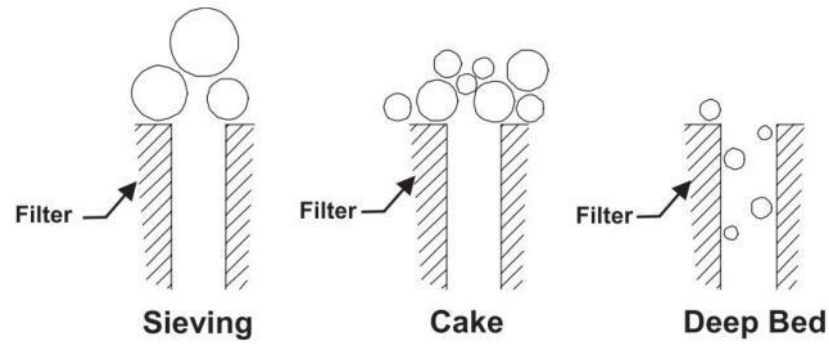
Inclusion engineering is another approach to modify the morphology of NMIs which could not be removed otherwise. The most commonly used method is a calcium treatment. Thereby, added calcium and present alumina or silica inclusions form liquid calcium aluminates and silicates, respectively, under steelmaking conditions which posses a globular shape. Nevertheless, the amount of added calcium has to be carefully calculated to prevent undesired side-effects [Cos18; Poi15; ZT03a], [Sch92, p.230], [Tur96, p.285] Also in the case of Ti-bearing steel, Zhang et al. [ZLJ16; Zha+18] observed the formation of liquid Al-Ti-Ca/Mg-O inclusions if calcium or magnesium were added to the steel melt.

... by steel melt filtration

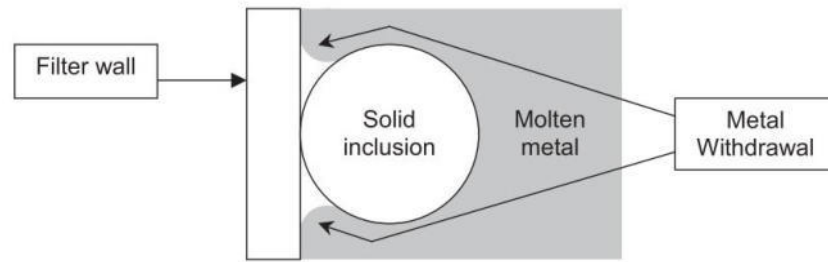
As presented in Figure 2.13a, there are basically three different kinds of filtration mechanism: sieving, cake, and deep bed filtration. To guarantee the melt flow, deep bed filtration is exploited for steel melt filtration. Thereby, non-metallic inclusions smaller than the filters macroporosity are deposited at the filter struts. [Kon+90; OM05] The deposition probability is influenced by the melt flow as well as by attraction forces between filter wall and inclusions, as discussed in Section 2.3.2 for the inclusion agglomeration tendencies. Once deposited, capillary forces and sintering effects keep the inclusion adhered, cf. Figure 2.13b. [Kon+90] Thereby, the presence of nano-bubbles should support the inclusion adsorption on the filter surface. [Dit+17] Inclusions might detach again due to high flow velocities or turbulences in the vicinity of the filter surface.

In 2003, Morgan [Mor03] gave a brief overview of the state of the art of filter

2. Literature Review



(a) Basic filtration mechanism.



(b) Principle of the deposition of a solid inclusion on the filter surface.

Figure 2.13.: Scheme of (a) possible filtration mechanism and (b) the adsorption of solid NMIs on the filter wall. [OM05, p. 188]

application in foundries and highlighted the benefits of implementing filters in the metal casting process:

- Filter improve the product's quality by removing NMIs, and slowing down the molten metal stream making it flow laminar (due to a pressure drop comparing the filter's entry and exit) resulting in an even mould filling. [Kon+90; Kar+14]
- The smoother flow of the melt reduces turbulences and splashing, both sources for reoxidation (and therewith the formation of new NMIs).
- That kind of flow regulation gives the opportunity to shorten the gating system and thus increase the yield.
- Overall, by reducing the amount of NMIs, internal scrap and customer returns can be reduced as well as faster process times can be realised. The number of repairs can be reduced [Asl+19]. In summary, energy can be saved and the process can be made more economical.

Thereby, following properties of a filter influence the filtration performance: (i) its chemistry, (ii) the surface roughness, and (iii) the geometry (surface area, macroporosity, strut thickness, slenderness) [Jan13c; VH14]. The first is in the focus of

this thesis, the other two are out of the scope. However, the impact of surface roughness [FP14; FP15; FP16; Dit+17; Voi+19] and the impact of the filter geometry on the melt flow through the filter [Wer+17; Jor+19] have been investigated in parallel work within the CRC 920.

2.4. Interactions of ceramic filter and molten steel

In the following section, the refractory–steel melt interactions which are of interest for the system under investigation are reviewed. In the beginning, general observations of refractories with molten steel are discussed, followed by insights from steel melt filtration experiments, and it is closed with prior studies within the CRC 920 on which this thesis is based.

2.4.1. Insights from searching appropriate refractory materials for steel melt processes

Appropriate refractory materials have to be chosen for steel melts as some alloy elements are highly reactive, e.g. manganese, chromium, and silicon. Thus, Sillo [Sil91] investigated refractory–steel interactions with crucibles of different refractory materials (alumosilicates, alumina with a phosphate bonding, magnesia-chrome, dolomite) under argon atmosphere. All these materials reacted with the melt; especially the aluminosilicate crucibles reacted with dissolved manganese and chromium. Basic refractories were attacked by dissolved silicon of the melt (reaction with magnesioferrite forming silicates), and reactions involving phosphorus as well as calcium resulted in the formation of liquid oxide phases with a low melting point at the refractory–steel interface. Further, Sillo observed always metallic droplets remaining on the refractory–steel melt interface. According to him, their morphology (spherical) and composition (high amount of iron and chromium, less manganese) suggest that they result from reactions within the liquid oxide layer (slag). In 2015, Poirier [Poi15] reviewed the influence of refractory materials on the steel quality. Thereby, he summarized reactions between refractory material and molten steel:

- Silica or iron oxide of the refractory can be reduced by dissolved aluminium of the steel melt.
- Dissolved magnesium or calcium have the potential to reduce alumina.
- Silica and chrome oxide are very reactive with all elements of the steel melt.
- Alumina and magnesia can react with dissolved calcium of the melt.

2. Literature Review

The case-study of clogging phenomena on Al_2O_3 -C SENs was already mentioned in Section 2.3.2. There, Poirier [PT94; Poi15] discussed how the dissolution of carbon from the refractory material in the steel melt triggered the formation of the alumina-based clogging layer on the nozzle wall.

Reactions with Ca and/or Si, as well as their oxides, are main reactions with alumina based refractories, as exemplified by Hnatko et al. [Hna+16], who performed corrosion tests with crucibles consisting of alumina mixed with 5 mass% $\text{CaO} \cdot 5\text{SiO}_2$. After 8 h in contact with molten steel at 1600 °C under N_2 atmosphere, they observed a $\text{CaO} \cdot 6\text{Al}_2\text{O}_3$ layer formed at the refractory-steel interface. Besides that, iron silicates were the main corrosion product.

In a series of studies, Fruhstorfer et al. [Fru+15; Fru+16a; Fru+16b; Fru+18] investigated the corrosion behaviour of different alumina-based crucibles with a highly corrosive steel melt¹⁴. Thereby, they described the corrosion mechanism of an alumina crucible in detail. Based on an $\text{MnO-SiO}_2\text{-Al}_2\text{O}_3$ phase diagram and the determined phases from the corroded samples, they explained the corrosion reactions as follows: Firstly, the diffusion of manganese from the steel melt into the alumina crucible resulted in the formation of manganese aluminate in the fine matrix fraction. Afterwards, silicon from the molten steel joined and led to the formation of manganese aluminosilicates ($2\text{MnO} \cdot 2\text{Al}_2\text{O}_3 \cdot 5\text{SiO}_2$) and 2:1 mullite. The melting temperature of the observed manganese aluminosilicate was below the casting temperature of 1580 °C and, thus, formed a liquid phase. The thermal mismatch of mullite and alumina led to mechano-chemical "microspalling", which caused strong surface erosion in combination with the streaming steel melt. In the case of crucibles made of mullite (2:1) such low melt phases formed, too, but no "microspalling" occurred, because there was no thermal expansion mismatch with secondary mullite formed during the interactions. Neither carbon-bonded alumina nor carbon-bonded AZT-crucibles were distinctly corroded by the steel melt.

2.4.2. Steel melt filtration

Ali et al. [AAM85] compared the filtration efficiency in dependency on the flow velocity of an extruded cordierite filter for an aluminium melt and an extruded alumina filter for an steel melt (1600 °C). For both filters, they observed a laminar flow of the melt through the filters. In the case of the alumina filter, high filtrations efficiencies (above 90 %) of inclusions of a size of 0.5 μm to 5 μm from a steel melt were observed. According to them, sintering effects are the main mechanism to capture

¹⁴This steel grade contained 0.16 mass% carbon, 0.21 mass% silicon, 0.63 mass% manganese, 1.52 mass% chromium and 0.03 mass% aluminium

2. Literature Review

inclusions from a metal melt. In a following article of the same year [AMA85], the authors described steel melt filtration trials using either an extruded alumina filter or tabular alumina with a particle size between 0.2 cm to 0.5 cm. In both cases, they reported a distinct reduction of the number of inclusions in the steel after filtration. They analysed filtered and non-filtered steel samples by quantitative metallography. They found that the removal efficiency depended on following factors:

- The melt velocity through the filter: An increase of the melt velocity decreased the filtration efficiency due to a reduced residence time of the melt within the filter.
- The height of the filter: The efficiency increased with an increasing height.¹⁵
- The inclusion size: The larger the inclusions, the higher the filtration efficiency. Inclusions larger than 2.5 μm were completely removed in their case.

In 1990, Kondrat'ev et al. [Kon+90] reviewed appropriate ceramic filters for steel melt filtration. According to them, oxygen from the air, which is entrapped in the refractory's open porosity, and oxygen dissolved in the molten steel result in the formation of an oxide phase at the filter–steel interface in the initial moment of contact between filter and steel melt. This oxide phase consists mainly of iron oxide. Due to the capillary absorption of the liquid oxide film, a reaction zone forms. The reaction zone as well as the oxide film are changed by depositing NMIs. Based on considerations regarding the high interface energy between steel melt and inclusions or filter, which is required for the separation of inclusions from the melt and their deposition on the filter, they assumed that MgO , Al_2O_3 and ZrO_2 , in contrast to SiO_2 , benefit refining. In case of their own experiments, however, they were not able to find reliable data indicating a specific effect of any of these oxides on the effectiveness of refining. They assumed that this was caused by the formation of an oxide film belonging to the Al-Mn-O system at the filter surface which saturated the surface layer of the refractory right from the very first contact. They concluded that refractory materials based on Al_2O_3 , ZrO_2 , and their mixtures are appropriate filter materials as they meet the specifications concerning the resistance to the physico-chemical effects of molten steels to the maximum extent and are easily available.

Recently, a polish research group successfully developed carbon-bonded alumina filters and tested them in industrial trials. [Asl+19] After laboratory trials, post-mortem analysis of the filters revealed a reactive zone with a thickness up to 400 μm

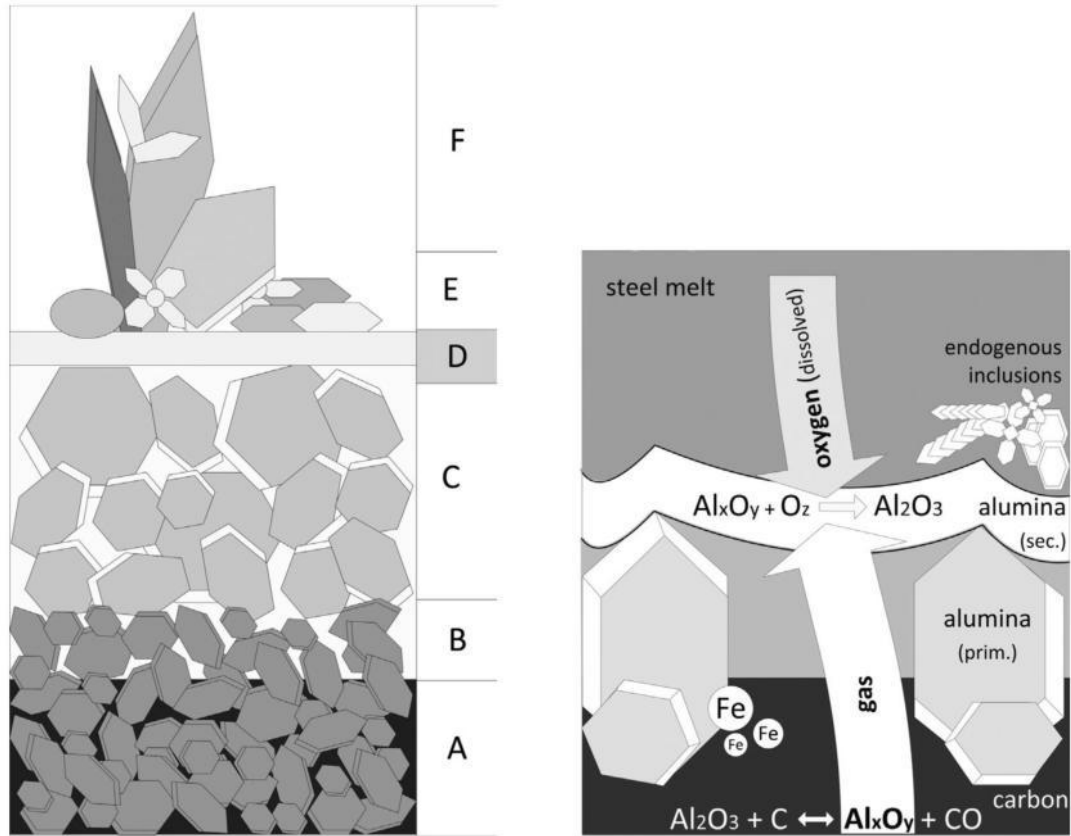
¹⁵It is important to note that the filter height is limited. Otherwise issues with the pressure gradient over the filter height and priming arise.

at the filter–steel interface. That zone was porous and consisted of a glassy phase, alpha-alumina inclusions, metal drops and $\text{MgO} \cdot \text{Al}_2\text{O}_3$ spinel. Thereby, no microstructural changes of the bulk filter material was observed. [Lip+14]

Despite the high demands, if filters were applied in continuous casting, attempts as described by Janiszewski [Jan13a; Jan13b] have been done. Janiszewski investigated the use of multi-hole mullite filters implemented successfully in a tundish in industrial trials. Thereby it was essential to preheat the filters with the tundish to prevent breaking off.

2.4.3. Prior studies of the CRC 920

Emmel [Emm14] developed carbon-bonded alumina filters, whereby a modified coal tar pitch was used as carbon-binder. These filters have been used as substrate material for the investigation of coated filters. To the authors knowledge, the effect of coatings on ceramic filters for steel melt filtration has not been investigated yet beyond the CRC 920. Emmel et al. [EA13; Emm+13] prepared the first coated Al_2O_3 –C filters and tested them in industrial trials. Dudczig et al. [Dud+14] described the corresponding laboratory trials by immersion tests in the inductively heated furnace part of the steel casting simulator (SCS). Therefore, they immersed an uncoated filter, an alumina coated one, and an MgO –C coated filter for 60 s in molten steel (42CrMo4) at about 1650 °C. The steel melts were pretreated to create defined endogenous alumina inclusions. After the immersion tests, a typical layers formed on the filters surface, cf. the scheme in Figure 2.14a. In the case of the uncoated and Al_2O_3 coated filter, the carbon-bonded alumina filter (A) was decarburised on its surface (B). That zone was about 5 µm to 10 µm thick, contained some iron-based particles and was observed on the coated as well as on the uncoated Al_2O_3 –C filter. On top of either the decarburised zone or the filter coating (C), a thin and dense alumina layer (D) has been formed. That layer was about 100 nm to 400 nm thick and copied the topography of the underlying grains. Near that thin alumina layer, densely packed small and mostly platelike particles were observed (E), followed by larger loosely packed particles of complex shapes (F). These attached particles consisted mainly of alumina. In the case of the MgO –C coated filter, a slightly other layer build-up was noticed: the MgO –C coating decarburised instead of the underlying Al_2O_3 –C material; between MgO –C and the decarburised magnesia, some iron-based droplets were again detected. Nevertheless, a thin MgO layer was observed on its surface on which some magnesia agglomerates were detected on the filter surface, but no alumina based particles. Further, secondary magnesium aluminate whiskers grew within the hollow struts of the filter. Thereby,



(a) Scheme of the observed layer build-up on the filter surfaces of immersed filters: unreacted $\text{Al}_2\text{O}_3\text{-C}$ (A), decarburised zone (B), applied coating (C), thin alumina layer (D), dense clogging zone (E), and loose clogging zone (F).

(b) Scheme of possible interactions between a carbon-bonded alumina filter and the steel melt resulting in the layer build-up of a).

Figure 2.14.: Layer build-up on the filter surface (a) and possible interactions (b) by Dudczig et al. [Dud+14, pp. 16735-16736]

they confirmed the low attribution on inclusion removal from the steel melt of the MgO-C coated filter which was stated by Emmel et al. [Emm+13]. Thus, they did not reproduce the considered possibility of Aneziris et al. [Ane+13d], who investigated MgO-C as a coating on carbon-bonded alumina filters, too, and observed the formation of secondary magnesia needles on the filter surface during the immersion tests. According to them, the partial consumption of dissolved oxygen by this formation might provide the possibility to decrease the formation of inclusions by reducing the total oxygen content of the melt.

Dudczig et al. [Dud+14] explained the interactions of the carbon-bonded alumina filter with the steel melt in the following way (cf. Figure 2.14b): They assumed that due to a carbo-thermal reduction of alumina within the filter material, which was catalytically promoted by iron of the melt, gaseous reaction products like $\text{CO}_{(g)}$

2. Literature Review

and alumina sub-oxides were formed. Since alumina is not wetted by liquid steel and the wetting angle even enhanced due to the rough filter surface, the liquid steel did not infiltrate the filter material. The gaseous alumina sub-oxides might react with dissolved oxygen from the melt at the filter–steel interface and form the thin alumina layer on the filter surface by reoxidation. The layer thickness, however, was limited by the low amount of dissolved oxygen within the deoxidised melt. That alumina layer was thought to be highly attractive to inclusions of the liquid steel and enhanced their deposition on the filter surface. As they observed a similar layer build-up on the alumina coating and iron-based droplets underneath it, they concluded that the steel components contributed to the carbo-thermal reduction of alumina as gases.

Zienert et al. [Zie+15] evaluated the experimental results of such immersion tests with a carbon-bonded alumina filter from a thermodynamic point of view and developed a thermodynamic model in the Fe-Al-O-C system. They excluded a carbo-thermal reduction of alumina and, instead, concluded that alumina dissolved partially in the iron melt and precipitated from it, whereby these interactions were triggered by the dissolution of carbon from the carbon-bonded filter surface into the melt. Thereby, a gas phase consisting mainly of CO with traces of iron and alumina sub-oxides is formed.

Storti [Sto18] developed and applied multi-walled carbon nanotubes (MWCNTs) coatings to accelerate the interactions between filter material and molten steel due to the high reactivity and fast dissolution of the nano-scaled carbon particles. In the following, the time-dependent behaviour of such coated Al_2O_3 –C filters was compared to uncoated ones by immersing them for 10 s, 30 s, 60 s and 300 s. [Sto+15; Sto+16a; Sto+16b; Sto+17c] In addition, the effect of Al_2O_3 nano-sheets mixed to the MWCNTs was investigated by immersing coated filters for 10 s, 60 s and 120 s. [Sto+17b; Sto18] On all these filters, a layer build-up on the filter surface similar to those described earlier by Dudczig et al. [Dud+14] was observed: Carbon from the coating and the surface of the Al_2O_3 –C filter dissolved in the melt and left a decarburised filter surface behind. On that zone, a thin in-situ formed alumina layer was detected on which further alumina particles were attached. Whereas the thickness of the in-situ formed thin alumina layer kept almost constant independently from the immersion time, the thickness of the layer with attached particles (mainly alumina) increased with immersion time. Storti assumed that the attached alumina particles with complex shapes formed mainly from alumina provided by the filter. After immersing filters for 60 s or longer, the artificially created endogenous alumina inclusions were detected on top of the attached alumina particles in form of inclusion clusters. From the irregular shape of these clusters, Storti deduced that

2. Literature Review

they grew in a region of the melt with high O and Al supersaturation. Thereby, the nano-coated filters showed generally a very similar layer-build up compared to uncoated filters for any testing time. [Sto18, p. 92] In a subsequent study, the in-situ formed alumina layer was investigated in more detail on a thin sample¹⁶ isolated by focused ion beam (FIB) to analyse its composition and crystal structure by EDS and EBSD. [SBA18]. Thereby, the layer consisted of α -Al₂O₃. Further, a concentration gradient of Al and O over the cross-sectional area of the in-situ formed layer was detected, whereby both concentrations decreased towards the side facing the steel melt interface. From that, a diffusion driven formation process of that in-situ layer was assumed, whose thickness was thus limited. Last but not least, Storti et al. [Sto+17a] investigated in a parallel work to this thesis the effect of two types of carbon-bonded calcium aluminate-based coatings (CaO · 2 Al₂O₃ or CaO · 6 Al₂O₃), which were immersed for 10 s at 1650 °C. Thereby, a layer-build up derivating from the aforementioned scheme was observed in case of the (CaO · 2 Al₂O₃)-C coated filter: The surface was highly porous and showed much entrapped steel. Partially sintered polyhedral particles made of Ca, Al, and O, the thin secondary layer, and the artificially generated endogenous inclusions were observed on both filter types. Regarding Al₂O₃ NMIs, the steel analysis indicated that both compositions resulted in a filtration efficiency close to 100 %.

Within his doctoral thesis, Salomon [Sal19] investigated interactions of filter materials with liquid steel excluding the influence of the melt flow by experiments using a spark plasma sintering (SPS) device and high heating rates.

By testing Al₂O₃-C (hollow cylinders and filter fragments) with molten steel (42CrMo4), he observed a decarburised, porous surface with "bowling pin" shaped steel residuals, cf. Figure 2.15. They penetrated the refractory material up to a thickness of 40 µm (determined by light microscopy and SEM), cf. Figure 2.16. He assumed pressureless penetration of the carbon-bonded alumina by the liquid steel. Despite the decarburisation of the Al₂O₃-C surface, he did not detect a change of the carbon content of the steel by EDS and wavelength dispersive X-ray spectrometry (WDS). It was almost constant (0.4 mass%). [Sal19, pp. 124–125]

In the case of the filter fragments, the decarburised zone on the filter surface as well as the penetration zone of steel residuals were of similar dimension. In addition, a thin oxide layer was observed directly on the surface of the filter, i.e. at the interface with the molten steel, which is similar to the above described observations by Storti [Sto18] and Dudczig et al. [Dud+14]. EDS analysis of this about 1 µm thick layer indicated that it consisted of alumina and point-analysis by EBSD verified the presence of α -Al₂O₃. On this layer, fine structured alumina particles

¹⁶The sample was prepared from a MWCNTs coated filter immersed for 10 s in 42CrMo4.

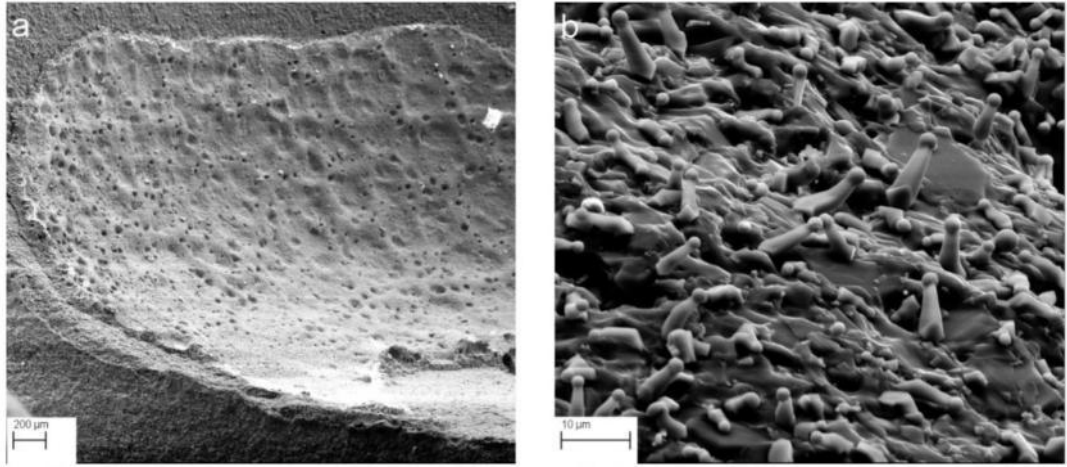


Figure 2.15.: Al₂O₃-C(hollow cylinder)-steel interface by SPS. a) Surface of the Al₂O₃-C refractory after steel contact within the SPS device, showing the porous decarburised layer on its surface. b) higher magnification, "bowling pin" shaped steel residuals remaining on the decarburised zone. [Sal+13, p. 1239]

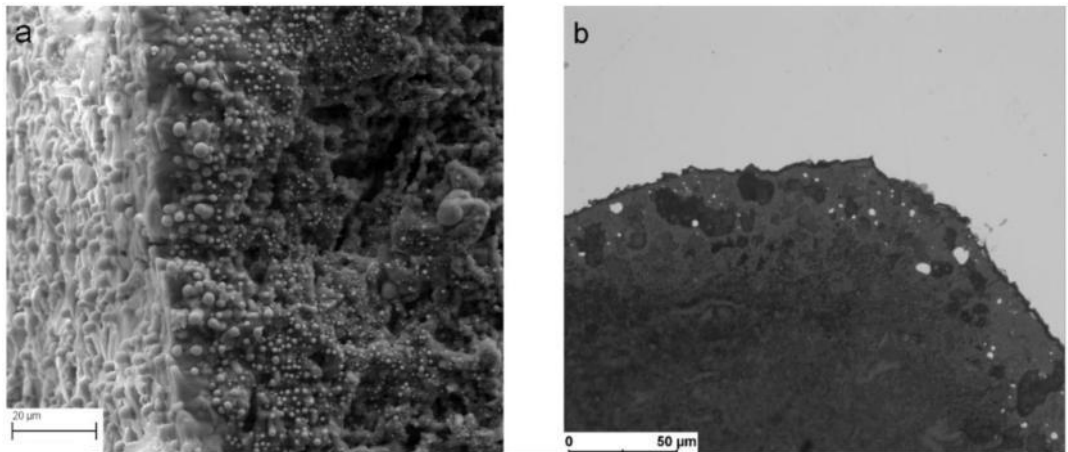


Figure 2.16.: Al₂O₃-C(hollow cylinder)-steel interface by SPS. Penetration depth of the liquid steel a) on a cross section of a fractured surface, and b) on a polished cross section with solidified steel. [Sal+13, p. 1239]

2. Literature Review

with iron-based droplets in between were found. The quickly solidified steel near the filter surface contained an increased content of aluminium (between 1 at % to 4.8 at % according to EDS analysis). Despite varying the holding time of the experiment from 1 min to 15 min, the steel penetration depth as well as the thickness of the thin alumina layer remained unchanged. He observed that exogenous inclusions deposited on the filter surface were also covered by the in-situ formed alumina layer and the subsequent layer build-up, joining inclusions and filter together. [Sal19, pp. 129–131] Salomon investigated alumina and carbonaceous alumina coated $\text{Al}_2\text{O}_3\text{--C}$ filter fragments using the SPS set-up as well. As these investigations ran parallel to the materials and experiments presented in this study, these results will be discussed in connection to the results obtained in this study, cf. Chapter 4. By comparing the results, it has to be taken in mind that the steel melt flow, which was deliberately suppressed in Salomon’s trials, will strongly influence the diffusion driven reactions between the refractory material and the liquid steel. Thus, it is expected that reactions are accelerated in the case of the immersion trials compared to the SPS trials. Furthermore, Salomon investigated interactions with MgO--C coated $\text{Al}_2\text{O}_3\text{--C}$ materials, too. Thereby, he verified the formation of a thin secondary magnesia layer at the filter–steel interface, which should form from an Mg and CO containing gas phase during the interactions. Further, he detected MgAl_2O_4 whiskers between substrate material and coating of the filter [Sal19, pp. 156–157], [Sal+15] He discussed vapour-liquid-solid reactions causing the whisker growth. [Sal19, pp. 162–164]

It is challenging to investigate the influence of the filter surface roughness on the steel melt filtration. Nevertheless, Fritzsche et al. [FP14; FP15; FP16] made efforts to develop a room temperature model, which was deduced from water-based experiments and calculations, to evaluate the effect of the surface roughness on the particle deposition during filtration. The resulting, new model included adhesive forces on rough surfaces, which was in excellent agreement with experimental results of water-based trials. Ditscherlein et al. [Dit+17] investigated the influence of surface roughness of carbon-bonded and ceramic-bonded materials used for filter production on adhesive forces at room temperature utilising an atomic force microscope. Thereby, they observed that nano-bubbles might have the potential to support particle adhesion. Heuzeroth et al. [HFP15] verified the beneficial effect of a non-wetting inclusion–filter system in a liquid medium on the filtration effect by water models at room temperature. Further, they confirmed that nano-bubbles are present in such a non-wetting system and contribute to the increased agglomeration tendency of the particles and enhanced adhesion on the filter medium. In case of aluminium melt filtration, Voigt et al. [Voi+19] reported an influence of the roughness on inclusion removal from the melt.

2. Literature Review

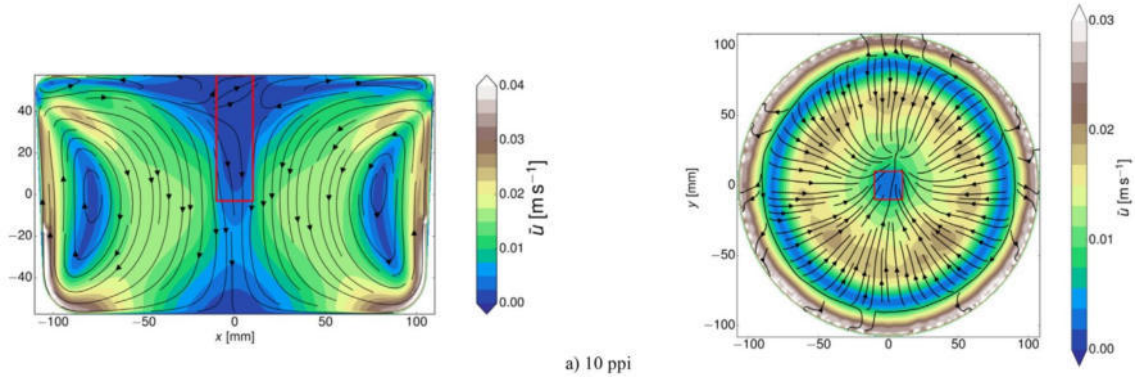


Figure 2.17.: Simulation of immersion trials using the SCS set-up: Time averaged flow field for the immersed ceramic filter (10 ppi). Left: vertical mid-plane, and right: horizontal plane at $y=17$ mm. The red box represents the location of the filter. [Asa+17, p. 6]

Asad et al. [Asa+16; Asa+17] developed a numerical model to simulate flow patterns and the inclusion removal by immersing ceramic filters into the melt using the inductively heated crucible of the SCS for immersion tests utilized within the CRC 920 as well as in this thesis. Due to the fixed filter position within the experimental set-up, they predicted low filtration efficiencies for 10 ppi filters as they were positioned in a region of low melt velocity, cf. Figure 2.17. [Asa+17] Thereby, their numerical model respected the filter and inclusion geometry, amongst others, but neither the chemical interactions nor the impact of nano-bubbles was considered in these first studies. They calculated a mass flow rate through the 10 ppi filter of 0.046 kg s^{-1} . [Asa+17] In a following study, they analysed the impact of different turbulence model methods on the resulting melt flow and inclusion transport within the numerical simulation of the induction crucible furnace used for the immersion tests. [ACS18] Subsequently, they extended their numerical model by the impact of CO nano-bubbles formation on the inclusion removal. Thereby, about 30 % of the initial amount of inclusions were removed after 10 s of simulated immersion time. Due to the enhanced concentration of carbon near the filter surface, the bubble size increased quickly if the bubbles are located close to the filter. This led to a high rising velocity of the NMIs causing enhanced melt velocity close to the filter wall. [Asa+18] Nevertheless, $\text{CO}_{(g)}$ bubbles not only formed on the filter wall, but also on the inclusion surface. Both contributed equally to the overall inclusion removal. [AAS19]

2.5. Summary and implications for the present thesis

The literature review showed that the agglomeration tendency and by this the deposition probability of non-metallic inclusions (NMIs) as well as the attraction forces towards the filter surface depend strongly on the wetting behaviour of NMIs by the melt. The wetting behaviour is on the one side determined by the surface tension of the melt (and therewith the chemical composition of the melt), and on the other side depends on the to be wetted particles properties, like phase (liquid, gaseous, solid), surface roughness, and shape. Thereby, strong agglomeration was observed on NMI-filter systems, which were both similar but bad wetted by the melt.

With these considerations in mind, regarding the usual kind of NMIs in the melt (alumina, Ca-aluminates, Ca-silicates, MnS), and considering the process conditions, the filter has to withstand a high thermal shock at initial casting, requires a sufficient permeability at high temperatures (above 1550 °C), and needs a sufficient strength to resist the thermo-mechanical stresses induced by the streaming melt. As a consequence, there is only a limited choice of possible filter materials including Al_2O_3 , ZrO_2 , and MgO , partly also mixtures of them and/or with CaO . Filters based on ZrO_2 were applied successfully for decades in steel melt filtration, but their high heat capacity demands a high overheating of the melt to prevent priming issues. Further, investigations regarding clogging of submerged entry nozzles (SENs) showed low clogging for ZrO_2 -based materials, which in return implies a low filtration efficiency. In comparison, carbon-bonded alumina materials seemed to be very promising, especially due to the beneficial thermo-mechanical properties (low heat capacity, high thermal conductivity, excellent thermal shock resistance). Carbon-bonded alumina filters were successfully implemented for steel melt filtration, too, over the recent years.

Within the CRC 920, the impact of coatings on Al_2O_3 -C filters to enhance the filtration of NMIs from molten steel has been investigated for the first time. Thereby, coating materials based on or at least containing Al_2O_3 , (carbon-bonded) MgO , and SiO_2 were evaluated. From these material combinations, alumina was most promising as thick clogging layers and high amounts of deposited particles were observed after contact with molten steel.

Based on these preliminary studies, alumina-based coatings on carbon-bonded alumina filters will be more closely investigated in this thesis. Storti [Sto18] evaluated already the influence of time on the filter-steel interactions by laboratory immersion tests with MWCNTs coated filters, but such tests were not performed for the oxide coatings. In contrast to the MWCNTs-based coatings, alumina based coatings will not completely dissolve during the immersion tests. The results of such

2. Literature Review

experiments will be presented and the role of an oxide coating and its influence on the filter–steel melt interactions discussed in the present thesis.

The reviewed theories regarding the interactions between refractory and molten steel agree that a liquid oxide film forms at the interface, which changes its chemical composition during interactions. In the initial moment, oxygen (provided by the open porosity of the refractory material or by reduction of oxide components at the interface) reacts with iron¹⁷ of the melt to form liquid iron oxide at the interface. Iron oxide is thermodynamically unstable under the process conditions and is easily reduced by other elements dissolved in the melt, e.g. by C, Si, Ca, Mg, Ti, Zr, Mn (cf. Ellingham diagram in Figure 2.4 on page 19). Thereby, impurities of the refractory material (esp. oxides of alkalis, Si, and Ca) might be reduced and could act as further oxygen source. That will continue until the most stable oxides, usually alumina, were formed at the interface.

Different explanations have been reported discussing what happens if the carbon-bonded material is applied. According to Dudczig et al. [Dud+14] and Khanna et al. [Kha+12], a carbo-thermic reduction of carbon-bonded alumina took place at the elevated temperatures. Carbon and gaseous reaction products like alumina sub-oxides and carbon monoxide were supposed to pass through the porous alumina coating to the filter–steel melt interface and were available for redox-reactions. Thermodynamic studies of Zienert et al. [Zie+15] indicated, however, that no carbo-thermal reduction of carbon-bonded alumina should have taken place under the conditions of the immersion tests. They suggested that the alumina of the filter partially dissolved in the molten steel. That reaction should have been accelerated by carbon, which is in accordance to the discussion of Poirier et al. [PT94; Poi15]. As the system was out of equilibrium, alumina may have precipitated at the filter surface due to a changing oxygen activity within the melt. The mentioned authors agree that carbon from the carbon-bonded filter should be involved in the observed in-situ layer and following secondary alumina formation, whereby iron acts supposedly as a catalyst. Furthermore, the formation of $\text{CO}_{(\text{g})}$ is described in both cases as a result of these interfacial reactions and the presence of bubbles as reaction side.

Especially in the case of carbon-bonded refractories, carbon at the surface will dissolve in the melt and reduce less stable oxides. Interestingly, graphite is well wetted by liquid iron or steel, but carbon-bonded alumina not. The reason might be the formation of $\text{CO}_{(\text{g})}$ at the interface (oxygen is provided by dissolving alumina). Decades ago, alumina was thought to be inert against an iron melt, but in the meantime it was shown that it reacts (dissolution) with the melt depending on the

¹⁷Iron—as main component of the steel melt—has the highest probability to meet and react with oxygen.

2. Literature Review

carbon content of the system. Thereby, it was found that with increasing amount of dissolved carbon, the aluminium activity increases, and thus more aluminium dissolve in the melt. These considerations result in the second object of this thesis, in which the influence of a small amount of carbon within the alumina coating on the time-depending interactions will be investigated.

During the first two experimental trials, it became obvious that the thermal shock resistance of the coating has to be improved. To improve it, a material combination will be tested which is known for its excellent thermal shock resistance: alumina-zirconia-titania (AZT) in the ratio 95:2.5:2.5. To the authors knowledge, this material combination has not been investigated as coating material for steel melt filtration up to now. Thereby, the influence of zirconia and/or titania combined with alumina on the filter-steel melt interactions is investigated. For both oxides different reactions with the melt are expected: While zirconia is a strong deoxidiser and not-wetted by the melt, titania is supposedly wetted by the melt and lowers the surface tension of the molten iron if it dissolves. These considerations lead to the third experimental series of this thesis.

3. Methodology

Carbon-bonded alumina filters as developed within the CRC 920 and as described in the previous chapter were used as substrates for the alumina-based coatings. Due to an easy handling, the coatings were applied by spray-coating with a slurry at room temperature and were subsequently heat treated, which was already established by prior investigations of Emmel et al. [EA13] and Dudczig et al. [Dud+14]. As will be shown later that resulted in a thin, porous coating on the filters. The used raw materials, the filter manufacturing procedure and application of the coatings will be described in the first two sections chapter. Subsequently, the immersion experiments and, finally, the utilised characterisation methods are presented.

3.1. Filter manufacturing I: carbon-bonded alumina filter substrate

Al_2O_3 -C filters were used as substrates for the functional coatings. They were produced following the same routine as described by Emmel and Aneziris [EA12], which based on the processing route patented by Schwartzwalder and Somers in 1963 [SS63]. Thereby, the carbon-bonded alumina filters were generated in two steps: impregnation and spray-coating. Impregnation slurry and spray-coating slurry were of the same composition except of the solids content. Table 3.1 presents both of them as "Substrate". That composition is based on composition no. 3 presented by Emmel and Aneziris [EA12], which was further optimized in the doctoral thesis of Emmel [Emm14].

Table 3.2 presents the particle size distribution of the raw materials used. Thereby, Martoxid MR 70 (Martinswerk, Germany) was chosen as alumina due to the fine particle size. Due to agglomeration issues during storage, Martoxid MR 70 was pretreated in the same way as described by Storti et al. [Sto+16a]. Therefore, a plastic canister containing 5 L was filled as follows: one third with small grinding balls (zirconia, 2 mm diameter) and large grinding balls (alumina, 30 mm diameter), and one third with the raw material MR 70 (about 1.5 kg), resulting in a two third filling. That container was placed for 40 min on a roller bank for deagglomeration.

3. Methodology

Table 3.1.: Ceramic slurry compositions.

	Substrate	A	AC	AC-T	AC-Z	AC-ZT
Raw materials (mass%)						
Al ₂ O ₃ Martoxid MR 70	66.0	75.0	70.31	68.44	68.44	66.56
Al ₂ O ₃ CL 370	0	25.0	23.44	22.81	22.81	22.19
ZrO ₂	0	0	0	0	2.5	2.5
TiO ₂	0	0	0	2.5	0	2.5
Carbores® P	20.0	0	6.25	6.25	6.25	6.25
N-991	6.3	0	0	0	0	0
AF 96/97	7.7	0	0	0	0	0
Additives (mass%)*						
C12C	1.5	1.5	1.5	1.5	1.5	1.5
Castament VP 95 L	0.3	0.3	0.3	0.3	0.3	0.3
Contraspum K 1012	0.1	0.1	0.1	0.1	0.1	0.1
Xanthan	0	0	0	0	0	0
Guaran	0	0	0	0	0	0
Total solids content (mass%) [†]						
Impregnation slurry	81.58	-	-	-	-	-
Spraying slurry	70.0	65.0	65.0	72.5	72.5	72.5

* Related to raw materials.

[†] Without additives.

3. Methodology

Table 3.2.: Particle size distribution of the raw materials.

Raw Material	d_{10} (μm)	d_{50} (μm)	d_{90} (μm)
MR70 deaggl.	0.34	0.83	1.72
CL370	0.17	1.44	6.76
TiO ₂	0.11	1.79	4.37
ZrO ₂	0.10	0.32	2.21
Carbores® P	3.04	18.23	90.64
AF 96-97 graphite	3.51	6.03	19.33
N-991 carbon black	0.76	2.16	5.72

Afterwards, the deagglomerated alumina powder was separated from the grinding balls by screening using a sieve with 1.6 mm mesh size, a sieving machine utilizing an amplitude of 0.7 mm for 2 min (to minimize wear) on the basis of Fruhstorfer et al. [FSA14].

The modified coal tar pitch Carbores® P (Rütgers, Germany) was chosen as binder for the substrate as well as for the carbon containing coatings, the carbon black Luvomaxx N-991 (Lehmann & Voss & Co., Germany) and the graphite AF 96/97 (Graphit Kropfmühl) as additional carbon source, and—according to Emmel [EA12]—to optimise the particle size distribution within the slurry. Further additives for the water based slurries were: ammonium lignin sulfonate T11B (Otto Dille, Germany) as wetting, dispersing and temporary binding agent, the modified polycarboxylate ether Castament VP 95L (BASF, Germany) as dispersing agent¹, and the alkyl polyalkylen glycol ether Contraspum K 1012 (Zschimmer & Schwarz, Germany) as anti-foaming agent.

Both alumina powders, the carbon raw materials, and lignin sulfonate were shortly (about 30 s) dry mixed in a Hobbart-type mixer (ToniTechnik, Germany). The liquid additives Castament VP 95L and Contraspum K 1012 were dispersed in 50 ml deionised water and were added to the powders. The residual amount of water was added stepwise to the mixture to guarantee thorough mixing. When the mixture formed a plastic mass, water addition was paused and that mass kneaded for 5 min to destroy agglomerates by shear force and enhance homogenization.

Firstly, polyurethane templates (Bulpren C 28720, 10 ppi, Eurofoam Deutschland GmbH, Germany) were impregnated by dipping the foam into the highly viscous impregnation slurry. Filter samples e.g. for cold crushing strength were made with

¹In the mean time, both products have been renamed by their suppliers and are called now C12C and MelPers® 9360, respectively.

3. Methodology

polyurethane templates sizing $50\text{ mm}^3 \times 50\text{ mm}^3 \times 20\text{ mm}^3$ and for immersion tests with a size of $125\text{ mm}^3 \times 25\text{ mm}^3 \times 20\text{ mm}^3$. The applied mass for different sample sizes was determined by keeping the ratio between mass after impregnation and applied mass by spray coating constant based on the $50\text{ mm}^3 \times 50\text{ mm}^3 \times 20\text{ mm}^3$ sizing filters, which are described in the following. The impregnated foams were rolled through rollers with a gap width of 4 mm to remove excess slurry. These impregnated filters weighted about 12 g. After 24 h drying at room temperature, the filters weight about 10.5 g. Secondly, they were spray coated to the final wet weight of $(26 \pm 1)\text{ g}$. Therefore, a spray gun SATAjet B (Sata, Germany) with a nozzle diameter of 1.4 mm was used and 3 bar pressurized air were applied. The distance between spray gun and filter was approximately 15 cm. After spray-coating, the filters were dried again for 24 h at room temperature.

The prepared filters were embedded in calcined petrol coke (0.2 mm to 2 mm, Müco Mücher & Enstripp GmbH & Co KG) and were heated up stepwise to $800\text{ }^\circ\text{C}$ following the temperature program in Figure 3.1, adapted from Emmel and Aneziris [EA12]: heating rate 1 K min^{-1} , holding time 30 min each 100 K beginning from $100\text{ }^\circ\text{C}$ on, and a holding time of 180 min at the final temperature.

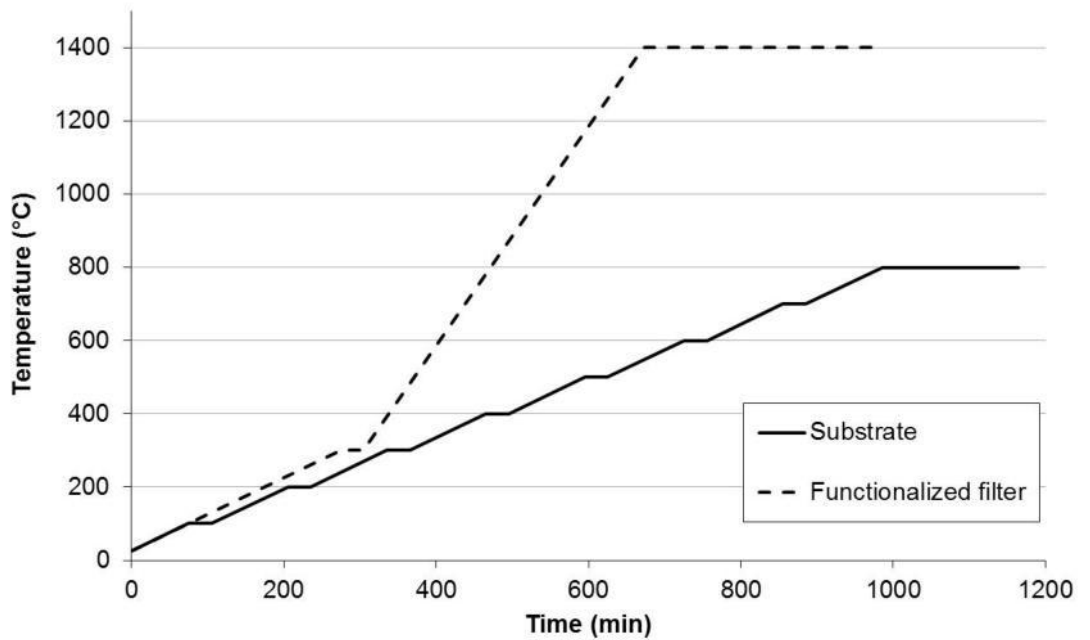


Figure 3.1.: Temperature regimes for filter production. Carbon-bonded substrates were stepwise heated up to $800\text{ }^\circ\text{C}$, solid line. After applying an alumina-based coating, the filters were again heated up to $1400\text{ }^\circ\text{C}$, dashed line.

3.2. Filter manufacturing II: alumina based coatings

The slurry composition of the coatings is also listed in Table 3.1. Thereby, following acronyms of the coatings are used in this work:

A Coating containing alumina

AC Coating containing alumina and carbon

AC-T Coating containing alumina, titania and carbon

AC-Z Coating containing alumina, zirconia and carbon

AC-ZT Coating containing alumina, zirconia, titania and carbon

Alumina coatings with/without carbon. Simply adding 6.25 mass% Carbores® P to the alumina spray-coating slurry of Emmel and Aneziris [EA13] resulted in a strong segregation and sedimentation of the slurry. Therefore, the alumina CL 370 used in the mentioned work was partly replaced by the finer alumina MR 70. As the lignin sulfonate acts as wetting agent according to Emmel et al. [EA12; EA13], the content was varied, too. Based on the slurry stability and the resulting flow behaviour (cf. Appendix A.1), the composition presented in Table 3.1 was chosen for the carbonaceous alumina coating "AC". By replacing the Carbores® P completely by the alumina raw materials in the appropriate ratio, the alumina coating "A" was obtained.

Coatings doped with zirconia and/or titania. The compositions of the doped coatings were derived from the carbonaceous alumina slurry composition. The appropriate ratio (by weight) of alumina was replaced by the desired amount of zirconia and/or titania (compositions "AC-Z", "AC-T", and "AC-ZT" in Table 3.1). Thereby, rutile TR-HP-2 (Crenox²) and the monolithic zirconia CS02 (ZirPro Saint-Gobain, France)³ were used as raw materials, which are both fine powders (cf. Table 3.2).

As this approach is kind of a prove-of-concept, the slurries were not further optimised within this work. It might be interesting in further work, however, to investigate, for example, the impact of the porosity or coating thickness on the filtration performance in more detail.

²In the meantime a part of Sachtleben, Germany.

³Unstabilised, i.e. without any dopant or additive, 99.0 % purity. According to the technical data sheet [SEP20], in sum 0.38 mass% of other oxides (SiO₂, Na₂O, Al₂O₃, TiO₂, Fe₂O₃, CaO and H₂O).

Preparation and application of the coatings. To prepare the coating slurries, all components were filled in a small plastic container (1000 ml) with about one third filling of alumina grinding balls (diameter 10.5 mm to 20 mm), and mixed for 60 min. The coatings were applied by spray coating similar to the coating step of the carbon-bonded substrates described above. Thereby, the filters were only shortly sprayed at each side resulting in about 5 g applied slurry, which was sufficient to yield a thin coating covering all filter struts. The coated filters were dried again for 24 h at room temperature and were placed in alumina crucibles filled with calcined petrol coke. Due to the fact that these crucibles were not as well sealed towards the furnace atmosphere as the steel crucibles used for the carbon-bonded substrates, the filters were covered with at least 5 cm petrol coke and a top-layer of alumina paper to inhibit an oxidation of the filters. Preparation and heat treatment of the coated filters were performed in accordance with Emmel and Aneziris [EA13], i.e. heating rate 1 K min^{-1} , holding time 30 min at 300°C to remove safely the residual water and decomposition products of the organic additives of the coated filters; with an increased heating rate of 3 K min^{-1} to the final temperature of 1400°C , which was hold for 300 min, cf. the dashed line in Figure 3.1.

3.3. Immersion tests

The immersion tests were carried out using an inductively heated melting system of the SCS (Systec GmbH, Germany). Therein, about 30 kg of the steel grade 42CrMo4 (Table 3.3 lists its composition) were remelted within an alumina-spinel crucible. Thereby, the temperature and oxygen content of the melt were monitored by a pO_2/T sensor system (Heraeus Electro-Nite GmbH & Co. KG, Germany). The crucibles were produced only for these experiments to avoid any CaO and silica impurities that may react with inclusions of the steel. Dudczig et al. [Dud+14] described the crucible composition in detail. The immersion time was taken by a stop watch as soon as the operator of the device observed that the filter was submerged in the melt. The mean steel mass flow rate through the filter during immersion was around 0.046 kg s^{-1} for a steel density of 7 g cm^3 and a dynamic viscosity of 6 mPa s as was simulated by Asad et al. [Asa+17]. After immersing a filter sample, the inductive heating was switched off and the steel freely cooled down. To evaluate the influence of the remelting process, a batch of steel was remelted without immersing a filter. Therefore, the final temperature was held for about 15 min before the heating was switched off. This sample is referred to as "without filter" in the following.

In the case of the alumina and carbonaceous alumina coatings, was steel was remelted at 1650°C and was pretreated prior to immersing a filter sample. The pre-

3. Methodology

Table 3.3.: Composition of the used 42CrMo4 steel

Element	C	Si	Mn	P	S	Cr
(mass%)	0.407	0.243	0.791	0.014	0.001	0.960
Element	Mo	Ni	Al	Co	Cu	Ti
(mass%)	0.183	0.098	0.035	0.004	0.027	0.002

treatment of the steel generated endogenous alumina inclusions. At four stages, the dissolved oxygen content and the temperature of the molten steel were determined, cf. Table B.1 on page X for details. First data was obtained after the steel was melted (stage 1). To oxidize the steel (stage 2), 0.5 mass% iron oxide, and for the subsequent deoxidation, 0.05 mass% aluminium (stage 3) were added. The quantity of both additives is referred to the steel mass. Finally, the dissolved oxygen content and temperature were determined again after immersing the corresponding filter (stage 4).

Similar to Storti [Sto18], the filters were immersed for 10 s, 30 s, 60 s and 120 s. Thereby, 10 s is the shortest immersion time, which can be performed reasonably with the experimental set-up, a contact time between 30 s and 60 s covers common casting times of discontinuous steel casting methods. To gain information what happens with longer immersion time, 120 s immersion was chosen, too. The whole procedure took about 15 min from melting to ending the immersion test. For that reason, reference trials without immersing a filter were conducted with a dwell time of 15 min at the final temperature.

In the case of the test series with zirconia and/or tinania doped coatings, the same steel grade was remelted at 1580 °C. The filters were all immersed for 30 s. Here, no artificially alumina inclusions were generated. The logged oxygen content and the temperature of the steel melt are summarised in Table 4.10 on page 114. In this test series, samples of the molten steel were taken before and after immersing the corresponding filter to evaluate the impact of immersing the filter on the amount and size of NMIs observed in the solidified steel samples. Silica containing samplers were used for that purpose.

3.4. Characterisation methods

Most of the characterization methods, especially the testing of the mechanical properties, were done on samples with the A or AC coating. As the focus was on the interactions with the molten steel, not all characterization methods were applied in

3. Methodology

the test series with zirconia and/or tinania doped coatings, as outlined below.

Rheology. The flow behaviour of all coating slurries was determined using a rheometer RheoStress RS 150 (HAAKE, Germany). A measurement vessel of the type 01038 Z40 DIN Ti and the measuring as well as the data evaluation program of RheoWin (3rd version) were used. Dynamic viscosity and shear stress were determined as a function of the shear rate following the same measurement program described by Emmel and Aneziris[EA13]. Thereby, the shear rate was changed linearly from 0.1 s^{-1} to 1000 s^{-1} with 10 s dwell time at each step. It was kept constant at the final value for 90 s and was subsequently reduced in descending order to the initial one.

Filter strut thickness. The strut diameter was determined on light microscopy images (20x magnification) using an image editing program (ImageJ 1.48v).

A filter sample volume of about $24\text{ mm} \times 24\text{ mm} \times 24\text{ mm}$ was characterised using a micro-focus X-ray computer tomography system CT-ALPHA (ProConX-Ray, Germany) to calculate the strut wall thickness. This device operated at 140 kV and 40 μA . Further, it was equipped with a 160 kV X-ray source and a Dexela 1512 detector (Perkin Elmer, Germany) with 1944×1526 active pixels. That resulted in a voxel size of $35\text{ }\mu\text{m} \times 35\text{ }\mu\text{m} \times 35\text{ }\mu\text{m}$ after reconstruction. The obtained data was evaluated by the visualization software VGStudioMax 2.1 (VolumeGraphics GmbH, Germany). The wall thickness distribution was analysed using the software MAVI (Fraunhofer, Germany) following the same routine described by Luchini et al. [Luc+18] which is based on morphological image processing.

Cold crushing strength. The cold crushing strength (CCS) was determined on samples with coatings A or AC sizing $50\text{ mm} \times 50\text{ mm} \times 20\text{ mm}$, whereby ten samples were tested for each type. An universal testing machine TT28100 (TIRA GmbH, Germany) with a 5 kN pressure cell was used. The tests were carried out using a displacement speed of 2 mm min^{-1} until a counteracting force of 2 N was generated. After that, the displacement speed was increased to 3 mm min^{-1} . The test stopped when the strength loss reached 90 %.

Chemical composition of the coating material. To prepare samples for XRD analysis, the coating slurry was cast on a sheet of aluminium foil and dried over night at room temperature. The dried material was crushed, sieved, and pressed with 40 MPa to little tablets ($d=15\text{ mm}$, $h=5\text{ mm}$) using an arbor press (DOP 2000, Holzmann Maschinen GmbH, Austria). The heat treatment of these tablets was exactly like the one of the coated filters (up to $1400\text{ }^{\circ}\text{C}$ within a coke bed, cf. Figure 3.1

3. Methodology

on page 57). Afterward, the tablets were ground to a particle size $<63\text{ }\mu\text{m}$ using a planetary micro mill PULVERISETTE 7 (FRITSCH GmbH, Germany) with zirconia vessels and grinding balls. That powder was characterized using an X'PERT Pro MPDPW 3040/60 diffractometer (PANalytical GmbH, Germany) with copper radiation. The data was qualitatively analysed using the software X'Pert Highscore.

In addition, the surface of the coated filter samples was analysed by secondary neutral mass spectroscopy (SNMS) using an INA-X (SPECS GmbH, Germany). The carbon-content was estimated using a carbon analyser G4 Icarus (Bruker Elemental GmbH, Germany).

Open porosity and shrinkage. The open porosity of the coated filter struts was determined by mercury porosimetry using a Pascal 140/440 (Porotec, Germany).

Shrinkage during the heat treatment was characterised using a dilatometer DIL 402 C (Netzsch, Selb, Germany). Coated $\text{Al}_2\text{O}_3\text{-C}$ sample bars with a size of $5\text{ mm} \times 5\text{ mm} \times 20\text{ mm}$ were heat treated within the equipment at 1400°C under argon atmosphere. Thereby, the samples were heated and cooled with a rate of 5 K min^{-1} .

Microstructure and phase analyses of the coated filters. The microstructure of the samples before and after the immersion tests was characterised by light and electron microscopy. For light microscopy, a digital light microscope VHX-2000 D (Keyence, Germany) equipped with an objective VH-Z20R was used. Carbon-sputtered samples were prepared and analysed by an electron microscope Philips XL 30 (Phillips, Germany) for the latter method. That unit was also equipped with an EDS detector (EDAX-Ametek, USA).

The filters' coatings were very brittle after the immersion tests. Due to that, sample preparation was quite challenging, especially for the destructive sample preparation. Hence, even despite a most careful treatment of the samples, detachment of the coating or in-situ formed layers could not be prevented. Furthermore, embedding was challenging due to a missing bonding between coating material and in-situ formed layer. That led to a large crack at the interface of the alumina coating and the in-situ formed layer because the embedding material detached the in-situ formed layer from the filter surface during cooling. Of course, EDS/EBSD characterization could not have been carried out at these rough interfaces. Thus, areas with remaining steel droplets were investigated. An SEM of the type Versa3D (FEI Company, USA) was used to determine the phase composition of deposited particles on such polished cross-sections (epoxy mounting EpoThin from Buehler). That SEM was not only equipped with EBSD and EDS, but also with a gallium-ion source for FIB

3. Methodology

preparation. Both the EBSD and EDS system were from EDAX-Ametek (USA). For FIB preparation, an area including a particle attached on the filter surface/coating material was selected. Thereby, trenches were generated on the polished sample by the gallium-ions in such a way that the EDS detector was able to examine the area of interest. Slice by slice, a layer was cut from the investigated part and after each cut, the elemental distribution was estimated by EDS.

Chemical composition of the steel. The chemical composition of the steel was determined using an arc spark optical emission spectrometer (OES) SPECTROMAXx (SPECTRO Analytical Instruments GmbH, Germany). For this characterization, samples of the size 40 mm × 40 mm × 10 mm were always cut from the same position of the solidified steel after each immersion test (2/3 of the height from the bottom, 1/3 of the diameter from the outside). Three measurements by spark emission spectrometer were carried out on one side of the steel samples.

In the meantime, a new spark OES device (Q2 ION, Bruker, Germany) was purchased and utilized for the steel samples of the test series with zirconia and/or tinania doped coatings. In that case, eight measurements were performed.

Inclusions remaining in the steel. The other side of the sample used to determine the chemical composition was carefully polished to 1 µm roughness to characterize inclusions remaining in the steel. Their distribution and chemical composition were determined by an automatic scanning electron microscopy (SEM) (ASPEX, FEI, USA). Thereby, a backscattered electrons (BSE) detector identified inclusions larger than 1 µm due to the different Z-contrast compared to the steel matrix. Afterwards, each particle was characterized by an automatic feature analysis (AFA) that includes energy dispersive X-ray spectrometry (EDS) as well. Thereby, position, geometry, orientation and chemical composition were determined.

Table 3.4 presents the rule-file that was applied to classify detected inclusions by their chemical composition in the case of the time-dependent immersion trials with filters A and AC. Such rule-files are not commonly available and were developed using reference specimens of a known composition and were adjusted to fit to the investigated system. Inclusions were categorized as “alumina inclusions” if their composition complied with following condition: Al >8 mass% and O >8 mass% and Mn <10 mass% and S <8 mass%, and Ca <5 mass%. Other inclusions were sorted step by step in further categories depending on their composition. “Dirt”-particles were defined as particles with a very high (>10 mass%) carbon content, which probably originated from organic residuals on the sample. Particles of the category “Fe-scratches” were attributed to indentations resulting from sample preparation.

3. Methodology

Table 3.4.: Rule-file used for the Aspex-SEM to identify inclusions that remained in solidified steel samples after immersion tests.

Chemical class	Element content (mass%)
Al_2O_3	$\text{Al} > 8$ and $\text{O} > 8$ and $\text{Mn} < 10$ and $\text{S} < 8$ and $\text{Ca} < 5$
Ca-aluminate	$\text{Ca} > 10$ and $\text{Al} > 5$
Mg-spinel	$\text{Al} > 8$ and $\text{Mg} > 0$ and $\text{S} < 5$ and $\text{Ca} < 5$
Al-Mn-Mg-Fe-Ca-silicate	$(\text{Si}/\text{Al}) > 0.4$ and $(\text{Al} + \text{Mn} + \text{Mg} + \text{Ca}) > 10$
SiO_2	$(\text{Si}/\text{Al}) \geq 0.4$ and $(\text{Si}/\text{O}) < 6.2$ and $\text{Al} < 3$ and $\text{Mg} < 3$ and $\text{Ca} < 3$ and $\text{K} < 5$ and $\text{S} < 10$
MnO-MnS	$\text{Mn} > 8$ and $(\text{Mn}/\text{S}) > 2$ and $\text{Al} < 20$ and $\text{Si} < 5$ and $\text{Ca} < 5$
CaO-CaS	$\text{Ca} > 5$ and $(\text{Ca}/\text{S}) < 2$
Dirt	$\text{C} > 10$
Fe-oxide	$\text{Fe} > 60$ and $\text{O} > 20$ and $(\text{Si} + \text{Al} + \text{Mn} + \text{Mg} + \text{Ca} + \text{Na}) < 10$
Fe-scratches	$\text{Fe} > 90$
Other	true

Iron oxide was likely formed during polishing if an inclusion fell out and the remaining steel surface oxidised. “Others” referred to any particles that misfitted the other categories.

To evaluate the test series with zirconia and/or tinania doped coatings, the rule-file was altered slightly. The reason was that, in the mean time, it was observed that the number of silica inclusions were incorrect due to misinterpretations: Part of them originated from residuals of the SiC-polishing mass, which was applied for sample preparation. The polishing cream was changed and the rule-file adjusted, cf. Table 3.5.

Due to the nature of the automatic analysis and the surface properties of the polished samples this characterization method is sensitive to errors as described by Fruhstorfer et al. [Fru+18] According to them, the first category (i.e. alumina) is the most accurate one. Based on that and due to the fact that these inclusions are most crucial for later application, the discussion focuses on this category.

Table 3.5.: Adjusted rule-file used for Aspex–SEM to identify inclusions that remained in solidified steel samples after the immersion test series with zirconia and/or tinania doped coatings.

Chemical class	Element content (mass%)
Al_2O_3	$\text{Al} > 2$ and $\text{O} > 5$ and $\text{Mn} < 10$ and $\text{S} < 8$ and $\text{Ca} < 5$
Ti-N	$\text{Ti} > 10$ and $\text{N} > 5$
Al-Mn-Mg-Fe-Ca-silicate	$(\text{Si}/\text{Al}) > 0.4$ and $(\text{Al} + \text{Mn} + \text{Mg} + \text{Ca}) > 10$
SiO_2	$(\text{Si}/\text{Al}) \geq 0.4$ and $(\text{Si}/\text{O}) < 6.2$ and $\text{Al} < 3$ and $\text{Mg} < 3$ and $\text{Ca} < 3$ and $\text{K} < 5$ and $\text{S} < 10$
MnO-MnS	$\text{Mn} > 8$ and $(\text{Mn}/\text{S}) \geq 1$ and $(\text{Al} + \text{Si} + \text{Ti} + \text{Cr}) < (\text{Mn} + \text{S})$
CaO-CaS	$\text{Ca} > 5$ and $(\text{Ca}/\text{S}) < 2$
Dirt	$\text{C} > 10$ or $\text{Na} > 5$
Fe-oxide	$\text{Fe} > 60$ and $\text{O} > 4$ and $(\text{Si} + \text{Al} + \text{Mn} + \text{Mg} + \text{Ca} + \text{Na}) < 10$
Fe-scratches	$\text{Fe} > 90$
Other	true

4. Results and Discussion

The first part of this chapter presents the properties of the manufactured filters. Characteristics of the coating slurries were determined in preliminary tests (cf. Appendix A.1 on page I) regarding the slurry development. In the following, the results of the immersion trials are presented, starting with a general description of the observed built-up layer-structure of the immersed filters (Section 4.2). Then, the time-depended interactions are regarded of the immersed alumina coated filters for several dwell times in the melt (Section 4.3). The impact of carbon on these interactions is shown subsequently (Section 4.4). Based on both experimental trials, the interactions between filter and steel melt are discussed and a working hypothesis formulated (Section 4.5). Finally, results regarding the influence of a zirconia and/or titania doping of the carbonaceous alumina coating on the filter–steel melt interactions are presented, discussed, and compared with the working hypothesis of this study (Section 4.6).

The sections regarding the alumina coated filters [Sch+17a] and regarding the effect of the titania dopant [Sch+19] have already been published.

4.1. Properties of the as-manufactured filters

4.1.1. Carbon-bonded alumina substrate

The microstructure of the uncoated carbon-bonded alumina filters manufactured following the routine described by Emmel [Emm14] is presented in Figure 4.1: The macroporosity is adapted from the polyurethane-foam and the surface reflected strongly the light of the light microscope. Burning out the polyurethane template left sharp-edged cavities in the porous filter struts (Figure 4.1 b). These findings are in accordance to Emmel [Emm14] and Storti [Sto18]. Higher magnification revealed an inhomogeneous surface of the strut with smooth and rough sites, cf. Figure 4.1 b with details in c) and d). On the one hand, that might origin from the spray coating process, as discussed by Wetzig et al. [Wet+18] and Luchini et al. [Luc+18]. Due to the fact that the dispersion of the slurry in the air-stream accelerated drying of the slurry droplets, they might build up the rough surface structure shown in

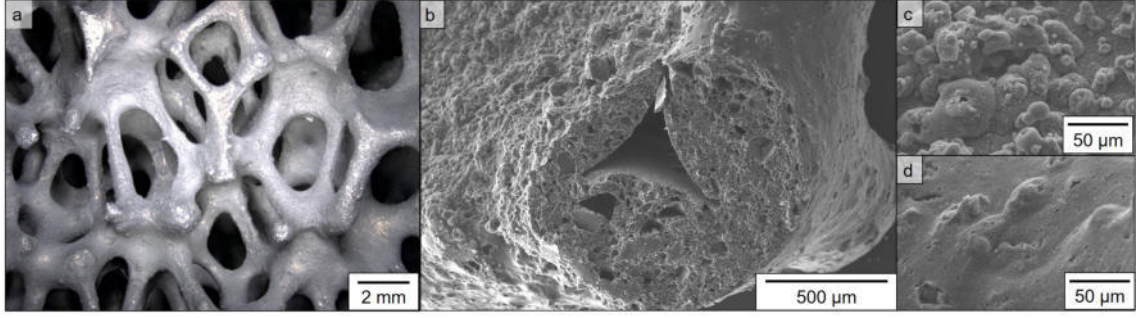


Figure 4.1.: Microstructure of an uncoated filter: (a) by light microscopy, (b) cross section of a strut by SEM (SE-mode), with details of the rough surface area (c) and the smooth surface area (d).

Figure 4.1 c. On the other hand, Carbores® P forms a liquid phase during the heat treatment which might result in the smoother surface.

4.1.2. Coated filter

Following properties have been evaluated on the filters with alumina (A) or alumina and carbon (AC) coating: the strut and coating thickness, the cold crushing strength, the microstructure of the coating, and the coating composition after coking.

Alumina coated filters after coking. Table 4.1 summarises the wall and strut thickness of uncoated and coated $\text{Al}_2\text{O}_3\text{-C}$ filters. Without coating, the mean wall thickness of the filter was $(250 \pm 100) \mu\text{m}$. The wall thickness distribution was best approximated by a normal distribution for all investigated filters (R^2 -values from 0.93 to 0.95). From the computer tomography (CT) data, it was seen that the average thickness of coating A was $20 \mu\text{m}$. The coating covered completely all filter struts, but the coating thickness was nevertheless inhomogeneous due to the spray process and the flow behaviour of the slurries: near the knots of the filter struts, the coating was thicker due to material accumulation and became thinner towards the middle of the filter struts, which is in excellent agreement with the results of Wetzig et al. [Wet+18] and Luchini et al. [Luc+18]. Figure 4.2 a) and b) present light micrographs of an alumina coated filter.

The determined CCS of coated filters was $(0.58 \pm 0.08) \text{ N mm}^{-2}$, which is about the double of the uncoated ones with $(0.27 \pm 0.04) \text{ N mm}^{-2}$. Although these results should not be directly compared to the data reported by Emmel and Aneziris [EA13] since they used a larger pressure cell (20 kN), the same trend was observed. A reason for the increase is that the applied coating is much denser than the porous substrate. Further, Emmel and Aneziris [Emm14] explained the increase by pressure stress

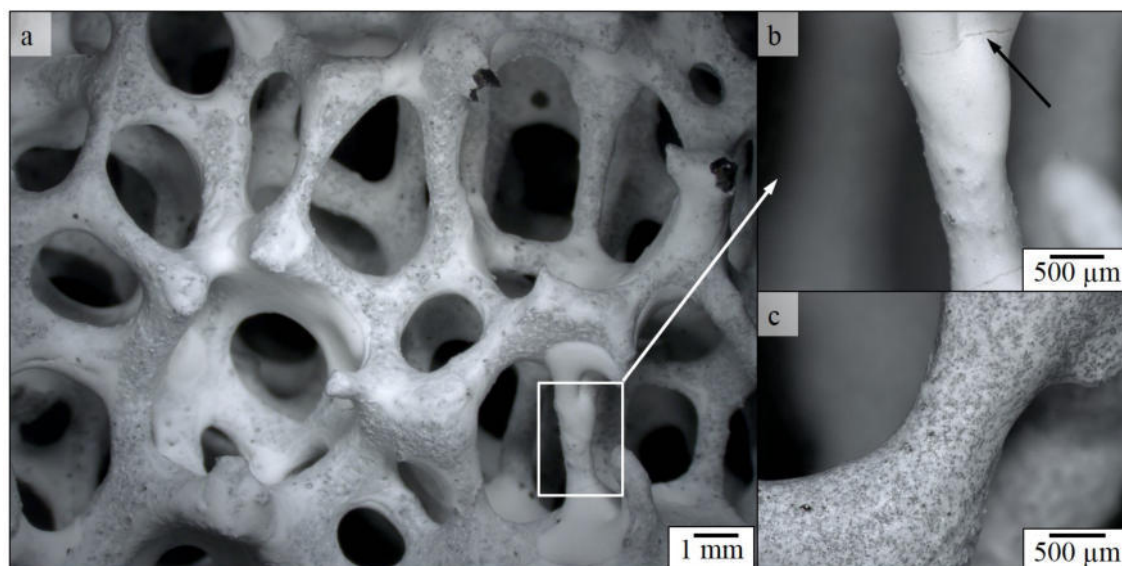


Figure 4.2.: Microstructure of A (a) or AC (c) coated filters after coking by light microscopy; b) detail of the white box in (a). Coating accumulations near the filter knots caused occasionally cracks during drying (black arrow in b). c) added carbon can be noticed as dark spots in the otherwise white coating.

that is caused by the coating shrinking onto the carbon-bonded filter during cooling after the heat treatment. Nevertheless, the filters demanded careful handling to avoid corners breaking off.

Figure 4.3 shows a fractured section of an alumina coated filter. Easily, the carbon-bonded alumina substrate can be distinguished from the alumina coating. There was always a gap between substrate and coating, which indicates that there is only the mechanical bonding between both due to the coating shrinking onto the substrate. The sintering up to 1400 °C under reducing atmosphere was sufficient to yield a stable coating, whereby single grains can be still distinguished. After that heat treatment, the coating material consisted of corundum. XRD did not detect any other phases.¹ An SNMS characterization of the coated coked filter surface revealed qualitatively that minor amounts of Si, Na and Ca were present.² A residual carbon content of 0.042 mass% was detected by the carbon analyser, which probably arose from the organic additives and the heat treatment in a coke bed. The coating was porous. The open porosity of fragments of alumina coated filter struts amounted about 34.3 vol% and is similar to data reported by Emmel and Aneziris [EA13].

¹cf. appendix Figure B.1 for data.

²The data can be found in appendix Figure B.3.

4. Results and Discussion

Table 4.1.: Strut thickness of coated filters.

Filter type	Wall thickness*		Coating thickness [†] (mm)	Strut diameter	
	Mean value (mm)	R^2		Mean value (mm)	Number of measured struts
uncoated	0.25 ± 0.10	0.95	–	0.72 ± 0.21	20
A	0.27 ± 0.11	0.94	0.02	0.77 ± 0.16	20
AC	0.31 ± 0.12	0.93	0.06	1.05 ± 0.17	20
AC-T	0.29 ± 0.11	0.95	0.04	0.81 ± 0.12	20
AC-Z	0.30 ± 0.12	0.94	0.05	0.93 ± 0.14	20
AC-ZT	0.30 ± 0.13	0.93	0.05	0.92 ± 0.18	15

* Normal distribution.

[†] The coating thickness is obtained by subtracting the wall thickness of the uncoated filter from the wall thickness of the coated filter.

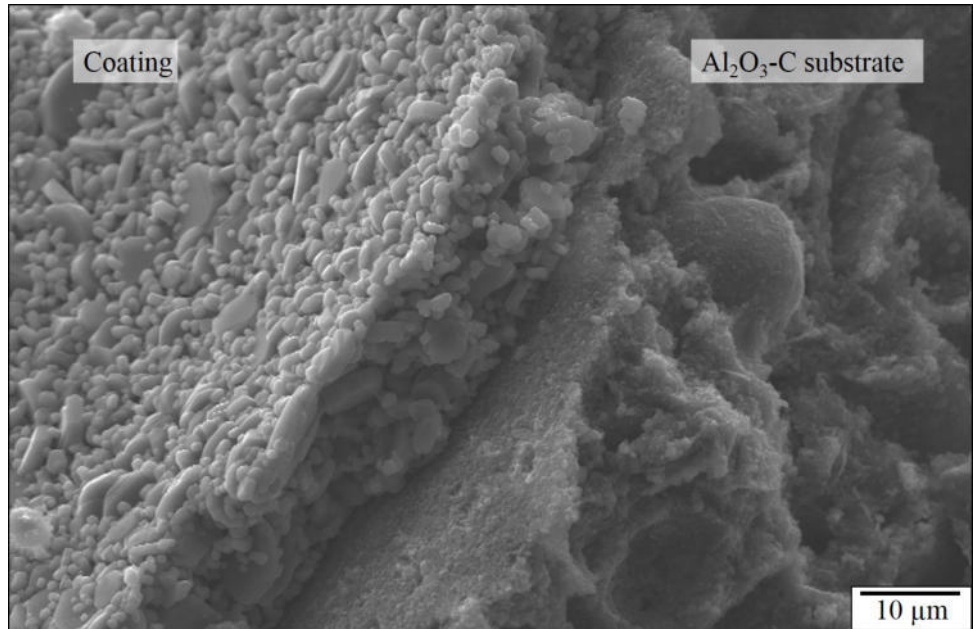


Figure 4.3.: Cross-section of an alumina coated filter fragment after coking by electron microscopy (SE mode). Alumina coating (left) and carbon-bonded alumina filter (right) are separated by a small gap.

AC coated filter after coking. According to the CT data, the average coating thickness was 60 μm for coating containing alumina and carbon (AC), cf. Table 4.1. Figure 4.2 c presents a light micrograph of an AC coated filter strut. The added carbon can be noticed as dark spots in the otherwise white coating. Similar to the alumina coated filter, some coating accumulations were found near the filter knots, which led occasionally to cracks within the coating, cf. appendix Figure B.6. The determined CCS of AC coated filters was $(0.46 \pm 0.08) \text{ N mm}^{-2}$ and thus tends to be lower than the CCS of the alumina coated ones. Further, the shrinkage of the AC coated samples determined by dilatometry was smaller than the one of the alumina coated samples (cf. appendix Figure B.5). That might have caused less pressure stress during cooling leading to the lower cold crushing strength.

Figure 4.4 shows a fractured section of an AC coated filter by electron microscopy. Carbon particles were embedded in the alumina matrix of the coating. After the heat treatment, the coating material consisted of corundum and carbon. XRD did not detect any other phases than alumina.³ A residual carbon content of 4.01 mass% was detected by the carbon analyser, which did not exactly meet the initially targeted 5 mass%, but was acceptable. The added amount of carbon was too small and not completely graphitized to cause significant peaks in the XRD pattern. The SNMS characterization of the coked, coated filter surface revealed qualitatively that minor amounts of Si, Na and Ca were present⁴, which was similar to the alumina coating described above. This coating was porous, too. The open porosity of the coated filter struts amounted about 35.2 vol% and was therewith slightly higher than the one of the alumina coated filters, but in the same range.

Influence of the carbon addition on the manufacturing and properties of coated filters

The addition of carbon to the alumina coating slurry of Emmel and Aneziris [EA13] required an adjustment of the slurry composition to yield a sufficiently stable slurry for the coating process. The coating application and the resulting coating thickness were not distinctly influenced by the carbon addition. The added amount of carbon seemed to have resulted in slightly less densification during the heat treatment, which is in accordance to the sintering behaviour of alumina under reducing atmosphere described in the literature [BGB88; Mir+90; Pap+97]. That might have caused the tendency of decreased shrinking and the slightly lower cold crushing strength of the AC coated filters. However, this had no noticeable disadvantages in the handling and application of the the AC coated filters.

³cf. appendix Figure B.2 for data.

⁴cf. appendix Figure B.4 for data.

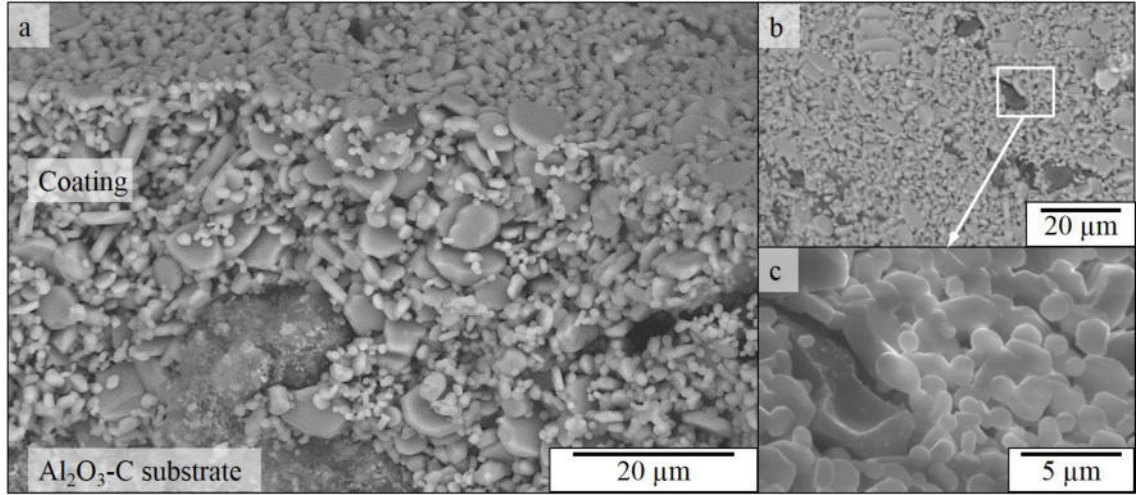


Figure 4.4.: Microstructure of an "AC" coated filters after coking by SEM. a) Cross-section of a coated filter fragment (BSE mode), b) top view on the coating (BSE mode) with detailed view (white box) in c) showing a carbon particle embedded in the alumina grains (SE mode).

Zirconia and/or titania doped coated filters As Table 4.1 summarises, the average thickness of coating AC-T, AC-Z, and AC-ZT were in the range of 40 µm to 50 µm, and thus were between the coating thicknesses of A-coated and AC-coated filters despite the higher solid content of the spray slurries. The determined strut thickness followed a similar trend as the wall thickness (cf. Table 4.1).

The addition of zirconia or titania did not lead to the formation of new phases: apart from α -Al₂O₃, only monoclinic zirconia and rutile were identified in the samples AC-Z and AC-T, respectively. Traces of zirconium titanates were determined in the coating AC-ZT, which might be related to Zr_{0.33}Ti_{0.67}O₂.⁵ As no traces of aluminum titanates were detected here, it is assumed that they did not form during the heat treatment under reducing atmosphere, in accordance with results reported by Naghizadeh et al. [NRG09].

Figure 4.5 presents the filter samples after coking. Spray coating of the AC-T slurry resulted in some accumulations of material on the filter struts, as displayed in Figure 4.5 a, which resulted in a few drying cracks. The AC-Z coated filter (Figure 4.5 b) and the AC-ZT coated filter (Figure 4.5 c) showed less accumulations and drying cracks, but the surface appeared rougher than the surface of previously described filters.

Figures 4.6 and 4.7 exemplify the microstructure by electron microscopy. Adding titania to the coating did not affect the microstructure distinctly, it is similar to

⁵Following ICDD cards were used: α -Al₂O₃ (80-0786, 81-1667, and 74-0323), rutile (87-0920, and 77-0441), monoclinic zirconium dioxide (37-1484, and 78-0047), Zr_{0.33}Ti_{0.67}O₂ (75-1739).

4. Results and Discussion

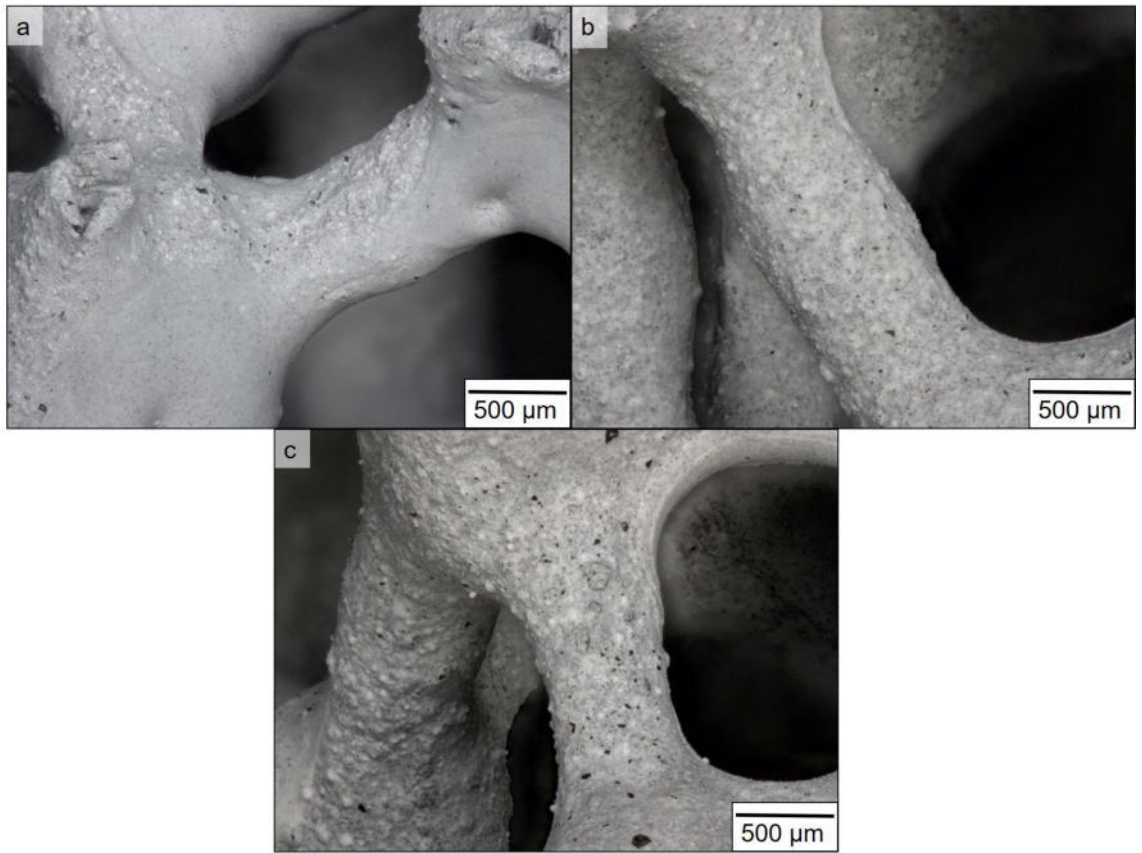


Figure 4.5.: Microstructure of coated filter with titania and/or zirconia doping by light microscopy: (a) AC-T, (b) AC-Z, (c) AC-ZT.

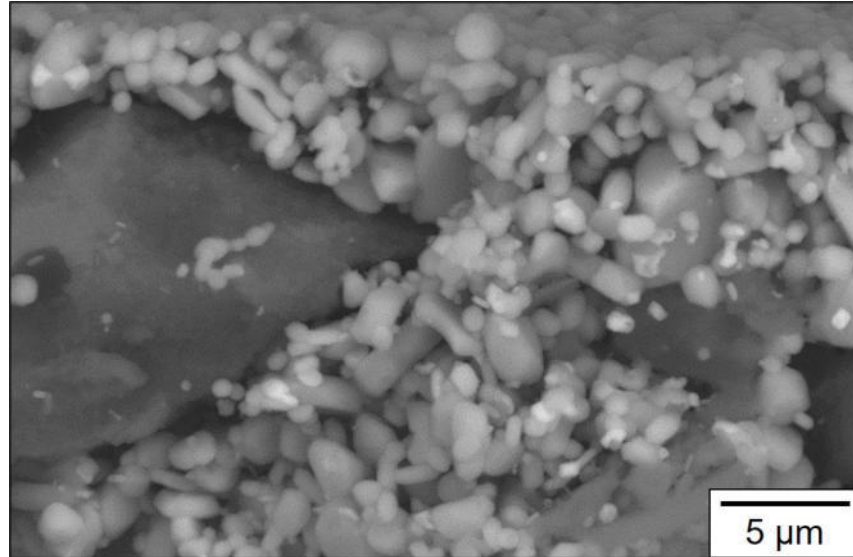


Figure 4.6.: Cross-section of the titania doped coating by SEM (BSE-mode): carbon - dark grey, alumina - grey, titania - bright-grey.

the AC coated filter with some titania grains detectable between the alumina ones, compare Figure 4.6 and Figure 4.4. Zirconia, on the other hand, is conspicuous by BSE-mode. It was confirmed by EDS, that the bright spots contained zirconium amongst other elements, whereas on the other greyish grains only aluminium and oxygen were detected. Further, the alumina grains appeared pimples by SE-mode, cf. Figure 4.7. The combinations of both dopants, ZrO_2 and TiO_2 , in the carbonaceous alumina coating resulted in a coating, where both oxides were well distributed. Again, EDS confirmed the presence of titanium and zirconium within the bright spots. Similar to the AC-Z coating, the grains of the coating appeared pimples.

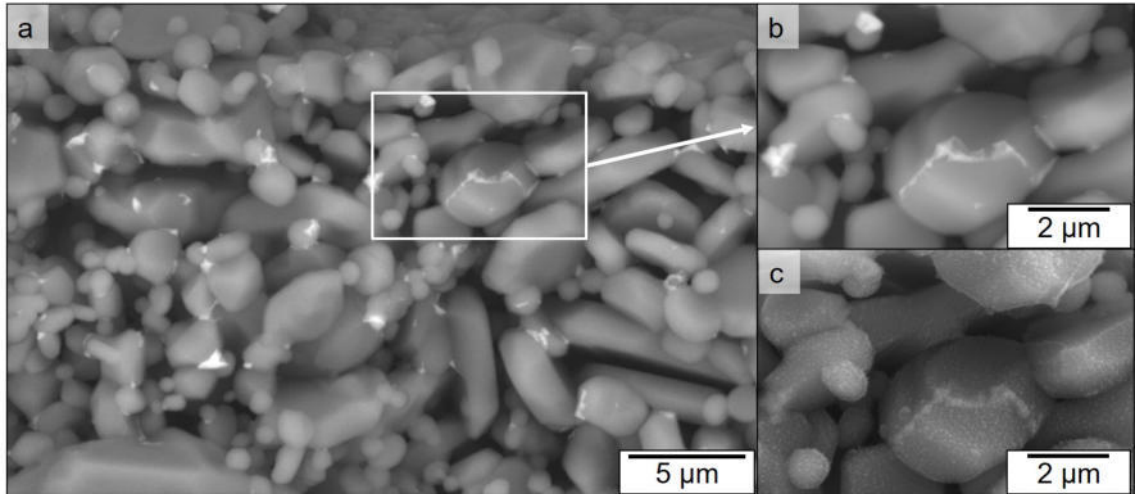


Figure 4.7.: Microstructure of coated filter with zirconia doping by SEM. (a) BSE-mode: carbon - dark grey, alumina - grey, zirconia - bright-grey. (b) Detailed view of the white box in a) (BSE-mode), and (c) SE-mode: pimpled surface of alumina grains.

4.2. Layer build-up on immersed filters

After all immersion tests, a typical layer build-up on the filter surface was observed, which is presented in Figure 4.8. The scheme (Figure 4.8a) illustrates that layer build-up: directly on the alumina grains at the filter surface was a thin, vitreous layer, which adapted the surface roughness without any detectable bonding with the coating material underneath. Secondary alumina crystals of divers shapes were attached on that thin layer. The outermost grains of the coating as well as the secondary alumina grains sintered strongly near the vitreous layer. Between the secondary crystals, iron-based beads were trapped. The iron-based beads were furthermore found at carbon particles near the surface, i.e. within the coating or at the coating–substrate interface depending on the carbon content of the coating. Occasionally, nano-sized alumina clusters were observed on the secondary alumina.

Overall, a similar layer build-up was observed on the filter surface of other immersion trials within the CRC 920 on alumina-based filters with or without coatings [Dud+14; Sto18] and after the SPS trials by Salomon [Sal19]. In the case of Salomons experiments, filter fragments or tiny filters with coating A or AC were tested in the SPS device (cf. Section 2.4.3 on page 47). Thus the interactions between filter and molten steel were investigated without macroscopic streaming effects and with high heating as well as cooling rates (up to 1300 K min^{-1}). Results with the coating containing alumina (A) coated filters have been already published [Sch+17a]. The steel powder used in the SPS experiments was of the same steel grade, 42CrMo4. The interactions of filter and molten steel were analysed post-mortem after dwell

4. Results and Discussion

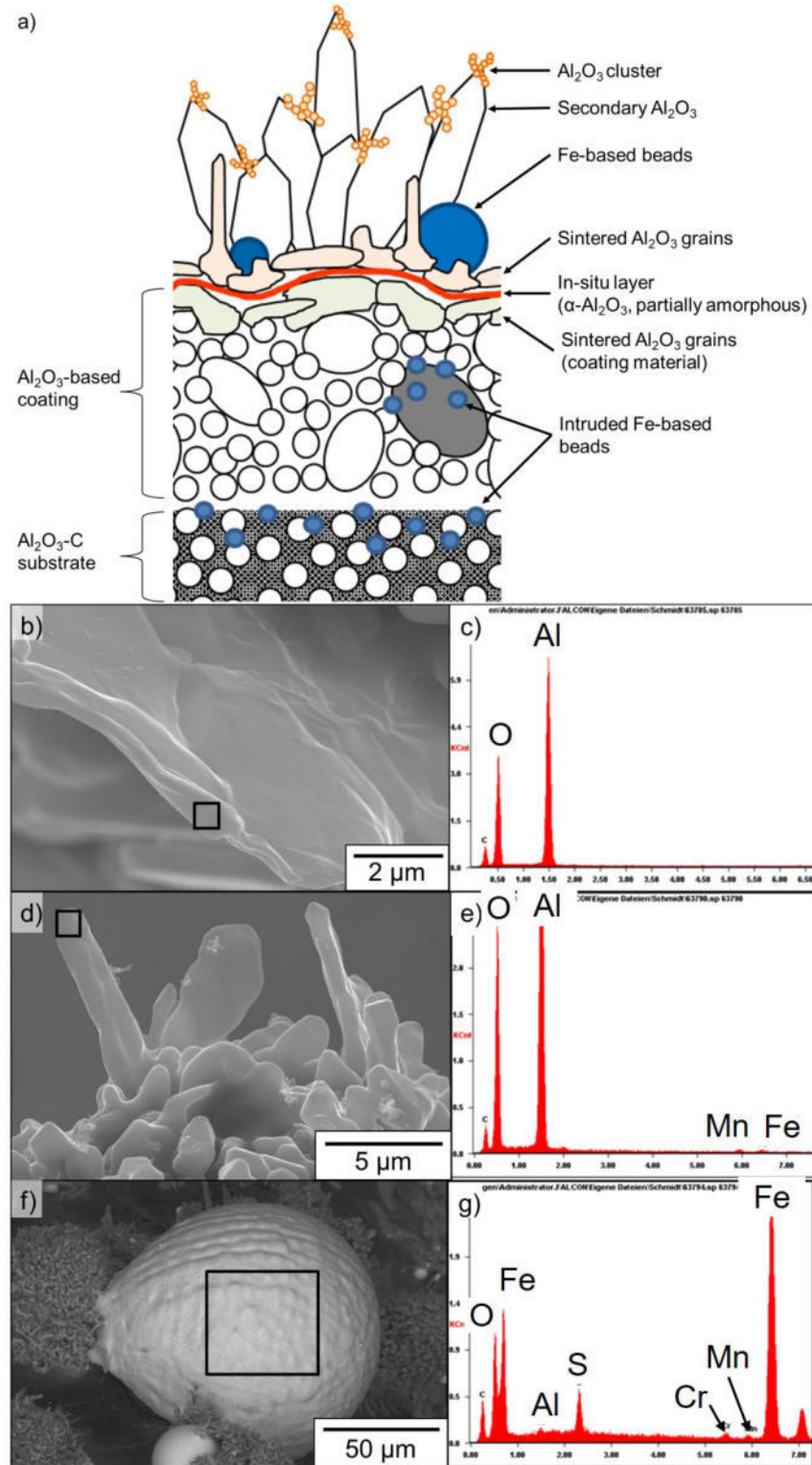


Figure 4.8.: Summarised layer build-up on the filter surface after immersion trials. (a) Schematic representation of the layered build-up. (b) – g) AC-T coated filter after 30 s immersion by SEM and EDS. Investigated areas are highlighted by the black box in the figure on the left and the resulted peaks shown on the right: b) + c) In-situ layer, d) + e) Secondary Al_2O_3 , f) + g) Remaining iron-based bead on the filter surface.

times of 1 min, 30 min and 60 min at 1600 °C. In general, Salomon [Sal19] observed interactions after longer dwell times (minutes to an hour) in his experimental set-up than the here presented immersion tests (dwell time seconds to two minutes). A major influence is believed to be the macroscopic flow of the melt passing the filter in case of the immersion tests. Another influence will have the higher melt temperature (immersion test series 1650 °C compared to 1600 °C during SPS trials), as it accelerates reactions and diffusion processes. In the following, the components of the layer build-up will be discussed in more detail.

4.2.1. In-situ formed, vitreous layer

The in-situ formed layer was very thin. The thickness, which was roughly estimated from sections like Figure 4.8 b, was in the range of a few hundred nanometers. The examination by light microscopy gave the impression that the entire immersed filter surface was covered with this glass-like light-reflecting layer and the secondary crystals. However, it was not found again on all of the polished cross-sections prepared for SEM and EBSD analysis, probably due to the very small thickness and the brittle nature of this layer. Figure 4.9 presents a cross-section taken from a filter with coating A after 120 s immersion, on which such a layer was examined. According to the EDS analysis, the vitreous layer contained mainly Al, O, and Fe, but also Ca, cf. Figure 4.9. Nevertheless, it is difficult to draw conclusions because overlapping signals cannot be excluded from the adjacent materials (alumina and solidified steel, respectively). EBSD suggested that the layer was more likely to be amorphous in that section. Nevertheless, reflections from a crystal lattice were found, but they could not have been related to any crystal without doubt (cf. the right figure in Figure 4.9). The EDS analysis in Figure 4.8 c verifies the presence of aluminium and oxygen. The small carbon peak cannot be related without doubt to the sample's chemistry as carbon was sputter coated on the sample's surface to ensure the electrical conductivity required for SEM characterisation.

Dudczig et al. [Dud+14] and Storti et al. [SBA18] reported that such an in-situ formed layer on the filter surface contained α -Al₂O₃ crystals. In the latter study, the vitreous layer was isolated by FIB preparation and characterized by EBSD and EDS. They detected a concentration gradient of Al and O over the cross-sectional area of the in-situ formed layer, whereby both concentrations decreased towards the side facing the steel melt interface. From their results, they assumed a diffusion driven formation process of that in-situ layer whose thickness was thus limited. For the first time in this material system, then, Salomon characterised the vitreous layer by transmission electron microscopy (TEM). In his case, it was mainly amorphous

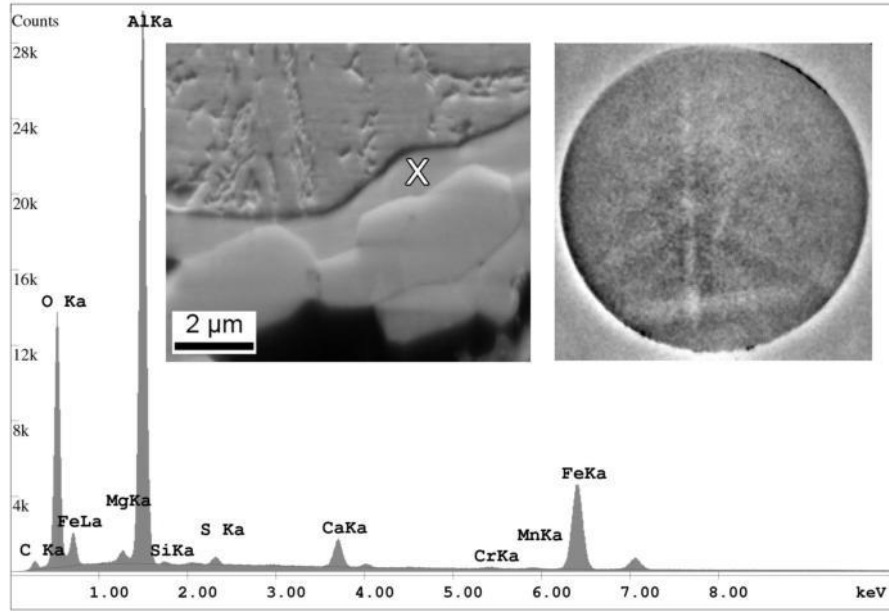


Figure 4.9.: Cross-section showing the vitreous layer (middle) of a filter with coating A (below) immersed for 120 s; above: solidified steel. EDS (bottom) and EBSD signals (right) of position “x”.

and contained also nano-crystalline components. Due to the overall varying composition of Fe and O (main components) and Al as well as Si, combined with the diffuse reflections of the crystalline phase, no clear phase assignment was possible. The estimated structure and lattice parameter indicated a cubic face-centred phase with a lattice parameter $a \approx 8.4 \text{ \AA}$. Magnetite ($\text{FeO} \cdot \text{Fe}_2\text{O}_3$, $a = 8.3969 \text{ \AA}$), hercynite (FeAl_2O_4 , $a = 8.15579 \text{ \AA}$), or γ -alumina ($a = 7.9 \text{ \AA}$, undistorted spinel structure) were assumed as possible phases, which might have been crystallised from the amorphous layer. However, according to Salomon [Sal19, p. 137–138] none of these phases are thermodynamically stable under experimental conditions if reactions between pure iron and corundum at the ceramic–steel interface are the basis of assumptions.

4.2.2. Secondary alumina particles

The secondary alumina crystals were mostly plate-like and distributed over the whole investigated surface. However, they were more crowded (bush-likely) near the metallic iron-rich beads. Their length varied in a range of $10 \mu\text{m}$ to $50 \mu\text{m}$ depending on the immersion time and composition of the coating, as will be shown in Sections 4.3, 4.4 and 4.6. EDS and EBSD investigations confirmed that these crystals consisted of trigonal α -alumina. These observations are in excellent agreement with data reported by Dudczig et al. [Dud+14], Storti et al. [Sto+15; Sto+16a] and Salomon [Sal19]. Figure 4.8 d and e, Figure 4.10, and Figure B.7 (appendix) present

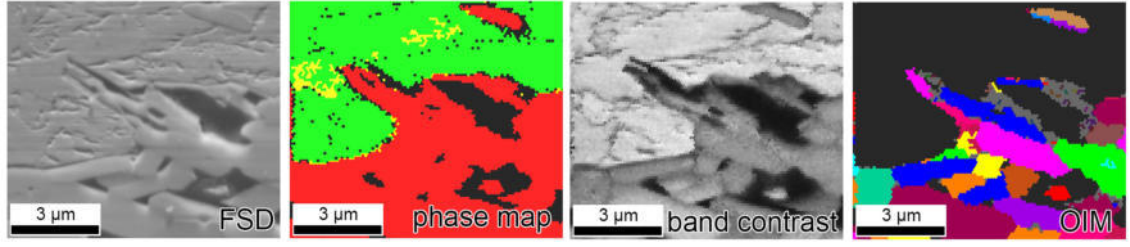


Figure 4.10.: Characterisation of the alumina coating and secondary crystals at the filter surface by EBSD combined with EDS. From left to right: Polished cross-section (SE-mode), phase distribution (red: α - Al_2O_3 , green: α -Fe, yellow: γ -Fe), crystallinity (band contrast), and grain orientation (OIM). OIM: grain orientation estimated only for alumina, black dots: unidentifiable spots, gray: indefinitely orientations due to low band contrast. Filter with coating A immersed for 120 s.

analyses of these alumina crystals. The morphology of these particles and EBSD examinations implied that they were polycrystalline. In addition, the grain orientation was determined (cf. Figure 4.10). The orientation of the attached crystals and the one of the alumina grains of the coating were not related in any way. Thus, these crystals did not grow directly from the coating material. Probably, they originated from heterogeneous nucleation at the filter–steel interface. These findings are in-line with the results of Salomon, who, too, observed that the orientation of the secondary corundum⁶ crystals was independent as well from the coatings alumina grains as from the solidified steel surrounding them. In his case, their length (up to 50 μm) kept unchanged with increasing dwell time⁷. [Sal19, p. 135–136] Furthermore, the grain size within the polycrystalline structures was in the range of endogenous inclusions. Hence, they may have also contributed to their formation.

The secondary alumina crystals were never covering the filter homogeneously: sometimes they formed bushy-like structures on a surface, sometimes single standing ones, and sometimes they covered a whole area like a forest. Usually, the borders of such areas followed the macrostructure of the filter, i.e. alongside the strut shape. Zienert et al. [Zie+20] discussed how inhomogeneities of the refractory surface⁸, like cracks, pores, and the sample’s edges, may influence the diffusion kinetics of the refractory–steel melt reactions. The conditions seemed to be favourable for the growth of larger secondary crystals at such inhomogeneities, as they found sec-

⁶Analysed by EBSD combined with EDS.

⁷Dwell times of 1 min, 30 min and 60 min at 1600 °C within the SPS set-up.

⁸They characterised the in-situ layer formation by immersing prismatic, pressed samples of the same Al_2O_3 –C material used for the filter substrate in molten 42CrMo4. Immersion times ranged from 5 s to 120 s.

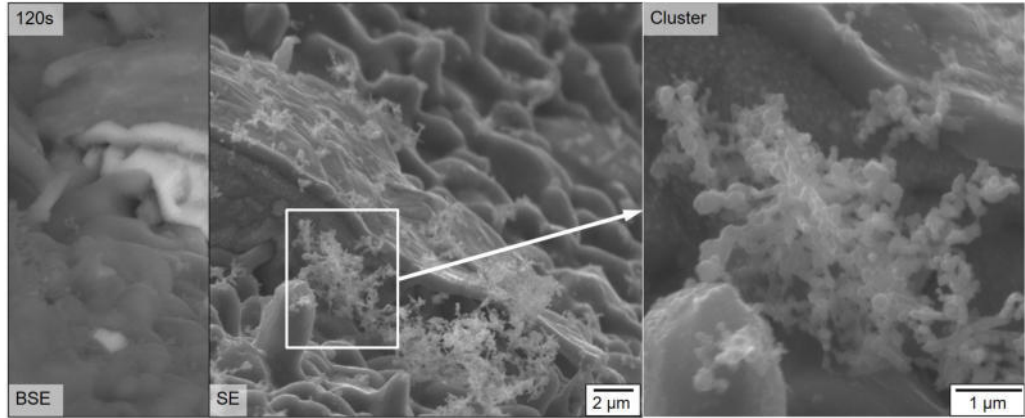


Figure 4.11.: Surface of a filter with coating A immersed for 120 s. Left: entrapped iron-based bead covered by secondary alumina and fine clusters, shown in BSE- and SE-mode. Right: higher magnification of such clusters; they were made of nano-sized particles.

secondary crystals sizing up to $50\text{ }\mu\text{m}$ there. In the case of the immersed filters of the present study, it can be assumed that the melt flow through the filter's macropores has a strong influence on these diffusion based reactions because locally higher deviations compared to the trials with prismatic samples of Zienert et al. [Zie+20] can be expected.

In addition, the detailed analysis of a cross-sectional view by Zienert et al. [Zie+20] revealed that a layer of alumina with trapped steel formed firstly at the samples surface, which was subsequently covered by an (Al, Fe, Mg, Mn)-containing spinel. Thereby, they noticed differences in the spinel's lattice parameters, which they explained by a varying oxygen content of the melt during formation. The small peaks of Mn and Fe detected by EDS in Figure 4.8e may result from such spinel phases.

4.2.3. Deposited cluster

Occasionally, very fine clusters were attached on the polycrystalline alumina particles (cf. Figure 4.11). These clusters were smaller than $5\text{ }\mu\text{m}$. They consisted of nanometer sized particles, as presented in the detail view of Figure 4.11. Due to their tiny size, their chemical and phase compositions were not satisfactorily estimated within this study. Unfortunately, they were not found again in any polished cross-section. Nevertheless, the morphology investigated by SEM (secondary electrons (SE)-mode) was in excellent agreement with reports of endogenous inclusions that originate from Al-killing during steelmaking [Sin74; DBW03; Dek+13; Lee+13; Zha13], and component failure that was traced back to alumina inclusions [Kre+15; KB13]. thus, the clusters are alumina with a high probability.

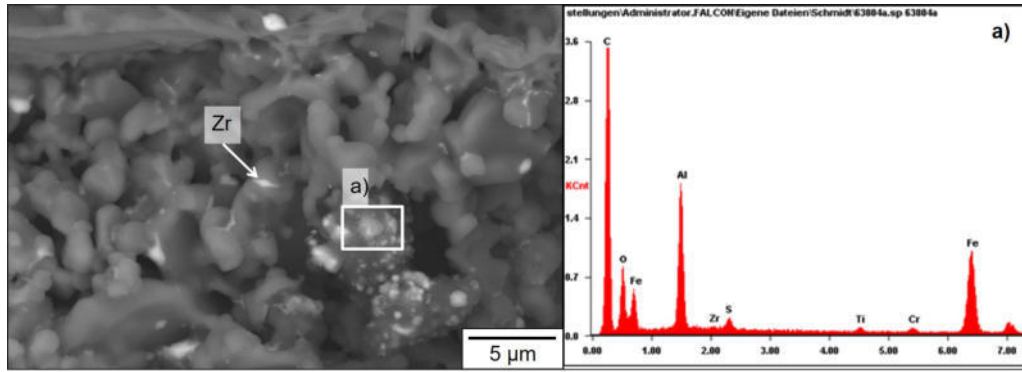


Figure 4.12.: Left: Cross-sectional view of the AC-ZT coating after the immersion trials. Bright spots on the carbon particles of the coating stand out in BSE-mode. An EDS analysis of the area in the white box reveal an iron-rich phase (a).

4.2.4. Iron-based beads and the decarburised zone

Figure 4.8 f) and g) show an iron-based bead remaining at the filter surface and its qualitative chemical composition. As well signals, which were related to the used steel grade, i.e. iron, chromium, and manganese, as such related to the refractory material, i.e. aluminium and oxygen, were detected. In addition, sulphur was usually observed, too, despite the fact that a very low-sulphur steel was purposely used ($S \approx 0.001$ mass%). In combination with sulphur remaining at the filter surface from the heat treatment in the coke bed, locally higher sulphur concentrations might have resulted in the formation of MnS during solidification of the iron-based beads. They were always surrounded by secondary crystals. Unfortunately, it was not possible in the present study to examine the chemical and phase compositions in more detail due to the lack of a suitable sample preparation and analysis method for these fine structures on the filter surface.

Dudczig et al. [Dud+14], Storti [Sto18, p. 59] and Salomon [Sal19, p. 132–134] reported a decarburised zone in means of a zone of the surface-near Al_2O_3-C with obvious microstructural changes and intruded steel particles. In case of Salomon that zone was about $10\mu m$ thick. Thereby, the decarburised zone was already formed after 1 min contact time on alumina coated filters and after 30 min in case of the AC coated filter. As reasons, Salomon [Sal19, p. 132–134] considered the higher coating thickness and initially worse wetting of the carbonaceous alumina coating. In the present study, intruded iron-based beads were also observed beneath the alumina based coating at the surface-near Al_2O_3-C . Microstructural changes within that zone were, however, not as obvious as described by the aforementioned authors. Bock et al. [Boc+19], too, could not observe such microstructural changes of the

substrate material in case of their immersion trials with Al_2O_3 -C filter coated with carbonaceous coatings of the system Fe-/Mg-/Mn-aluminates. If carbon was present in the coating, however, iron-rich beads were found on the surface of these carbon particles as exemplified in Figure 4.12. Thereby, signals of iron and chromium were detected. Overlapping signals from the surrounding coating material AC-ZT had been received (Al, O, Zr, and Ti). The modified coal tar pitch added as carbon particles to the coating contained low amounts of sulphur. No other main alloy elements of the steel, like molybdenum or manganese, were found.

4.3. Impact of immersion time: Alumina coated filters

The immersion test series presented in Schmidt et al. [Sch+17a] has been extended by a sample which was immediately removed from the melt after dipping in. To simplify the denotation of that sample, it will be referred to as "1 s immersed" in the following.

4.3.1. Filters after immersion

Figure 4.13 gives an overview of the alumina coated filters immersed for different dwell times. From left to right, following filters are shown: a coked filter before immersion, the "1 s immersed" sample and after immersion for 10 s, 30 s, 60 s and 120 s. Already by eye, the immersed part of the filter can be easily distinguished from the not-immersed part by a dark grey band, which is in accordance to observations by Emmel [Emm14] and Storti [Sto18]. The coating stayed on all filters, which were immersed at least for 10 s. The 1 s-sample, however, stands out as the immersed part suffered from strong spalling of the coating.

Figure 4.14 a) and b) give an impression of the typical microstructure of the "1 s immersed" filter by light microscopy. Obviously, large parts of the coating have been flaked off, exposing the underlying carbon-bonded alumina substrate. Thereby, the black colour indicates that the coating detached after immersion during cooling down, as the carbon of the substrate was not significantly oxidised. At the lowest part of the filter, which stayed longest in the melt, spots with a glassy phase were occasionally detected, cf. Figure 4.14 c. As that glassy phase is only observed at the bottom of the filter and nowhere else on the immersed part, entrained slag can be excluded as origin. It is assumed that this phase is similar to the vitreous phase described in Section 4.2.1 on page 76. No other traces of interactions were found on the remaining coating.

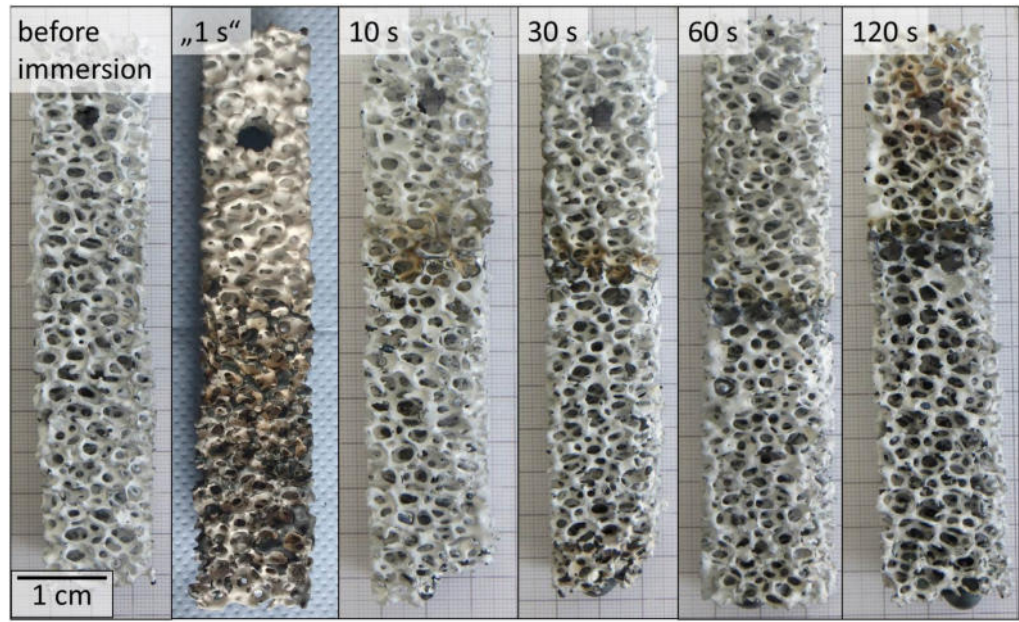


Figure 4.13.: Filters with coating A after immersion for different dwell times: before immersion, after a very short dip in the melt ("1 s"), after 10 s, 30 s, 60 s and 120 s immersion.

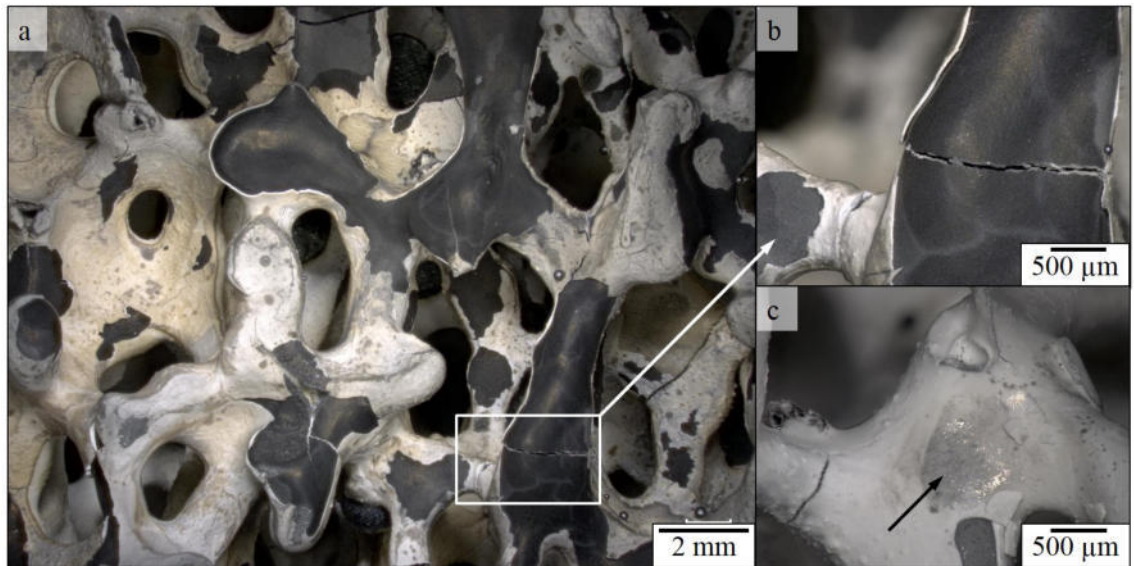


Figure 4.14.: Filter with coating A after 1 s immersion - Microstructure by light microscopy: a) typical microstructure of the immersed part showing strong spalling, with a detailed view (white box) in b) of a cracked filter strut. c) detail of the bottom area of the filter with glassy spots (black arrow).

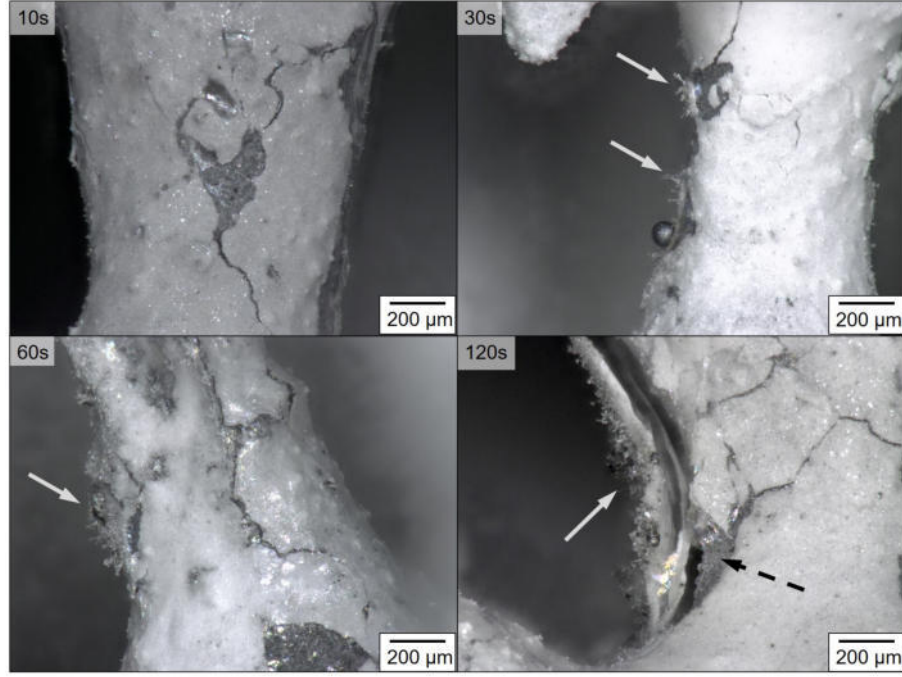


Figure 4.15.: Microstructure of alumina coated filters after immersion trials with varying immersion time by light microscopy. White solid arrows: newly formed crystals on the filter surface, in the cases of 60 s and 120 s even encapsulating small steel drops. Dashed black arrow: transparent thin layer made clearly visible by the coating flaking off from the substrate.

Figure 4.15 presents the microstructure by light microscopy of filter struts after at least 10 s immersion. Some cracks were found on all samples. They were more pronounced the longer the filters were immersed, cf. appendix Figure B.8. Nevertheless, the coatings still adhered to the filter. Additionally, some steel droplets were attached on the filter surface. Either they were left as droplets of different sizes or, especially near the filters bottom, they filled some macro-pores. Secondary crystals covered the entire immersed filter surface. The longer the filters were dipped (up to 60 s immersion), the longer were these crystals, cf. white arrows in Figure 4.15; up to 120 s immersion, no further increase of the crystals length was observed. In the case of the 60 s and 120 s samples, the secondary crystals even encapsulated small steel drops or sprouted on the steel that remained in the macro-porosity. The filter surface sparkled due to the thin, vitreous layer populated with secondary crystals. By incident, this transparent layer was made clearly visible by a part of the coating flaking off from the substrate, as highlighted by the dashed black arrow in Figure 4.15 on the sample immersed for 120 s. The vitreous layer covered small cracks and exposed substrate material, cf. Figure 4.15. The way in which the remaining steel beads are covered by the secondary crystals gives the impression that the crystals have only fully crystallised after the filter has been withdrawn from the melt.

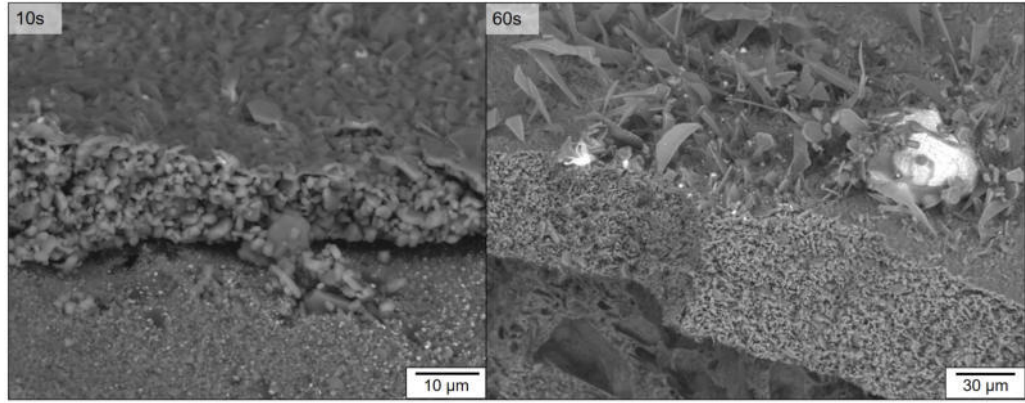


Figure 4.16.: Microstructure of alumina coated filters after immersion trials with varying immersion time by SEM. From bottom to top: Al_2O_3 -C substrate, alumina coating, layer build-up on the filter surface, after 10 s immersion (left), and after 60 s immersion (right), both BSE-mode.

The microstructure of the filter surface was characterised in more detail by SEM. Figure 4.16 exemplifies the observed microstructure by means of samples immersed for 10 s and 60 s. Already after 10 s immersion, the layer build-up described in Section 4.2 on page 74 is formed in an initial state: the vitreous layer covered the filter's coating, and small secondary alumina crystals were attached on it as shown in the left side of that figure. In the lower part of that image, some coating was detached during sample preparation. The exposed carbon-bonded alumina clearly showed some bright spots in BSE-mode of SEM: the iron-based beads. With longer immersion time, the secondary crystals became larger and an iron-rich phase was also detected between them. After 60 s, fine clusters were occasionally attached on the secondary crystals; they covered the investigated area completely after 120 s, cf. Figure 4.11 on page 79. Between 60 s to 120 s the secondary crystals stopped growing distinctly in length, but their shape became clearly rounded, which is attributed to ongoing sintering. Distinct sintering of the alumina grains occurred within the coating near the vitreous layer as well as for secondary crystals on top of it. What was observed on larger scales using light microscopy was also confirmed under higher resolution: the iron-rich beads were increasingly encapsulated by the secondary crystals with increasing immersion time.

4.3.2. Steel characterization

Table 4.2 summarises the process parameters of the immersion trials with A coated filters. The fluctuations in the process parameters are caused by the experimental set-up and were in an acceptable, usual range. After immersing the alumina coated filters, the oxygen content of the steel melt always increased. Compared to the

4. Results and Discussion

Table 4.2.: Parameters during immersion trials of the alumina coated filters. The logged oxygen content (a_O) and the temperature (T) of the melt were measured before (bI)* and after immersing (aI) a filter. Thereby, a positive temperature difference (ΔT) describes an increase in temperature between both measurements points. The time between these two measurements (Δt) is listed.

time filter immersed (s)	a_O (ppm)		ratio $a_O(aI)/a_O(bI)$	T (°C)		ΔT (K)	Δt (min)
	bI	aI		bI	aI		
10	7.2	22.4	3.1	1635	1653	18	15.0
30	6.2	19.5	3.2	1628	1637	8	20.0
60	7.0	25.6	3.7	1638	1660	22	20.0
120	10.3	29.3	2.8	1654	1662	9	17.0

* After the oxidation-deoxidation pre-treatment, cf. Section 3.3.

value before filter immersion, it approximately tripled. The target temperature of 1650 °C was satisfactorily achieved and maintained over the test duration. Due to the handling of the revolver system used to immerse either the pO_2/T sensor system or the filter sample, the test duration time was 15 min to 20 min. Overall, the immersion tests with the steel casting simulator were very time-consuming: They required three working days to test one filter sample, including the preparation of the test, the immersion of the filter and the post-processing of the test. For that reason, only one filter each type was immersed and characterised. Thus, statistic analyses of the obtained data were not possible due to the low amount of values. From the solidified steel, one sample was prepared and analysed as described in Section 3.4 on page 61. Sample "without filter" denotes the steel sample, which was remelted and pre-treated but no filter immersed, as described in Section 3.3 on page 59.

Table 4.3 is an extract with relevant results of the chemical analysis by spark optical emission spectrometer, which is presented completely in the appendix (Table B.2). Due to remelting and the pretreatment, the carbon content determined tended to decrease. Immersing the filters did not result in a carbon pick-up of the melt. However, it has to be mentioned that spark optical emission spectrometer analysis is not suitable for precise analysis of the carbon content due to the low molecular weight of carbon. The other main alloying elements (Si, Mn, Cr, and Mo) seemed also to decrease slightly after remelting. Immersing a filter did not lead to significant changes of these alloy elements: with regard to them, the steel

4. Results and Discussion

still meets the specification for 42CrMo4 as prescribed in the standard DIN EN ISO 683-2:2018-09 [DINb].

The aluminium content, however, was distinctly influenced by the remelting and pre-treatment procedure: For the trial without a filter, the aluminium content is almost halved in comparison to the "as received" steel sample. It is reasonable to assume that in the course of oxidation–deoxidation pre-treatment, the dissolved aluminium in the melt reacts to form NMIs, which were deposited on the crucible wall, for example. This is in agreement with results obtained by Fruhstorfer et al. [Fru+18]. They, too, observed a sharp drop of the aluminium content of the steel⁹ after remelting in the inductively heated melting device of the SCS, which they explain with the formation of calcium aluminates. In the present study, the calcium content dropped sharply in the course of remelting and reached the detection limit of the analysis method. Based on the present data, it is impossible to discuss any effects on the calcium content. Nevertheless, it would seem reasonable to assume that calcium reacts with dissolved aluminium and oxygen or alumina also in this study.

Immersing filters led to a further reduction of the amount of aluminium to an eighth of the value after remelting (sample without immersing a filter). It appears that the residence time of the filters in the molten steel did not have a significant influence on the aluminium content in the investigated framework. If there was an influence, it was lost in the fluctuation of the measured values and the low initial concentration in such a way that changes were below the detection limit of the characterisation method.

Table 4.4 summarizes the inclusions detected using the Aspex-SEM, classified by their chemical class. The chemical classes "Dirt", "Fe-oxide" and "Fe-scratches" were excluded from the following evaluation as they arose rather from sample preparation than from the experiment itself. Unfortunately, a year after this characterisation, the author's research team detected that the used polishing agent based on SiO₂ and therewith was able to create artificial SiO₂ inclusions by smearing the polishing agent in open pores. Thus, this inclusion category cannot be discussed here. Negligible numbers of MnO-MnS type inclusions were observed, which is owed to the very low sulphur content of that steel. Neither Ca-aluminate, Mg-spinel, Al-Mn-Mg-Fe-Ca-silicate nor CaO-CaS type inclusions were identified in the steel samples. For that reasons the following discussion of remaining inclusions focuses on the Al₂O₃ class. The inclusion size distribution of that class is given in Table 4.5. Immersing the filters distinctly decreased the number as well as the total area of alumina inclusions. That effect was highest for the shortest immersion time of 10 s. With

⁹They used another steel grade, 18CrNiMo7-6, as in the present study, 42CrMo4.

4. Results and Discussion

Table 4.3.: Chemical composition (extract) of the steel before and after the immersion tests of the alumina coated filters. Sample "without filter" refers to the remelting trial with a dwell time of 15 min after the pre-treatment.

Element	Content in the steel sample (mass%)						max.
	as	without	Dwell time of the immersed filter (s)				standard deviation
	received	filter	10	30	60	120	
C	0.407	0.350	0.339	0.331	0.348	0.316	0.024
Si	0.243	0.204	0.210	0.221	0.219	0.216	0.006
Mn	0.791	0.697	0.772	0.745	0.790	0.748	0.041
Cr	0.960	0.940	1.008	0.998	1.019	0.998	0.053
Mo	0.183	0.165	0.171	0.172	0.176	0.172	0.016
Al	0.035	0.016	0.002	< 0.001	< 0.001	0.003	0.001

increasing immersion time, however, the total amount and total area of remaining alumina inclusions increased again. The major amount of inclusions sized $1\text{ }\mu\text{m}^2$ to $3\text{ }\mu\text{m}^2$ for the remelted steel sample, and drifted up to $10\text{ }\mu\text{m}^2$ if a filter was immersed. A maximum coarsening was observed when the alumina coated filter was immersed for 30 s (up to $20\text{ }\mu\text{m}^2$). For longer immersion periods, the inclusion size tended to decrease again, cf. the highlighted cells in Table 4.5. Furthermore, a few inclusions larger than $50\text{ }\mu\text{m}^2$ were found if a filter was immersed, independently from the investigated immersion time. In summary, despite the coarsening effect of immersing a filter, the total area of alumina inclusions is decreased by using a filter and therewith demonstrating a filtration effect of up to 31.4% less alumina inclusions regarding the total inclusion area.

Table 4.4.: Number of inclusions remaining in the solidified steel from the test series with filter type A, classified by their chemistry according to Table 3.4. Sample "without filter" refers to the remelting trial with a dwell time of 15 min after the pre-treatment.

Chemical class	Number of Inclusions*				
	without filter	Immersion time (s)			
		10	30	60	120
Al ₂ O ₃	1248	371	381	439	597
Ca-aluminate	0	0	0	0	0
Mg-spinel	0	0	0	0	0
Al-Mn-Mg-Fe-Ca-silicate	0	0	0	0	1
SiO ₂	5	9	46	18	85
MnO-MnS	6	0	1	0	0
CaO-CaS	0	0	0	0	0
Dirt	17	11	14	6	1
FeO-oxide	0	1	7	2	53
FeO-scratches	6	2	4	2	0
Other	116	9	30	16	56

* Normalized to 100 mm² of search area.

4. Results and Discussion

Table 4.5.: Inclusion size distribution of NMIs of the class "Al₂O₃" of the immersion trials with filter type A. Size class contains $x < 20\%$, $20\% \leq x < 25\%$ or $x \geq 25\%$ of the total amount of Al₂O₃ inclusions. Sample "without filter" refers to the remelting trial with a dwell time of 15 min after the pre-treatment.

Immersion	Number of Inclusions*						
time (s)	size class: particle area (μm ²)						
	0.1 – 1	1 - 3	3 - 5	5 - 10	10 – 20	20 - 30	30 - 50
without filter	276	432	206	245	79	9	1
10	49	87	57	76	64	17	13
30	43	75	55	86	78	29	12
60	52	104	61	107	81	22	9
120	99	155	86	126	83	23	15

Immersion	Number of Inclusions*					Total area
time (s)	size class: particle area (μm ²)				Total	of Inclusions [†]
	50 – 80	80 - 130	130 - 200	200 - 500		(10 ³ μm ²)
without filter	0	0	0	0	1248	5.1
10	7	1	0	0	371	3.5
30	3	0	0	0	381	3.6
60	3	1	0	0	439	3.7
120	5	2	0	0	597	4.6

* Normalized to 100 mm² of search area.

[†] Calculated from the sum of the products resulting from multiplying the average value of each size class and the corresponding number of alumina inclusions.

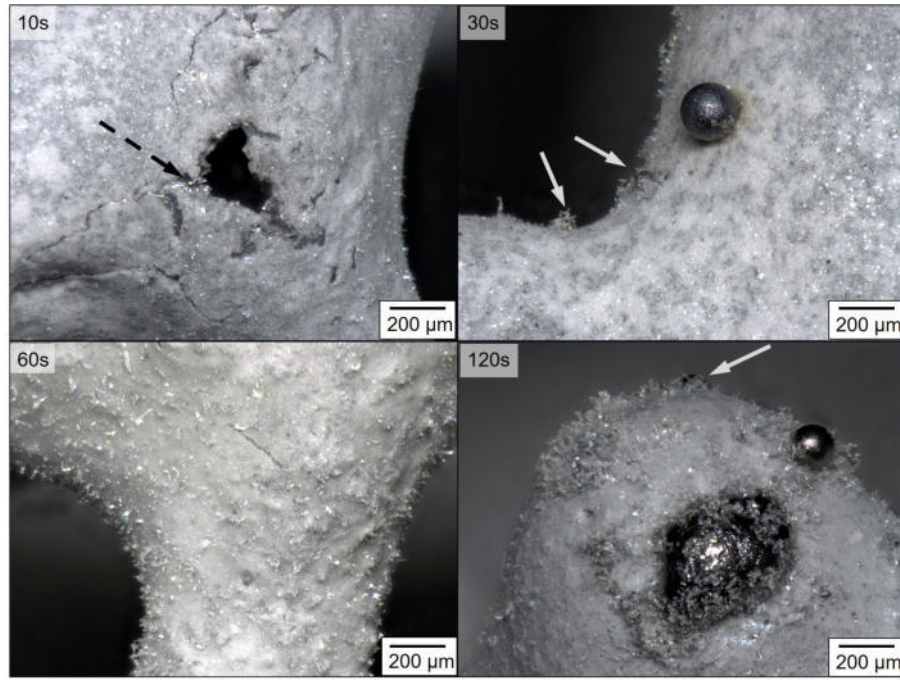


Figure 4.17.: Microstructure of AC coated filters after immersion trials with varying immersion time by light microscopy. Dashed black arrow: the vitreous layer made clearly visible near an hole. White solid arrows: Secondary crystals on the filter surface encapsulating small steel drops.

4.4. Influence of Carbon: Carbonaceous alumina coating

As it is known from the literature that alumina reacts with the melt depending on the carbon content of the system, the influence of a small amount of carbon added to the alumina coating on the time-depending interactions has been investigated here. The obtained results of the immersion trials with such carbonaceous alumina coated filters are presented in the following section. The experimental procedure and dwell times of the filters in the melt were the same as for the immersion trials of the alumina coated filters shown in the preceding section.

4.4.1. Microstructure after immersion

Figure 4.17 presents the filter surfaces after the immersion tests by light microscopy. Already after 10 s immersion, the vitreous layer covering the whole filter surface (as highlighted by the black dashed arrow in Figure 4.17) was observed. Some steel droplets stuck onto the filter surface and some cracks and areas, where the coating spalled, were present, too. Overall, the findings were similar to the ones of the pure alumina coated filters described in the previous section. Darker shades of the

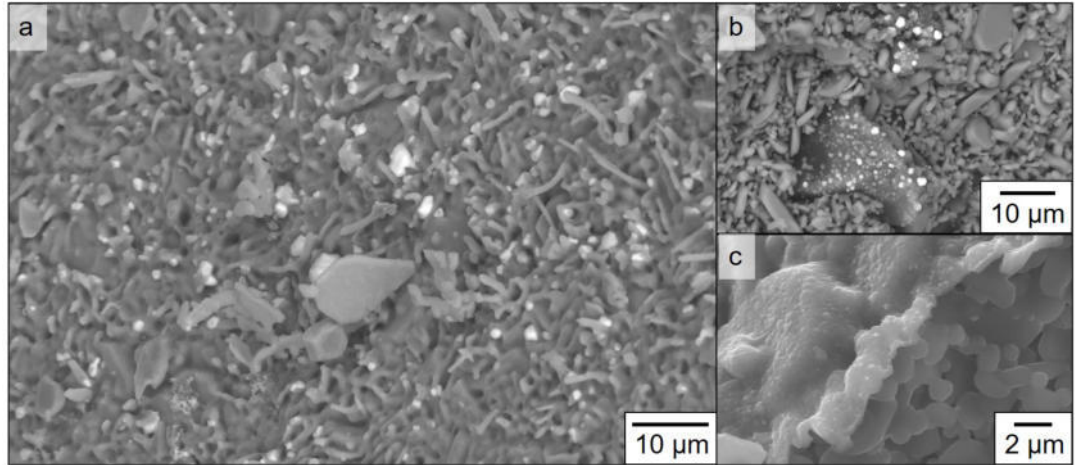


Figure 4.18.: Microstructure of an AC coated filter after 30 s immersion by electron microscopy: a) top view: surface with secondary crystals and iron-based beads (bright spots), BSE-mode, b) cross-section of the AC coating: iron-based beads on carbon particles, BSE-mode, and c) pimples in-situ layer (left) on sintered alumina grains of the coating(right), SE-mode.

coating indicated that carbon is still present in the coating. By increasing immersion time, the secondary crystals on the filter surface became larger and increasingly encapsulated metallic beads, cf. solid arrows in Figure 4.17. The coating showed less cracks and flaking off from the substrate compared to the filters with coating A. Nevertheless, flaking off became also more pronounced with increasing immersion time (cf. appendix Figure B.8).

As there was no quantitative analysis of the secondary crystal amount and length, it can only qualitatively be stated that there is a tendency to more secondary crystals if the filters were coated with the carbonaceous alumina coating compared to the pure alumina one. Again, a bushy-like growth of secondary crystals is observed near remaining metallic beads. After 120 s, occasionally the metallic beads became more flat, losing their globular shape. That indicates a change in the wetting behaviour, and is probably caused by interfacial reactions and phase formation.

The microstructure analysis by SEM revealed after 10 s immersion a similar layer build-up compared to the alumina coated filter immersed for the same time: iron-based beads between carbon-bonded substrate and the AC coating, and the vitreous layer covering the filter surface with secondary alumina on top of it. In difference to the alumina coated filter, the secondary crystals were longer, up to 20 µm, and some iron-based beads could be found between them. Additionally, the iron-based beads were observed on the carbon particles of the coating, as exemplified on the 30 s immersed filter in Figure 4.18 b. These observations imply that the filter–melt

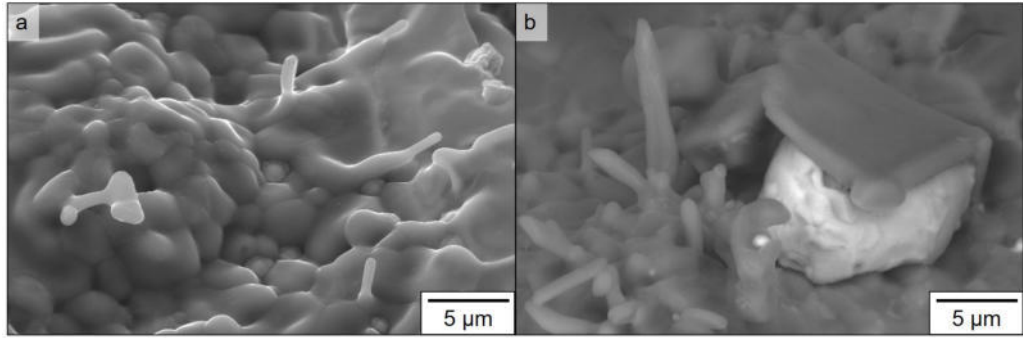


Figure 4.19.: Microstructure of an AC coated filter after 120s immersion by electron microscopy: a) top view: surface with highly sintered secondary crystals, SE-mode, and b) top view: iron-based bead enclosed by secondary corundum, BSE-mode.

interactions were indeed accelerated during the first seconds of contact by the carbon added to the coating.

With increasing immersion time, more differences were found compared to the carbon-free coated filters:

- Morphology of the secondary alumina crystals: In addition to the platelike crystals with sharp edges, blunted needles as shown in Figure 4.18a were observed. All in all, secondary crystals sintered together more intensively with increasing immersion time, cf. Figure 4.19 after 120 s immersion.
- In the case of 30 s immersion, the vitreous layer appeared pimpled, cf. Figure 4.18c. That was not observed on the filters immersed for 10 s, 60 s and 120 s. There, the vitreous layer appeared smooth in the area under investigation.
- No clusters were observed on the investigated filter surface.

In addition, cross-sections of polishes samples of trials with 10 s and 30 s immersion periods revealed a thicker (about 1 µm) layer covering the secondary crystals. While this layer only partially appeared on the 10 s immersed sample, it covered the entire secondary crystals in the examined area of the 30 s immersed sample. According to EBSD that layer was amorphous. EDS analysis indicated that it consisted of Si, O, Na, Ca, S, and P. Further, signals from Al and O as well as Fe and Cr were detected, cf. Figure 4.20. Due to the stimulated sample volume with an extension in the µm range, however, overlapping signals from the adjacent sample material—alumina and steel, respectively—cannot be distinguished. That layer was not observed after 60 s and 120 s in the areas under investigation.

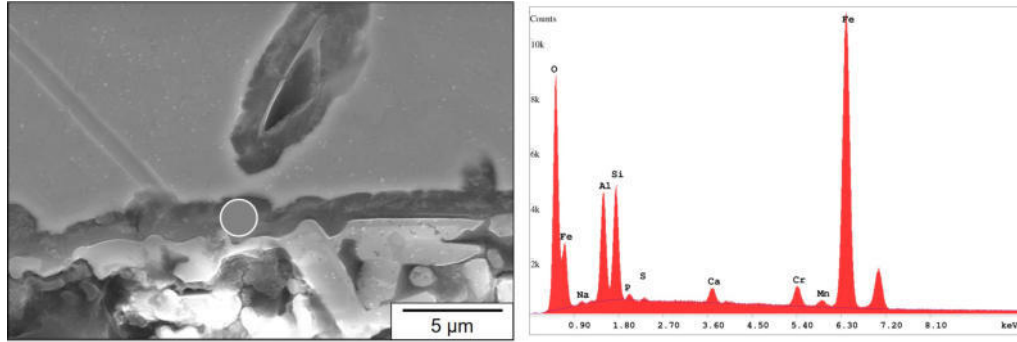


Figure 4.20.: Microstructure analysis of an AC coated filter after 30 s immersion by electron microscopy. Left: polished cross-section showing the alumina coating, the layer build-up at the interface and adjacent steel (bottom to top). The tunnel-like structure in the middle of the steel area is a secondary alumina crystal surrounded by a Si- and Ca- containing layer. Right: EDS-signal of the marked spot in the left figure, i.e. such a layer on the secondary crystals.

4.4.2. Steel characterization

Overall, the fluctuations in the process parameters of the immersion experiments presented in Table 4.6 were in an acceptable, usual range. Compared to the immersion trials with the alumina coated filters, the ratio of the oxygen content before and after immersing the filter samples was lower for all immersion periods, cf. Table 4.2 on page 85. That indicates that less oxygen was released by immersing the AC coated filters, or more consumed during the filter–steel melt interactions. The oxygen/temperature measurements including the filter sample immersion took less time than in the aforementioned test series with filter type A.

Table 4.7 is an extract with relevant results of the chemical analysis by spark optical emission spectrometer, which is presented completely in the appendix (Table B.3). Similar to the trials with the alumina coated filters, the remelting and the pretreatment resulted in a slight decrease of the alloying elements. Immersing a filter did not lead to significant changes of the main alloying elements (Si, Mn, Cr, and Mo): with regard to them, the steel still meets the specification for 42CrMo4 as prescribed the standard DIN EN ISO 683-2:2018-09 [DINb]. Again, only the aluminium content is distinctly decreased after immersing an AC coated filter for 10 s. Compared to the immersion trials of the alumina coated filters, however, the aluminium content increased with increased immersion times; the highest value was obtained after 30 s immersion, whereby it still kept below the value obtained without immersing any filter.

For the same reasons as discussed for the alumina coated filters, only the inclusions

4. Results and Discussion

Table 4.6.: Parameters during immersion trials of the AC coated filters. The logged oxygen content (a_O) and the temperature (T) of the melt were measured before (bI)* and after immersing (aI) a filter. Thereby, a positive temperature difference (ΔT) describes an increase in temperature and a negative a decrease between both measurements points. The time between these two measurements (Δt) is listed.

time filter immersed (s)	a_O (ppm)		ratio $a_O(aI)/a_O(bI)$	T (°C)		ΔT (K)	Δt (min)
	bI	aI		bI	aI		
10	7.9	14.1	1.8	1641	1622	-18	12.5
30	9.4	14.0	1.5	1654	1649	-6	9.75
60	12.5	27.3	2.2	1655	1665	11	9.25
120	11.8	24.7	2.1	1645	1659	14	12.0

* after the oxidation-deoxidation pre-treatment, cf. Section 3.3.

of the Al_2O_3 class, cf. Tables 4.8 and 4.9, are evaluated in the following. Immersing the filter for 10 s distinctly decreased the number as well as the total area of alumina inclusions. With increasing immersion time, however, the total amount and total area of remaining alumina inclusions increased again. Strong coarsening of the inclusions was observed. As a result, the total area of alumina inclusions became larger compared to the sample without filter if a filter was immersed for 30 s, 60 s and 120 s. From that it appears that the steel became contaminated using these filters. The major amount of inclusions sized $1 \mu m^2$ to $3 \mu m^2$ for the remelted steel sample, and drifted up to $20 \mu m^2$ if a filter was immersed. Compared to the alumina coated filter trials no backward drift of the coarsening effect was observed. In summary, only in the case of immersing an AC coated filter for 10 s, a positive filtration effect was found: 39 % less alumina inclusions regarding the total inclusion area. Longer immersion time resulted in more and coarser inclusions classified as Al_2O_3 ones.

4. Results and Discussion

Table 4.7.: Chemical composition (extract) of the steel before and after the immersion tests with the AC coated filters. Sample “without filter” refers to a trial during which molten steel was pretreated and instead of immersing a filter, the temperature was just hold for 15 min.

Element	composition (mass%)						max.
	as	without	After immersion (s)				standard
	received	filter	10	30	60	120	deviation
C	0.407	0.350	0.338	0.346	0.337	0.342	0.010
Si	0.243	0.204	0.213	0.213	0.209	0.215	0.010
Mn	0.791	0.697	0.747	0.771	0.739	0.757	0.022
Cr	0.960	0.940	0.992	1.004	0.975	0.994	0.023
Mo	0.183	0.165	0.178	0.175	0.166	0.174	0.007
Al	0.035	0.016	0.002	0.008	0.004	0.003	0.001

Table 4.8.: Number of inclusions remaining in solidified steel after immersion trials with filter type AC, classified by their chemistry according to Table 3.4. Sample “without filter” refers to a trial during which molten steel was pretreated and instead of immersing a filter, the temperature was just hold for 15 min.

Chemical class	Number of Inclusions*				
	without filter	Immersion time (s)			
		10	30	60	120
Al ₂ O ₃	1248	361	566	722	866
Ca-aluminate	0	0	0	0	0
Mg-spinel	0	0	0	0	0
Al-Mn-Mg-Fe-Ca-silicate	0	1	0	0	0
SiO ₂	5	0	31	52	75
MnO-MnS	6	0	1	0	1
CaO-CaS	0	0	0	0	0
Dirt	17	4	189	4	2
FeO-oxide	0	0	27	37	72
FeO-scratches	6	0	13	0	0
Other	116	2	93	54	82

* Normalized to 100 mm² of search area.

4. Results and Discussion

Table 4.9.: Inclusions of the class "Al₂O₃" remaining in solidified steel after immersion trials with the filter type AC, classified by size. Size class contains $x < 20\%$, $20\% \leq x < 25\%$ or $x \geq 25\%$ of the total amount of Al₂O₃ inclusions. Sample "without filter" refers to a trial during which molten steel was pretreated and instead of immersing a filter, the temperature was just hold for 15 min.

Immersion	Number of Inclusions*						
time (s)	size class: particle area (μm^2)						
	0.1 – 1	1 - 3	3 - 5	5 - 10	10 – 20	20 - 30	30 - 50
without filter	276	432	206	245	79	9	1
10	44	75	53	80	74	23	9
30	40	85	65	113	131	68	46
60	103	174	119	143	111	37	24
120	59	117	99	175	211	106	65

Immersion	Number of Inclusions*				Total area	
time (s)	size class: particle area (μm^2)				Total	of Inclusions [†]
	50 – 80	80 - 130	130 - 200	200 - 500		($10^3 \mu\text{m}^2$)
without filter	0	0	0	0	1248	5.1
10	1	0	0	0	361	3.1
30	15	4	0	0	566	6.9
60	7	2	0	0	722	6.2
120	25	6	1	0	866	12.8

* Normalized to 100 mm^2 of search area.

[†] Calculated from the sum of the products resulting from multiplying the average.

4.5. Discussion: Impact of time on and role of carbon in the filter–steel melt interactions

On all alumina-based coated filters, immersed for at least 10 s, layers formed on the filter surface. In that cases, there was no disastrous spalling of the coating. The layer build-up consisted of iron-based beads in the interface-near $\text{Al}_2\text{O}_3\text{--C}$ zone right below the coating and a thin vitreous alumina-based layer directly on the coating, on which secondary corundum polycrystals were attached. This is in line with the layer build-up reported by previous filter immersion trials [Dud+14; Emm+13] and by parallel works to the present thesis [Sto18; Geh+18; Sal19] within the CRC 920, independently if the carbon-bonded alumina filter was coated by a porous alumina-based coating or not. As it had not been tested before, the addition of carbon to the coating material provided the new insight that the iron-based beads also formed on its surface. That leads to the questions, how the layers might have been built up and what role the coating played in this.

4.5.1. Formation of the observed layer build-up

As mentioned before, the observed layer build-up on the alumina-based coated filters appeared similar to the layer build-up observed on uncoated $\text{Al}_2\text{O}_3\text{--C}$ filters. In the latter case, the formation is described by dissolution and precipitation of alumina in and from the steel melt, respectively, that is triggered by the dissolution of carbon and the resulting locally increased carbon content of the melt. Thereby a gas mainly consisting of $\text{CO}_{(\text{g})}$ is formed. With this hypothesis formulated by Zienert et al. [Zie+15], interactions between a $\text{Al}_2\text{O}_3\text{--C}$ refractory material and liquid steel seem reasonable. Not only in the two cases presented in that study, i.e. the sessile drop experiments conducted by Khanna et al. [Kha+11] and the filter immersion tests conducted by Dudczig et al. [Dud+14], Salomon [Sal19, p. 172] also applied it to interpret his results obtained from the SPS trials of the $\text{Al}_2\text{O}_3\text{--C}$ refractory material—uncoated as well as coated with compositions A or AC— and liquid 42CrMo4. Further, he could recognize $\text{CO}_{(\text{g})}$ evolution in positive correlation with the carbon content of the ceramic sample in his experimental set-up, which he linked with the dissolution and precipitation processes of alumina. [Sal19, pp. 140–142] Having in mind that an increased carbon-content of an iron melt decreases the wetting angle on an alumina or $\text{Al}_2\text{O}_3\text{--C}$ substrates, cf. Section 2.2.4 on page 23, and that carbon tend to decrease the surface tension of an iron melt [Kee88], it seems consistent that local enrichments of carbon in the melt at the interface increase the reactivity with the refractory. Poirier and Thillou [PT94] described this increased

4. Results and Discussion

reactivity with an increased activity of aluminium in the steel melt if the otherwise low-carbon steel is enriched with carbon at the filter–steel interface. To sum up, the presence of dissolved carbon at the filter–steel melt interface seems to be essential to promote the alumina dissolution and precipitation processes.

The main carbon sources of the system under investigation were the carbon-bonded alumina substrate and—if added—the carbon particles of the coating. This is where the role of the porous coating is revealed. It offers transport paths from the substrate towards the filter–steel interface. The importance of porosity has been indicated by Gehre et al. [Geh+18], whereby in that study the influence of the coating’s porosity was overlapped by the highly reactive alumina-based phase composition applied by flame-spray coating, which has been compared to the porous corundum one.

Poirier and Thillou [PT94] mentioned that $\text{CO}_{(g)}$ forming within the refractory usually decompose in the liquid steel as a result of the lower CO partial pressure present in (ultra) low carbon steel grades. It is known from the used modified coal tar pitch (Carbores® P) that it transforms into graphite-like structures with increasing temperature. During sample preparation, the filters were heated to a maximum temperature of 1400 °C. Thus, it is assumed that the decomposition of the modified coal tar pitch continued under releasing $\text{CO}_{(g)}$ when the filters were heated up to about 1650 °C during the immersion trials. Degassing tests of coated filters up to the process temperatures of the immersion trials might enlighten, how much $\text{CO}_{(g)}$ can be formed that way and contribute to the filter–steel interactions. Such experiments were not conducted within the frame of this thesis. Nevertheless, this is probably not the only mechanism that would be able to provide carbon at the interface: solid-phase diffusion might also contribute [Zie20]. Dudczig et al. [Dud+14] and Salomon [Sal19, p. 132] observed microstructural changes of the Al_2O_3 –C near the substrate-alumina coating interface that were explained by decarburisation of that zone in both studies. Usually, iron-based beads were also found there. In the case of the AC coated samples, that decarburised zone formed only after the test with the longer dwell time, i.e. after 30 min. [Sal19, p. 132] In the present study as well as in the case of Bock et al. [Boc+19], such microstructural changes were not observed, the iron-based beads were nevertheless found. Probably, the coating’s thickness as well as the short immersion times (≤ 120 s) limited carbon diffusion from the substrate towards the filter–steel interface in such a way that the interactions were enabled but not strong enough to alter the substrate’s microstructure distinctly.

Another mechanism might be indicated by the iron-based beads found on carbon of the coating or the substrate material of the filter. From the viewpoint of the steel, it appeared as they formed on the first carbon encountered. Their origin, however,

4. Results and Discussion

cannot be proven beyond doubt here. Nevertheless, a discussion approach will be pursued: Sillo [Sil91] reported of spherical metal droplets remaining in the investigated refractories after melting tests. These droplets were mainly made of iron and chromium, and were observed near corundum or galaxite crystals. From their spherical appearance, Sillo deduced that they should have origin from either a gaseous or liquid phase. Due to the lack of manganese in these droplets, Sillo concluded that they resulted from reactions within a liquid oxide phase at the refractory–steel melt interface. Otherwise, if a gaseous phase would be the source of the metallic droplets, he would have expected an increased Mn content due to the higher volatility of manganese compared to Fe and Cr. In the present study, EDS analysis implied that the observed beads contained iron and chromium, but neither manganese or molybdenum or other main alloy elements of the steel. Assuming now that the iron-based beads found in the present study were of a similar origin as described by Sillo, it would imply that an Fe-Cr-rich oxide phase with low viscosity at the process temperatures would have penetrated the porous alumina coating and reacted with carbon it first encountered. The different oxidation states of chromium allow it thereby to interact in a variety of complex ways in redox-reactions. [IWA+70; KM79a] Further, such an oxide phase would have been reduced by carbon and the metallic beads remained. Thereby, gaseous reactions products, like $\text{CO}_{(\text{g})}$, could have been formed. However, no signs of such an oxide phase were found post mortem on the coating’s alumina grains, and it is not known, which kind of oxide phases were formed at the filter–steel melt interface during the immersion trials.

To summarize, from the obtained results it remains an open question how the interactions were initiated in presence of the porous alumina-based coating. However, it seems reasonable that the coating’s porosity provide transport paths for carbon, either as solid or gaseous phase. That way carbon is provided at the coating–steel melt interface and local enrichments of carbon in the liquid steel may enable the alumina dissolution and precipitation processes. Thereby, CO bubbles reaching the coating–steel interface either dissolve in the melt and provide carbon as well as oxygen or act as reaction sides for further redox-reactions, as outlined in Section 2.2.2 on page 14.

At the filter–steel interface, the supply of dissolved oxygen will result in the formation of a thin liquid oxide film at the coated filter surface. The composition of that oxide film is expected to constantly change due to the ongoing redox-reactions with dissolved carbon, oxygen, iron, aluminium, and other elements at the filter–steel interface. Nevertheless, it should contain at least iron oxide, alumina, lime, silica, chromium oxide, and solid solutions of them. The molten steel flowing by accelerates these diffusion-driven reactions by supplying fresh melt, mixing the boundary layer

and removing reaction products. From these considerations, it can be expected that the reactions taking place were beyond the thermodynamic equilibrium. Already after the short immersion time of 10 s, the vitreous layer on the filter surface was observed. It might have formed from the oxide film, which solidified when the filter was removed from the melt and cooled down. In that case, the chemical composition of the oxide phase as well as the cooling conditions will influence the phase composition determined post mortem. That might explain why Salomon [Sal19, p. 137–138] detected iron and oxygen as main components of that layer, which were accompanied by aluminium and silicon, whereas after the filter immersion trials (Dudczig [Dud+14] and the present results) mainly aluminium and oxygen were detected.

The determined grain orientation of the secondary corundum was found to be independent from the coating’s alumina grains and thus implied heterogeneous nucleation as origin. The required nuclei were provided either as a product of redox-reaction or from alumina NMIs deposited from the melt. The nano-crystalline components observed by Salomon [Sal19, p. 137–138] might describe such nuclei. It is assumed that the vitreous layer solidified from a liquid oxide phase at the filter surface. The metallic iron-rich beads remaining between the secondary alumina crystals—and especially how they were partially encapsulated by them—indicated that the secondary alumina crystallised completely during cooling down after the immersion test.

4.5.2. What happens with increasing immersion time?

The requirements for the formation of the vitreous layer and the secondary aluminium oxide crystals are given within the first seconds during of filter–steel contact, as they were observed on filters immersed for 10 s but not if only dipped into the melt. After 30 s immersion, secondary alumina formed more distinct and the iron-based beads were found between them. An increase of the crystal length was only observed for 60 s steel contact. Overall, the thickness of the vitreous layer did not change distinctly for the investigated immersion times. Cluster deposited on secondary alumina were only found on the alumina coated filter immersed for 60 s and 120 s.

Intensive sintering of the interface-near alumina in comparison to the alumina grains within the residual coating was observed. As the liquid oxide film on the filter surface should contain also lime and silica, e.g. from impurities of the refractory material or from the liquid steel, liquid-phase sintering of the interface-near alumina is assumed. If the filter surface becomes denser due to sintering of alumina, the

4. Results and Discussion

material transport through the porous coating, and therewith the carbon supply essential for the alumina dissolution–precipitation processes, is cut off. From that it is reasonable to assume that the dissolution–precipitation processes slowed down and might finally come to an end at the filter–steel interface. Here, that should have been the case between 30 s and 60 s immersion.

Alternatively, the interactions still took place, but the dissolution and precipitation processes reached a kind of equilibrium. However, observations reported by Zienert et al. [Zie+20] support the first explanation: They immersed prismatic $\text{Al}_2\text{O}_3\text{--C}$ samples¹⁰ in molten 42CrMo4 for different dwell times. Thereby, gas formed intensely close to the refractory’s surface during the first ≈ 40 s of contact with the steel melt. From 60 s immersion on, the gas formation came to an end. As $\text{CO}_{(\text{g})}$ formation is considered as side-product of the alumina dissolution and precipitation processes, the decrease and absence of gas formation indicate that such processes might have come to an end. Interestingly, their findings fall within a similar time frame as the results of the present thesis, despite the samples of Zienert et al. were of a different geometry and uncoated, which will certainly influence the kinetics of the filter–steel melt interactions.

If the carbon supply is stopped, reduction reactions at the filter–steel interface will decrease resulting in a thickening of the oxide film at the filter–steel interface. Based on the findings of Section 2.3.2 on page 31, the presence of a liquid phase on the filter surface should decrease the attraction of solid inclusions from the melt and therewith their deposition. Subsequent reduction of oxides within that oxide film will be caused by aluminium and result in the formation of solid alumina. From that, the observed cluster of the samples 60 s and 120 s might have formed, which is just an alternative explanation to the deposition of endogenous alumina inclusions. In addition, the presence of a liquid oxide layer will increase the probability that the steel melt flowing past will entrain parts of it and thus generate new inclusions. These considerations might explain, why more inclusions of the Al_2O_3 class were observed in the steel samples with increasing immersion time of the filter. Storti, too, found the lowest amount of inclusions remaining in the solidified steel when the filters were immersed for the lowest immersion period under investigation, i.e. 10 s. [Sto18, p. 77] From that a short filter operation time or a delayed sintering of the surface-near alumina appears beneficial.

Data obtained by the automatic software interpreting the X-ray signals for EDS analysis have to be handled with care, as the accuracy of quantitatively analysis of the chemical composition suffers tremendously from surface roughness of the sample. [NR15] Further, the amount of NMIs in the analysed steel sample might be

¹⁰composition is based on the substrate material used in the present study.

4. Results and Discussion

influenced by an inhomogeneous microstructure. As the steel samples cooled down freely and uncovered¹¹ segregation during solidification cannot be excluded.

When discussing the results regarding the immersion trials post-mortem, it should be noted that the melt changes continuously during the test duration. Remelting, the pretreatment (i.e. oxidation and deoxidation) and the high temperatures let the melt "work" again in the sense of reactions taking place. Further, interactions with the crucible material cannot be excluded. The crucible material was kept constant in the here presented trials as it was beyond the scope of this thesis to evaluate to the impact of the crucible material on the filter–steel melt interactions. Nevertheless, inclusion might deposit there as well. The influence of the crucible material is more closely investigated by Fruhstorfer et al. [Fru+18], whereby their experimental series did not include the crucible material used in the present study. As the liquid steel is not covered by a slag, a thin oxide film will also form at the steel–atmosphere interface. Due to the flow induced by inductive heating, such oxide films will be entrained and serve as additional source of inclusions. Unfortunately, it could not be evaluated within this thesis to which extent this effect influences the detected area of NMIs for the different immersion periods investigated here. The lack of melt coverage enables further free evaporation of gaseous phases from the melt. From that, the formation of a metallic fume over the melt surface is assumed, which condensates on cooler surfaces of the SCS housing. Metallic dust within the housing was found. [Dud19]

Interestingly, the filtration efficiency of the here presented immersion trials are higher than the ones predicted by numerical simulations by Asad et al. [Asa+17]. The main reasons for these differences should be the following ones:

- Within the simulations, interfacial reactions between filter and steel had not been considered. But, as shown here, they should have a positive effect on the deposition of alumina-based inclusions from the melt.
- Unlike the here described immersion tests, the filter did not rotate in the simulation, which in turn should influence the flow pattern near and within the filter.
- Gas bubbles resulting from the interactions might have been entrained by the melt flow. As presented in Section 2.2.2 on page 14, bubbles have the potential to capture inclusions, too, and carry them to the crucible or steel melt surface.

In combination, the real filtration effect was enhanced compared to the calculations, despite the fact that the filter position within the steel casting simulator might not

¹¹In means of a slag, which thermally isolated the melt against the atmosphere and therewith benefits a controlled solidification.

have been optimal. Thereby, the simulations by Asad et al. [Asa+17] illuminated an drawback of the experimental set-up: the filtration potential of the filters might be misinterpreted compared to industrial casting trials as the filters were in a position with low steel melt velocity. On the one side, filtration efficiency might be underestimated as there is a lower probability for inclusions to come in contact with the filter surface. On the other side, an accelerated melt flow might increase the probability that layers from the filter surface might be (partially) re-entrained. The later studies of Asad et al. [Asa+18; AAS19] showed how local changes of the melt flow velocity, e.g. due to rising bubbles, distinctly influence the inclusion deposition behaviour. These considerations underline, how complex the predictions of filtration efficiencies are and suggest that results from the SCS tests cannot be transferred one-to-one to casting tests on an industrial scale. Nevertheless, they provide valuable insights into filter–steel interactions and thus the potential of filter coatings for increased inclusion deposition.

4.5.3. Effect of carbon added to the alumina coating on the filter-steel interactions

The addition of carbon to the alumina coating did indeed seem to benefit the thermal shock behaviour of the coated filters: qualitatively less cracks and coating flaking off from the substrate were observed. The interactions resulting in the growth of the layers on the filter surface seemed to be accelerated within the first seconds of filter–steel melt contact if carbon was added to the alumina coating of the filters. This is not reflected in the results of the analysis of the inclusions remaining in the solidified steel: The area and amount of detected alumina–NMIs were in a similar range if a filter of the type A or AC was immersed for 10 s. With increasing immersion time, even more and larger alumina-based inclusions have been detected if filters of type AC were immersed. On the filter surface, strong sintering of the secondary alumina as well as the surface-near alumina grains of the coating was observed. In addition, a Si- and Ca-containing layer on top of the secondary crystals was found after immersing these filters for 10 s or 30 s.

Without the macro-streaming effects of the melt, Salomon [Sal19, p. 134] described the effect of carbon on the interactions slightly different: In his case, the interactions started later when carbon was added to the alumina coating, but they were all the more intense for it. Salomon assumed that as well the greater coating thickness as the worse initial wetting of the AC-coating in comparison to the alumina coating contributed to that observation. Afterwards, Salomon found the AC-coating decarburised and cracked.

The wetting behaviour of the alumina-based coatings with varied carbon-content, including the here presented types A and AC, with the 42CrMo4 alloy was analysed by Yan et al. [Yan+18]. They, too, observed an increasing wetting angle with increasing carbon-content in the coating. Additionally, the ceramic samples became also rougher with increasing carbon-content. That experimental series underlined the huge impact of surface roughness on the wetting angle. Otherwise, an increased carbon-content of the coating should have benefited wetting. As discussed in Section 2.2.4 on page 23, carbon from the refractory that dissolves in the molten steel decreases the melt's surface tension and should therewith result in lower wetting angles.

But not only the surface roughness, the density of the coating is altered, too, if carbon is added to the coating as presented in Section 4.1.2 on page 67. A lower density of the coating should benefit transport processes through it. Additionally, the carbon inside the coating shortens the transport paths towards the filter–steel melt interface. The combination might sufficiently accelerate the start of reaction chains, which resulted in the more advanced layer-build up found on the AC coated filter in comparison to the A coated filter after 10 s immersion.

Due to the accelerated start of interactions, a higher filtration effect might be expected after 10 s immersion compared to the carbon-free alumina coated filter. But as mentioned above that was not the case. It can be assumed that the enhanced sintering of the alumina grains at the filter surface counteract the transport processes and therewith cut off the carbon supply necessary for the reduction reactions in the liquid oxide layer at the filter–steel melt interface. Silica and lime detected at the filter surface of AC coated filters immersed for 10 s or 30 s would enable liquid state sintering of alumina, cf. Section 2.1.2 on page 6.

4.5.4. Summary of the time dependent filter–steel interactions

Thus, from the presented results and the literature, the following formation mechanism of the layer build-up on the filter surface appears reasonable, cf. Figure 4.21:

The here presented results imply that carbon of the carbon-bonded alumina substrate took part in the filter–steel interactions, which could have been only possible due to the coatings porosity. An iron-rich fluid might have passed the alumina coating by the pores, too, without leaving a trace that could have been detected post-mortem. When carbon was reached, reactions—like the reduction of an oxide phase—occurred, leaving metallic iron-rich beads at the surface of the carbon-bonded substrate and carbon particles of the carbonaceous alumina coating. Whether they were the start of the carbon diffusion towards the filter–steel interface

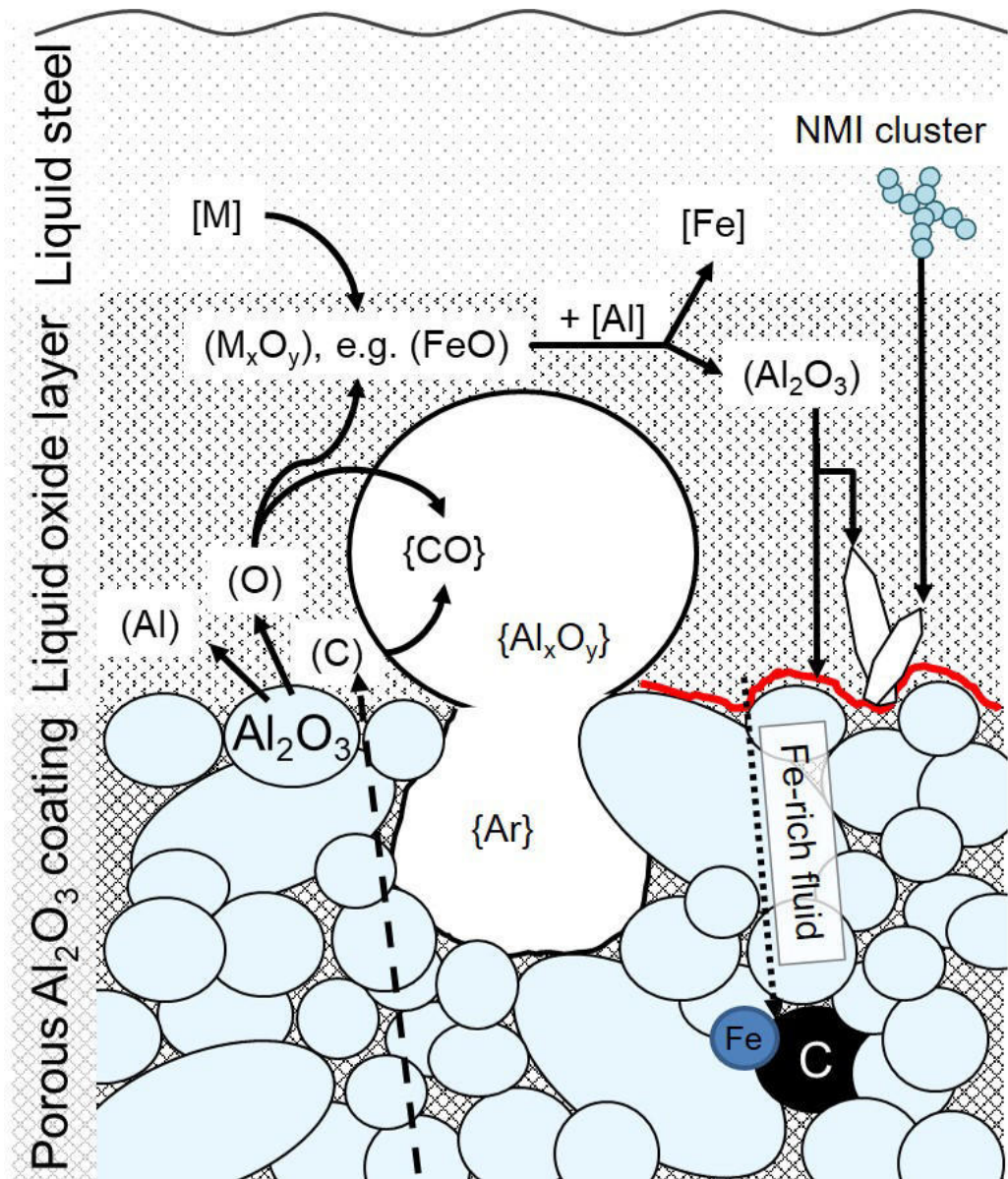


Figure 4.21.: Scheme of filter–steel interactions: Carbon from the filter triggered dissolution and precipitation processes of the coating’s alumina at the filter surface. Various redox-reactions took place in the ionic melt between the alumina-based coating and the metallic melt. Gas bubbles enabled these reactions. It is assumed that an iron-rich fluid entered the coating, reacted with the first carbon particles it encountered and metallic beads resulted from these reactions. It is important to note that reaction paths are not balanced to keep the scheme simple.

4. Results and Discussion

(e.g. as $\text{CO}_{(\text{g})}$) or if carbon diffused itself ($\text{C}_{(\text{s})}$), cannot be answered yet. The presence of dissolved carbon at the filter–steel melt interface is essential to promote the alumina dissolution and precipitation processes.[PT94; Poi15; Zie+15; Sal19]. As a result, the melt was locally supersaturated with aluminium, which reacted with dissolved oxygen to form secondary corundum. During these interactions, a liquid oxide layer was formed directly at the ceramic surface and provided nano-crystalline nuclei for heterogeneous nucleation of secondary corundum. This layer solidified amorphous. Despite a clear phase assignment was not possible, reasonable phases are hercynite, magnetite or γ -alumina according to Salomon [Sal19, p. 137–138]. Storti et al. [SBA18] reported the presence of α - Al_2O_3 and detected mainly iron, oxygen and aluminium in that thin layer.

During these interactions, it cannot be excluded that deposited endogenous inclusions from the steel melt served as nuclei, too. Due to their heterogeneous nucleation, the secondary corundum crystals did not adopt the orientation of the alumina grains of the coating. By forming a dense layer, the growth of secondary corundum impeded its own formation because the carbon supply of the underlying substrate was cut off. As they grow due to ongoing redox-reactions during cooling, metallic iron-rich beads remained between the secondary alumina crystals.

It is reasonable to assume that a liquid oxide layer formed at the ceramic–steel melt interface at the process temperatures. That liquid oxide film included oxides resulting from oxidation of elements of the steel melt as well as oxides origin from impurities of the refractory material. Such a layer might have covered the filter struts inhomogeneously, e.g. being more pronounced at impurity accumulations of the coating. Additionally, its thickness should be influenced by the melt flow passing by as the speed of the melt flow influences diffusion processes. Further, local turbulences may entrain such a liquid oxide film. Its composition is determined by the ongoing redox-reactions and thus the supply of carbon, aluminium and oxygen. Thereby, spinel solid solutions with manganese and/or chromium can act as oxygen buffer.[KM79a; KM79b]

The lowest amount of inclusions remaining in the solidified steel were observed when the filters were immersed for 10 s, i.e. the lowest immersion period under investigation, which is in line with the observations of Storti.[Sto18, p. 77] Despite the addition of carbon accelerated the formation of secondary corundum, these interactions seem to hinder a positive filtration performance of the filters. The formation of a liquid oxide film, which not only should decrease attraction forces towards solid NMIs of the melt, as in the case of an liquid calcium aluminate phase presented by Tsujino et al. [Tsu+94], but also have the potential to create NMIs by entrainment of that oxide film, is therefore treated as negative impact on the filtration performance.

4.6. Impact of Carbonaceous Alumina-Zirconia-Titania coatings

In the last section of the thesis, the alumina-based coating is modified by a doping of ZrO_2 and/or TiO_2 . Whereas ZrO_2 acts as strong deoxidiser, TiO_2 lowers the surface tension of liquid iron, and therewith might influence the interactions with NMIs. Further, the combination of both dopants is known to posses excellent thermal shock properties, which are essential for the filter coating to avoid spalling. To the authors knowledge, these material combinations have not been investigated yet as filter coating. To evaluate the impact of such dopants, following filter samples were investigated in the following test series: a) an uncoated $\text{Al}_2\text{O}_3\text{--C}$ filter as reference, coated filters with b) a pure alumina coating ("A"), c) a carbonaceous alumina coating ("AC"), d) a coating like c) doped with titania ("AC-T"), e) a coating like c) doped with zirconia ("AC-Z"), and f) a coating like c) with a mixture of both dopants ("AC-ZT"). Properties of the coated filters before the steel contact have been presented in Section 4.1.2 on page 67. It has to be noted that the immersion parameters have been modified as described in Section 3.3 on page 59, thus the results of the following section cannot be directly compared with the two immersion trials shown in the previous sections. For that reason, samples A, AC, and the uncoated substrate were included as references in this experimental series.

4.6.1. Microstructure after immersion tests

Figure 4.22 presents the filter samples after 30 s immersion by light microscopy. The uncoated filter showed the usual cracks alongside the edges of the hollow struts, which were left by the polyurethane foam burnt out. The by now familiar glassy film covered the struts and some remaining steel droplets were attached, in line with reports by Emmel [Emm14], Dudczig et al. [Dud+14] and Storti [Sto18]. The A coated and AC coated filter appeared similar to the ones described in the previous chapter, cf. Sections 4.3 and 4.4.1, respectively: some flaking off the coating (which was less if coated with AC), the glassy film covering the filter struts, the attached steel droplets and secondary crystals. If the coating containing alumina, titania and carbon (AC-T) was applied on the filter, more steel remained in the macro-porosity, which resulted in large cracks around them. The dark colour of the carbon-bonded substrate underneath indicate that the coating cracked during cooling due to the shrinkage of the steel. Otherwise, the carbon-bonded alumina would be oxidised. That implies a stronger adhesion of the steel on the AC-T coating compared to the

4. Results and Discussion

uncoated, A or AC coated filters. On the bottom part¹² of the filter with AC-T coating, two kind of colour change were observed, cf. Figure 4.22 "AC-T". The coating neighbouring the steel-filled macro-pores appeared yellowish. Some pink struts were found, too. McKee and Aleshin [MA63] described similar colour changes when they investigated the solubility of titania in alumina under reduced atmosphere. They discussed them with the formation of Ti_2O_3 . Interesting observations were made if zirconia was added instead of titania: many free-standing, thin films remained in the macro-pores, as highlighted by the black arrow in Figure 4.22 "AC-Z". There, a steel ball remaining in the macro-pores presents another characteristic of that sample. The remaining steel beads were covered by a bright layer, whose sharp edges/shape imply the formation of a crystalline phase, cf. Figure C.1 on page XVIII (appendix) for a detailed view. The combination of zirconia and titania (AC-ZT) resulted in similar observation, but less and smaller single-standing walls were found. The colour of the alumina-based coating was not distinctly changed.

By electron microscopy, the uncoated filter revealed the known layer build-up, cf. Figure 4.23, as described in Section 4.2 on page 74. Bright spots were underneath the vitreous layer within a few micrometers into the carbon-bonded material. EDS analysis of these spots indicated that they were iron-based. The filter surface appears sintered with some single-standing secondary crystals sizing $5\text{ }\mu\text{m}$ to $20\text{ }\mu\text{m}$ (Figure 4.23b). Occasionally, clusters of nano-sized particles were observed on the filter surface, a detail is given in Figure 4.23c.

Compared to the uncoated filter, more secondary crystals were observed on the filter with coating A, whereby their length was similar. Some steel remained near the contact area to the thin, in-situ formed layer (compare Figure 4.24 b and c: bright gray phase in c) belongs to an iron-based phase, regarding the EDS). Some clusters were observed, too, cf. the upper section of Figure 4.24b.

Figure 4.25 presents the carbonaceous alumina coated filter after 30 s immersion. It shows the typical build-up including the thin layer (Figure 4.25c), crystals with embedded steel and many small cluster (Figure 4.25b). Within the investigated sections, they sized up to $100\text{ }\mu\text{m}$ in tuft-like crystal bundles and otherwise up to $20\text{ }\mu\text{m}$. It is assumed, that the complex flow behaviour of the steel melt within the filter (including turbulences on the struts and within the macro-pores of the filter) influenced the contact time of melt and filter surface and therewith the interactions at the filter surface. These may result in the inhomogeneous distribution of the secondary crystals as presented in Figure 4.25a.

Sample AC-T exemplifies an detailed EDS analysis, presented in Figure 4.26, whereby the in-situ layer, secondary Al_2O_3 , and iron-based beads on the filter surface

¹²Being the part of the filter immersed longest.

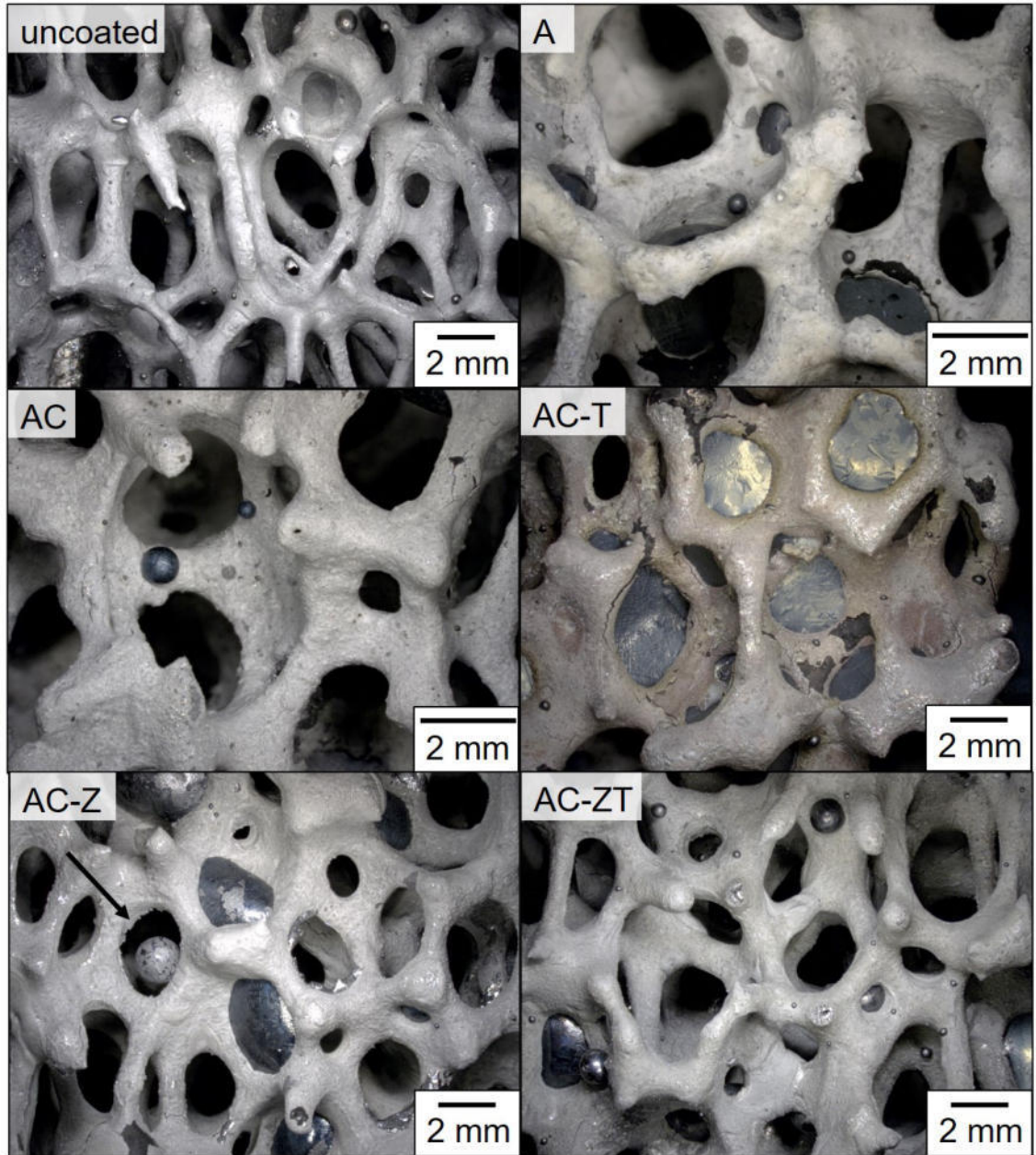


Figure 4.22.: Microstructure of coated filter with or without titania and/or zirconia doping and the uncoated filter after 30 s immersion by light microscopy.

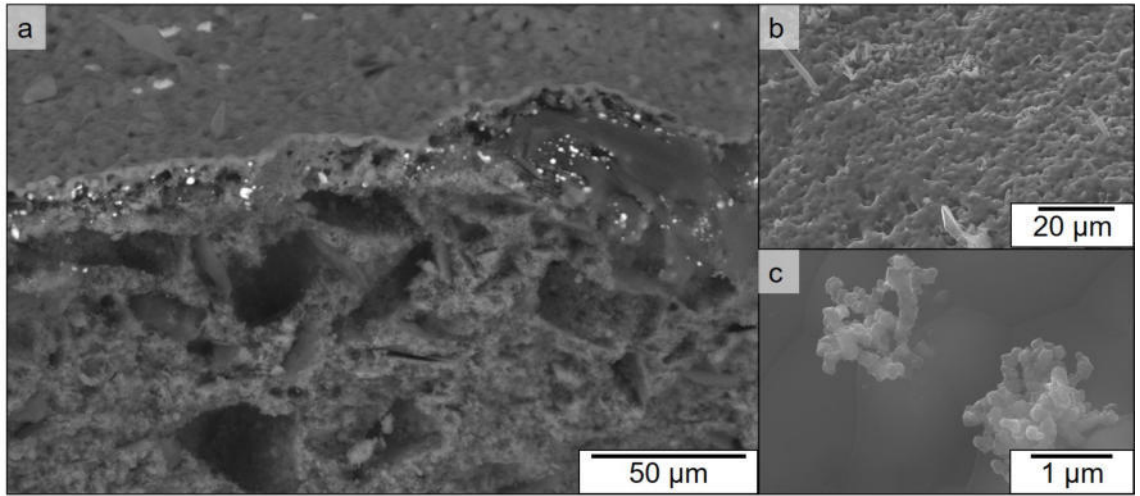


Figure 4.23.: Microstructure of an uncoated filter after 30 s immersion by SEM: a) cross-section of in-situ formed layer and infiltrating steel (bright spots), BSE-mode; b) top view on single-standing secondary crystals, SE-mode; c) detailed view on clusters on top of the in-situ formed layer, SE-mode.

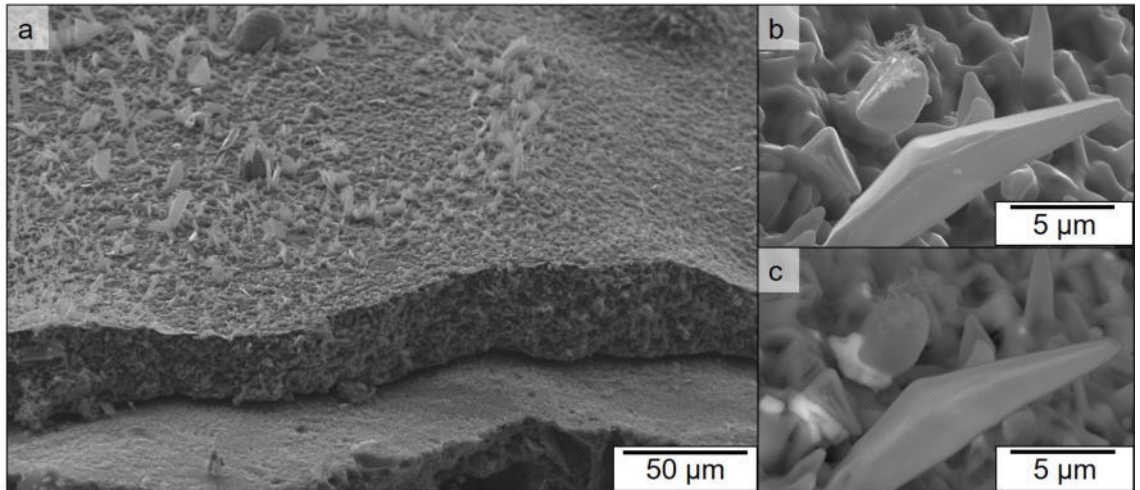


Figure 4.24.: Microstructure of a filter with coating A after immersion 30 s by SEM: cross-section of the $\text{Al}_2\text{O}_3\text{--C}$ substrate, alumina coating, in-situ formed layer with secondary crystals (bottom to top), SE-mode; b) top view on secondary inclusions and clusters, SE-mode and c) BSE-mode, bright-gray: iron-based phase, middle gray: alumina.

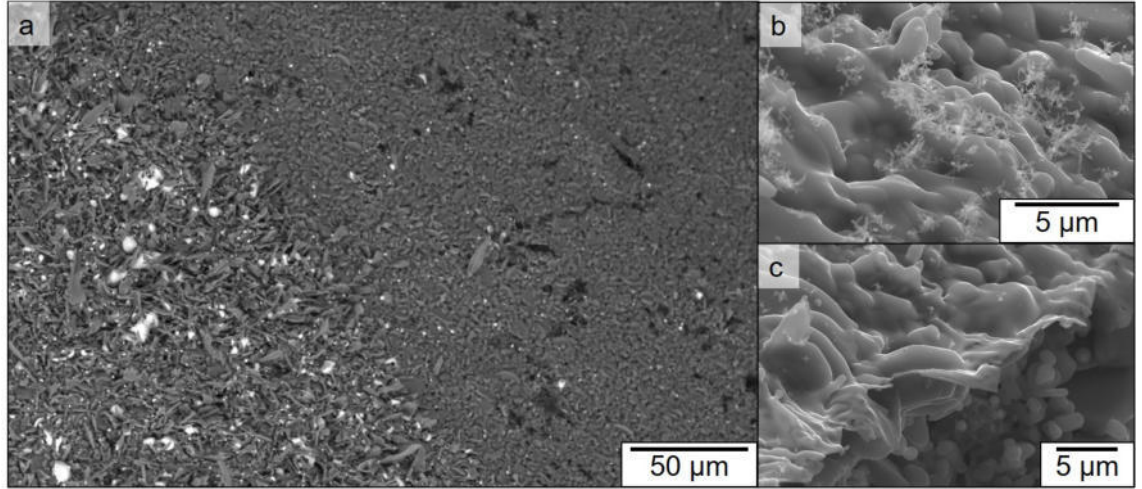


Figure 4.25.: Microstructure of a filter with coating AC after 30 s immersion by SEM: top view on the secondary crystals covering the filter surface, BSE-mode: bright spots - iron-based phase. b) top view clusters on in-situ formed layer, SE-mode, and c) cross-section of the in-situ formed layer, coating underneath, SE-mode.

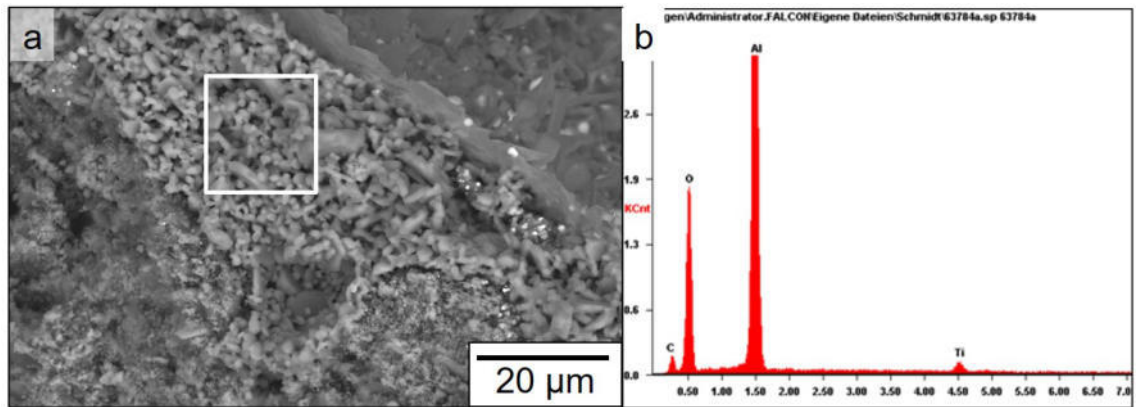


Figure 4.26.: Microstructure of a filter with coating AC-T after 30 s immersion by SEM and EDS. Investigated areas are highlighted by the box in the figure on the left and result in the peaks presented on the right of the AC-T coating. Characterisation of the in-situ layer, secondary Al_2O_3 , and iron-based beads on the filter surface are shown in Figure 4.8 on page 75.

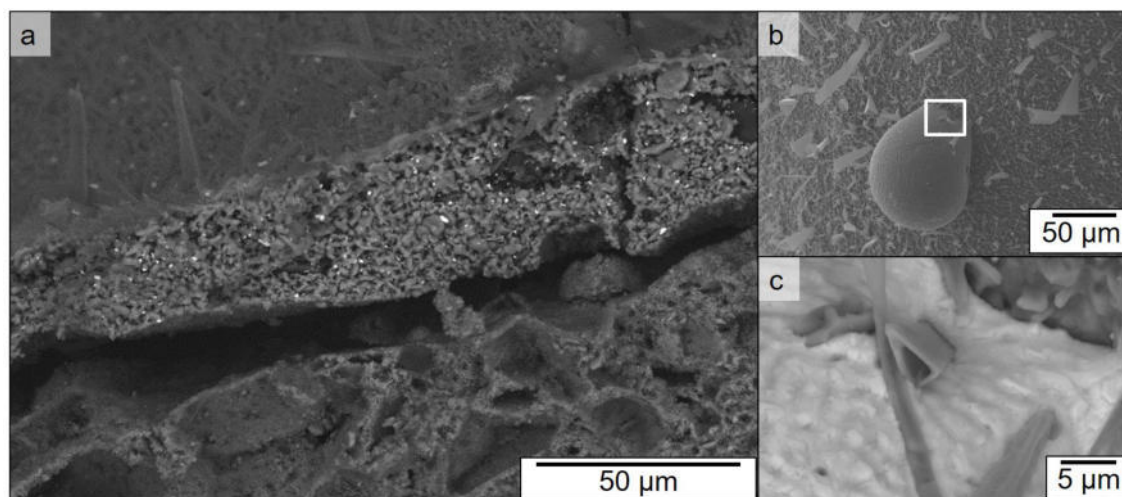


Figure 4.27.: Microstructure of a filter with coating AC-Z after 30 s immersion by SEM: a) cross-section of the $\text{Al}_2\text{O}_3\text{-C}$ substrate, AC-Z coating, in-situ formed layer with secondary crystals (bottom to top), BSE-mode; b) top view of remaining steel bead with secondary crystals growing through (Detailed view of the box in c)), b) SE-mode and c) BSE-mode.

are shown in Figure 4.8 on page 75. After the immersion test, there is still titanium in the coating, cf. Figure 4.26. The thin, in-situ formed layer on the coating should consist of alumina as implied by the EDS analysis. This layer was about 200 nm thick. An analysis of the secondary crystals indicated that they consisted of alumina with traces of manganese and iron. Their length ranged from 5 μm to 15 μm . Smaller clustered particles were observed on these crystals. An EDS analysis of a remaining iron-based bead showed the usual elements of this steel grade: iron, manganese and chromium. Additionally sulphur, aluminium and oxygen are detected. The remaining steel beads seemed to be connected to the secondary crystals, indicating joint phase formation.

Compared to the AC-T coated filter, the coating containing alumina, zirconia and carbon (AC-Z) showed distinct longer crystals, mainly in the shape of needles or funnels. Their length were in the range of 30 μm to 50 μm . Bright spots between the alumina grains of the coating contained zirconium. It was observed here and also in other samples that iron-containing beads were found on carbon particles either within the coating or at the carbon-bonded substrate underneath. As Figure 4.27b and Figure 4.27c illustrate, the crystals even spike remaining steel droplets at the filter surface. No clusters were observed in the area under investigation.

The filter with the AC-ZT revealed a mixture of the two just described samples. The crystal length on the surface laid between AC-T and AC-Z with a length in the

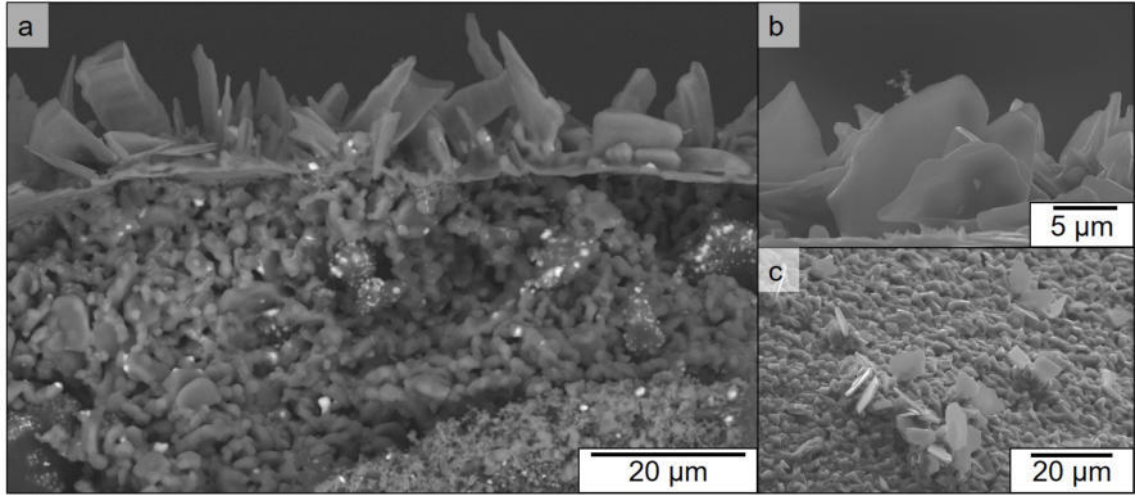


Figure 4.28.: Microstructure of a filter with coating AC-ZT after 30 s immersion by SEM: a) cross-section of the $\text{Al}_2\text{O}_3\text{--C}$ substrate, AC-ZT coating, in-situ formed layer with secondary crystals (bottom to top), BSE-mode; b) side view secondary crystals and cluster, BSE-mode; c) top view on filter surface, SE-mode.

range of $10\text{ }\mu\text{m}$ to $20\text{ }\mu\text{m}$. These crystals were mainly platelike (Figure 4.28), and seldom small clusters were attached on them (Figure 4.28b.) Again, iron-based beads were attached on the carbon particles of the coating. The coating still contained Ti- and/or Zr-rich phases (bright spots under BSE-mode as discussed for sample AC-Z).

4.6.2. Steel characterisation

Table 4.10 presents the parameters of the immersion tests and summarises how the parameters varied due to the experimental set-up. It was found that at 1580°C the melt viscosity was too high for a successful sample taking in the cases of immersing filter samples A, AC and AC-T. Thus no steel samples were tried to be obtained from the residual immersion trials. In these cases, the target temperature have been kept quite constant during the dwell time. Overall, the variation of the process parameters was in an usual and acceptable range. In the case of the three trials with failed sample taking attempts, the oxygen situation might have been altered due to the silica containing samplers, as described by Fruhstorfer et al. [Fru+18].

Table 4.11 is an extract with relevant results of the chemical analysis by spark optical emission spectrometer, which is presented completely in the appendix (Table C.1). Immersing a filter did not lead to significant changes of the main alloying elements (Si, Mn, Cr, Mo): with regard to them, the steel still meets the specification for 42CrMo4 as prescribed by the standard DIN EN ISO 683-2:2018-09 [DINb].

4. Results and Discussion

Table 4.10.: Parameters during immersion trials with titania and/or zirconia doping of the coating. The logged oxygen content (a_O) and the temperature (T) of the melt were measured before (bI) and after immersing (aI) a filter. Thereby, a positive temperature difference (ΔT) describes an increase in temperature between both measurements points. The time between these two measurements (Δt) is listed.

filter type	a_O (ppm)		ratio	T (°C)		ΔT (K)	Δt (min)
	bI	aI		bI	aI		
without filter	9.0	6.9	0.8	1598	1588	-10	15.9*
uncoated	27.8	22.1	0.8	1578	1598	20	9.8
A	10.0	15.2	1.5	1584	1548	-36	23.1 [†]
AC	6.3	8.7	1.4	1574	1598	24	23.8 [†]
AC-T	7.0	13.9	2.0	1592	1546	-46	22.0 [†]
AC-Z	5.6	4.9	0.9	1576	1577	1	24.1
AC-ZT	7.3	8.4	1.1	1578	1585	7	9.7

* time between start and end of the dwell time.

[†] including taking a steel samples before and after immsering the filter.

The titanium content was too low to detect significant changes if they were present. The remelting itself resulted in a drop of the aluminium content: 0.029 mass% of the "as received" sample to 0.018 mass% after remelting. Immersing a filter lowered the content further: lowest values of around 0.008 mass% were observed after immersing the uncoated filter and alumina coated one. After immersing the AC-T coated filter, the aluminium content was on the same level as of the remelted sample, after immersing the AC-Z, the content was even slightly higher. The samples of immersing AC and coating containing alumina, zirconia, titania and carbon (AC-ZT) were in between with contents around 0.014 mass%.

Table 4.12 summarizes the inclusions detected using the Aspex-SEM and classified by chemical class. The sample "without filter" refers to a steel sample that was remelted, but no filter immersed. Instead, that steel batch was cooled down after a dwell time of 15 min. The chemical classes "Dirt", "Fe-oxide" and "Fe-scratches" were excluded from the following evaluation as they arose rather from sample preparation than from the experiment itself. Negligible numbers of Ti-N, Al-Mn-Mg-Fe-Ca-silicate, SiO₂, and CaO-CaS type inclusions were identified in the steel samples. A few MnO-MnS type inclusions were observed, which is owed to the very low sulphur content of that steel. As an side effect, the as received sam-

Table 4.11.: Chemical composition of the steel before and after the immersion tests. Sample "without filter": a dwell time of 15 min.

Element	composition (mass%)										max. standard deviation
	as		without		immersed filter type						
	received	filter	uncoated	A	AC	AC-T	AC-Z	AC-ZT			
Fe	97.32	97.32	97.35	97.44	97.40	97.4	97.36	97.27		0.088	
C	0.394	0.354	0.365	0.343	0.340	0.361	0.369	0.374		0.012	
Si	0.230	0.231	0.229	0.229	0.231	0.236	0.234	0.239		0.011	
Mn	0.691	0.698	0.672	0.653	0.665	0.648	0.666	0.696		0.027	
Cr	0.947	1.002	0.997	0.953	0.973	0.956	0.972	1.007		0.035	
Mo	0.169	0.168	0.178	0.167	0.175	0.174	0.173	0.182		0.014	
Al	0.029	0.018	0.008	0.009	0.015	0.017	0.021	0.014		0.001	
Ti	0.0031	0.0033	0.0034	0.0029	0.0032	0.0033	0.0032	0.0036		0.0004	

ple¹³ exemplified how the remelting process altered the kind of detected inclusions: before remelting, the main amount of detected inclusion were sorted in category CaO-CaS and after remelting in Al₂O₃. Thereby, the size distribution of the CaO-CaS categorised inclusions follow the same pattern as the alumina inclusions of the just remelted sample, i.e. the major inclusions size was 1 μm^2 to 3 μm^2 . It is assumed that during remelting the former as CaO-CaS inclusions categorised NMIs were transformed to such that were categorised as Al₂O₃ type NMIs, e.g. by reactions with alumina from the crucible or dissolved aluminium from the melt. For that reason, the inclusion size of category CaO-CaS is presented in Table 4.13 for the as received steel sample and the following discussion of remaining inclusions focuses on the ones of the Al₂O₃ class in case of the remelted steel samples with or without immersing a filter. Immersing the filters resulted usually in coarsening of the detected alumina inclusions: The major amount of inclusions sized 1 μm^2 to 3 μm^2 for the remelted steel sample, and drifted up to 10 μm^2 to 20 μm^2 if a filter was immersed. Based on the detected alumina inclusions in the steel samples, only if the filter with the titania doped coating was immersed, the inclusions remained small (major inclusions size 1 μm^2 to 3 μm^2). Immersing the uncoated filter resulted in a broad distribution of the alumina inclusion size. In addition, it resulted in the highest amount of large inclusions, i.e. the strongest coarsening and contamination, followed by the steel sample with the alumina coated filter immersed. Only in the case of the AC-T coated filter, the total area of alumina inclusions was decreased compared to the remelting trial without immersing a filter, despite the fact that the total number of inclusions was higher. Thereby, it can be seen from Table 4.13 that the alumina inclusions were bimodally distributed in the case of the remelted steel sample, with major inclusion size of the categories 1 μm^2 to 3 μm^2 and 10 μm^2 to 20 μm^2 , whereas the inclusions of the steel sample with AC-T coated filter immersed were monomodal distributed with a major inclusion size in category 1 μm^2 to 3 μm^2 .

4.6.3. Discussion

By microstructural analysis, no accelerated sintering of the alumina grains of the coating due to the addition of titania was observed. Considering the relatively low temperature of the heat treatment (1400 °C) and the reducing atmosphere, this is not a surprise. It is in line with the study of McKee and Aleshin [MA63] who reported no further densification of Ti-doped alumina under hydrogen atmosphere. Same reasons apply for the lack of new phases examined by XRD. In the unlikely event that

¹³Not discussed in the previous section due to the fact that the pretreatment (oxidation-deoxidation steps) will completely change the inclusion situation.

Table 4.12.: Number of inclusions remaining in solidified steel after immersion tests of the AZT-test series, classified by their chemistry (according to Table 3.5).

Chemical class	Number of Inclusions*							
	as		without		type of filter immersed			
	received	filter†	uncoated	A	AC	AC-T	AC-Z	AC-ZT
Al ₂ O ₃	16	143	303	259	171	322	169	176
Ti-N	15	2	5	6	10	7	12	6
Al-Mn-Mg-Fe-Ca-silicate	0	0	0	0	0	0	0	1
SiO ₂	8	1	2	1	3	2	5	1
MnO-MnS	0	33	19	24	32	39	47	36
CaO-CaS	221	2	1	3	2	3	4	2
Dirt	9	26	49	75	32	59	59	42
FeO-oxide	1007	573	165	336	694	688	464	554
FeO-scratches	61	346	708	379	1237	357	2207	431
Other	203	101	115	104	150	95	231	127

* Normalized to 100 mm² of search area.

† 15 min dwell time.

Table 4.13.: Inclusions of the class "Al₂O₃" remaining in solidified steel after the immersion tests of the AZT-test series, classified by size. Size class contains $x < 20\%$, $20\% \leq x < 25\%$ or $x \geq 25\%$ of the total amount of Al₂O₃ inclusions.

filter type	Number of Inclusions*												Total area of Inclusions [†] (10 ³ μm ²)
	size class: particle area (μm ²)												
	0.1 – 1	1 - 3	3 - 5	5 - 10	10 – 20	20 - 30	30 - 50	50 – 80	80 - 130	130 - 200	200 - 500		
immersed													
as received [‡]	51	58	38	43	22	4	3	1	0	0	0	221	1.3
remelted [◊]	20	36	14	18	31	19	4	0	0	0	0	143	1.5
uncoated	19	50	28	49	56	36	42	20	3	0	0	303	5.7
A	18	47	26	52	73	29	11	1	1	1	0	259	3.3
AC	1	18	17	37	55	28	10	4	1	1	0	171	2.8
AC-T	53	109	54	30	8	4	2	1	0	0	0	322	1.0
AC-Z	8	25	25	41	48	14	5	2	0	0	0	169	2.0
AC-ZT	14	35	27	38	45	13	2	2	0	0	0	176	1.7

* Normalized to 100 mm² of search area.

[†] Calculated from the sum of the products resulting from multiplying the average value of each size class and the corresponding number of alumina inclusions.

[‡] NMIs of category CaO-CaS.

[◊] 15 min dwell time.

4. Results and Discussion

any aluminium titanates and/or zirconates formed during the heat treatment, they probably decomposed due to the reducing atmosphere as discussed by Naghizadeh et al. [NRG09] and Fruhstorfer et al. [Fru+16a]. Despite that, a positive effect of the $\text{ZrO}_2/\text{TiO}_2$ -doping of the coating on its thermal shock behaviour was qualitatively observed in the present study.

Remarkable is the decreased area of alumina inclusions in the solidified steel if the AC-T filter was immersed. Usually, immersing filters caused larger alumina inclusions, probably due to cluster formation, but in the case of AC-T, the alumina inclusions remained as small as of the just remelted steel sample. As mentioned above, titania of the coating might have been partially reduced by dissolved carbon or aluminium of the melt. Both reducing agents should have been available in high concentrations at the interface of filter and melt due to interfacial reactions described by Zienert et al. [Zie+15] and Schmidt et al. [Sch+17a]. In that case, locally high titanium concentrations are expected, which lower the surface tension of the melt. [Kee88; MZZ06] A decreased surface tension will result in an increased wetting of alumina [MZZ06]. Dorrer et al. [Dor+19] observed the formation of different kinds of alumina-titanate inclusions of sizes between $1\text{ }\mu\text{m}$ to $3\text{ }\mu\text{m}$ in Ti-stabilized ultra low carbon steels depending on the Ti/Al-ratios. They explained their findings with the potential of titanium to change the morphology of alumina inclusions. The data obtained by automatic SEM/EDS presented here did not indicate a pronounced formation of such inclusions. Nevertheless, the wetting of the melt on the AC-T coated filter was obviously changed in comparison with the TiO_2 -free coated filter, which is in line with results reported by Dubberstein et al. [Dub+11]. An increased wetting should be beneficial for interfacial reactions by providing a larger contact area between filter and melt. Further, if the surface tension of the melt is decreased, less oxygen is required for a certain aluminium content to nucleate alumina inclusions according to Yang et al. [Yan+13], and the driving force of cluster formation of alumina inclusions, i.e. to reduce the surface in contact with the melt, might be reduced, too. [Sin74] That implicates that if the surface tension is lowered due to e.g. the addition of titanium, alumina inclusions form easier. If they form easier, they consume available oxygen in proximity, which explains why they kept small. This should result in more, but smaller alumina inclusions.

In contrast, it is estimated from the amount of applied coating material that a maximum of about 1.8 ppm titanium would be added to the whole steel melt if all titania of the coating would be dissolved homogeneously. As titanium was still detected within the coating after immersion by EDS, that was not the case. That raises the question if this amount was sufficient to cause the observed alumina inclusion modification. The impact of the varying process parameters of the trials as

4. Results and Discussion

reason for the differences in the detected alumina inclusions as discussed in Schmidt et al. [Sch+17a], seems less in the frame of the increased amount of tested samples presented here: despite the fact that the process parameters of the trials with filters A and AC-T were similar, the amount, size distribution and total area of the alumina inclusions differ distinctly, cf. Table 4.13.

Despite that, SEM indicated an enhanced deposition of endogenous alumina inclusions on the AC-coated filter compared with the AC-T coated one. That might be due to following reasons: 1) partially dissolved titanium decreased the surface tension of the steel melt and therewith less alumina inclusions were deposited due to a decreased driving force to coagulate, and 2) the added titania modified grain growth of alumina structures deposited on the filter surface and enhanced sintering of deposits with already existing alumina particles in such a way that deposited alumina inclusions could not be distinguished anymore from the alumina crystal structures as in the case of the titania-free coated filter sample. 3) From that, it has to be considered if the clusters observed on the filter surface are really endogenous inclusions from the melt (they appear here occasionally despite no pretreatment to generate them was applied) or if they simply nucleated during the immersion trials in the liquid oxide film.

The addition of zirconia to the coating did not result in such distinct influences of the alumina-NMIs situation and in combination with titania the positive effect of the single titania doping became smaller. As strong oxidiser, the interactions should be similar to alumina: An almost inert behaviour is expected and a small amount of zirconia might be dissolved too, which would lead to the formation and precipitation of zirconia as soon as oxygen is available either as dissolved element or by reducing less stable oxides, similar to the reactions with alumina. Also the literature did not indicate a contribution of zirconia to the deposition of alumina-based NMIs. [Tsu+94; Sve+18] Thereby, the reactivity of the stabilisation agents, like lime, has to be considered, e.g. regarding liquid phase formation, which influences attraction forces towards NMI. [Tsu+94; Sal+18] But here, unstabilised, highly pure zirconia was used. Nevertheless, the extensive crystallisation of the secondary alumina on the surface of the ZrO_2 -doped filter sample is remarkable. As stable oxide, zirconia seemed to have accelerated the formation of secondary alumina by providing nucleation sides.

In combination of both dopants, XRD indicated the formation of titania zirconates, which might reduce the ability of titanium to dissolve and therewith the change of the wetting to the liquid steel.

A decarburised zone as obvious in Figure 4.23a, was not found on all samples, e.g. AC-T and AC-Z. Or not as pronounced as for the uncoated sample. Similar

findings were reported by Bock et al. [Boc+19] investigating carbon-bonded alumina filters coated with different coatings of the system Fe-Mg-Mn-Al-O-C in contact with molten steel. These immersion tests were performed in line with the procedure described in Section 3.3 on page 59, i.e. including the pretreatment of the steel. They stated no change of the underlying carbon-bonded substrate after 10 s immersion and did not observe any cluster on the filter surface. Despite that, they found the typical layer build-up on the filter surface consisting of an in-situ formed layer, secondary crystals and steel beads, as well as steel remaining in the macro-porosity of the filters. Interestingly, they found the most and largest secondary crystals on a filter coated with an 1:1 mixture of FeO- and MnO-aluminate. The MgAl_2O_4 coated filter showed the smallest amount of secondary crystals. If it is really the case that the underlying, carbon-bonded substrate material was not distinctly involved in the interactions of these filters, then it might be the case that the catalytic effect of iron oxide (cf. the discussion of Rzehak in Section 2.2.2) and manganese oxide (might behave similar to iron oxide) in combination with the carbon provided by the coating are sufficient to trigger the alumina dissolution and precipitation processes. Thereby, Fe-Mn-O spinels might have acted as oxygen buffer. [KM79b] These spinels can be reduced by either dissolved carbon or aluminium of the melt. The interactions might even be speeded up in such a way that very early a diffusion barrier towards the underlying substrate material is built up so fast that its contribution is negligible compared to the alumina-based coated filters described before. Carbon from the coating material might have been sufficient to trigger the dissolution processes of the coating material, as assumed by Salomon [Sal19].

4.6.4. Summary: Influence of the titania and/or zirconia doping of the coating.

All tested filters withstood the immersion tests in molten steel (1580 °C). Despite only the formation of zirconia titanates was detected by XRD in sample AC-ZT, qualitatively all three doped coatings showed an improved thermal shock behaviour in comparison to the doping-free coatings on the immersed filters. In the case of the zirconia addition (2.5 mass%), a coarsening of the alumina inclusions detected in the solidified steel sample was observed, as was the case for the non-doped coated filters A and AC. The addition of titania (2.5 mass%), on the other hand, enhanced wetting of the filter by the steel melt in comparison to the titania-free coated ones. After immersing the AC-T filter, alumina inclusions of the steel melt were modified: they were more in number, but distinctly smaller compared to trials without filter and/or the immersion of the other ones. Partially dissolved titanium from the coating has

4. Results and Discussion

the potential to lower the surface tension of the steel melt and therewith the contact angle on alumina. Thereby, interfacial reactions might have been supported. A combination of zirconia and titania (each 2.5 mass%) did not show that influence on the alumina inclusion. Probably, the formation of zirconia titanates prevented titanium from dissolution.

Especially the decreased average area of the alumina inclusions remaining in the steel is interesting because the particle size of inclusions strongly influences the fatigue life of a steel product. According to Seleznev et al. [Sel+20], an increased maximum size of inclusions, especially plate-like alumina, decreases the fatigue toughness. The deformability of a steel product, however, is determined by the amount of non-metallic inclusions. Thus, the modification of alumina inclusions by adding titania to the filter coating might present a way to tailor these inclusions depending on the product's application.

It was found that the hypothesis formulated in the previous section regarding the interactions and formation mechanism could have been applied to explain the observed results with Ti and/or Zr-doped alumina based coated filters.

5. Conclusion and Outlook

In this thesis, the time dependent interactions between Al_2O_3 -C filter, which were coated with a porous alumina based coating, and molten 42CrMo4 steel have been investigated as these considerations have not been done so far to the authors knowledge.

The here presented results imply that carbon of the carbon-bonded alumina substrate took part in the filter-steel interactions, which could have been only possible due to the coatings porosity (cf. Figure 4.21 on page 105). An iron-rich fluid passed the alumina coating by the pores, too, without leaving a trace that could have been detected post-mortem. Only when carbon is reached, subsequent reactions resulted in metallic iron-rich beads at the surface of the carbon-bonded substrate and carbon particles of the carbonaceous alumina coating. Whether they are the start of the carbon diffusion towards the filter-steel interface (e.g. as $\text{CO}_{(\text{g})}$) or if carbon diffused itself ($\text{C}_{(\text{s})}$), cannot be answered yet. The presence of dissolved carbon at the filter-steel melt interface is essential to promote the alumina dissolution and precipitation processes [PT94; Poi15; Zie+15; Sal19]. Thereby, the melt was locally supersaturated with aluminium, which reacted with dissolved oxygen to form secondary corundum. During these interactions, a liquid oxide layer was formed directly at the ceramic surface and provided nano-crystalline nuclei for heterogeneous nucleation of secondary corundum. This layer solidified amorphous after the immersion during cooling with a thickness of about 100 nm to 200 nm—independently from the investigated coatings [Emm14; Sto18; Dud+14; Sch+17a; Boc+19] and immersion times. Despite a clear phase assignment was not possible, reasonable phases are hercynite, magnetite or γ -alumina according to Salomon [Sal19, p. 137–138]. Storti et al. [SBA18] found α - Al_2O_3 by EBSD, and detected mainly iron, oxygen and aluminium by EDS.

Due to the presence of bubbles acting as nuclei, e.g. in the open porosity of the filter, dissolved carbon and oxygen were able to react and form $\text{CO}_{(\text{g})}$. In the meantime, dissolved aluminium could either reduce aforementioned less stable oxides at the interface or react with dissolved oxygen of the melt to form secondary alumina at the filter-melt interface. It cannot be excluded that deposited endogenous inclusions from the steel melt served as nuclei, too. Due to their heterogeneous nucleation, the

5. Conclusion and Outlook

secondary corundum crystals did not adopt the orientation of the alumina grains of the coating. By forming a dense layer, the growth of secondary corundum impeded its own formation because the carbon supply of the underlying substrate was cut off. As they grow due to ongoing redox-reactions during cooling, metallic iron-rich beads remain between the secondary alumina crystals.

It is reasonable to assume that a liquid oxide layer formed at the ceramic–steel melt interface at the process temperatures (1580 °C to 1650 °C). That liquid oxide film included oxides resulting from oxidation of elements of the steel melt as well as oxides originating from impurities of the refractory material. Such a layer might have covered the filter struts inhomogeneously, e.g. be more pronounced at impurity accumulations of the coating. Additionally, its thickness and the resulting formation and growth of secondary inclusions should be influenced by the melt flow passing by as the speed of the melt flow influences diffusion processes.[Zie+20] Further, local turbulences might have entrained such a liquid oxide film. The composition is determined by the ongoing redox-reactions and in the case of the immersed filters should be determined by the available carbon, aluminium and oxygen supply. Thereby spinel solid solutions with manganese and/or chromium can act as oxygen buffer.[KM79a; KM79b]

From the available data, it was not possible to draw conclusions about the amount of alumina in the built-up layers, only about the morphology. Nor it is known up to now to what extent the observed layer build-up on the filter surface originates from the alumina filter, e.g. by dissolution and precipitation reactions with the melt, or from deposited inclusions.[Sch+17a; Zie+15; Fru+18] Thus, limited conclusions about the deposition of inclusions can be drawn from the filter surface itself, which is why the examination of the solidified steel is essential to draw conclusions regarding the filtration effect.

The lowest amount of inclusions remaining in the solidified steel was observed when the filters were immersed for 10 s, i.e. the lowest immersion period under investigation, which is in line with the observations of Storti.[Sto18, p. 77] Despite the addition of carbon accelerated the formation of secondary corundum, these interactions seem to hinder a positive filtration performance of the filters. The formation of a liquid oxide film, which not only should decrease attraction forces towards solid NMIs of the melt, as in the case of an liquid calcium aluminate phase presented by Tsujino et al. [Tsu+94], but also have the potential to create NMIs by entrainment of that oxide film, is therefore treated as negative impact on the filtration performance.

During the first two experimental trials, it became obvious that the thermal shock resistance of the alumina coating has to be enhanced, despite it was slightly improved by the carbon addition. For such, a material combination, which has not been

5. Conclusion and Outlook

investigated as coating material up to now and is known for its excellent thermal shock resistance, was tested: alumina-zirconia-titania (AZT) in the ratio 95:2.5:2.5. Thereby, the influence of zirconia or titania with alumina was investigated. The observed thermoshock behaviour of the doped coatings was indeed suitable. Interestingly, the addition of titania enhanced wetting of the filter by the steel melt in comparison to the titania-free coated ones. Partially dissolved titanium from the coating has the potential to lower the surface tension of the steel melt and therewith the contact angle on alumina. Thereby, interfacial reactions might have been supported. As a result, alumina inclusions of the steel melt were modified: they were more in number, but distinctly smaller compared to trials without filter and/or the immersion of the other filter types. Especially, the decreased average area of the alumina inclusions is interesting because the particle size of inclusions strongly influences the fatigue life of a steel product. According to Seleznev et al. [Sel+20], an increased maximum size of inclusions, especially plate-like alumina, decreases the fatigue toughness. The deformability of a steel product, however, is determined by the amount of non-metallic inclusions. Thus, the modification of alumina inclusions by adding titania to the filter coating might present a way to tailor these inclusions depending on the product's application.

What are the implications of the hypothesis formulated here for steel melt filtration? To eliminate the risk of contaminating the steel melt with NMIs resulting from the formation of the liquid oxide layer at the filter surface there are following possibilities how to deal with it: a) Avoiding the formation of such a layer because a liquid film usually reduced the attraction force towards solid NMIs in the melt. That might be achieved, for example, by applying a denser coating, as suggested by Gehre et al. [Geh+18] and, thereby, cutting off the carbon-supply. In such cases, impurities of the coating material which form liquid oxide phases at the process temperatures should be avoided at all costs. b) Providing a material combination at the filter surface which result in a suitable liquid oxide phase composition that benefit the precipitation and dissolution of NMIs as known from slag utilization in the steelmaking process. Nevertheless, it has to be pointed out that all alumina-based coated filters contributed to the filtration of especially alumina-based NMIs, and outperformed the uncoated carbon-bonded alumina filter.

Unsurprisingly, the here presented investigations leave some open question and tasks which could not have been answered within the scope of this theses. Up to now, the formation of the iron based droplets is not clear. Did they form from a liquid, as discussed by Sillo [Sil91], or a gaseous phase, as assumed by Dudczig et al. [Dud+14] and Zienert et al. [Zie+15]? How is their formation influenced by an oxide layer? A detailed characterisation of these metallic beads might enlighten

5. Conclusion and Outlook

their formation process. Unluckily, they could not have been successfully prepared for combined EDS and EBSD characterisation here.

Further, the formation of secondary alumina at the interface result in the question if the observed alumina particles attached on the filter surface are a result of the interactions, therewith the dissolving alumina of the filter material, or from elements and inclusions of the melt, which would result in the desired decrease of alumina based inclusions. Future investigation might tackle this question by introducing a tracer element or by using another deoxidation agent, which is no component of the immersed filter or typical inclusions of the melt, to distinguish at least between the generated endogenous inclusions by deoxidation (pretreatment of the steel) and the secondary crystals resulting from the dissolution and precipitation processes of the filter material. Another interesting aspect—especially for the industrial application—is the service life of such coatings, which is worth to be considered in future investigations. Last, but not least, as the here presented filter types for immersion tests were a kind of prove-of-concept, the slurries were not completely optimised within this work. Nevertheless, there is an optimization potential regarding the impact of the porosity or coating thickness on the filtration performance.

Bibliography

- [21] *GESTIS Substance Database*. 1.02.2021. URL: <https://www.gestis-database.dguv.de/data?name=001780>.
- [AAM85] S. Ali, D. Apelian, and R. Mutharasan. “Refining of aluminium and steel melts by the use of multi-cellular extruded ceramic filters”. In: *Canadian Metallurgical Quarterly* 24.4 (1985), pp. 311–318.
- [AAS19] Amjad Asad, Christos G. Aneziris, and Rüdiger Schwarze. “Numerical Investigation of Filtration Influenced by Microscale CO Bubbles in Steel Melt”. In: *Advanced Engineering Materials* 4 (2019), p. 1900591. DOI: 10.1002/adem.201900591.
- [ACS18] Amjad Asad, Kinnor Chattopadhyay, and Rüdiger Schwarze. “Effect of Turbulence Modeling on the Melt Flow and Inclusions Transport in a Steel Filtration Experiment”. In: *Metallurgical Transactions B* 49.5 (2018), pp. 2270–2277. ISSN: 0360-2141. DOI: 10.1007/s11663-018-1343-3.
- [All08] M. Allibert, ed. *Slag atlas*. 2. ed., Repr. without change. Düsseldorf: Verl. Stahleisen, 2008. ISBN: 3-514-00457-9.
- [AMA85] D. Apelian, R. Mutharasan, and S. Ali. “Removal of inclusions from steel melts by filtration”. In: *Journal of Materials Science* 20.10 (1985), pp. 3501–3514. ISSN: 0022-2461. DOI: 10.1007/BF01113756.
- [Ane+07] Christos G. Aneziris et al. “Functional Refractory Material Design for Advanced Thermal Shock Performance Due to Titania Additions”. In: *International Journal of Applied Ceramic Technology* 4.6 (2007), pp. 481–489. ISSN: 1546542X. DOI: 10.1111/j.1744-7402.2007.02174.x.
- [Ane+08] Christos G. Aneziris et al. “Verfahren zur Herstellung eines thermoschock- und korrosionsbeständigen Keramikwerkstoffes auf der Basis eines zirkondioxidfreien feuerfesten Oxides”. DE 102005036394 B4. 2008.

- [Ane+10] Christos G. Aneziris et al. “Thermal Shock Performance of Fine Grained Al₂O₃ Ceramics With TiO₂ and ZrO₂ Additions for Refractory Applications”. In: *Advanced Engineering Materials* 12.6 (2010), pp. 478–485. ISSN: 14381656. DOI: 10.1002/adem.201000037.
- [Ane+13a] Christos G. Aneziris et al. “Alumina coatings on carbon bonded alumina nozzles for active filtration of steel melts”. In: *Ceramics International* 39.3 (2013), pp. 2835–2843. ISSN: 02728842. DOI: 10.1016/j.ceramint.2012.09.055.
- [Ane+13b] Christos G. Aneziris et al. “In situ observation of collision between exogenous and endogenous inclusions on steel melts for active steel filtration”. In: *Metallurgical and Materials Transactions B: Process Metallurgy and Materials Processing Science* 44.4 (2013), pp. 954–968. DOI: 10.1007/s11663-013-9828-6.
- [Ane+13c] Christos G. Aneziris et al. “Interactions between exogenous spinel inclusions with endogenous inclusions in a steel melt”. In: *Advanced Engineering Materials* 15.12 (2013), pp. 1168–1176. DOI: 10.1002/adem.201300155.
- [Ane+13d] Christos G. Aneziris et al. “Reactive Filters for Steel Melt Filtration”. In: *Advanced Engineering Materials* 15.1-2 (2013), pp. 46–59. ISSN: 14381656. DOI: 10.1002/adem.201200199.
- [Arn+15] M.-O. Arnold et al. *Stahlguss: Herstellung - Eigenschaften - Anwendungen*. 2015. URL: <https://www.kug.bdguss.de/publikationen-normen-und-richtlinien/publikationen/#c1193>.
- [Asa+16] Amjad Asad et al. “Numerical study of particle filtration in an induction crucible furnace”. In: *International Journal of Heat and Fluid Flow* 62 (2016), pp. 299–312. ISSN: 0142727X. DOI: 10.1016/j.ijheatfluidflow.2016.10.002.
- [Asa+17] Amjad Asad et al. “Numerical Modeling of Flow Conditions during Steel Filtration Experiments”. In: *Advanced Engineering Materials* 19.9 (2017), p. 1700085. DOI: 10.1002/adem.201700085.
- [Asa+18] Amjad Asad et al. “Numerical Assessment of a Filtration Experiment Influenced by Microscale Carbon Monoxide Bubbles Arising in Steel Melt”. In: *JOM* 70.12 (2018), pp. 2927–2933. ISSN: 1047-4838. DOI: 10.1007/s11837-018-3117-4.

- [ASK21] ASK Chemicals. *UDICELL-Filter*. 2.02.2021. URL: <https://www.ask-chemicals.com/de/giessereiloesungen/produkte/filter-fuer-giessereianwendungen/udicell-filter>.
- [Asł+19] M. Asłanowicz et al. “Ceramic-Carbon Filters for Molten Metal Alloys Filtration”. In: (2019). DOI: 10.24425/AFE.2019.127101.
- [ASU07] Christos G. Aneziris, Wolfgang Schärfl, and B. Ullrich. “Microstructure evaluation of Al₂O₃ ceramics with Mg-PSZ- and TiO₂-additions”. In: *Journal of the European Ceramic Society* 27.10 (2007), pp. 3191–3199. ISSN: 09552219. DOI: 10.1016/j.jeurceramsoc.2007.01.006.
- [Bal+11] Efthymios Balomenos et al. “Carbothermic Reduction of Alumina: A Review of Developed Processes and Novel Concepts”. In: *Proceedings / EMC 2011, European Metallurgical Conference*. Ed. by Jens Harre. Clausthal-Zellerfeld: GDMB, 2011, pp. 729–744. ISBN: 9783940276414.
- [BCG04] Somnath Basu, Shiv Kumar Choudhary, and Narendra U. Girase. “Nozzle Clogging Behaviour of Ti-bearing Al-killed Ultra Low Carbon Steel”. In: *ISIJ International* 44.10 (2004), pp. 1653–1660. ISSN: 0915-1559. DOI: 10.2355/isijinternational.44.1653.
- [Bec81] Paul F. Becher. “Transient Thermal Stress Behavior in ZrO₂-Toughened Al₂O₃”. In: *Journal of the American Ceramic Society* 64.1 (1981), pp. 37–39. ISSN: 0002-7820. DOI: 10.1111/j.1151-2916.1981.tb09555.x.
- [BGB88] A. Bettinelli, J. Guille, and J. C. Bernier. “Densification of alumina at 1400°C”. In: *Ceramics International* 14.1 (1988), pp. 31–34. DOI: 10.1016/0272-8842(88)90015-6.
- [Bir16] Jean-Pierre Birat. “Steel cleanliness and environmental metallurgy”. In: *Metallurgical Research & Technology* 113.2 (2016), p. 201. ISSN: 2271-3646. DOI: 10.1051/metal/2015050.
- [BM18] Wolfgang Bleck and Elvira Moeller. *Handbuch Stahl: Auswahl, Verarbeitung, Anwendung*. München: Carl Hanser Verlag GmbH & Co. KG, 2018. ISBN: 978-3-446-44961-9. DOI: 10.3139/9783446449626.
- [Boc+19] Benjamin Bock et al. “Impact of spinel forming systems (Fe-/Mg-/Mn-Al-O) as functional coating materials for carbon-bonded alumina filters on steel melt filtration”. In: *Ceramics International* 45.4 (2019), pp. 4499–4508. DOI: 10.1016/j.ceramint.2018.11.131.

Bibliography

- [Bon+94] L. Bonhomme-Courty et al. “Preparation of $\text{Al}_2\text{TiO}_5\text{-ZrO}_2$ mixed powders via sol-gel process”. In: *Journal of Sol-Gel Science and Technology* 2.1-3 (1994), pp. 371–375. ISSN: 0928-0707. DOI: 10.1007/BF00486273.
- [CB78] J. J. Cleveland and R. C. Bradt. “Grain Size/Microcracking Relations for Pseudobrookite Oxides”. In: *Journal of the American Ceramic Society* 61.11-12 (1978), pp. 478–481. ISSN: 00027820. DOI: 10.1111/j.1151-2916.1978.tb16121.x.
- [Cha81] Manas Chanda. “Phases and Phase Transformation in Iron-Carbon System”. In: *Science of engineering materials*. Ed. by Manas Chanda. London: Macmillan, 1981, pp. 65–101. ISBN: 978-0-333-31816-4.
- [Cos18] André Luiz Vasconcellos da Costa e Silva. “Non-metallic inclusions in steels – origin and control”. In: *Journal of Materials Research and Technology* 7.3 (2018), pp. 283–299. ISSN: 22387854. DOI: 10.1016/j.jmrt.2018.04.003.
- [Dan02] C. A. Daniels. *Ceramics: Structure and properties*. Washington D. C.: Abyss Books, 2002. ISBN: 0-9713404-0-4.
- [DBW03] R. Dekkers, Bart Blanpain, and Patrick Wollants. “Crystal growth in liquid steel during secondary metallurgy”. In: *Metallurgical and Materials Transactions B* 34.2 (2003), pp. 161–171. ISSN: 1073-5615. DOI: 10.1007/s11663-003-0003-3.
- [Dek+13] R. Dekkers et al. “Non-metallic inclusions in aluminium killed steels”. In: *Ironmaking & Steelmaking* 29.6 (2013), pp. 437–444. ISSN: 0301-9233. DOI: 10.1179/030192302225004584.
- [DINa] DIN-Normenausschuss Eisen und Stahl. *DIN EN 10020:2000-07, Begriffsbestimmung für die Einteilung der Stähle*. Berlin.
- [DINb] DIN-Normenausschuss Eisen und Stahl. *DIN EN ISO 683-2:2018-09, Für eine Wärmebehandlung bestimmte Stähle, legierte Stähle und Automatenstähle Teil_2: Legierte Vergütungsstähle (ISO_683-2:2016); Deutsche Fassung EN_ISO_683-2:2018*. Berlin. DOI: 10.31030/2862242.
- [DINc] DIN-Normenausschuss Materialprüfung. *DIN EN 10247:2017-09, Metallographische Prüfung des Gehaltes nichtmetallischer Einschlüsse in Stählen mit Bildreihen; Deutsche Fassung EN_10247:2017*. Berlin. DOI: 10.31030/2690587.

- [Dit+17] Lisa Ditscherlein et al. “Impact of the Roughness of Alumina and Al₂O₃-C Substrates on the Adhesion Mechanisms in a Model System”. In: *Advanced Engineering Materials* 19.9 (2017), p. 1700088. DOI: 10.1002/adem.201700088.
- [Dor+19] Philipp Dorrer et al. “Study on the Influence of FeTi-Addition on the Inclusion Population in Ti-Stabilized ULC Steels and Its Consequences for SEN-Clogging”. In: *Steel Research International* 105 (2019), p. 1800635. ISSN: 16113683. DOI: 10.1002/srin.201800635.
- [Dra21] Drache GmbH. *Schaumkeramikfilter im Stahlguss, Superlegierungsguss - Drache GmbH*. 2.02.2021. URL: <https://www.drache-gmbh.de/cerazirk-zro2-filter.html>.
- [Dub+11] T. Dubberstein et al. “Some Thermophysical Properties of Liquid Cr-Mn-Ni-Steels”. In: *Steel Research International* 82.9 (2011), pp. 1122–1128. ISSN: 16113683. DOI: 10.1002/srin.201100096.
- [Dud+12] Steffen Dudczig et al. “Nano- and micrometre additions of SiO₂, ZrO₂ and TiO₂ in fine grained alumina refractory ceramics for improved thermal shock performance”. In: *Ceramics International* 38.3 (2012), pp. 2011–2019. DOI: 10.1016/j.ceramint.2011.10.036.
- [Dud+13] Steffen Dudczig et al. “Application of Oxide Coatings for Improved Steel Filtration with the Aid of a Metal Casting Simulator”. In: *Advanced Engineering Materials* 15.12 (2013), pp. 1177–1187. DOI: 10.1002/adem.201300121.
- [Dud+14] S. Dudczig et al. “Characterization of carbon-bonded alumina filters with active or reactive coatings in a steel casting simulator”. In: *Ceramics International* 40.10 (2014), pp. 16727–16742. DOI: 10.1016/j.ceramint.2014.08.038.
- [Dud19] Steffen Dudczig. *Metallic fume SCS: personal conversation*. Ed. by Anne Schmidt. 6.10.2019.
- [EA12] Marcus Emmel and Christos G. Aneziris. “Development of novel carbon bonded filter compositions for steel melt filtration”. In: *Ceramics International* 38.6 (2012), pp. 5165–5173. DOI: 10.1016/j.ceramint.2012.03.022.
- [EA13] Marcus Emmel and Christos G. Aneziris. “Functionalization of carbon-bonded alumina filters through the application of active oxide coatings for steel melt filtration”. In: *Journal of Materials Research* 28.17 (2013), pp. 2234–2242. DOI: 10.1557/jmr.2013.56.

- [EB09] Iván Egry and Jürgen Brillo. “Surface Tension and Density of Liquid Metallic Alloys Measured by Electromagnetic Levitation †”. In: *Journal of Chemical & Engineering Data* 54.9 (2009), pp. 2347–2352. ISSN: 0021-9568. DOI: 10.1021/jc900119n.
- [Egr+10] I. Egry et al. “Surface tension of liquid metals and alloys—recent developments”. In: *Advances in colloid and interface science* 159.2 (2010), pp. 198–212. DOI: 10.1016/j.cis.2010.06.009.
- [Ell] Ellingham Diagrams. *Ellingham diagram*. URL: http://web.mit.edu/2.813/www/readings/Ellingham_diagrams.pdf.
- [Ell+91] D. B. Ellson et al. “The Oxidation Behaviour of Alumina-Graphite Carbon Bonded Refractories”. In: *Materials Science Forum* 34-36 (1991), pp. 731–734. ISSN: 1662-9752. DOI: 10.4028/www.scientific.net/MSF.34-36.731.
- [Ell44] H. J. T. Ellingham. “Reducibility of oxides and sulphides in metallurgical processes”. In: *Journal of the Society of Chemical Industry* 63.5 (1944), pp. 125–133. ISSN: 03684075. DOI: 10.1002/jctb.5000630501.
- [Emm+13] Marcus Emmel et al. “Influence of the chemistry of surface functionalized ceramic foam filters on the filtration of alumina inclusions in steel melts”. In: *Advanced Engineering Materials* 15.12 (2013), pp. 1188–1196. DOI: 10.1002/adem.201300118.
- [Emm+14] Marcus Emmel et al. “In situ spinel formation in Al₂O₃–MgO–C filter materials for steel melt filtration”. In: *Ceramics International* 40.8 (2014), pp. 13507–13513. ISSN: 02728842. DOI: 10.1016/j.ceramint.2014.05.033.
- [Emm14] Marcus Emmel. “Development of active and reactive carbon bonded filter materials for steel melt filtration”. Dissertation. Freiberg, Germany: TU Bergakademie Freiberg, 2014.
- [FLH56] L. M. FOSTER, G. LONG, and M. S. HUNTER. “Reactions Between Aluminum Oxide and Carbon The Al₂O₃–Al₄C₃ Phase Diagram”. In: *Journal of the American Ceramic Society* 39.1 (1956), pp. 1–11. ISSN: 00027820. DOI: 10.1111/j.1151-2916.1956.tb15588.x.
- [FM87] Bernhard Freudenberg and Alain Mocellin. “Aluminum titanate formation by solid-state reaction of fine Al₂O₃ and TiO₂ powders”. In: *Journal of the American Ceramic Society* 70.1 (1987), pp. 33–38. ISSN: 00027820.

- [FP14] Jörg Fritzsche and Urs Alexander Peuker. “Particle adhesion on highly rough hydrophobic surfaces: The distribution of interaction mechanisms”. In: *Colloids and Surfaces A: Physicochemical and Engineering Aspects* 459 (2014), pp. 166–171. ISSN: 09277757. DOI: 10.1016/j.colsurfa.2014.07.002.
- [FP15] Jörg Fritzsche and Urs Alexander Peuker. “Wetting and Adhesive Forces on Rough Surfaces – An Experimental and Theoretical Study”. In: *Procedia Engineering* 102 (2015), pp. 45–53. ISSN: 18777058. DOI: 10.1016/j.proeng.2015.01.105.
- [FP16] Jörg Fritzsche and Urs Alexander Peuker. “Modeling adhesive force distributions on highly rough surfaces”. In: *Powder Technology* 289 (2016), pp. 88–94. ISSN: 00325910. DOI: 10.1016/j.powtec.2015.11.057.
- [Fru+15] Jens Fruhstorfer et al. “Microstructure and strength of fused high alumina materials with 2.5wt% zirconia and 2.5wt% titania additions for refractory applications”. In: *Ceramics International* 41.9 (2015), pp. 10644–10653. DOI: 10.1016/j.ceramint.2015.04.164.
- [Fru+16a] Jens Fruhstorfer et al. “Corrosion of Carbon Free and Bonded Refractories for Application in Steel Ingot Casting”. In: *steel research international* 87.8 (2016), pp. 1014–1023. ISSN: 16113683. DOI: 10.1002/srin.201600023.
- [Fru+16b] Jens Fruhstorfer et al. “Erosion and corrosion of alumina refractory by ingot casting steels”. In: *Journal of the European Ceramic Society* 36.5 (2016), pp. 1299–1306. DOI: 10.1016/j.jeurceramsoc.2015.11.038.
- [Fru+18] Jens Fruhstorfer et al. “Interface Analyses Between a Case-Hardened Ingot Casting Steel and Carbon-Containing and Carbon-Free Refractories”. In: *Metallurgical and Materials Transactions B* 49.3 (2018), pp. 1499–1521. ISSN: 1073-5615. DOI: 10.1007/s11663-018-1216-9.
- [Fru74] R. J. Fruehan. “The effect of zirconium, cerium, and lanthanum on the solubility of oxygen in liquid iron”. In: *Metallurgical Transactions* 5.2 (1974), pp. 345–347. ISSN: 0360-2133. DOI: 10.1007/BF02644100.
- [FSA14] Jens Fruhstorfer, Stefan Schafföner, and Christos G. Aneziris. “Dry ball mixing and deagglomeration of alumina and zirconia composite fine powders using a bimodal ball size distribution”. In: *Ceramics International* 40.9, Part B (2014), pp. 15293–15302. DOI: 10.1016/j.ceramint.2014.07.027.

- [Geh+18] Patrick Gehre et al. “Interaction of slip- and flame-spray coated carbon-bonded alumina filters with steel melts”. In: *Journal of the American Ceramic Society* 20 (2018), p. 3501. ISSN: 00027820. DOI: 10.1111/jace.15431.
- [Gle+18] Johannes Gleinig et al. “Characterization of Nonmetallic Inclusions in 18CrNiMo7-6”. In: *Metallurgical and Materials Transactions B* 213 (2018), p. 427. ISSN: 1073-5615. DOI: 10.1007/s11663-018-1431-4.
- [Har45] Fritz Hartmann. “Die Bewegung von Schlacketeilchen im flüssigen Stahl”. In: *Stahl und Eisen* 65.3/4 (1945), pp. 29–36.
- [HC06] M. Heyrman and C. Chatillon. “Thermodynamics of the Al–C–O Ternary System”. In: *Journal of The Electrochemical Society* 153.7 (2006), E119. ISSN: 00134651. DOI: 10.1149/1.2203091.
- [Her+19a] Andreas Herdering et al. “Additive manufactured polyamide foams with periodic grid as templates for the production of functional coated carbon-bonded alumina foam filters”. In: *Ceramics International* 45.1 (2019), pp. 153–159. ISSN: 02728842. DOI: 10.1016/j.ceramint.2018.09.146.
- [Her+19b] Andreas Herdering et al. “Additive Manufactured Polymer Foams as Templates for Customized Ceramic Foams - Comparison of SLS and FFF Techniques”. In: *Interceram - International Ceramic Review* 68.4 (2019), pp. 30–37. ISSN: 0020-5214. DOI: 10.1007/s42411-019-0013-z.
- [HES12] M. Halmann, M. Epstein, and Aldo Steinfeld. “Vacuum Carbothermic Reduction of Bauxite Components: A Thermodynamic Study”. In: *Mineral Processing and Extractive Metallurgy Review* 33.3 (2012), pp. 190–203. ISSN: 0882-7508. DOI: 10.1080/08827508.2011.562950.
- [HFP15] Fabian Heuzeroth, Jörg Fritzsche, and Urs Alexander Peuker. “Wetting and its influence on the filtration ability of ceramic foam filters”. In: *Particuology* 18 (2015), pp. 50–57. ISSN: 16742001. DOI: 10.1016/j.partic.2014.06.001.
- [HFS07] M. Halmann, A. Frei, and Aldo Steinfeld. “Carbothermal reduction of alumina: Thermochemical equilibrium calculations and experimental investigation”. In: *Energy* 32.12 (2007), pp. 2420–2427. ISSN: 03605442. DOI: 10.1016/j.energy.2007.06.002.

- [Him+18] C. Himcinschi et al. “Innovative carbon-bonded filters based on a new environmental-friendly binder system for steel melt filtration”. In: *Journal of the European Ceramic Society* 38.16 (2018), pp. 5580–5589. DOI: 10.1016/j.jeurceramsoc.2018.08.029.
- [Hna+16] M. Hnatko et al. “Corrosion of engineering ceramic materials by molten iron Part II: Alumina”. In: *Corrosion Science* 109 (2016), pp. 230–237. ISSN: 0010938X. DOI: 10.1016/j.corsci.2016.04.007.
- [Hol+13] Lauri Holappa et al. “Active Tundish Slag”. In: *steel research international* 84.7 (2013), pp. 638–648. ISSN: 16113683. DOI: 10.1002/srin.201200209.
- [HS11] Dorian A. H. Hanaor and Charles C. Sorrell. “Review of the anatase to rutile phase transformation”. In: *Journal of Materials Science* 46.4 (2011), pp. 855–874. ISSN: 0022-2461. DOI: 10.1007/s10853-010-5113-0.
- [Ikr+14] M. Ikram-ul-Haq et al. “A Novel X-ray Micro-diffraction Approach for Structural Characterization of Trace Quantities of Secondary Phases in Al₂O₃-C/Fe System”. In: *Metallurgical and Materials Transactions B* 45.6 (2014), pp. 1970–1973. ISSN: 1073-5615. DOI: 10.1007/s11663-014-0201-1.
- [ISF17] M. Ilatovskaia, G. Savinykh, and O. Fabrichnaya. “Thermodynamic description of the ZrO₂-TiO₂-Al₂O₃ system based on experimental data”. In: *Journal of the European Ceramic Society* 37.10 (2017), pp. 3461–3469. ISSN: 09552219. DOI: 10.1016/j.jeurceramsoc.2017.03.064.
- [IWA+70] Nobuya IWAMOTO et al. “Study on Phase Diagram of Fe-Cr-O System”. In: *Tetsu-to-Hagane* 56.6 (1970), pp. 727–733. ISSN: 0021-1575. DOI: 10.2355/tetsutohagane1955.56.6{\textunderscore}727.
- [Jan+18a] Ondřej Jankovský et al. “Nano-functionalization of carbon-bonded alumina using graphene oxide and MWCNTs”. In: *Journal of the European Ceramic Society* 38.14 (2018), pp. 4732–4738. DOI: 10.1016/j.jeurceramsoc.2018.04.068.
- [Jan+18b] Ondřej Jankovský et al. “Unique wettability phenomenon of carbon-bonded alumina with advanced nanocoating”. In: *Applied Materials Today* 13 (2018), pp. 24–31. ISSN: 23529407. DOI: 10.1016/j.apmt.2018.08.002.

- [Jan13a] Krystian Janiszewski. “Industrial application of liquid steel filtration out of dispersed nonmetallic phase in the continuous casting machine”. In: *Metallurgija* 52.1 (2013), pp. 71–74.
- [Jan13b] Krystian Janiszewski. “Refining of liquid steel in a tundish using the method of filtration during its casting in the CC machine”. In: *Archives of Metallurgy and Materials* 58.2 (2013), pp. 513–521.
- [Jan13c] Krystian Janiszewski. “The slenderness ratio of the filter used in the process of liquid steel filtration as the additional parameter of the filter form”. In: *Steel Research International* 84.3 (2013), pp. 288–296. ISSN: 16113683. DOI: 10.1002/srin.201200077.
- [JKC09] Woo-Gwang Jung, Oh-Duck Kwon, and Mun-Kyu Cho. “Nozzle Clogging Mechanism in Continuous Casting for Titanium-Containing Steel”. In: *Korean Journal of Materials Research* 19.9 (2009), pp. 473–480. ISSN: 1225-0562. DOI: 10.3740/MRSK.2009.19.9.473.
- [Jor+19] Pedro Jorge et al. “Characterization of laminar flow in periodic open-cell porous structures”. In: *Chemical Engineering Science* 201 (2019), pp. 397–412. ISSN: 00092509. DOI: 10.1016/j.ces.2019.02.010.
- [Jun+04] In-Ho Jung et al. “Thermodynamic evaluation and optimization of the MnO-Al₂O₃ and MnO-Al₂O₃-SiO₂ systems and applications to inclusion engineering”. In: *Metallurgical and Materials Transactions B* 35.2 (2004), pp. 259–268. ISSN: 1073-5615. DOI: 10.1007/s11663-004-0027-3.
- [Kap03] Era Kapilashrami. “Investigation of interactions between liquid iron containing oxygen and aluminosilicate refractories”. PhD Thesis. Stockholm, Sweden: KTH Royal Institute of Technology, 2003.
- [Kar+14] A. Karwiński et al. “The Use of Innovative Ceramic-Carbon Bonded Filters Used for Filtration of Liquid Alloys and Evaluation of the Filtration Efficiency”. In: *Archives of Foundry Engineering* 14.3 (2014), pp. 29–32. DOI: 10.2478/afe-2014-0056.
- [KB13] C. Klinger and D. Bettge. “Axle fracture of an ICE3 high speed train”. In: *Engineering Failure Analysis* 35 (2013), pp. 66–81. DOI: 10.1016/j.engfailanal.2012.11.008.
- [Kee+86] B. J. Keene et al. “Comparison of surface tension measurements using the levitated droplet method”. In: *Metallurgical Transactions B* 17.1 (1986), pp. 159–162. ISSN: 0360-2141. DOI: 10.1007/BF02670828.

Bibliography

- [Kee88] B. J. Keene. “Review of data for the surface tension of iron and its binary alloys”. In: *International Materials Reviews* 33.1 (1988), pp. 1–37. ISSN: 0950-6608. DOI: 10.1179/imr.1988.33.1.1.
- [KG08] Ik Jin Kim and Ludwig J. Gauckler. “Excellent thermal shock resistant materials with low thermal expansion coefficients”. In: *Journal of Ceramic Processing Research* 9.3 (2008), pp. 240–245. ISSN: 1229-9162. URL: http://jcpr.kbs-lab.co.kr/thesis/online_2.php?cate_idx=6&sub_cate_idx=25.
- [KG12] Ik Jin Kim and Ludwig J. Gauckler. “Formation, Decomposition and Thermal Stability of Al₂TiO₅ Ceramics: Review”. In: *Journal of Ceramic Science and Technology* 3.2 (2012), pp. 49–60. URL: <http://www.ceramic-science.com>.
- [Kha+11] R. Khanna et al. “Chemical Interactions of Alumina–Carbon Refractories with Molten Steel at 1823 K (1550 °C): Implications for Refractory Degradation and Steel Quality”. In: *Metallurgical and Materials Transactions B* 42.4 (2011), pp. 677–684. ISSN: 1073-5615. DOI: 10.1007/s11663-011-9520-7.
- [Kha+12] Rita Khanna et al. “Carbothermic Reduction of Alumina at 1823 K in the Presence of Molten Steel: A Sessile Drop Investigation”. In: *ISIJ International* 52.6 (2012), pp. 992–999. ISSN: 0915-1559. DOI: 10.2355/isijinternational.52.992.
- [Kha+16] Rita Khanna et al. “Carbothermic Reduction of Alumina at 1823 K: On the Role of Molten Iron and Reaction Mechanisms”. In: *ISIJ International* 56.7 (2016), pp. 1300–1302. ISSN: 0915-1559. DOI: 10.2355/isijinternational.ISIJINT-2016-037.
- [Kim+14] Dami Kim et al. “Mechanical Properties of Al₂TiO₅ Ceramics for High Temperature Application”. In: *Current Nanoscience* 10.1 (2014), pp. 154–158. ISSN: 15734137. DOI: 10.2174/1573413709666131109005.
- [Kim10] Ik Jin Kim. “Thermal stability of Al₂TiO₅ ceramics for new diesel particulate filter applications-a literature review”. In: *Journal of Ceramic Processing Research* 11.4 (2010), pp. 411–418. ISSN: 1229-9162. URL: http://jcpr.kbs-lab.co.kr/thesis/online_2.php?cate_idx=4&sub_cate_idx=20.
- [KM79a] C. K. Kim and A. McLean. “Thermodynamics of iron alumino-chromite spinel inclusions in steel”. In: *Metallurgical Transactions B* 10.4 (1979), pp. 585–594. ISSN: 0360-2141. DOI: 10.1007/BF02662561.

- [KM79b] C. K. Kim and A. McLean. “Thermodynamics of iron-manganese aluminate spinel inclusions in steel”. In: *Metallurgical Transactions B* 10.4 (1979), pp. 575–584. ISSN: 0360-2141. DOI: 10.1007/BF02662560.
- [KMK84] Makoto Kishimoto, Katsumi Mori, and Yasuji Kawai. “Surface Tension of Liquid Fe-Ti and Fe-C-Ti Systems under H₂ Atmosphere”. In: *Journal of the Japan Institute of Metals* 48.4 (1984), pp. 413–417. ISSN: 0021-4876. DOI: 10.2320/jinstmet1952.48.4\textundersco413.
- [Kon+90] A. S. Kondrat’ev et al. “Possibilities of filter-refining of metals and the required characteristics of the filter elements: A review”. In: *Refractories* 31.7 (1990), pp. 384–391. DOI: 10.1007/BF01281545.
- [Kre+15] Dominik Krewerth et al. “Application of full-surface view in situ thermography measurements during ultrasonic fatigue of cast steel G42CrMo4”. In: *International Journal of Fatigue* 80 (2015), pp. 459–467. ISSN: 0142-1123. DOI: 10.1016/j.ijfatigue.2015.07.013.
- [KS05] E. Kapilashrami and Seshadri Seetharaman. “Wetting characteristics of oxygen-containing iron melts on refractory oxides”. In: *Journal of Materials Science* 40.9-10 (2005), pp. 2371–2375. ISSN: 0022-2461. DOI: 10.1007/s10853-005-1961-4.
- [Lee+01] S. H. Lee et al. “Separation and dissolution of Al₂O₃ inclusions at slag/metal interfaces”. In: *Journal of Non-Crystalline Solids* 282.1 (2001), pp. 41–48. ISSN: 00223093. DOI: 10.1016/S0022-3093(01)00327-1.
- [Lee+13] Young Seok Lee et al. “Morphologies of Alumina Nano- and Microparticles at the Fe/Al₂O₃ Interface and the Effects of Reaction Time and Substrate Roughness on Size Distribution”. In: *ISIJ International* 53.3 (2013), pp. 547–549. ISSN: 0915-1559. DOI: 10.2355/isijinternational.53.547.
- [Li+11] Jiuqiang Li et al. “Low-temperature Synthesis of Aluminium Carbide”. In: *ISIJ International* 51.6 (2011), pp. 870–877. ISSN: 0915-1559. DOI: 10.2355/isijinternational.51.870.
- [Lip+14] B. Lipowska et al. “Cast steel filtration trials using ceramic-carbon filters”. In: *Archives of Foundry Engineering* 14.4 (2014), pp. 61–66.
- [Liu+19] Yu Liu et al. “A Review of Physical and Numerical Approaches for the Study of Gas Stirring in Ladle Metallurgy”. In: *Metallurgical and Materials Transactions B* 50.1 (2019), pp. 555–577. ISSN: 1073-5615. DOI: 10.1007/s11663-018-1446-x.

- [LTT93] P. Lefort, D. Tetard, and P. Tristant. “Formation of aluminium carbide by carbothermal reduction of alumina: Role of the gaseous aluminium phase”. In: *Journal of the European Ceramic Society* 12.2 (1993), pp. 123–129. ISSN: 09552219. DOI: 10.1016/0955-2219(93)90132-B.
- [Luc+18] B. Luchini et al. “Carbon-bonded alumina foam filters produced by centrifugation: A route towards improved homogeneity”. In: *Ceramics International* 44.12 (2018), pp. 13832–13840. DOI: 10.1016/j.ceramint.2018.04.228.
- [MA63] William Dean McKEE and Eugene Aleshin. “Aluminum Oxide-Titanium Oxide Solid Solution”. In: *Journal of the American Ceramic Society* 46.1 (1963), pp. 54–58. ISSN: 0002-7820. DOI: 10.1111/j.1151-2916.1963.tb13771.x.
- [Mir+90] Pilar Miranzo et al. “Effect of Sintering Atmosphere on the Densification and Electrical Properties of Alumina”. In: *Journal of the American Ceramic Society* 73.7 (1990), pp. 2119–2121. ISSN: 0002-7820. DOI: 10.1111/j.1151-2916.1990.tb05282.x.
- [Miz+13] Toshiaki Mizoguchi et al. “Influence of Unstable Non-equilibrium Liquid Iron Oxide on Clustering of Alumina Particles in Steel”. In: *ISIJ International* 53.4 (2013), pp. 639–647. ISSN: 0915-1559. DOI: 10.2355/isijinternational.53.639.
- [Moh+16] Mahdi Mohammadi-Ghaleni et al. “Comparison of CFD Simulations with Experimental Measurements of Nozzle Clogging in Continuous Casting of Steels”. In: *Metallurgical and Materials Transactions B* 47.6 (2016), pp. 3384–3393. ISSN: 1073-5615. DOI: 10.1007/s11663-016-0798-3.
- [Mor03] Eric Morgan. “Analyzing steel alloy filtration”. In: *Modern Casting* 93.9 (2003), pp. 42–45.
- [Mor87] R. Morrell. *Handbook of Properties of Technical and Engineering Ceramics. Part 2: Data Reviews. Section I: High-Alumina Ceramics*. Handbook of properties of technical & engineering ceramics Data reviews. London: H.M.S.O, 1987. ISBN: 0114800537.
- [MZZ06] Kusuhiro Mukai, Liangcai Zhong, and Masafumi Zeze. “Interfacial Properties of Molten Low Carbon Steel Containing Ti, Nb or B in Relation to the Behavior of Fine Particles in Continuous Casting Process”. In:

- ISIJ International* 46.12 (2006), pp. 1810–1816. ISSN: 0915-1559. DOI: 10.2355/isijinternational.46.1810.
- [NF72] V. I. Nizhenko and L. I. Floka. “Effect of carbon on the surface properties of liquid iron”. In: *Soviet Powder Metallurgy and Metal Ceramics* 11.10 (1972), pp. 819–823. ISSN: 0038-5735. DOI: 10.1007/BF00844707.
- [NPS10] Yoon-Chae Nah, Indhumati Paramasivam, and Patrik Schmuki. “Doped TiO₂ and TiO₂ nanotubes: synthesis and applications”. In: *Chemphyschem : a European journal of chemical physics and physical chemistry* 11.13 (2010), pp. 2698–2713. DOI: 10.1002/cphc.201000276.
- [NR15] Dale E. Newbury and Nicholas W. M. Ritchie. “Performing elemental microanalysis with high accuracy and high precision by scanning electron microscopy/silicon drift detector energy-dispersive X-ray spectrometry (SEM/SDD-EDS)”. In: *Journal of Materials Science* 50.2 (2015), pp. 493–518. ISSN: 0022-2461. DOI: 10.1007/s10853-014-8685-2.
- [NRG09] R. Naghizadeh, H. R. Rezaie, and F. Golestani-fard. “The influence of composition, cooling rate and atmosphere on the synthesis and thermal stability of aluminum titanate”. In: *Materials Science and Engineering: B* 157.1-3 (2009), pp. 20–25. ISSN: 09215107. DOI: 10.1016/j.mseb.2008.12.002.
- [NY99] I. A. Novokhatskii and I. V. Yaroshenko. “Cluster adsorption on oxide inclusions in liquid steel”. In: *Materials Science* 35.5 (1999), pp. 657–663. ISSN: 1068-820X. DOI: 10.1007/BF02359352.
- [OM05] Rudolph A. Olson III and Luiz C. B. Martins. “Cellular ceramics in metal filtration”. In: *Advanced Engineering Materials* 7.4 (2005), pp. 187–192. DOI: 10.1002/adem.200500021.
- [ONH87] Yutaka Ohya, Zenbe-e Nakagawa, and Kenya Hamano. “Grain-Boundary Microcracking Due to Thermal Expansion Anisotropy in Aluminum Titanate Ceramics”. In: *Journal of the American Ceramic Society* 70.8 (1987), pp. 184–186. ISSN: 0002-7820. DOI: 10.1111/j.1151-2916.1987.tb05720.x.
- [Pap+97] E. Papin et al. “Point Defects Effect on the Sintering of Alumina”. In: *Key Engineering Materials* 132-136 (1997), pp. 232–235. ISSN: 1662-9795. DOI: 10.4028/www.scientific.net/KEM.132-136.232.

- [Par+18] Hyun Sik Park et al. “A study on the wetting behavior of liquid iron on forsterite, mullite, spinel and quasi-corundum substrates”. In: *Ceramics International* 44.15 (2018), pp. 17585–17591. DOI: 10.1016/j.ceramint.2018.05.226.
- [Par90] Fred J. Parker. “Al₂TiO₅-ZrTiO₄-ZrO₂ Composites: A New Family of Low-Thermal-Expansion Ceramics”. In: *Journal of the American Ceramic Society* 73.4 (1990), pp. 929–932. ISSN: 0002-7820. DOI: 10.1111/j.1151-2916.1990.tb05138.x.
- [PJL06] Jin-Hong Park, In-Ho Jung, and Hae-Geon Lee. “Dissolution Behavior of Al₂O₃ and MgO Inclusions in the CaO–Al₂O₃–SiO₂ Slags: Formation of Ring-like Structure of MgAl₂O₄ and Ca₂SiO₄ around MgO Inclusions”. In: *ISIJ International* 46.11 (2006), pp. 1626–1634. ISSN: 0915-1559. DOI: 10.2355/isijinternational.46.1626.
- [Poi15] Jacques Poirier. “A review: influence of refractories on steel quality”. In: *Metallurgical Research & Technology* 112.4 (2015), p. 410. ISSN: 2271-3646. DOI: 10.1051/metal/2015028.
- [PT94] Jacques Poirier and Bruno Thillou. “Contribution of the Refractory Material of Submerged Nozzles to Clogging: 37th International Colloquium on Refractories, Aachen”. In: *Stahl und Eisen Special* Oct. (1994), pp. 114–118.
- [RBS11] Poulomi Roy, Steffen Berger, and Patrik Schmuki. “TiO₂ nanotubes: synthesis and applications”. In: *Angewandte Chemie (International ed. in English)* 50.13 (2011), pp. 2904–2939. DOI: 10.1002/anie.201001374.
- [RBV14] Bruno Henrique Reis, Wagner Viana Bielefeldt, and Antônio Cezar Faria Vilela. “Absorption of non-metallic inclusions by steelmaking slags—a review”. In: *Journal of Materials Research and Technology* 3.2 (2014), pp. 179–185. ISSN: 22387854. DOI: 10.1016/j.jmrt.2014.03.011.
- [Reg+13a] D. Regonini et al. “A review of growth mechanism, structure and crystallinity of anodized TiO₂ nanotubes”. In: *Materials Science and Engineering: R: Reports* 74.12 (2013), pp. 377–406. ISSN: 0927796X. DOI: 10.1016/j.mser.2013.10.001.
- [Reg+13b] D. Regonini et al. “Electrospun TiO(2) fiber composite photoelectrodes for water splitting”. In: *ACS applied materials & interfaces* 5.22 (2013), pp. 11747–11755. DOI: 10.1021/am403437q.

- [Rha+13] M. A. Rhamdhani et al. “Alternative Al production methods: Part 1 - a review of indirect carbothermal routes”. In: *Mineral Processing and Extractive Metallurgy* 122.2 (2013), pp. 87–104. ISSN: 0371-9553. DOI: 10.1179/1743285513Y.0000000036.
- [Ros60] R. Rosegger. “Use of aluminium in deoxidation”. In: *Iron and Coal Trades Review* 15 (1960), pp. 131–140.
- [RRA04] B. Rand, V. P. S. Ramos, and A. S. Ahmed. “The role of carbon in refractories”. In: *Iranian Journal of Materials Science and Engineering* 1.3 (2004), pp. 9–15. URL: http://ijmse.iust.ac.ir/browse.php?a_code=A-10-1-18&slc_lang=en&sid=1&ftxt=1.
- [RW07] Gerald Routschka and Hartmut Wuthnow, eds. *Taschenbuch Feuerfeste Werkstoffe: Aufbau, Eigenschaften, Prüfung*. 4. Aufl. Essen: Vulkan-Verl., 2007. ISBN: 978-3-8027-3157-0.
- [Rze13] Dominik Rzehak. “Beschleunigte Entkohlung von Stahlschmelzen im Vakuum durch Kombination von Sauerstoff und Metalloxiden”. PhD thesis. Aachen, Germany: RWTH Aachen, 2013.
- [Sal+13] Anton Salomon et al. “Dynamic, in situ generated interfaces between carbon-bonded alumina filters and steel during spark plasma sintering/field-assisted sintering”. In: *Advanced Engineering Materials* 15.12 (2013), pp. 1235–1243. DOI: 10.1002/adem.201300119.
- [Sal+15] Anton Salomon et al. “Reaction mechanism between the carbon bonded magnesia coatings deposited on carbon bonded alumina and a steel melt”. In: *Journal of the European Ceramic Society* 35.2 (2015), pp. 795–802. DOI: 10.1016/j.jeurceramsoc.2014.09.033.
- [Sal+18] Uxia Dieguez Salgado et al. “Fluid Force-Induced Detachment Criteria for Nonmetallic Inclusions Adhered to a Refractory/Molten Steel Interface”. In: *Metallurgical and Materials Transactions B* 49.4 (2018), pp. 1632–1643. ISSN: 1073-5615. DOI: 10.1007/s11663-018-1271-2.
- [Sal+19] Vânia R. Salvini et al. “Innovation in ceramic foam filters manufacturing process”. In: *International Journal of Applied Ceramic Technology* 16.1 (2019), pp. 378–388. DOI: 10.1111/ijac.13062.
- [Sal19] Anton Salomon. “Untersuchung von mittels Spark-Plasma-Sintertechnologie und unter Ausschluss von Strömungseffekten erzeugten Grenzflächen zwischen Metallschmelzen und Filterkeramik”. PhD thesis. Freiberg, Germany: TU Bergakademie Freiberg, 2019.

- [SBA18] Enrico Storti, Harry Berek, and Christos G. Aneziris. “Focused ion beam preparation and microscopy investigation of secondary layer on carbon-bonded alumina filter after steel contact”. In: *Ceramics International* 44.12 (2018), pp. 14502–14509. DOI: 10.1016/j.ceramint.2018.05.065.
- [SC05] Michael Scheffler and Paolo Colombo, eds. *Cellular ceramics: Structure, manufacturing, properties and applications*. Chichester: John Wiley distributor, 2005. ISBN: 3-527-31320-6. DOI: 10.1002/3527606696.
- [Sch+17a] Anne Schmidt et al. “Functionalized Carbon-Bonded Filters with an Open Porous Alumina Coating: Impact of Time on Interactions and Steel Cleanliness”. In: *Advanced Engineering Materials* 19.9 (2017), p. 1700170. DOI: 10.1002/adem.201700170.
- [Sch+17b] Christina Schröder et al. “Interactions between Exogenous Magnesia Inclusions with Endogenous Inclusions in a High Alloyed Steel Melt”. In: *Advanced Engineering Materials* 19.9 (2017), p. 1700146. DOI: 10.1002/adem.201700146.
- [Sch+19] Anne Schmidt et al. “Interactions between Carbon-Bonded Alumina Filters and Molten Steel: Impact of a Titania-Doped Filter Coating”. In: *Advanced Engineering Materials* 45 (2019), p. 1900647. DOI: 10.1002/adem.201900647.
- [Sch92] Klaus Schwerdtfeger, ed. *Metallurgie des Stranggießens: Gießen und Erstarren von Stahl*. Düsseldorf: Verl. Stahleisen, 1992. ISBN: 3514003505.
- [Sel+20] Mikhail Seleznev et al. “Effect of Filter Functional Coating on Detrimental Nonmetallic Inclusions in 42CrMo4 Steel and Its Resulting Mechanical Properties”. In: *Advanced Engineering Materials* 22.2 (2020), p. 1900540. ISSN: 14381656. DOI: 10.1002/adem.201900540.
- [SEP20] SEPR – SAINT-GOBAIN ZIRPRO. *CS zirconia - Technical Data Sheet*. 2020. URL: https://www.zirpro.com/sites/imdf.zirpro.com/files/documents/zirpro-tds-cs_zirconia-zirconium_oxide-202012-e.pdf.
- [Sha16] Mohammad Shamsuddin. *Physical chemistry of metallurgical processes*. Hoboken, New Jersey: John Wiley & Sons Inc, 2016. ISBN: 978-1-119-07832-6.

- [Sil91] Cyrill Eyewu Sillo. “Microstructural and Chemical Studies of Stainless Steel/Refractory Interaction”. In: *Journal of the American Ceramic Society* 74.3 (1991), pp. 541–550. ISSN: 00027820. DOI: 10.1111/j.1151-2916.1991.tb04057.x.
- [Sin74] S. N. Singh. “Mechanism of alumina buildup in tundish nozzles during continuous casting of aluminum-killed steels”. In: *Metallurgical Transactions* 5.10 (1974), pp. 2165–2178. ISSN: 0360-2133. DOI: 10.1007/BF02643930.
- [SMM88] Kaoru Shinme, Tohru MATSUO, and Mitsuyuki Morishige. “Acceleration of nitrogen removal in stainless steel under reduced pressure”. In: *ISIJ International* 28.4 (1988), pp. 297–304. ISSN: 0915-1559. DOI: 10.2355/isijinternational1966.28.297.
- [SS63] Karl Schwartzwalder and Arthur V. Somers. “Method of making porous ceramic articles”. 3,090,094. 1963.
- [SST07] Hermann Salmang, Horst Scholze, and Rainer Telle. *Keramik (German Edition)*. Dordrecht: Springer, 2007. ISBN: 978-3-540-63273-3.
- [Sto+15] Enrico Storti et al. “Development of multi-walled carbon nanotubes-based coatings on carbon-bonded alumina filters for steel melt filtration”. In: *Journal of the European Ceramic Society* 35.5 (2015), pp. 1569–1580. DOI: 10.1016/j.jeurceramsoc.2014.11.026.
- [Sto+16a] Enrico Storti et al. “Functional coatings on carbon-bonded ceramic foam filters for steel melt filtration”. In: *Steel Research International* 86 (2016), n/a–n/a. ISSN: 16113683. DOI: 10.1002/srin.201500446.
- [Sto+16b] Enrico Storti et al. “Short-time performance of MWCNTs-coated Al₂O₃-C filters in a steel melt”. In: *Journal of the European Ceramic Society* 36.3 (2016), pp. 857–866. DOI: 10.1016/j.jeurceramsoc.2015.10.036.
- [Sto+17a] Enrico Storti et al. “Calcium Aluminate Reactive Coatings on Carbon-Bonded Alumina Filters for Clean Steel Approaches”. In: *Steel Research International* 88.11 (2017), p. 1700247. ISSN: 16113683. DOI: 10.1002/srin.201700247.
- [Sto+17b] Enrico Storti et al. “Filter Functionalization with Carbon Nanotubes and Alumina Nanosheets for Advanced Steel Filtration”. In: *steel research international* 88.10 (2017), p. 1700142. ISSN: 16113683. DOI: 10.1002/srin.201700142.

- [Sto+17c] Enrico Storti et al. “Impact of Nanoengineered Surfaces of Carbon-Bonded Alumina Filters on Steel Cleanliness”. In: *Advanced Engineering Materials* 19.9 (2017), p. 1700153. ISSN: 14381656. DOI: 10.1002/adem.201700153.
- [Sto18] Enrico Storti. “Functionalization of carbon-bonded ceramic foam filters with nano-scaled materials for steel melt filtration”. PhD thesis. Freiberg, Germany: TU Bergakademie Freiberg, 2018.
- [Sve+16] J. K. S. Svensson et al. “Studies of new coating materials to prevent clogging of submerged entry nozzle (SEN) during continuous casting of Al killed low carbon steels”. In: *Ironmaking & Steelmaking* (2016), pp. 1–11. ISSN: 0301-9233. DOI: 10.1179/1743281215Y.0000000065.
- [Sve+18] J. K. S. Svensson et al. “Implementation of an YSZ coating material to prevent clogging of the submerged entry nozzle (SEN) during continuous casting of Ce-treated steels”. In: *Ironmaking & Steelmaking* 45.2 (2018), pp. 105–113. ISSN: 0301-9233. DOI: 10.1080/03019233.2016.1245916.
- [TGD63] E. T. Turkdogan, P. Grieveson, and L. S. Darken. “ENHANCEMENT OF DIFFUSION-LIMITED RATES OF VAPORIZATION OF METALS”. In: *The Journal of Physical Chemistry* 67.8 (1963), pp. 1647–1654. ISSN: 0022-3654. DOI: 10.1021/j100802a017.
- [Til91] G. Tilloca. “Thermal stabilization of aluminium titanate and properties of aluminium titanate solid solutions”. In: *Journal of Materials Science* 26.10 (1991), pp. 2809–2814. ISSN: 0022-2461. DOI: 10.1007/BF00545574.
- [TSP05] Robert B. Tuttle, Jeffrey D. Smith, and Kent D. Peaslee. “Interaction of alumina inclusions in steel with calcium-containing materials”. In: *Metallurgical Transactions B* 36.6 (2005), pp. 885–892. ISSN: 0360-2141. DOI: 10.1007/s11663-005-0090-4.
- [Tsu+94] Ryoji Tsujino et al. “Mechanism of Deposition of Inclusion and Metal in ZrO₂-CaO-C Immersion Nozzle of Continuous Casting”. In: *ISIJ International* 34.11 (1994), pp. 853–858. ISSN: 0915-1559. DOI: 10.2355/isijinternational.34.853.
- [Tur96] E. T. Turkdogan. *Fundamentals of steelmaking*. Vol. 614. Book / The Institute of Materials. London: The Institute of Materials, 1996. ISBN: 0901716804.

- [ves21] vesuvius Corporate Website. *Filtrations- und Gießsysteme*. 2.02.2021. URL: <https://www.vesuvius.com/en/our-solutions/de-de/foundry/steel-foundry/filtration-and-gating-systems.html>.
- [VH14] U. Voigt and L. R. Horvath. “Rohrförmige Hochleistungsfilter in Schaumkeramik für die Gießereiindustrie: High performance tubular foam ceramic filters for the foundry industry”. In: *Giesserei-Praxis* 11 (2014), pp. 494–502.
- [Voi+19] Claudia Voigt et al. “Impact of the Filter Roughness on the Filtration Efficiency for Aluminum Melt Filtration”. In: *Light Metals 2019*. Ed. by Corleen Chesonis. Vol. 41. The Minerals, Metals & Materials Series. Cham: Springer International Publishing, 2019, pp. 1063–1069. ISBN: 978-3-030-05863-0. DOI: 10.1007/978-3-030-05864-7{\textunderscore}130.
- [VP94] P. Virro-Nic and J. Pilling. “Thermal expansion and microstructures of melted Al₂O₃-ZrO₂-TiO₂ ceramics”. In: *Journal of Materials Science Letters* 13.13 (1994), pp. 950–954. ISSN: 0261-8028. DOI: 10.1007/BF00701434.
- [VSS06] Martin Valdez, George S. Shannon, and Seetharaman Sridhar. “The Ability of Slags to Absorb Solid Oxide Inclusions”. In: *ISIJ International* 46.3 (2006), pp. 450–457. ISSN: 0915-1559. DOI: 10.2355/isijinternational.46.450.
- [Wan+16] L. J. Wang et al. “Some Aspects of Interfacial Phenomena in Steel-making and Refining”. In: *Metallurgical and Materials Transactions B* 47.4 (2016), pp. 2107–2113. ISSN: 1073-5615. DOI: 10.1007/s11663-016-0631-z.
- [Wer+17] Eric Werzner et al. “Influence of Foam Morphology on Effective Properties Related to Metal Melt Filtration”. In: *Advanced Engineering Materials* 19.9 (2017), p. 1700240. ISSN: 14381656. DOI: 10.1002/adem.201700240.
- [Wet+18] Tony Wetzig et al. “Application of exchangeable carbon-bonded alumina foam filters in an industrial tundish for the continuous casting of steel”. In: *Ceramics International* (2018). DOI: 10.1016/j.ceramint.2018.09.105.
- [Yan+13] Wen Yang et al. “Nucleation, Growth, and Aggregation of Alumina Inclusions in Steel”. In: *JOM* 65.9 (2013), pp. 1173–1180. ISSN: 1047-4838. DOI: 10.1007/s11837-013-0687-z.

- [Yan+15] Wen Yang et al. "Population Evolution of Oxide Inclusions in Ti-stabilized Ultra-low Carbon Steels after Deoxidation". In: *Journal of Iron and Steel Research International* 22.12 (2015), pp. 1069–1077. ISSN: 1006-706X. DOI: 10.1016/S1006-706X(15)30114-X.
- [Yan+18] Wen Yan et al. "Wettability phenomena of molten steel in contact with alumina substrates with alumina and alumina-carbon coatings". In: *Journal of the European Ceramic Society* 38.4 (2018), pp. 2164–2178. DOI: 10.1016/j.jeurceramsoc.2017.12.001.
- [Yin+97a] Hongbin Yin et al. "'In-situ' Observation of Collision, Agglomeration and Cluster Formation of Alumina Inclusion Particles on Steel Melts". In: *ISIJ International* 37.10 (1997), pp. 936–945. ISSN: 0915-1559. DOI: 10.2355/isijinternational.37.936.
- [Yin+97b] Hongbin Yin et al. "Characteristics of Agglomeration of Various Inclusion Particles on Molten Steel Surface". In: *ISIJ International* 37.10 (1997), pp. 946–955. ISSN: 0915-1559. DOI: 10.2355/isijinternational.37.946.
- [YZY96] Akira Yamaguchi, Shaowei Zhang, and Jingkun Yu. "Effect of Refractory Oxides on the Oxidation of Graphite and Amorphous Carbon". In: *Journal of the American Ceramic Society* 79.9 (1996), pp. 2509–2511. ISSN: 0002-7820. DOI: 10.1111/j.1151-2916.1996.tb09009.x.
- [ZF15] Tilo Zienert and Olga Fabrichnaya. "Interface reactions between steel 42CrMo4 and mullite". In: *Journal of the European Ceramic Society* 35.4 (2015), pp. 1317–1326. ISSN: 09552219. DOI: 10.1016/j.jeurceramsoc.2014.10.033.
- [Zha+06] Lifeng Zhang et al. "Large Inclusions in Plain-carbon Steel Ingots Cast by Bottom Teeming". In: *ISIJ International* 46.5 (2006), pp. 670–679. ISSN: 0915-1559. DOI: 10.2355/isijinternational.46.670.
- [Zha+18] Tongsheng Zhang et al. "Transient Behavior and Thermodynamics of Inclusions in Al-Ti-Deoxidized and Ca-Treated Steel". In: *Metallurgical and Materials Transactions B* 49.6 (2018), pp. 3534–3543. ISSN: 1073-5615. DOI: 10.1007/s11663-018-1410-9.
- [Zha13] Lifeng Zhang. "Nucleation, growth, transport, and entrapment of inclusions during steel casting". In: *JOM* 65.9 (2013), pp. 1138–1144. ISSN: 1047-4838. DOI: 10.1007/s11837-013-0688-y.

- [Zie+15] Tilo Zienert et al. “Interface reactions between liquid iron and alumina-carbon refractory filter materials”. In: *Ceramics International* 41.2, Part A (2015), pp. 2089–2098. DOI: 10.1016/j.ceramint.2014.10.004.
- [Zie+20] Tilo Zienert et al. “Characterization of the In Situ-Formed Oxide Layer at the Steel Melt/Carbon-Bonded Alumina Interface”. In: *Advanced Engineering Materials* 22.2 (2020), p. 1900811. ISSN: 14381656. DOI: 10.1002/adem.201900811.
- [Zie20] Tilo Zienert. *Festphasendiffusion von C an die Filteroberfläche ist unter den Bedingungen der Tauchversuche möglich: personal conversation*. Ed. by Anne Schmidt. 18.02.2020.
- [ZLJ16] Tongsheng Zhang, Chengjun Liu, and Maofa Jiang. “Effect of Mg on Behavior and Particle Size of Inclusions in Al-Ti Deoxidized Molten Steels”. In: *Metallurgical and Materials Transactions B* 47.4 (2016), pp. 2253–2262. ISSN: 1073-5615. DOI: 10.1007/s11663-016-0706-x.
- [ZS03] Liangyi Zhao and Veena Sahajwalla. “Interfacial Phenomena during Wetting of Graphite/Alumina Mixtures by Liquid Iron”. In: *ISIJ International* 43.1 (2003), pp. 1–6. ISSN: 0915-1559. DOI: 10.2355/isijinternational.43.1.
- [ZT00] L. Zhang and S. Taniguchi. “Fundamentals of inclusion removal from liquid steel by bubble flotation”. In: *International Materials Reviews* 45.2 (2000), pp. 59–82. ISSN: 0950-6608. DOI: 10.1179/095066000101528313.
- [ZT03a] Lifeng Zhang and Brian G. Thomas. *Inclusions in continuous casting of steel*. 2003.
- [ZT03b] Lifeng Zhang and Brian G. Thomas. “State of the Art in Evaluation and Control of Steel Cleanliness”. In: *ISIJ International* 43.3 (2003), pp. 271–291. ISSN: 0915-1559. DOI: 10.2355/isijinternational.43.271.

A. Preliminary tests: Slurry development

A.1. Coatings A and AC

In the beginning, it was observed that simply adding 6.25 mass% Carbores® P to the alumina spray-coating slurry of Emmel and Aneziris [EA13] resulted in strong segregation and sedimentation of the slurry as exemplified after 45 min in Figure A.1a. The segregation has easily been observed due to the different colours of the components: white - alumina, black - carbon, and yellowish/brown - lignin sulfonate. The extreme state is shown in Figure A.1b after 24 h. Thus, two parameters have been changed to enhance the slurry stability:

Particle size: The alumina CL 370 used by Emmel and Aneziris [EA13] was partly replaced by the finer¹ alumina MR 70. The ration between CL 370:MR 70 has been altered as follows: 100:0, 50:50, and 0:100. These were later extended to 75:25 and 25:75.

Content of ligning sulfonate: According to Emmel et al. [EA12; EA13], lignin sulfonate acts as wetting agent. Thus, its initial content of 1.5 mass% was changed to 0.75 mass% and 2.25 mass%.

All coating slurries were prepared as described in Section 3.2 on page 58. In addition to the photo documentation, the sedimentation tendency was quantified by determining the change of height of the sediment (h) in comparison to the filling height of the vessels (h_0), cf. Figure A.1d. The change of height is presented by the graphs of Figure A.2 for all investigated compositions. Usually, the slurry stability was documented directly after filling the glass vessel (0 min), after 2 min, 5 min, 10 min, 30 min and 60 min, as well as after 24 h. Thereby, the once filled glass vessels were sealed and stored undisturbed at room temperature. Only in the case of the two compositions with the ratio CL 370:MR 70 equals 100:0 and 0:100, both with 1.5 mass% lignin sulfonate, data points of 10 min, 30 min and 60 min were replaced

¹cf. Table 3.2 on page 56.

A. Preliminary tests: Slurry development

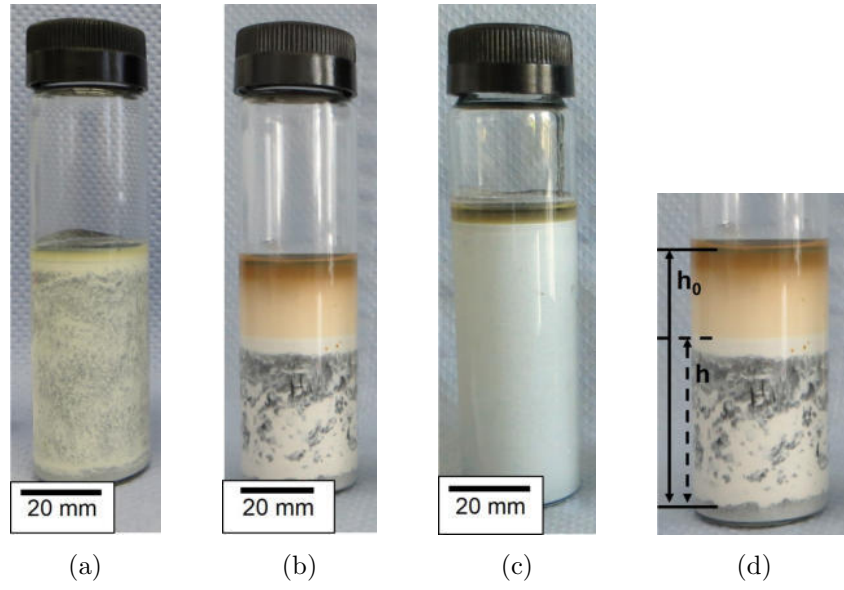


Figure A.1.: Slurry development AC: Decomposition of the carbonaceous alumina slurry based on the alumina coating slurry of Emmel and Aneziris [EA13] (1.5 mass% lignin sulfonate, 100% CL 370) after a) 45 min and b) after 24 h, compared with c) the stable composition chosen as final coating slurry AC within this thesis (1.5 mass% lignin sulfonate, ratio CL 370:MR 70 equals 25:75) after 24 h. d) detail of b) sediment height (h , dashed arrow and line) versus the filling height (h_0 , black arrow and line) used to evaluate the sedimentation tendency of the slurries.

A. Preliminary tests: Slurry development

by one data point after 45 min. After these two compositions, the documentation time was extended to the above described ones. As the information obtained by these two compositions were sufficient to assess their sedimentation behaviour, the missing data points had not been repeated. After mixing and filling the vessels to assess the stability of the slurries, their flow behaviour was determined as described in Section 3.4 on page 60. From one batch mixed slurries, three measurements with the rheometer were conducted.

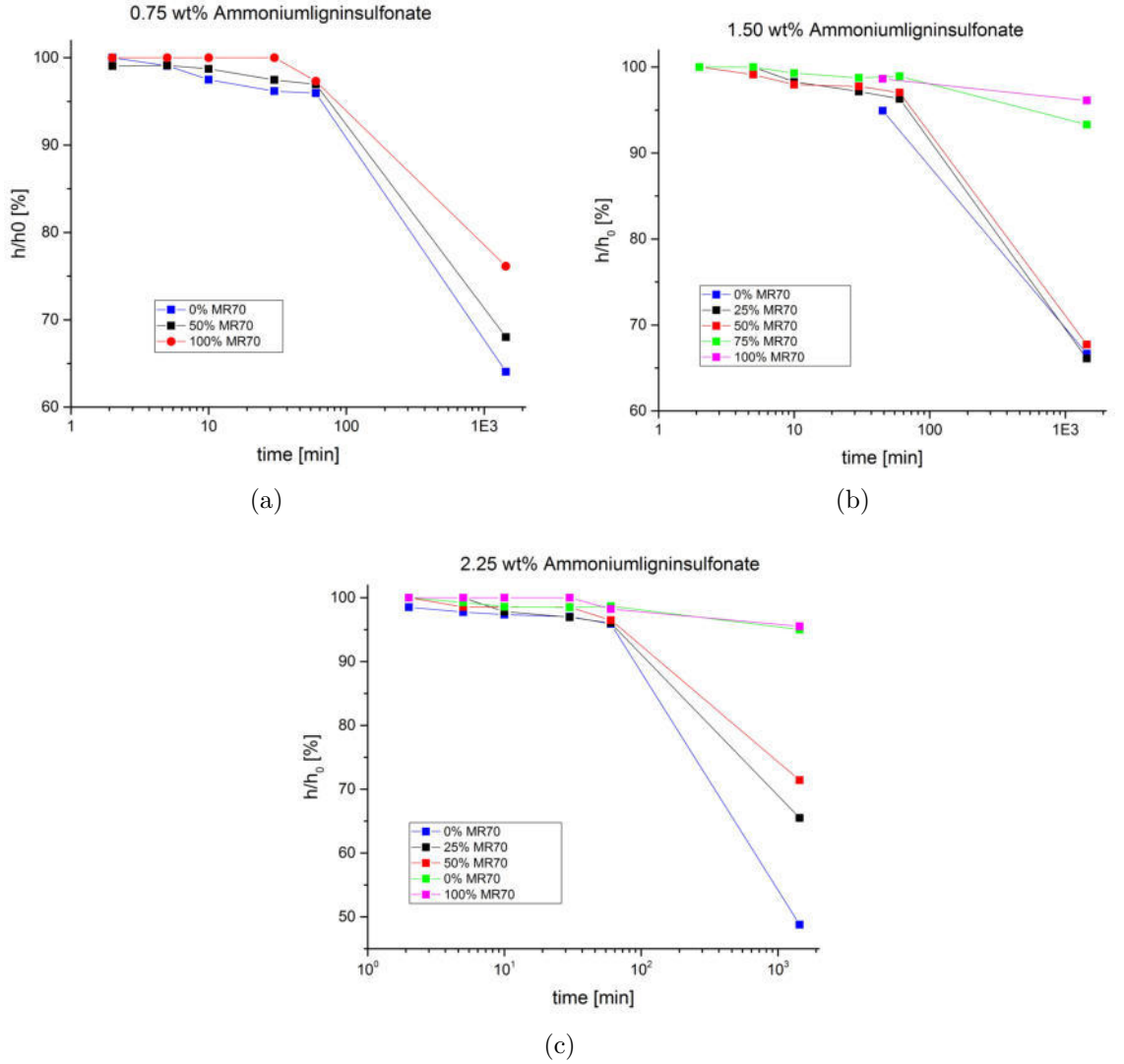


Figure A.2.: Slurry compositions with a) 0.75 mass% lignin sulfonate, b) 1.5 mass% lignin sulfonate, c) 2.25 mass% lignin sulfonate.

It was observed that—within the frame of the investigated parameters—the influence of the lignin sulfonate content was less significant compared to the particle size distribution (by substituting CL 370 with MR 70). Thereby, slurries with at least 75 % MR 70 in the alumina content and at least 1.5 mass% lignin sulfonate appeared sufficiently stable for the here used spray coating process. Thus, their dy-

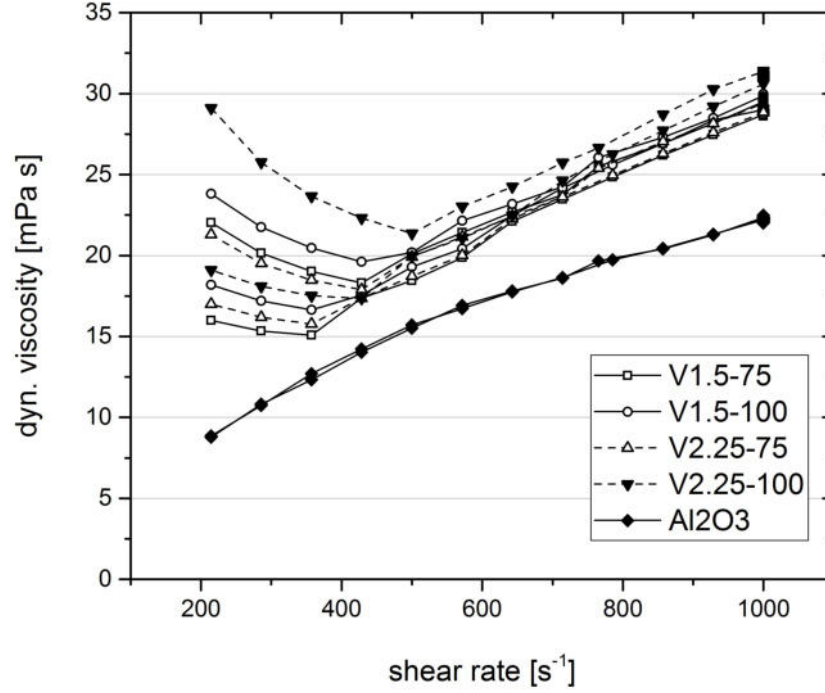


Figure A.3.: Slurry development AC - Rheology: dynamic viscosity vs. shear rate for the four stable slurry compositions: 1.5 mass% lignin sulfonate, ratio CL 370:MR 70 equals 25:75 (V1.5-75), 1.5 mass% lignin sulfonate, ratio CL 370:MR 70 equals 0:100 (V1.5-100), 2.25 mass% lignin sulfonate, ratio CL 370:MR 70 equals 25:75 (V2.25-75), 2.25 mass% lignin sulfonate, ratio CL 370:MR 70 equals 0:100 (V2.25-100), and the alumina coating—1.5 mass% lignin sulfonate, 100 % CL 370—slurry (Al₂O₃) according to Emmel and Aneziris [EA13]

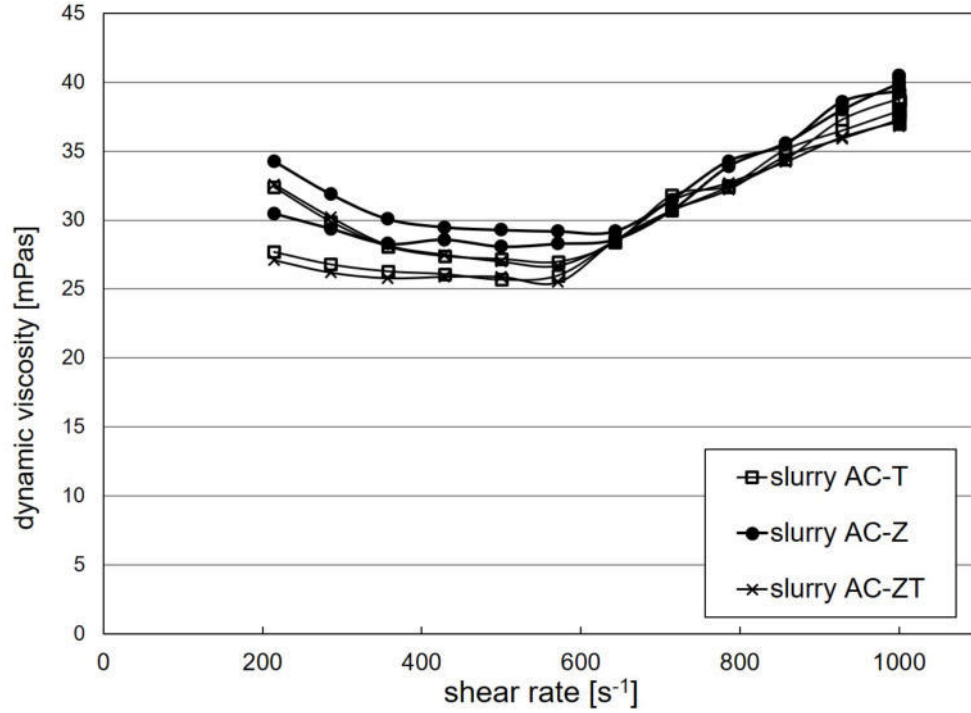


Figure A.4.: Slurry development zirconia and/or titania doped coatings - Rheology: dynamic viscosity vs. shear rate for the slurries AC-Z, AC-T, and AC-ZT.

dynamic viscosity is presented by Figure A.3. Their flow behaviour was quite similar and their dynamic viscosity at the highest shear rate ranged between 28 mPas to 32 mPas, which were higher than the one of the carbon-free alumina coating slurry developed by Emmel and Aneziris [EA13] (22 mPas). Nevertheless, these slurries were suitable for spray coating.

Based on the slurry stability and the resulting flow behaviour, the composition with the ration CL 370:MR 70 equals 25:75, and 1.5 mass% lignin sulfonate was chosen for the carbonaceous alumina coating (cf. Table 3.1, "AC"). By replacing the Carbores® P completely with the alumina raw materials in the appropriate ratio, the alumina coating ("A") was obtained.

A.2. AC coatings with ZrO₂ and/or TiO₂

Replacing alumina by the appropriate amount of zirconia, titania, and the mixture of both to obtain the desired doping amount resulted in sufficiently stable slurries. Thereby, the solids content of the slurries AC-Z, AC-T, and AC-ZT was higher than for slurries A and AC (65 mass%), i.e. 72.5 mass%. That resulted in an enhanced dynamic viscosity ranging from 37 mPas to 40 mPas at the highest shear rate as presented in Figure A.4. Nevertheless, these slurries were suitable for spray coating.

B. Filters with coating A or AC

B.1. Chemical and Phase analysis of the coating material

Figures B.1 and B.2 present the results from XRD characterisation of the coating materials A and AC, respectively.

B. Filters with coating A or AC

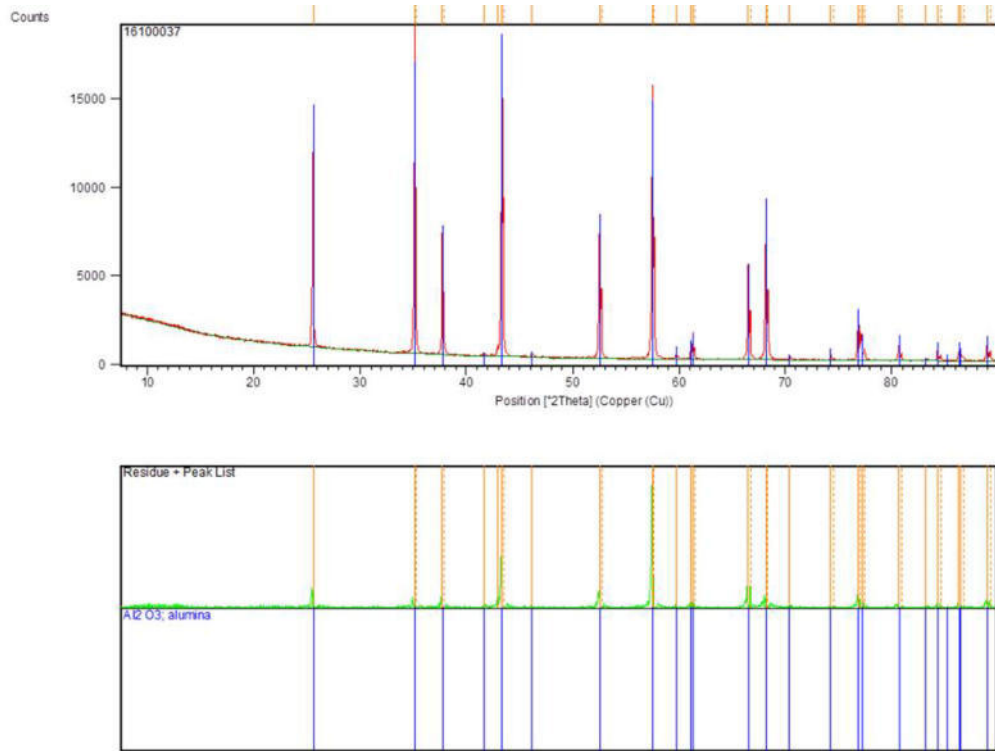


Figure B.1.: XRD of Coating A after coking.

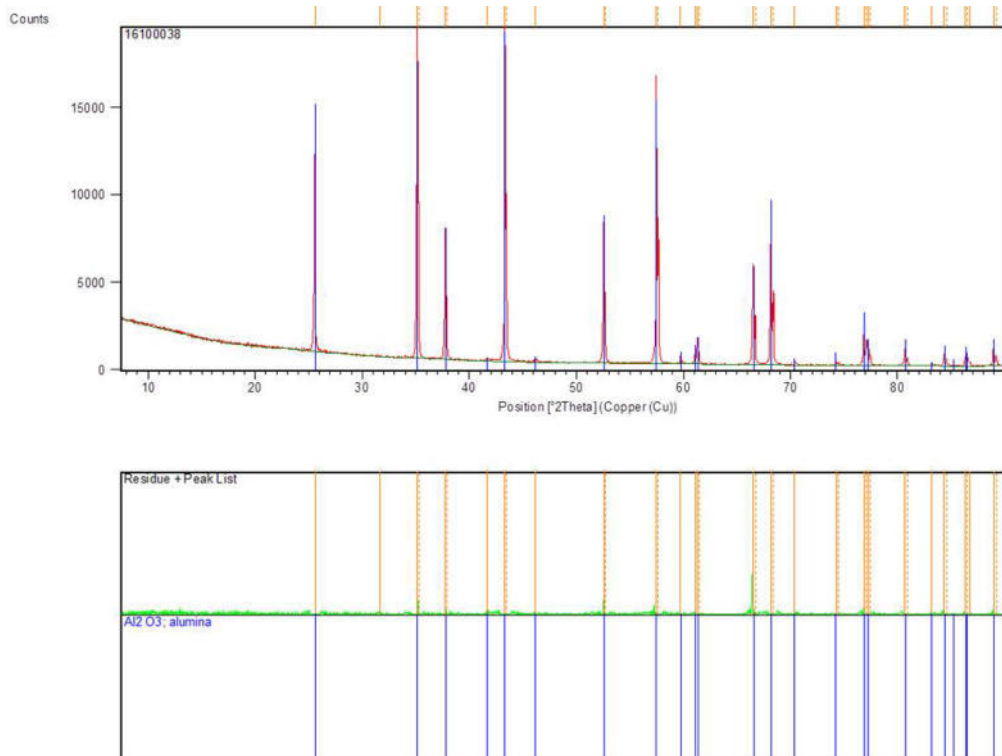


Figure B.2.: XRD of Coating A after coking.

B. Filters with coating A or AC

Figures B.3 and B.4 present the results from SNMS characterisation of the coating materials A and AC, respectively. The detected signals of copper and krypton derived from the characterisation method.

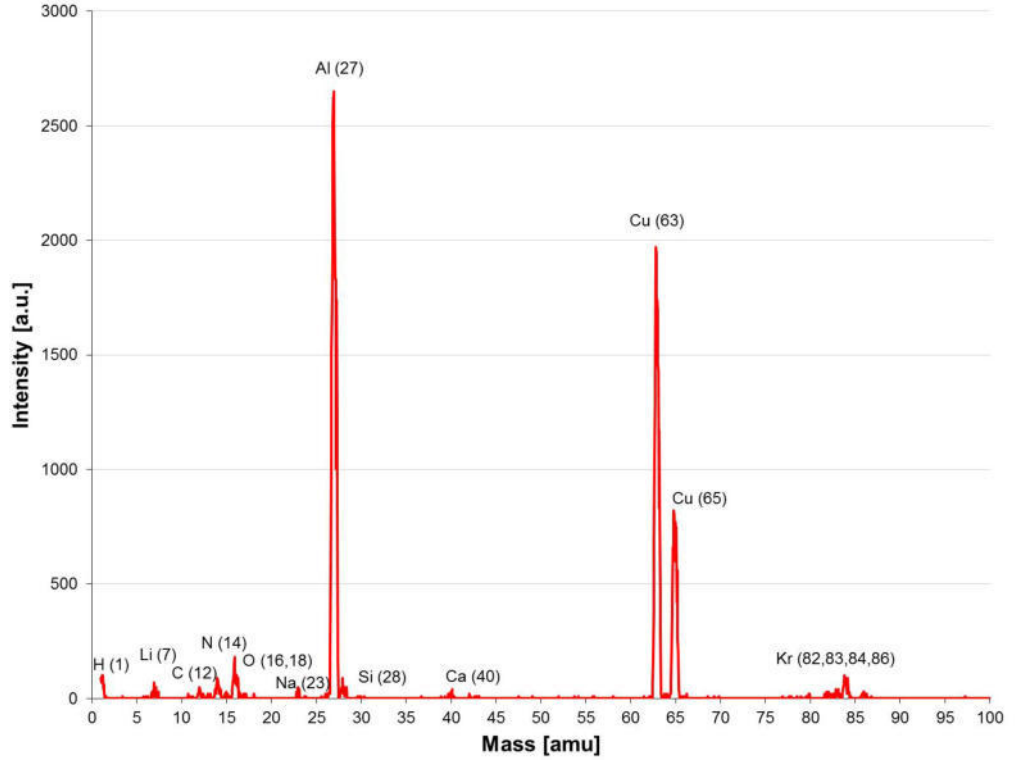


Figure B.3.: SNMS of an alumina coated filter.

Figure B.5 presents the thermal elongation of coated sample bars from room temperature up to 1400°C.

B. Filters with coating A or AC

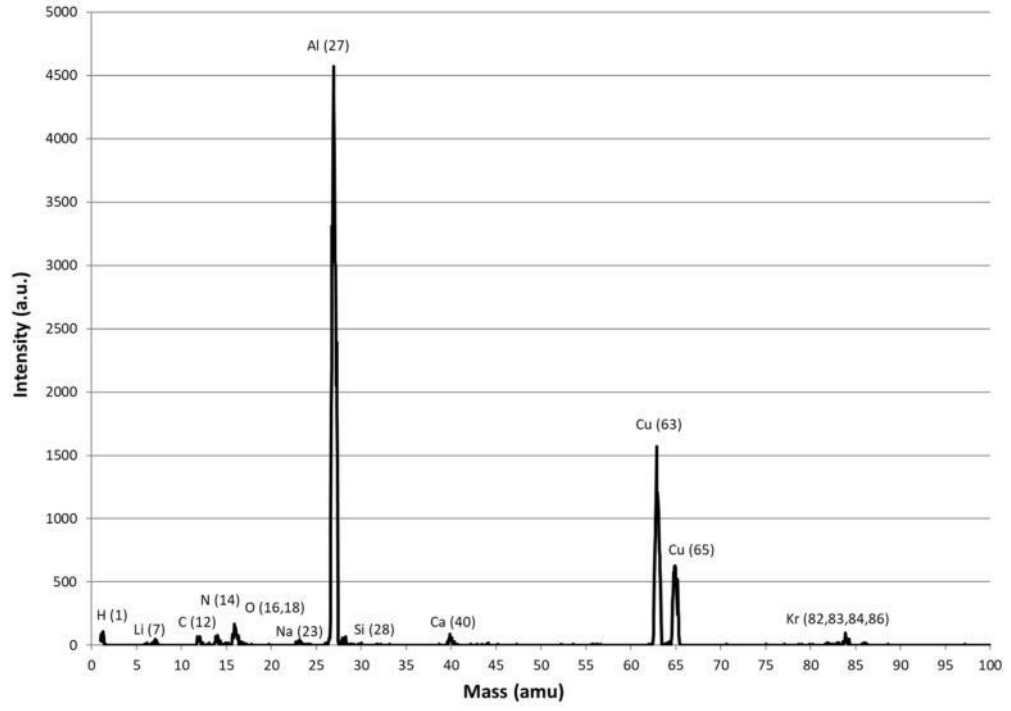


Figure B.4.: SNMS of an AC coated filter.

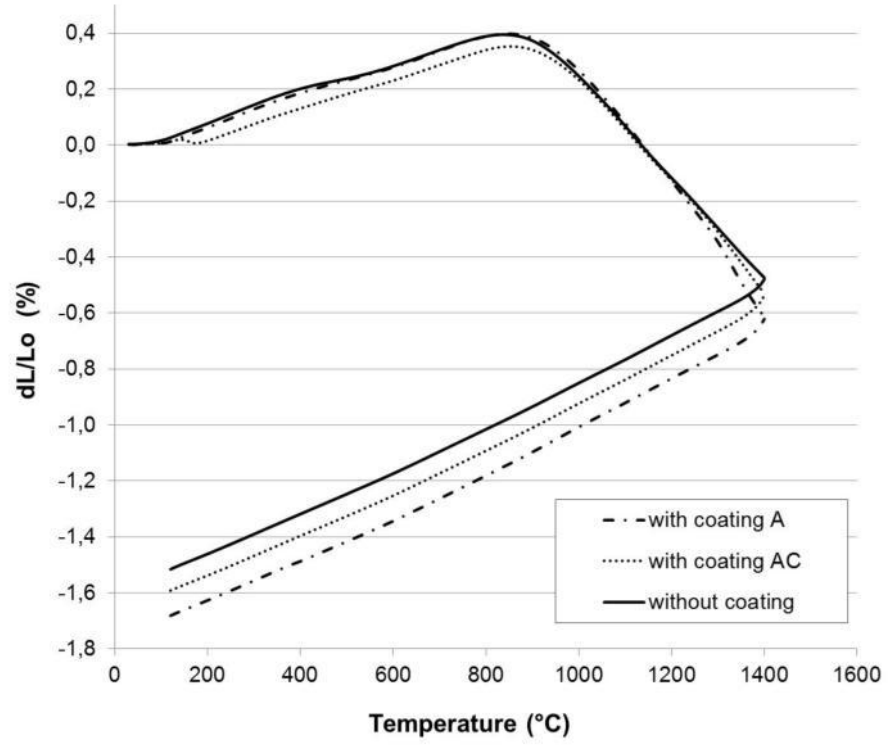


Figure B.5.: Shrinkage of alumina coated, carbonaceous alumina or uncoated samples.

Table B.1.: Parameter of the immersion trials with varying immersion duration of filters A and AC. The logged oxygen content (a_O) and the temperature (T) of the steel melt were determined after remelting (stage 1), the oxidation step (stage 2), the deoxidation step (stage 3), and after immersing the corresponding filter (stage 4).

Filter type	immersion time (s)	a_O (ppm)				T (°C)			
		Stage				Stage			
		1	2	3	4	1	2	3	4
without filter		14.6	53.9	6.6	-	1642	1632	1627	-
A	10	16.0	58.9	7.2	22.4	1657	1642	1635	1653
A	30	17.0	53.5	6.2	19.5	1654	1632	1628	1637
A	60	11.7	53.4	7.0	25.6	1651	1646	1638	1660
A	120	24.4	74.6	10.3	29.3	1660	1663	1654	1662
AC	10	25.3	71.1	7.9	14.1	1672	1659	1641	1622
AC	30	17.3	60.0	9.4	14.0	1657	1666	1654	1649
AC	60	17.5	61.6	12.5	27.3	1667	1655	1655	1665
AC	120	19.2	67.5	11.8	24.7	1657	1655	1645	1659

B.2. Parameters of the immersion trials

In the case of the alumina (A) and carbonaceous alumina (AC) coated filters, the molten steel was pretreated prior to immersing a filter sample. The pretreatment of the steel generated endogenous alumina inclusions. At four stages, the dissolved oxygen content and the temperature of the steel were determined, cf. Table B.1. First data was obtained after the steel was melted (stage 1). To oxidize the steel (stage 2), 0.5 mass% iron oxide, and for the subsequent deoxidation, 0.05 mass% aluminium (stage 3) were added. The quantity of both additives is referred to the steel mass. Finally, the dissolved oxygen content and temperature were determined again after immersing the corresponding filter (stage 4).

B.3. Microstructure characterisation

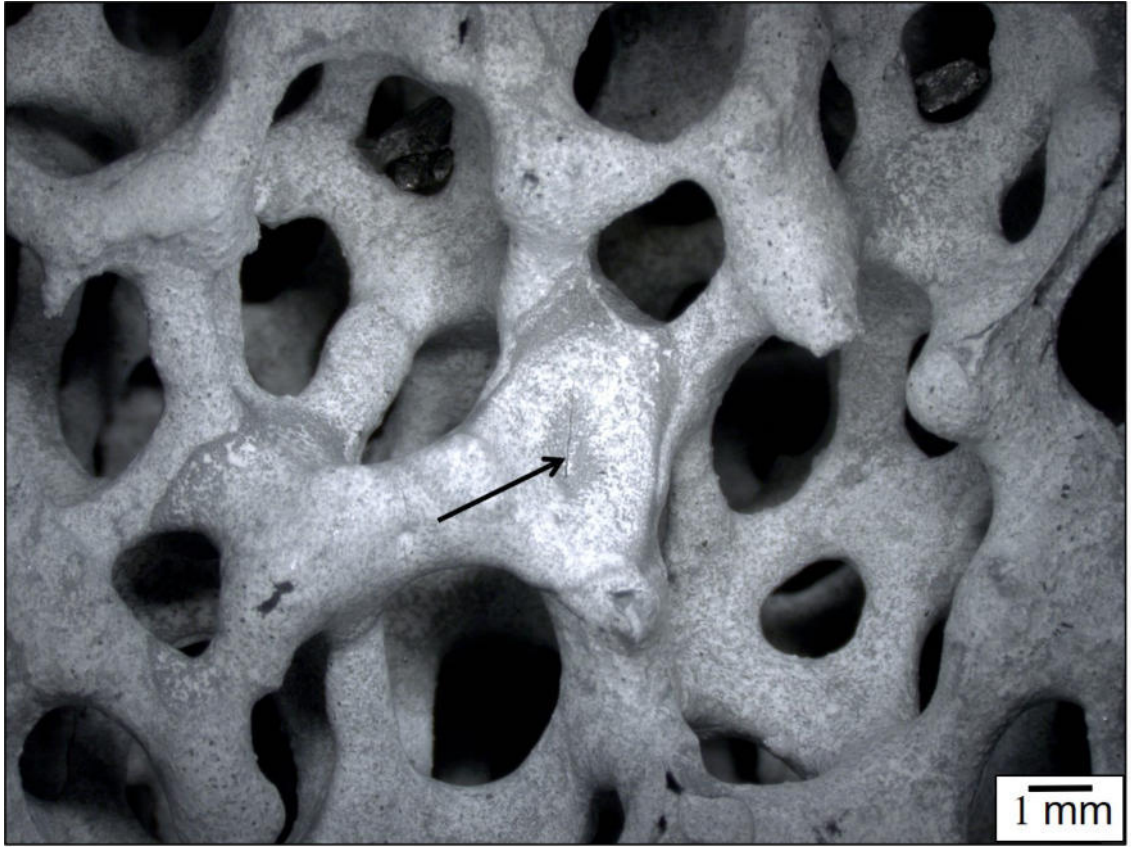


Figure B.6.: Microstructure of an AC coated filter after coking by light microscopy.
The black arrow highlights a crack caused by coating accumulations near a filter knot.

B. Filters with coating A or AC

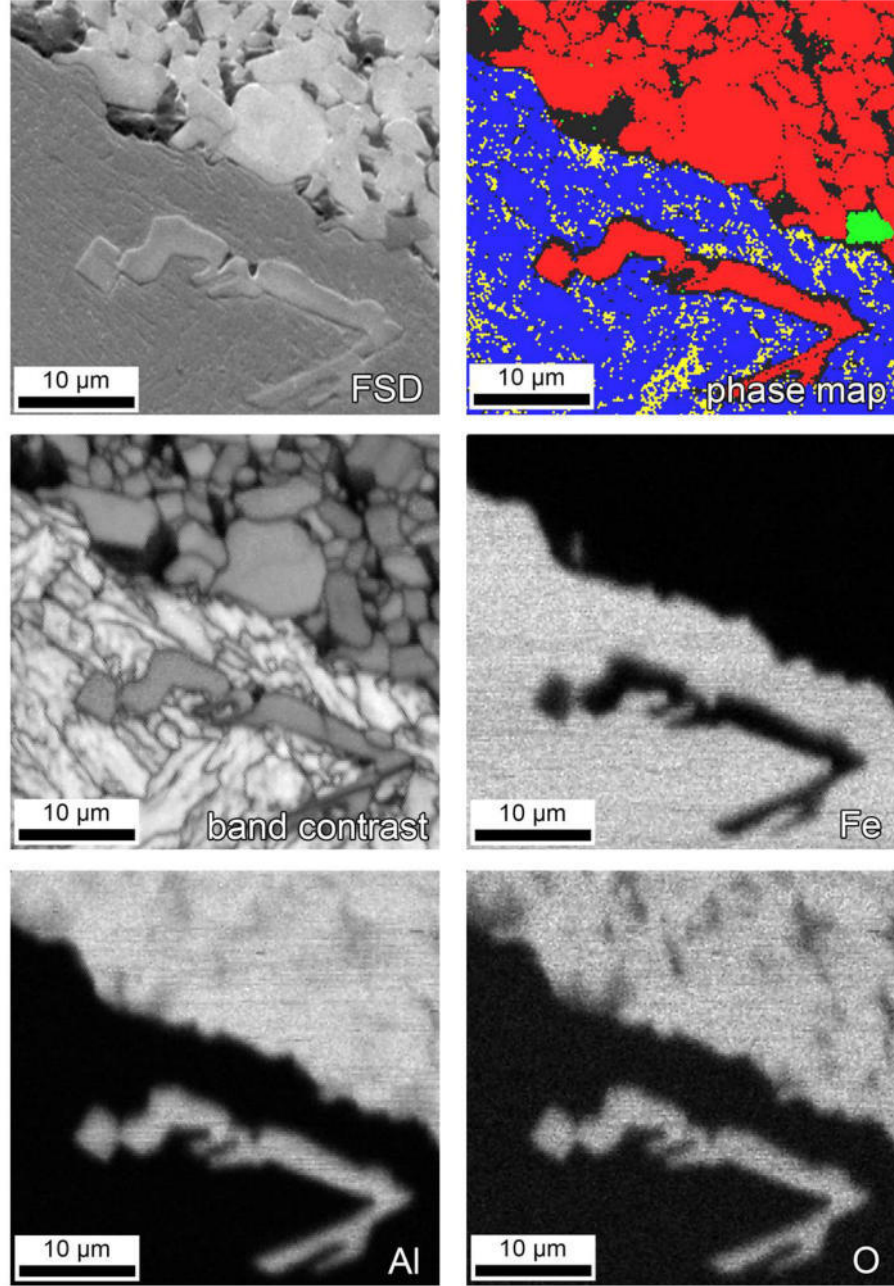


Figure B.7.: Phase distribution (red: α - Al_2O_3 , blue: α -Fe, yellow γ -Fe and green: spinel), crystallinity (band contrast) and element distribution (O, Fe and Al) by EDS and EBSD. Filter A immersed for 120 s

B. Filters with coating A or AC

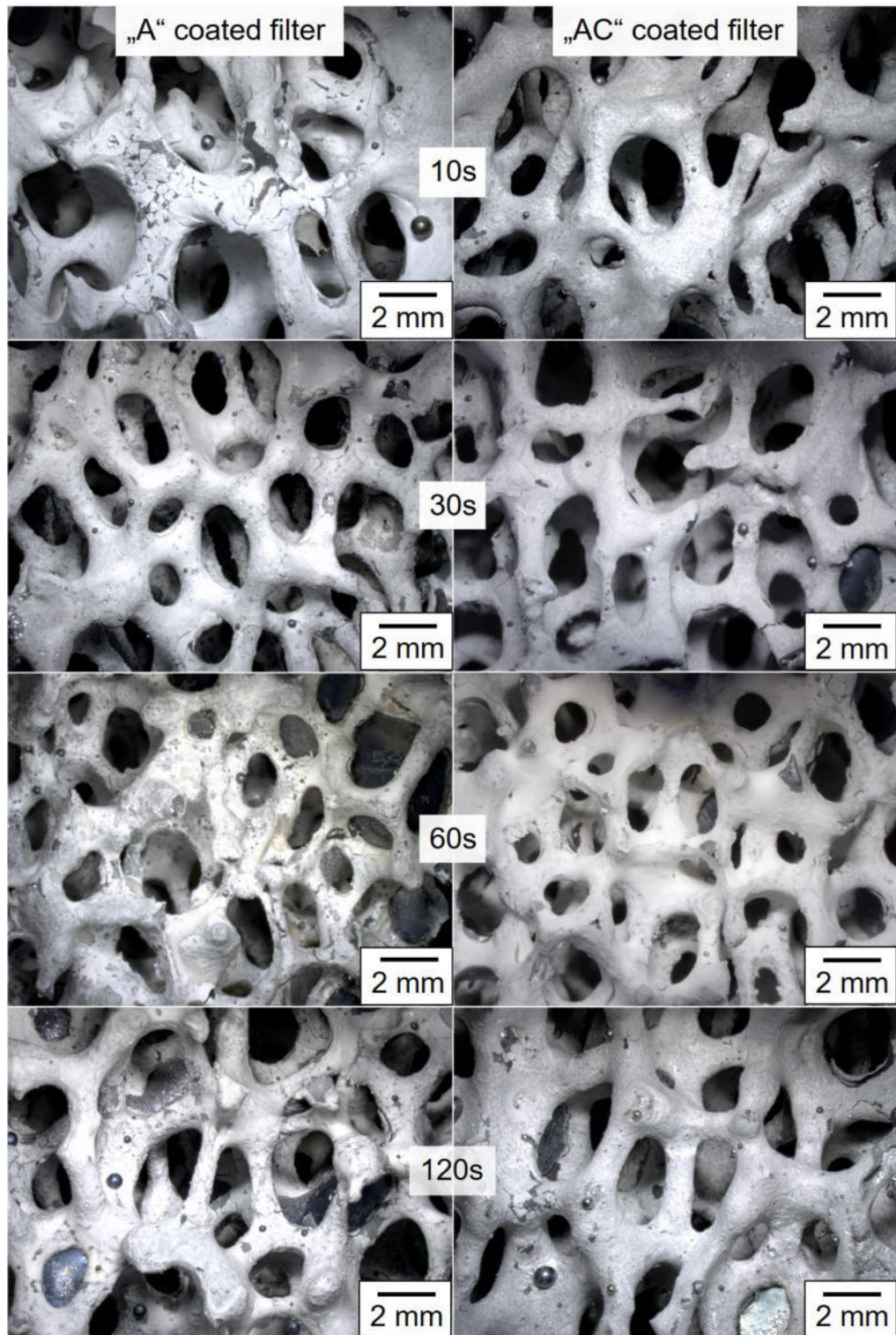


Figure B.8.: Microstructure of immersed filters by light microscopy. Left column: alumina coated filters ("A"), right: "AC" coated filters. From top to bottom increasing immersion times: 10 s, 30 s, 60 s, and 120 s.

B.4. Steel composition

Table B.2.: Chemical composition (complete) of the steel before and after the immersion tests of the alumina coated filters. Sample "without filter" refers to the remelting trial with a dwell time of 15 min after the pre-treatment.

Element	Content in the steel sample (mass%)						max.
	as	without	Dwell time of the immersed filter (s)				standard
	received	filter	10	30	60	120	deviation
Fe	97.2	97.5	97.3	97.4	97.3	97.4	0.15
C	0.407	0.350	0.339	0.331	0.348	0.316	0.024
Si	0.243	0.204	0.210	0.221	0.219	0.216	0.006
Mn	0.791	0.697	0.772	0.745	0.790	0.748	0.041
P	0.014	0.014	0.010	0.011	0.012	0.009	0.004
S	0.001	< 0.003	< 0.003	< 0.003	< 0.003	< 0.003	0.0 ¹
Cr	0.960	0.940	1.008	0.998	1.019	0.998	0.053
Mo	0.183	0.165	0.171	0.172	0.176	0.172	0.016
Ni	0.098	< 0.005	0.047	0.044	0.047	0.049	0.003
Al	0.035	0.016	0.002	< 0.001	< 0.001	0.003	0.001
Co	0.004	< 0.002	< 0.002	< 0.002	< 0.002	< 0.002	0.0 ¹
Cu	0.027	0.022	0.027	0.027	0.027	0.028	0.0009
Nb	0.001	0.002	0.008	0.006	0.005	0.009	0.003
Ti	0.002	0.004	< 0.001	0.002	0.002	0.002	0.0008
V	0.005	0.003	0.004	0.005	0.004	0.005	0.001
W	0.032	0.015	0.015	0.015	0.015	0.015	0.0035 ¹
Sn	0.003	0.002	0.002	0.002	0.002	0.002	0.0002 ¹
B	0.003	0.001	0.001	0.001	0.001	0.001	0.0001 ¹
Ca	0.0012	0.0001	0.0002	0.0002	0.0002	0.0002	0.001 ¹
Zr	0.0015	0.004	0.005	0.005	0.004	0.005	0.001
As	0.007	0.005	0.005	0.005	0.005	0.005	0.0 ¹

¹ below detection limit

Table B.3.: Chemical composition (complete) of the steel before and after the immersion tests of the AC coated filters. Sample "without filter" refers to the remelting trial with a dwell time of 15 min after the pre-treatment.

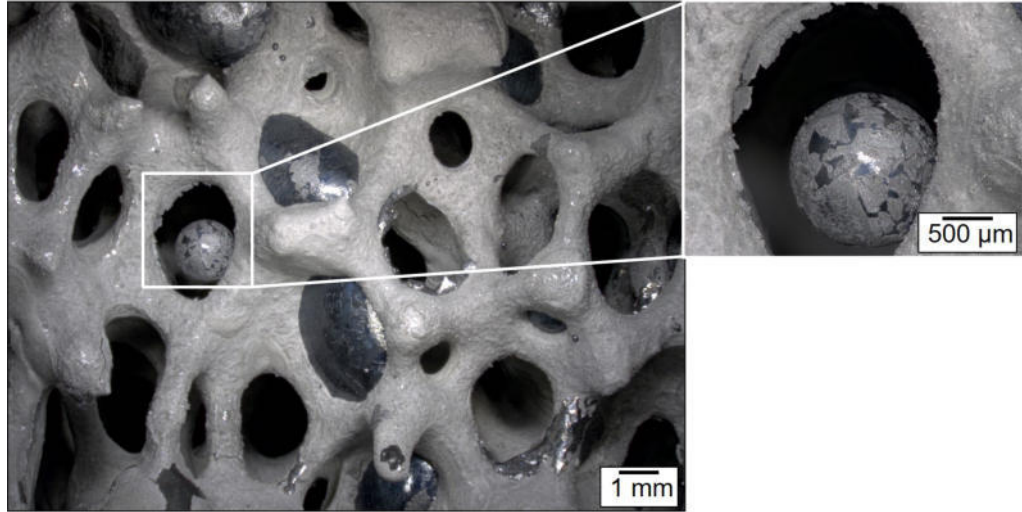
Element	Content in the steel sample (mass%)						max.
	as	without	Dwell time of the immersed filter (s)				standard
	received	filter	10	30	60	120	deviation
Fe	97.2	97.5	97.4	97.3	97.4	97.3	0.12
C	0.407	0.350	0.338	0.346	0.337	0.342	0.01
Si	0.243	0.204	0.213	0.213	0.209	0.215	0.01
Mn	0.791	0.697	0.747	0.771	0.739	0.757	0.022
P	0.014	0.014	0.012	0.012	0.010	0.013	0.002
S	0.001	< 0.003	< 0.003	< 0.003	< 0.003	< 0.003	0.0 ¹
Cr	0.960	0.940	0.992	1.004	0.975	0.994	0.023
Mo	0.183	0.165	0.178	0.175	0.166	0.174	0.007
Ni	0.098	< 0.005	0.051	0.049	0.043	0.049	0.005
Al	0.035	0.016	0.002	0.008	0.004	0.003	0.0012
Co	0.004	< 0.002	< 0.002	< 0.002	< 0.002	< 0.002	0.0 ¹
Cu	0.027	0.022	0.028	0.028	0.026	0.027	0.0013
Nb	0.001	0.002	0.006	0.004	0.004	0.004	0.004
Ti	0.002	0.004	0.002	0.002	0.001	0.002	0.0008
V	0.005	0.003	0.004	0.004	0.003	0.004	0.001
W	0.032	0.015	0.015	0.016	0.015	0.015	0.0035 ¹
Sn	0.003	0.002	0.002	0.002	0.002	0.002	0.0002 ¹
B	0.003	0.001	0.001	0.001	0.001	0.001	0.0001 ¹
Ca	0.0012	0.0001	0.0003	0.0002	0.0002	0.0002	0.0001 ¹
Zr	0.0015	0.004	0.004	0.005	0.003	0.004	0.001
As	0.007	0.005	0.005	0.005	0.005	0.005	0.0 ¹

¹ below detection limit

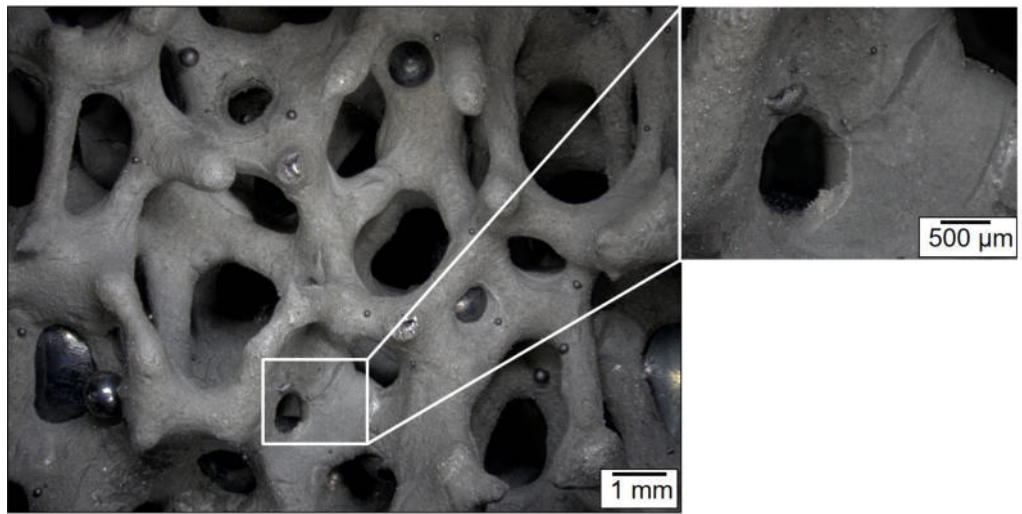
C. Supplement information for the filters with ZrO_2 and/or TiO_2 in the coating

If zirconia is added to the carbonaceous alumina coating, many free-standing, thin films remained in the macro-pores and the remaining steel beads were covered by a bright layer, as presented by the detailed views given in Figure C.1.

Table C.1 presents all elements determined by arc spark optical emission spectrometer (OES). Eight measurements were performed. The mean value for each sample and the maximum standard deviation for all measured samples is given in Table C.1.



(a)



(b)

Figure C.1.: Supplement information: Microstructure after immersion by light microscopy, filters AC-Z (a) and AC-ZT (b).

Table C.1.: Chemical composition of the steel before and after the immersion tests. Sample “without filter” refers to a trial, during which molten steel melt and held for 15 min, but no filter immersed. Mean values of eight measurements on one sample.

Element	composition (mass%)										max. standard deviation
	as received	without filter	immersed filter type								
			uncoated	A	AC	AC-T	AC-Z	AC-ZT			
Fe	97.32	97.32	97.35	97.44	97.40	97.4	97.36	97.27	0.088		
C	0.394	0.354	0.365	0.343	0.340	0.361	0.369	0.374	0.012		
Si	0.230	0.231	0.229	0.229	0.231	0.236	0.234	0.239	0.011		
Mn	0.691	0.698	0.672	0.653	0.665	0.648	0.666	0.696	0.027		
P	0.077	0.071	0.072	0.069	0.072	0.070	0.070	0.077	0.006		
S	0.013	0.014	0.016	0.015	0.015	0.015	0.014	0.015	0.002		
Cr	0.947	1.002	0.997	0.953	0.973	0.956	0.972	1.007	0.035		
Mo	0.169	0.168	0.178	0.167	0.175	0.174	0.173	0.182	0.014		
Ni	0.059	0.062	0.055	0.057	0.058	0.057	0.055	0.058	0.005		
Cu	0.025	0.024	0.024	0.025	0.024	0.025	0.024	0.026	0.001		
Al	0.029	0.018	0.008	0.009	0.015	0.017	0.021	0.014	0.001		
Co	0.005	0.005	0.005	0.004	0.005	0.005	0.005	0.005	0.002		
Nb				<0.005					-		
Ti	0.0031	0.0033	0.0034	0.0029	0.0032	0.0033	0.0032	0.0036	0.0004		
V	0.005	0.005	0.004	0.004	0.004	0.004	0.004	0.004	0.000		
W	0.024	<0.02	<0.02	0.022	<0.02	0.024	0.023	0.021	0.01		
B				<0.001					-		
Sn	0.005	0.006	0.006	0.005	0.005	0.006	0.006	0.006	0.001		